

**Kinematic Signatures of Galaxy Evolution: The Energetics
of AGN Outflows and the Accurate Identification of
Merging Galaxies**

by

Rebecca Nevin

B.A., Whitman College, 2013

M.S., University of Colorado, 2016

A thesis submitted to the
Faculty of the Graduate School of the
University of Colorado in partial fulfillment
of the requirements for the degree of
Doctor of Philosophy
Department of Astrophysics and Planetary Science

2019

This thesis entitled:
Kinematic Signatures of Galaxy Evolution: The Energetics of AGN Outflows and the
Accurate Identification of Merging Galaxies
written by Rebecca Nevin
has been approved for the Department of Astrophysics and Planetary Science

Prof. Julia Comerford

Prof. Mitchell Begelman

Prof. Jeremy Darling

Dr. Benjamin Oppenheimer

Prof. Bryan Zahartos

Date _____

The final copy of this thesis has been examined by the signatories, and we find that both the content and the form meet acceptable presentation standards of scholarly work in the above mentioned discipline.

Nevin, Rebecca (Ph.D., Astrophysics)

Kinematic Signatures of Galaxy Evolution: The Energetics of AGN Outflows and the Accurate Identification of Merging Galaxies

Thesis directed by Prof. Julia Comerford

Both galaxies and supermassive black holes grow and evolve over cosmic time. My work utilizes the kinematics of the stars and gas in galaxies to investigate some key processes that drive this evolution: Active galactic nucleus (AGN) feedback and galaxy mergers. I will first present my work modeling AGN-driven biconical outflows and examine the potential for these biconical outflows to drive feedback that regulates star formation in their host galaxies. Then, I will focus on merging galaxies, and how progress in our understanding of galaxy evolution is slowed by the difficulty of making accurate galaxy merger identifications. My approach to improving the accuracy of galaxy merger identification involves using N-body/hydrodynamical simulations of merging galaxies to create mockup images and kinematic maps of galaxies that match the specifications of observational surveys. From these, I create a classification tool that identifies merging galaxies of different gas fractions, mass ratios, and merger stages. I will discuss the strengths and limitations of the classification technique and then my plans to apply the classification to Sloan Digital Sky Survey imaging as well as the >10,000 observed galaxies in the MaNGA (Mapping Nearby Galaxies at Apache Point) integral field spectroscopy survey. Through accurate identification of merging galaxies in the MaNGA survey, I will advance our understanding of supermassive black hole growth in galaxy mergers and other open questions related to galaxy evolution.

Acknowledgements

This work would not have been possible without a ton of support from both my excellent research group and my external support network of family and friends. Also, being part of a supportive scientific community has made a huge difference to me. I have felt accepted by both the AGN outflow community as well as the MaNGA community.

Thanks goes to all of my excellent mentors on all levels; there are too many to list, the people who have inspired me to pursue science, science communication, and science writing.

Thanks to my boss, Julie, who is so much more than a boss. I was so proud to be your first PhD student!

Thank you to my brilliant friends, who have helped me with aggravating coding problems, machine learning queries, and have been a phenomenal source of emotional support. All of you are so important.

Thanks to my extremely handsome and supportive boyfriend Killian, who will (hopefully) be receiving an honorary PhD along with mine.

I would lastly like to acknowledge half-caf americanos: Without you, this work would not have been completed. You are the perfect amount of caffeine without the jitters.

Contents

Chapter

1	Introduction	1
1.1	Galaxy Evolution	1
1.2	The Importance of AGN for Galaxy Evolution	4
1.2.1	The Kinematics of AGN Outflows	16
1.3	The Importance of Galaxy Mergers for Galaxy Evolution	19
1.3.1	The Kinematics of Galaxy Mergers	22
1.4	Tools of the Trade	30
1.4.1	Longslit Spectroscopy	30
1.4.2	Integral Field Spectroscopy	31
1.4.3	Imaging	34
1.5	Summary of the Following Thesis Work	37
2	The Origin of Double-Peaked Narrow Lines in AGN II: Kinematic Classifications for the Population at $z < 0.1$	39
2.1	Introduction	39
2.2	Methods	43
2.2.1	Sample Selection	43
2.2.2	Data Reduction	45
2.2.3	Extracting and Characterizing OIII Profiles	45

2.2.4	The Luminosity of the NLR	52
2.3	Analysis	53
2.3.1	Kinematic Classification	53
2.4	Results	68
2.4.1	Kinematic Classification	68
2.5	Discussion	77
2.5.1	What are the expected kinematic classifications of dual AGNs?	77
2.5.2	A size-luminosity relationship for the NLR reveals the nature of the photoionized region	80
2.6	Conclusions	88
3	The Origin of Double-Peaked Narrow Lines in Active Galactic Nuclei III: Feedback from Biconical AGN Outflows	90
3.1	Introduction	90
3.2	Methods	93
3.2.1	Selection Criteria for Analytic Modeling	93
3.2.2	Analytic Outflow Models	96
3.2.3	Markov Chain Monte Carlo parameter estimation	104
3.2.4	Verifying the Models	111
3.3	Results	113
3.3.1	Bicone and Disk Orientation	113
3.3.2	Energy Diagnostics	114
3.4	Discussion	117
3.4.1	This sample of biconical outflows is biased to be very large and energetic	117
3.4.2	The biconical outflows in this sample are large and energetic	119
3.4.3	Selection, illumination, and obscuration effects explain the best fit models	124

3.4.4	The outflows have random orientations	128
3.4.5	Type 1 vs Type 2 AGNs	130
3.4.6	The outflows are energetic enough to drive feedback	132
3.5	Conclusion	135
4	Accurate Identification of Galaxy Mergers with Imaging	137
4.1	Introduction	138
4.2	Methods	140
4.2.1	N-body/Hydrodynamics Merger Simulations	140
4.2.2	Radiative Transfer Simulations	142
4.2.3	SDSS-izing images from the simulations	146
4.2.4	Measuring Stellar Bulge Separations	152
4.2.5	Creating the Classification Scheme	153
4.3	Results	168
4.3.1	Analyzing the LD1 Coefficients	168
4.3.2	Observability Timescales	171
4.4	Discussion	176
4.4.1	The signs of the LD1 coefficients are consistent with previous work	176
4.4.2	LDA lengthens the timescale of observability of merging galaxies	181
4.4.3	The coefficients of LD1 change with mass ratio	186
4.4.4	The coefficients of LD1 do not change (significantly) with gas fraction	189
4.4.5	The LDA technique is accurate and precise at identifying merging galaxies	190
4.4.6	Testing the Technique on SDSS Galaxies	194
4.5	Conclusion	200
5	Accurate Identification of Galaxy Mergers with Kinematics	202
5.1	Introduction	203

5.2	Methods	207
5.2.1	GADGET-3/SUNRISE Overview	207
5.2.2	Preparing Mock MaNGA Kinematic Maps	210
5.2.3	AGN Contamination	217
5.2.4	Comparing Velocity Maps	220
5.2.5	Preparing Kinematic Predictors	220
5.2.6	Linear Discriminant Analysis	230
5.3	Results	231
5.3.1	LDA Data Preparation	231
5.3.2	Predictor Selection	235
5.3.3	Classification Results	237
5.3.4	Observability Timescale	244
5.3.5	Accuracy and Precision	245
5.4	Discussion	246
5.4.1	The behavior of the LD1 coefficients are consistent with previous work	246
5.4.2	The predictors evolve non-linearly with time; the LDA incorporates this behavior	257
5.4.3	The classification changes with mass ratio	258
5.4.4	The classification does not change with gas fraction	260
5.4.5	The observability timescale is long for most runs but shorter than for the imaging technique	260
5.4.6	The kinematic LDA is precise but not accurate at identifying merging galaxies	262
5.4.7	LDA is one of many statistical and machine learning classification tech- niques; it has limitations and advantages	263
5.5	Preliminary Conclusions	264

6	Conclusion	267
	Bibliography	271
	Appendix	
A	Appendix of Tables	287
B	Appendices of Chapters 3 and 4	309
B.1	Investigating Outflow vs Rotational Kinematics	309
B.2	18 Biconical Models	319
B.3	Initial Conditions	323
B.4	Merging Galaxy Priors	324
B.5	Testing the Assumptions of LDA with Multivariate Analysis	326
B.6	Forward Stepwise Variable Selection and k-fold Cross-Validation	332
B.7	LDA Performance: Accuracy and Precision of the Classifier	334

Tables

Table

A.1	Summary of longslit observations	287
A.2	Measured Luminosities	288
A.3	Kinematic Classification Part 1	289
A.4	Kinematic Classification Part 2	290
A.5	Kinematic Classification Statistics	291
A.6	Rotation-dominated galaxy velocity separation	291
A.7	Summary of observations for outflows	292
A.8	Best fit biconical models	293
A.9	Symmetric bicone model parameters	293
A.10	Asymmetric bicone model parameters	294
A.11	Nested bicone model parameters	294
A.12	J0930+3430 outflow model parameters	295
A.13	Alignment of bicones	296
A.14	Energy diagnostics	297
A.15	Mass outflow rates from the literature	298
A.16	AGN host galaxies and matched sample	299
A.17	J0749+4514 IFS and longslit model	301
A.18	GADGET-3/SUNRISE simulations	301
A.19	Isolated simulated galaxies parameters	301

A.20 LDA coefficients	302
A.21 LDA coefficients for interaction terms	303
A.22 Observability timescales	304
A.23 LDA performance	304
A.24 Key simulation parameters and matched isolated galaxies.	304
A.25 LD1 predictor coefficients prior to the predictor selection	305
A.26 The final primary LD1 coefficients for the kinematic classification with and without interaction terms	306
A.27 LD1 interaction coefficients for the kinematic classification	307
A.28 LDA observability time for the kinematic classification	308
A.29 Accuracy and precision of the kinematic LDA classification	308

Figures

Figure

1.1	The dichotomy of local galaxies on the color-mass diagram	3
1.2	The observed galactic stellar mass function and the halo mass function . . .	8
1.3	Feedback from a powerful quasar-driven outflow	14
1.4	Bolometric luminosity function for AGN	15
1.5	Rotation curves of spiral galaxies	24
1.6	Slow and fast rotators	26
1.7	Example longslit observation	32
2.1	Akaike emission line fitting	46
2.2	Multiple Gaussian fitting	48
2.3	Asymmetry measurement for emission lines	50
2.4	Spatial centroiding of emission lines in 2D spectra	51
2.5	Toy model of a dual AGN	54
2.6	Toy model from a different PA	55
2.7	J1018+5127 emission profiles	57
2.8	Kinematic classification scheme for DPAGN	59
2.9	Cartoon of main kinematic classifications	61
2.10	‘Outflow’ profiles	64
2.11	‘Ambiguous’ and ‘Rotation Dominated’ profiles	66

2.12	SDSS images of ‘Ambiguous’ and ‘Rotation Dominated’ galaxies	67
2.13	Simulating Gaussian noise in a spectrum	71
2.14	Asymmetry of rotation-dominated galaxies	74
2.15	OIII and H α profiles of J1018+5127	78
2.16	J1018+5127 profiles	81
2.17	Size-luminosity relationship for the NLR	84
3.1	Integrated SDSS OIII profiles	97
3.2	Different biconical outflow models	99
3.3	Three bicone models with example velocity profiles	101
3.4	Best fit model for J0930+3430	105
3.5	Triangle plot for MCMC parameters	109
3.6	Four observed PAs for J0930+3430	112
3.7	Comparison of outflow energetics from the literature	121
3.8	sSFR vs outflow energy for outflow host galaxies	133
4.1	Mock images	147
4.2	Mock images over time	148
4.3	Predictor histograms (pre-LDA)	165
4.4	Major merger LDA histograms	166
4.5	Minor merger LDA histograms	167
4.6	Color visualization of predictor importance	170
4.7	<i>Gini</i> – M_{20} predictor space	172
4.8	<i>CA</i> predictor space	173
4.9	$n - A_S$ predictor space	174
4.10	LD1 values with time	177
4.11	Time evolution of predictors for a major merger simulation	182
4.12	Time evolution of predictors for a minor merger simulation	183

4.13 GalaxyZoo re-classification	198
4.14 GalaxyZoo spiral galaxies	199
5.1 Images and stellar velocity maps for the q0.5_fg0.3 simulation	211
5.2 Median trend of S/N with wavelength for MaNGA galaxies	215
5.3 Illustration of the process of MaNGA-izing datacubes	216
5.4 AGN contamination	218
5.5 Stellar kinematic comparison between GADGET-3 and SUNRISE	221
5.6 The bounded Absolute Radon Transform	223
5.7 kinemetry fit and kinemetry residuals	228
5.8 Box and whisker plot for the predictors for the q0.2_fg0.3_BT0.2 simulation .	234
5.9 Ellipticity (ϵ) trend with v_{asym}	236
5.10 LD1 histograms for the major merger kinematic classifications	238
5.11 LD1 histograms for the minor merger kinematic classifications	239
5.12 The changing sensitivity of LD1 for the kinematic classifications	243
5.13 Kinematic classification confusion matrices	245
5.14 Time evolution in $\Delta\text{PA}-A_2$ predictor space	248
5.15 Time evolution in $v_{\text{asym}}-\sigma_{\text{asym}}$ predictor space	252
5.16 Time evolution in $\lambda_{R_e}-\epsilon$ predictor space	255
B.1 IFS maps for J0749+4514	312
B.2 Longslit PAs for J0749+4514	315
B.3 As Figure 3.3, but for the remaining 15 galaxies not shown there.	322
B.4 LDA accuracy with prior choice	327
B.5 Histograms of predictor values	330
B.6 Hinton visual correlation matrix	331
B.7 Variable Selection for the LDA	332
B.8 Confusion matrices for LDA	336

Chapter 1

Introduction

In this introductory chapter, I will cover some relevant motivation for my thesis work. In Section 1.1, I will introduce and provide a framework for galaxy evolution. Then, I will focus on the evolution of Active Galactic Nuclei (AGN) and the importance of AGN-driven feedback (Section 1.2). I will also focus on the importance of galaxy mergers for driving evolution (Section 1.3). I also incorporate an introduction to the kinematics of AGN and galaxy mergers in Sections 1.2.1 and 1.3.1, respectively. I will then introduce the tools of the trade; the observational techniques of optical longslit, integral field spectroscopy (IFS), and imaging in Section 1.4. Finally, I will foreshadow how this thesis work contributes to addressing some of the questions posed in this introduction in Section 1.5.

1.1 Galaxy Evolution

In the current Λ cold dark matter (Λ CDM) framework for structure formation in the universe, galaxies form as gas cools at the center of dark matter halos (e.g., White & Rees 1978; White & Frenk 1991; Cole et al. 2008). These galaxies then grow through gas accretion and mergers from small, irregular galaxies with high rates of star formation to large, quiescent galaxies with lower rates of star formation in the local universe (e.g., Glazebrook et al. 1995; Lilly et al. 1995; Giavalisco et al. 1996).

Observations of galaxy properties such as mass, star formation rate, and color find that there is also a dichotomy in measured properties for galaxies in the local universe. Not only

are galaxies evolving over cosmic time, but they are also actively undergoing evolutionary processes in the local universe. Figure 1.1 illustrates this dichotomy for local SDSS galaxies on the SFR-M (star formation rate and mass) parameter space. The galaxies are divided into a population of large and red galaxies and a population of smaller and blue star-forming galaxies. These two populations can also be described as different morphological types; the larger redder galaxies are generally elliptical, or early-type galaxies, and the smaller, diskier, and bluer galaxies are spiral, or late-type galaxies.

Here I use these trends to generally motivate galaxy evolution. However, these trends do not always hold, and much work in recent years has found that there are very interesting exceptions that offer clues into galaxy evolution. For instance, not all elliptical galaxies are ‘red and dead’ and not all disks are blue and actively star forming (e.g., Schawinski et al. 2014).

Over the lifetimes of galaxies, various processes are working to both transform the morphological structures of galaxies while simultaneously shutting down star formation. This cessation of star formation can take many forms, from violently expelling the gas from the galaxy, to simply preventing cold molecular gas from forming stars through pressure support; in all cases, I refer to the prevention or slowing of star formation as ‘quenching’ and the processes that couple energy to the gas to drive quenching as ‘feedback’, which I discuss in more detail in Section 1.2.

Many different processes can play a role in galaxy evolution, including both secular and environmental processes. Secular processes operate over a variety of timescales and are driven by the internal properties of a galaxy. For instance, morphological quenching, mass quenching, and AGN feedback can be considered ‘secular’ or internal evolutionary processes. Morphological quenching applies when the internal structure of a galaxy can affect its star formation. For instance, Bluck et al. (2014) find that the gravitational potential of a galaxy’s bulge can prevent the gas there from forming stars. Bars are also a form of morphological quenching, since they provide a mechanism for molecular gas to migrate, funneling gas into

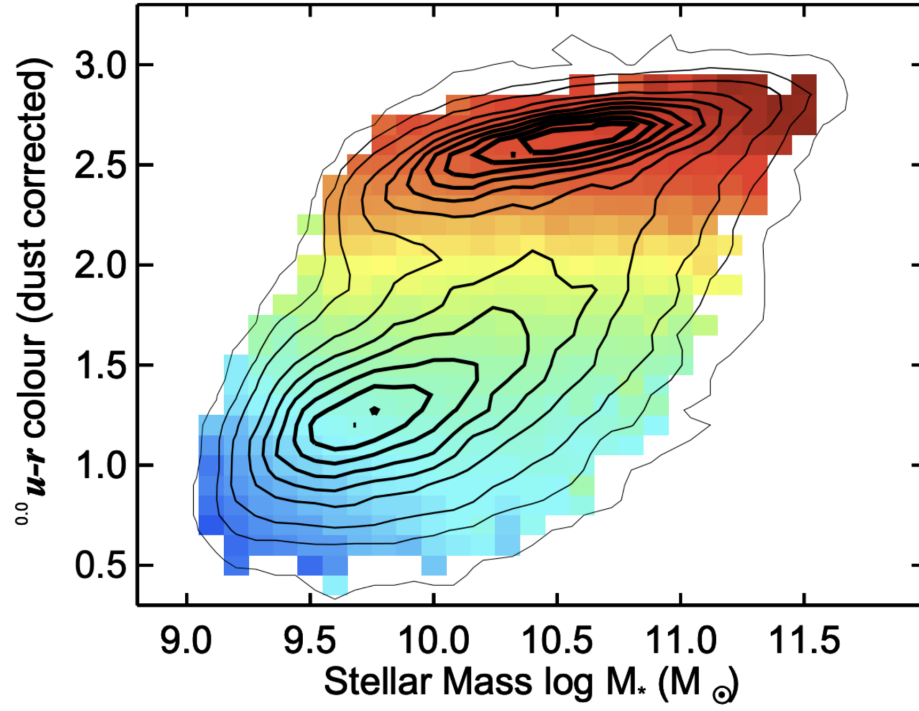


Figure 1.1: Color-mass diagram adapted from Schawinski et al. (2014). Local SDSS galaxies exhibit a dichotomy shown by the contours on this diagram. The color of each 0.1×0.1 dex panel corresponds to the specific star formation rate ($\text{sSFR} = \text{SFR}/M$) of galaxies in that bin. The bimodality shows a population of larger, red, relatively quenched galaxies (upper right) and a population of smaller, blue, star forming galaxies (lower left).

the central regions of a galaxy and leading to rapid and exhaustive star formation (Sheth et al. 2004). Mass quenching is any process that is dependent on a galaxy’s mass; supernova feedback could be a mass quenching mechanism (Peng et al. 2010, 2012). AGN feedback is discussed in great detail in Section 1.2.

Environmental processes happen externally and include mergers, tidal disruption from galaxy-galaxy gravitational interactions, and hydrodynamic interactions with the hot intergalactic medium (IGM). As I discuss in much more detail in Section 1.3, galaxy-galaxy mergers can transform the morphologies, kinematics, and star formation properties of galaxies (e.g., Toomre 1977; Mihos & Hernquist 1994, 1996; Hopkins et al. 2006). Mergers are external evolutionary processes because they depend on the galaxy environment; they are more likely to occur in high density regions. Likewise, galaxy ‘harassment’ events, which I am renaming ‘encounters’, are more frequent in these busy environments, and can act to drive or suppress star formation in galaxies. Hydrodynamic interactions like ram pressure can remove the gas from a galaxy when the cold interstellar medium (ISM) of an infalling galaxy in a cluster encounters the hot IGM (e.g., Gunn & Gott 1972; Abadi et al. 1999).

These evolutionary processes all operate on different timescales and spatial scales and they can often interact in complicated ways to drive galaxy evolution. For instance, AGN feedback can be both secular and external, occurring in isolated galaxies as well as recently merged ones with fresh reservoirs of gas near the center (as a result of recent mergers, e.g., Hopkins et al. 2005). This picture with AGN feedback is quite complicated and I have dedicated multiple chapters to it in this work. It illustrates the point that none of these processes can be studied in isolation and it is therefore necessary to investigate the complex interplay between these processes.

1.2 The Importance of AGN for Galaxy Evolution

Most if not all galaxies host a supermassive black hole (SMBH). SMBHs dwarf normal ‘stellar mass’ black holes, with masses ranging from 10^6 - $10^9 M_{\odot}$. While the masses of these

SMBHs are large, they are minuscule when compared to the masses of their host galaxies; in fact, the mass of galaxy bulges alone far exceeds that of the SMBH ($M_{BH} \sim 10^{-3} M_{bul}$). Therefore, the gravitational sphere of influence of the SMBH is relatively small compared to that of the host galaxy.

However, the observational correlations between SMBH mass and stellar bulge properties such velocity dispersion (σ_*), the most famous of which is known as the M_{BH} - σ_* relation, indicate that SMBHs and their host galaxies are evolutionarily intertwined (e.g., Magorrian et al. 1998; Ferrarese & Merritt 2000; Gebhardt et al. 2000; Merritt 2000; McConnell & Ma 2013). One explanation for these correlations is that various evolutionary processes such as repeated galaxy mergers grow the SMBH and the galaxy simultaneously (Jahnke & Macciò 2011). Another school of thought is that SMBHs are powerful drivers of galaxy evolution and are influencing their host galaxies. As described in Chapter 1.1, galaxy evolution proceeds through many different processes and depends on the properties of the galaxy such as the environment and redshift, meaning that a combination of different process may be at work. For instance, SMBHs may be less important for explaining observational correlations such as the M_{BH} - σ_* relationship for lower mass dwarf galaxies, where star formation driven feedback dominates.

Since this section focuses on the role that SMBHs play in galaxy evolution, I discuss the second explanation for the M_{BH} - σ_* relationship in more depth. The sphere of influence of the SMBHs gravity is minuscule, so a physical coupling between the host galaxy and the energy of active galactic nuclei (AGN, which are SMBHs that are actively accreting gas) could explain these scaling relations. Assuming a radiative efficiency for the AGN of 10%, the energy radiated by the AGN is then $E_{BH} = 0.1M_{BH}c^2$. The binding energy of the bulge of the galaxy is $E_{bul} = M_{bul}\sigma_*^2$, where σ is the pressure support, or velocity dispersion of the stars in the bulge, which is typically less than 300 km s^{-1} . Therefore, while the mass of the bulge is much greater than that of the SMBH, the energy ratio is: $E_{BH}/E_{bul} \sim 10^{-4}(c/\sigma)^2 = 100$. The energy of an AGN thus far exceeds the binding energy

of the bulge of a galaxy. The coupling of the energy of the AGN to the galaxy is known as ‘AGN feedback’. If some fraction of this energy can be efficiently coupled to the host galaxy, then AGN have the potential to have an important impact on galaxy evolution.

In this section, I define AGN feedback as a self-regulatory process that couples the energy injected by an AGN into the galaxy to the gas of a galaxy; this can act to either shut down or incite star formation. In this way, feedback can be either negative or positive, respectively. Unless otherwise specified, when I refer to ‘feedback’, I am referring to negative feedback. Also in terms of definitions, there are many different types of feedback, for example, star formation driven feedback or AGN-driven feedback. Here, I focus on AGN-driven feedback, since it is most relevant to the work in the first few chapters of this thesis.

AGN feedback is often referred to as the ‘F-word’ in astrophysics. This is because it is often invoked as a vague term, without attention to the details of the energy coupling of the AGN to the gas of the host galaxy. Feedback is also over utilized as a cure-all to disperse the tension between large-scale cosmological simulations of the dark matter halo mass function and the observational stellar mass function of galaxies in the universe. In this thesis, I strive to remain specific about the details of the feedback processes and how they directly impact the host galaxy.

Figure 1.2 introduces the theoretical origin of feedback from the tension between cosmological simulations and the observed stellar mass function. Here, Mutch et al. (2013) compare a Schechter function fit to the redshift zero stellar mass function (in blue, from Bell et al. 2003) to the dark matter halo mass function from the Millennium Simulation (in red). These functions have been scaled using the baryon fraction, yet still differ on the high and low mass ends. Supernova feedback is often invoked to explain this discrepancy at low masses, where it can more efficiently operate (on low mass galaxies), ejecting gas from the galaxies, and halting efficient formation of halos. At the high mass end, it is believed that AGN feedback can shut down star formation and halt more stellar mass creation.

In addition to resolving tension between large-scale cosmological simulations and ob-

servations of galaxies as well as providing an explanation for AGN-galaxy co-evolution, AGN feedback may be important for explaining bulk properties of local galaxies. For instance, the bimodal color distribution of galaxies in the local universe introduced in Section 1.1 requires quenching of star formation in galaxies via a ‘feedback mechanism’ (e.g., Bell et al. 2004; Brown et al. 2007; Faber et al. 2007; Silk 2011). In models, AGN-driven feedback provides this mechanism to evacuate gas from a galaxy and quench star formation and the growth of the SMBH (e.g., Di Matteo et al. 2005; Hopkins et al. 2005; Springel 2005; Croton et al. 2006).

Despite the utility of AGN feedback in regulating galaxy and SMBH growth, there is limited direct evidence for feedback operating on host galaxies. There are many proposed mechanisms to deliver energy from the AGN to the ISM of the host galaxy, but little is known about the energy, geometry, and efficiency of these mechanisms.

There are two main modes of AGN feedback: quasar and radio mode. The quasar, wind, or radiative mode applies to the AGN in this work; it is more radiatively efficient, and operates for more luminous AGN, close to the Eddington limit, $L_{Edd} = 4\pi GM_{BH}m_p c / \sigma_T$ (Combes 2014), where σ_T is the cross-section for Thomson scattering between charged particles and photons. The quasar mode of feedback mostly applies to pushing cold gas around in galaxies (Fabian 2012). Radio mode feedback is also known as kinetic mode and operates for AGN at a lower Eddington fraction ($L < L_{Edd}$). This tends to apply to very large galaxies with powerful jets and hot halos.

In this work, I focus on the quasar mode of AGN feedback, which operates for a larger fraction of AGN host galaxies in the universe, since powerful radio galaxies are relatively rare (they constitute $\sim 5\text{-}10\%$ of AGN; Rafter et al. 2009). It is also more relevant to the coupled growth of AGN and their host galaxies, since it releases more energy on scales that are relevant to the bulge of the host galaxy. It is important to note that while radio and quasar mode feedback are the two main modes, many AGN exist in an intermediate territory where both modes of feedback could operate.

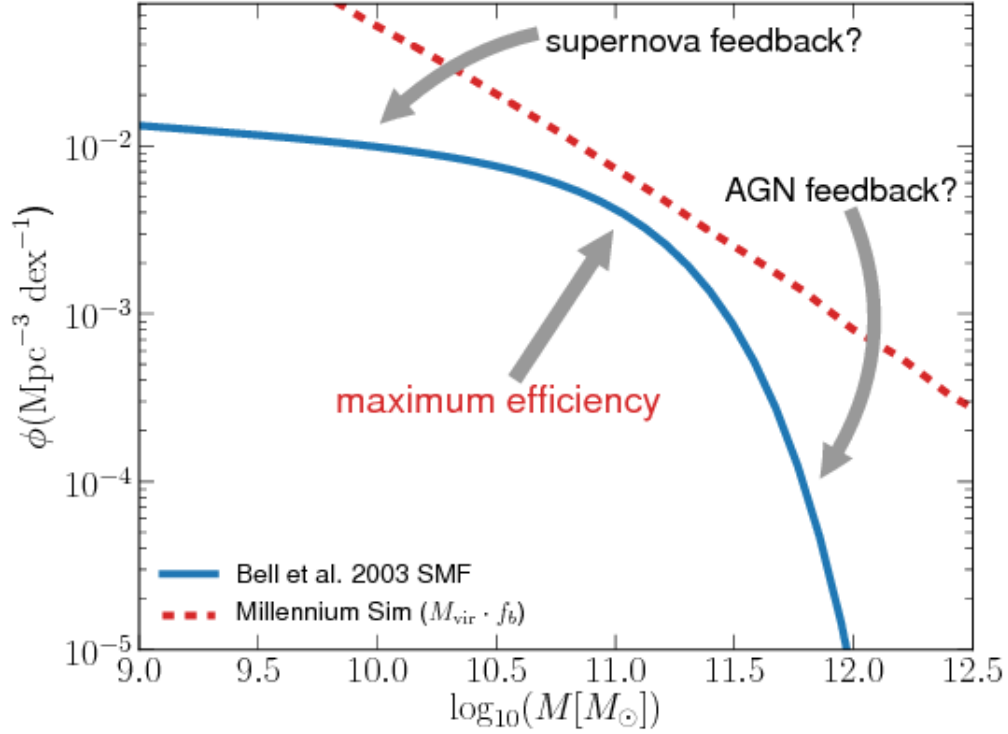


Figure 1.2: The mass function for dark matter halos (from the Millenium simulation, red dashed line) and the observed stellar mass function (from Bell et al. (2003), blue solid line), Figure from Mutch et al. (2013). The halo mass function has been multiplied by the universal baryon fraction in order to demonstrate the maximum possible stellar mass content as a function of halo mass. The closer the stellar mass function is to this red dashed line, the more efficient star formation is in halos of the corresponding mass. If galaxies were to form stars with a fixed efficiency at all halo masses, then the slope of the stellar mass function would be identical to that of the halo mass function. The differing slopes at both high and low masses indicates that star formation (as a function of halo mass) is less efficient in these regimes. At low masses, this is commonly attributed to efficient gas ejection due to supernova feedback, whereas at high masses energy from AGN feedback is thought to be able to effectively reduce the efficiency of gas cooling. However, many other physical processes may also contribute in both regimes.

Quasar mode AGN feedback can drive powerful winds, which are also known as AGN outflows (I use the two terms interchangeably throughout this thesis). I will now go into some detail on the theory of AGN winds including their launching and driving mechanisms in order to provide context for the investigation of AGN outflow kinematics and energetics in Section 1.2.1 and Chapter 3. The theoretical models can shed light on the nature of AGN winds, providing testable predictions for their energetics, momentum fluxes, multi-phase nature, and how they might affect their host galaxies. However, due to the multi-phase nature of AGN outflows and the different size scales they operate over, this picture is fairly complicated. I first offer some background into the various observed phases of AGN outflows, and then I will address the theory behind the nature (momentum vs energy-conserving) of outflows as well as their driving mechanism.

Starting from the smallest spatial scales, and working our way up, warm absorbers (WAs) and ultra-fast outflows (UFOs) are two classes of outflows that occur in UV/soft X-ray and hard X-ray observations, respectively. WAs are observed in about half of local Seyfert (low-luminosity) galaxies; they have outflow velocities on the order of $\sim 100 \text{ km s}^{-1}$, while UFOs are rarer and are observed to have relativistic speeds. Both are very wide-angle outflows that occur on the sub-pc scale ($\sim 10^{-4} - 10^{-2} \text{ pc}$; Reeves et al. 2009; Tombesi et al. 2011, 2012). This class of AGN outflows is extremely important for probing the launching mechanism of the quasar mode of feedback; it is possible that this wind then continues on to become the kpc-scale ionized narrow-line region (NLR) winds that are the focus for this thesis (Morganti 2017). Therefore, while kpc-scale NLR winds are more relevant for directly probing how the energy from the AGN outflow is coupled to the ISM on kpc-scales in a galaxy, smaller-scale WAs or UFOs are critical for investigating the launching mechanism for AGN winds.

Next, cold molecular gas outflows are also observed in both neutral atomic (HI) and molecular (i.e., CO) gas phases, with velocities $> 1000 \text{ km s}^{-1}$. They occur on pc scales. Of additional interest is the fact that this type of outflow can have a very high mass. Ciccone

et al. (2014) find that the momentum of outflows of molecular gas are boosted by a factor of 20 in comparison to the energy input by the AGN, L_{AGN}/c . This is a key clue that this phase of the outflow is an energy-driven outflow, as discussed below.

The phase of AGN outflows in this work (Chapter 3) is the NLR winds. I define the NLR as a low density ($n_H < 10^6 \text{ cm}^{-3}$) spatially extended region that extends from hundreds of parsecs to ~ 30 kpc surrounding the central AGN. It is characterized by the forbidden narrow emission lines that I utilize to study the kinematics of the region (the definition of narrow is $\Delta v < 1000 \text{ km s}^{-1}$ in FWHM; e.g., Schmitt et al. 2003; Osterbrock & Ferland 2006; Hainline et al. 2013). This type of outflow has velocities in the range 10^2 to 10^3 km s^{-1} and tends to have biconical geometry (e.g. Müller-Sánchez et al. 2011; Fischer et al. 2013; Crenshaw et al. 2015; Müller-Sánchez et al. 2016; Fischer et al. 2017; Nevin et al. 2017).

A current question in the theory of AGN winds is if they conserve momentum or energy. This is important because it affects the velocity and hence energetics of the wind and therefore how it might impact the host galaxy. While observed outflows are probably somewhere between the limits of energy- and momentum-conserving, the amount to which they conserve energy is important. If a shocked wind cools inefficiently, then energy is conserved, but momentum is not. For instance, very fast winds are energy-conserving because radiative losses are low (Faucher-Giguère & Quataert 2012). In this limit, the momentum is boosted with time due to shocks by hot gas. This predicts that AGN outflows could have a measured momentum flux that is larger than that of the output momentum flux, which is observed with the cold molecular gas outflows in Ciccone et al. (2014).

However, AGN winds are multi-phase so this picture may be more complicated. For instance, outflows may transition from momentum- to energy-conserving at ~ 1 kpc, which is the relevant scale for the kpc-scale outflowing winds in this work (King et al. 2011). Other work such as King & Pounds (2015) indicates that the nature of the outflow may change with time. For instance, outflows could begin as momentum conserving if they are able to cool

efficiently, and then over time the SMBH will grow and enter an energy-conserving phase that is more energetic and is able to boost the momentum at larger scales, having a larger effect on the ISM during this phase. By measuring the kinematics of observed outflows (Section 1.2.1), it is possible to link the theory to the observations and make predictions about the potential for the outflow to drive feedback in the host galaxy.

AGN winds can be launched from the accretion disk via a variety of proposed launching mechanisms including thermal heating, radiation pressure, and magnetic driving (Krolik & Begelman 1986; Murray & Chiang 1995; Bottorff & Ferland 2000). It is somewhat unclear which mechanisms dominate and a combination of these may explain the varied observations of kinematics of different phases of AGN outflows. While these mechanisms are central to the study of AGN outflows that occur on unresolvable or pc-scales, they are no less relevant to the kpc-scale AGN in this work. Kpc-scale winds must still be driven by some mechanism, although it is unclear where this acceleration takes place. They are located so far from the nucleus that multiple different factors may be important.

Recent work has focused specifically on the NLR outflows and finds that they can be credited to either radiative driving, where the AGN radiation acts as a heat source that can also supply momentum (Fischer et al. 2017), or to the entrainment of clouds in a highly ionized wind (Kraemer et al. 2007). Crenshaw et al. (2010) predict that at large radii, the kinematics are dominated by deceleration due to interaction with the ambient medium. Some work suggests that kpc-scale AGN winds are accelerating material in-situ (Revalski et al. 2018) as opposed to the material originating near the nucleus. Determining the kinematics of the NLR outflows, as well as their geometries, sizes, and relationship with the luminosity of the central AGN can address some of these questions about driving mechanisms as well as energy vs momentum conservation in the outflow itself and can allow us to make conclusions about the potential of the outflow to drive feedback in the host galaxy.

I will now transition into a discussion of feedback in the host galaxies of AGN outflows. Since there are many different types/luminosities of AGN and AGN outflows in the universe,

a relevant question is how AGN feedback operates in general for galaxies that host AGN; this addresses the overall impact of AGN feedback on galaxy evolution. To address this, it is necessary to examine the most commonly observed types of AGN outflows and to characterize if this type of outflow drives positive or negative feedback processes in the host galaxy. Here I carefully describe how best to determine if AGN feedback is operating in galaxies and I introduce examples of positive and negative feedback in the literature in preparation for Section 1.2.1, which introduces the kinematic approach to AGN feedback.

It is difficult to directly prove that AGN-driven outflows are driving feedback in the host galaxy. Part of this difficulty stems from the fact that the timescales between the outflow and the effect on star formation may be delayed. This means that making the causal connection between the evidence for an outflow and the evidence for suppressed or enhanced star formation is difficult. For instance, Woo et al. (2017) find that for a sample of $\sim 110,000$ Type-2 AGN in SDSS the active galaxies that host strong outflows have similar specific star formation rates (sSFRs) to inactive galaxies. However, the active galaxies without strong outflows have much lower sSFRs relative to the inactive galaxies, indicating that there may be a delay of dynamical time for the impact on star formation to appear. There could also be other processes like merging galaxies that complicate this picture; for example, a merger could trigger both AGN activity and star formation, also on different timescales (Hopkins et al. 2008). Therefore, it is difficult to directly link a visible outflow to the cessation of star formation; additionally, AGN are also known to operate on ‘duty-cycles’ meaning that they can turn on and off.

While we do have to deal with problems of timing with AGN, one way to more directly study feedback is to increase the number of careful observations from IFS or other spatially-resolved tools. This has been done for $z \sim 1-3$ galaxies and reveals that areas affected by the outflow have lower star formation (e.g., Cresci et al. 2015; Carniani et al. 2016). However, some galaxies with AGN-driven outflows can demonstrate positive feedback as well. For instance, Cresci et al. (2015) find that an obscured $z = 1.59$ quasar has a cavity in its gas

which surrounds a fast outflow ($v = 1500 \text{ km s}^{-1}$). Simultaneously, there is triggered star formation at the edges of this cavity. Therefore, AGN outflows may have a dual effect of driving both positive and negative feedback.

Another option to investigate feedback is to study the cold molecular gas in galaxies since this gas is directly responsible for star formation. Brusa et al. (2015) find that the gas content of a $z \sim 1.5$ obscured quasar with an AGN-driven outflow observed in the NIR is significantly lower than expected for the stellar mass, sSFR, and redshift of the galaxy. This suggests that in this case, the cold molecular gas phase is significantly depleted by the AGN outflow.

Since the most direct evidence to date for AGN-driven feedback exists for only a small handful of case studies, there are still several open questions such as if the type or scale of feedback varies with properties like AGN luminosity. These case studies indicate that feedback does not operate over the entire galaxy (it is not global in scale), at least from one episode of AGN-driven outflow. However, the direct evidence for feedback listed above is limited to higher luminosity and high energy AGN outflows that are localized to small areas of the galaxy. It could be true that different types of AGN outflows or luminosities drive different modes of feedback. In the past it was believed that in order to drive feedback, AGN forcibly ejected all gas from the galaxy. However, perhaps AGN have the potential to drive a ‘maintenance-mode’ form of feedback where they heat and ionize the gas, which prevents star formation from proceeding from the existing gas.

In order to address some of the questions about the prevalence and overall effectiveness of feedback, it becomes necessary to study a larger sample of galaxies. One way to do this is to move away from the case studies of quasars, which are high luminosity AGN (we refer to AGN with $L_{bol} > 10^{45} \text{ erg s}^{-1}$ as quasars in this thesis). We show an example of a quasar-driven outflow from Greene et al. (2012) in Figure 1.3. This class of outflow, known as a ‘super-bubble’ has an extremely high velocity and large size, extending to $\sim 15 \text{ kpc}$ from the quasar. This type of AGN, while energetic, are rare and only constitute a small fraction

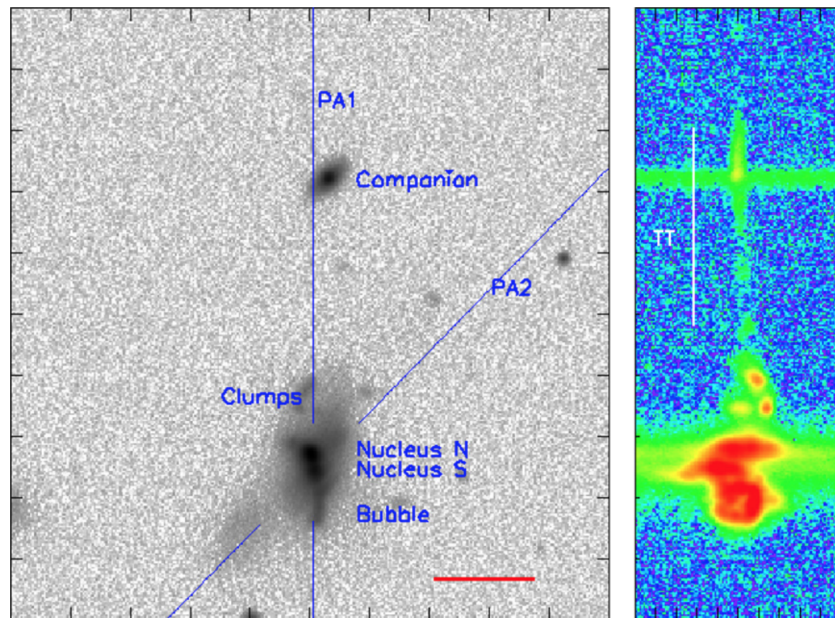


Figure 1.3: A galaxy with a powerful quasar-driven outflow from Greene et al. (2012). The r -band Magellan image of the galaxy is on the left, with the main galaxy in the south and the companion galaxy in the north (N is up and E is to the left). The red scale bar indicates $10''.0$ (22 kpc) and the blue lines are the positions of the spectroscopic slits, labeled ‘PA1’ and ‘PA2’. The longslit spectrum from PA1 is shown in the panel on the right, where the spectral dimension is the x-axis and the spatial dimension is the y-axis. The spatial scale is the same as in the image, and the horizontal scale is 3842 km s^{-1} . This slice of spectrum is centered on $[\text{OIII}]\lambda 5007$; the bubble feature associated with the southern galaxy is ionized and has a large velocity dispersion, meaning that it is not gravitationally bound. It also has a large spatial extent (~ 15 kpc from the galaxy towards the companion galaxy). There is a tidal feature (TT) that connects the two merging galaxies, shown by the vertical white line.

(1%) of the AGN in the universe.

I include the AGN bolometric luminosity function in Figure 1.4, which shows the fraction of radiatively efficient AGN found at various bolometric luminosities. Moderate-luminosity AGN are defined as those with $43 < \log L_{\text{bol}} \text{ erg s}^{-1} < 45$ (local moderate-luminosity AGN are also known as Seyferts in this work). The AGN described in this thesis are moderate-luminosity and account for 10% of the total AGN population at low redshifts ($z < 0.1$) (e.g., Silverman et al. 2006; Ueda et al. 2014).

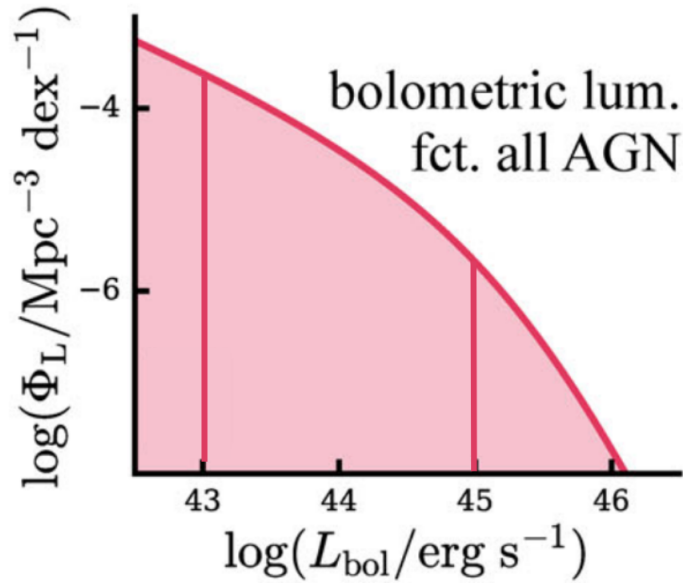


Figure 1.4: Bolometric luminosity function for all radiatively efficient AGN adapted from Weigel et al. (2017). The vertical lines at 10^{43} and $10^{45} \text{ erg s}^{-1}$ demarcate the moderate-luminosity AGN range.

In addition to representing a larger fraction of the AGN population, the moderate-luminosity outflows in this thesis also operate on kpc-scales, coincident with circumnuclear star formation. This has the advantage of allowing me to more directly assess the effects of outflows on the ISM of the host galaxies (Crenshaw et al. 2015). I can do this by investigating the properties of the host galaxy in addition to the properties of the outflow such as its orientation with respect to the star forming disk of the galaxy. If moderate-luminosity AGN are capable of driving feedback, they are so common that they could contribute more

significantly to galaxy evolution in the universe than the rarer high luminosity AGN outflows.

1.2.1 The Kinematics of AGN Outflows

Kinematics are key for studying NLR AGN outflows; they can reveal the energetics and geometry of the outflow and therefore address some open questions in the area of AGN feedback:

- What is the energy of AGN outflows?
- What is the geometry of AGN outflows and how might this affect the efficiency of the coupling of the energy to the ISM?
- What are assumptions that are being made about these two quantities and how is this affecting the conclusions about AGN-driven feedback?

By measuring the kinematics of AGN outflows in Chapters 2 and 3, I directly address these questions in this thesis work.

Kinematics are necessary in order to quantify the energy from outflows, and to therefore better understand the ability of outflows to drive feedback. The most common diagnostics to do this are the mass outflow rate (\dot{M}_{out}) and the kinetic luminosity ($L_{KE} = 1/2 \dot{M}_{\text{out}} v^2$). The kinetic luminosity is often compared to the bolometric luminosity (L_{KE}/L_{bol}) of the AGN to derive a fraction that describes the amount of accretion power that is present in the outflow. Di Matteo et al. (2005) find that if this fraction is greater than 0.05-0.1, then the wind can drive feedback in the host galaxy. Hopkins & Elvis (2010) lower this energy threshold to $0.005 L_{KE}/L_{\text{bol}}$ using a two stage feedback model in which the outflow first disrupts a cold cloud, which will expand in the perpendicular direction. This expansion alone may be sufficient to prevent star formation. The disrupted cloud is more susceptible to ionization and momentum coupling from the outflow, so it could also become part of the outflow. This

ratio, L_{KE}/L_{bol} , is useful in determining if an outflow has the theoretical potential to drive feedback in its host galaxy.

But how is L_{KE} measured? There are two basic methods, one of which relies upon the geometry of the outflow, and one of which relies on the luminosity of the emitting gas. The geometric approach uses the equation $\dot{M}_{out} = 2m_p n_e v A f$ to measure the mass outflow rate, where n_e is the electron density, v is the outflow velocity, A is the surface area of the outflow, and f is a volume filling factor which accounts for how ‘clumpy’ the gas is. There are numerous uncertainties in this measurement including the electron density, the velocity, the surface area, and the filling factor. Based on the assumptions made, the measurement can vary by a couple dex, so it is critical to carefully consider each of the assumptions and utilize physical motivations for each decision. In this work, we pursue this first approach but are careful to analytically model the geometry of the outflow and to measure the electron density. The luminosity-based approach to measuring mass outflow rates converts an observed luminosity of emission lines such as $H\beta$ or $[OIII]$ to a mass using a conversion factor. This method often assumes a spherical geometry. The luminosity-based technique can be more stable, but has the disadvantage of making a global measurement, meaning that it cannot probe the geometry or spatially-resolved energetics of the outflow. Revalski et al. (2018) offers a detailed comparison of the two techniques for a single AGN outflow and I additionally compare luminosity-based techniques with the geometric approach used in Chapter 3.

An additional uncertainty in the determination of the outflow energetics is the measurement of v , or the outflow velocity. This quantity can be measured from integrated spectra (it is often used as a global offset velocity for blueshifted wings where a spherical geometry of the outflow is assumed), or it can be measured using a spatially resolved methodology. I utilize the spatially resolved data from longslit observations to measure v using a penalized multi-Gaussian fitting technique to determine the velocity centroids of different Gaussian components that are physically tied to walls of a biconical outflow. This method makes

assumptions about the physical model but fits a spatially resolved velocity at each position, which is a more careful approach than fitting a global velocity offset value, which can overestimate the outflow energetics.

A key question in the energetics of AGN outflows is how efficiently they couple their energy to the galaxy's ISM. If an outflow has a narrow opening angle and is oriented perpendicular relative to the galaxy disk, it will have a minimal impact on the star-forming gas in the disk of the host galaxy regardless of its energy content. It is therefore important to determine both the geometry of the outflow and how the outflow is oriented with respect to the star-forming disk of the host galaxy. The geometry of the outflow can either be assumed, directly observed from images of the galaxy, or measured from the kinematics. For instance, some authors assume a spherical geometry with a 180° opening angle, which can overestimate the energetics of the outflow and always allows the outflow to deliver energy to the galaxy disk.

Instead, theory predicts a bicone model for the NLR of an outflow. This is expected from the unified model of AGN; a thick torus provides the collimation necessary to produce a biconical outflow (Antonucci & Miller 1985). The outflow does not necessarily have to be aligned perpendicular to the disk of the galaxy, in fact Fischer et al. (2013) find no alignment between the inclinations of a sample of Seyfert galaxies with biconical outflows and the photometric major axes of their host galaxies. The technique I use to measure the geometry of the outflow and its orientation is to model the geometry of the outflow using the spatially-resolved velocity centroids. This can provide the inclination, opening angle, size, and orientation on the sky of the outflow.

The kinematics of ionized gas in NLR outflows allow for the careful determination of the outflow energetics, which can help estimate if an outflow has the theoretical potential to impact its host galaxy. Additionally, the kinematics can reveal the geometry of the outflow, which can determine the efficacy of the outflow in delivering this energy to the ISM.

1.3 The Importance of Galaxy Mergers for Galaxy Evolution

One key goal of extragalactic astronomy is quantifying the importance of galaxy-galaxy mergers for driving galaxy evolution. Mergers can explain how galaxies form, grow, and build up structure; mergers can fuel SMBHs as AGN, drive star formation, and lead to the assembly of structure like bars or central bulges. In fact, the merging of dark matter halos is one of the key predictions of the Λ CDM model of the universe, which is the central tenet of how galaxy evolution proceeds throughout cosmic time. However, there is much tension on how important different types of mergers are for evolutionary processes in the universe and much of this contention stems from the difficulty of cleanly and unambiguously identifying merging galaxies. Additionally, galaxy mergers can be extraordinarily long processes (they last for \sim Gyrs) and they have different signatures at different moments in time. Here I briefly outline some of the key findings surrounding how and if galaxy mergers can drive evolution and touch on some of the leading methods to identify mergers. I will also describe some of the history of using galaxy merger simulations to better understand the process of merging.

I will begin by posing the question: Do major mergers drive evolution? It is clear that major mergers, which are the most extreme form of merger (where the mass ratio is greater than 1:4), do drive evolutionary processes. For example, simulations find that tidal torques from major mergers can drive gas accretion and observations of ultra-luminous infrared galaxies (ULIRGs), which are local major mergers, reveal that major mergers are indeed responsible for driving both star formation and AGN activity (e.g., Joseph & Wright 1985; Sanders & Mirabel 1996). However, these galaxies are extreme cases of mergers.

If this same question is posed much more generally, asking instead if major mergers are the primary drivers of evolution in the universe, the answer is unclear. Some work indicates that major mergers are indeed primarily responsible for driving both star formation (Mihos & Hernquist 1994, 1996) and fueling AGN (Di Matteo et al. 2005; Hopkins et al. 2005; Ellison

et al. 2011; Koss et al. 2012; Treister et al. 2012; Satyapal et al. 2014). However, other work suggests that minor mergers or continuous ‘cold flow’ gas accretion are the most important mechanism for shaping the morphologies of galaxies, driving star formation, and contributing to the mass growth of SMBHs (e.g., Noeske et al. 2007; Daddi et al. 2007; Cisternas et al. 2011; Kocevski et al. 2012; Kaviraj 2013; Villforth et al. 2014). Other studies find that mergers are unimportant and that secular instabilities driven by disks and spiral arms in the local universe can dominate galaxy evolution. These secular instabilities can grow pseudo-bulges locally and contribute to significant gas inflows (e.g., Bournaud 2016).

It should be noted here that although this is beyond the scope of this thesis, the fraction of galaxies that are merging is thought to depend on the redshift, increasing towards $z \sim 2$ (e.g., Conselice et al. 2008). This is an interesting topic unto itself and very important for understanding galaxy evolution. Here we focus on understanding mergers in the local universe in the hope that we can extend the technique to higher redshift galaxies, where mergers are more ubiquitous, using telescopes such as *JWST*.

One main reason that the relative import of different types of mergers is unknown is that it is difficult to build a clean observational sample of galaxy mergers (major and minor). Imaging studies that rely upon one or a couple of imaging predictors can fail to accurately identify mergers, which leads to inconclusive results (e.g., Conselice 2014 and references therein). One method to identify merging galaxies is pair studies, which identify merging galaxies as those that have a low line of sight velocity difference such as $100\text{--}500 \text{ km s}^{-1}$ (e.g., López-Sanjuan et al. 2012; Tasca et al. 2014). Methods such as this can be used to measure the merger fraction, or relative number of galaxies that are merging for various epochs in the universe. However, each individual method has various biases. For instance, the pair study technique can identify false positives (galaxies that are superimposed along the line of sight but not merging) and false negatives (it only identifies major mergers that are during their early stages of merging and misses many different types and stages of mergers).

Recent work has relied increasingly upon non-parametric tools to identify merging

galaxies from imaging surveys, such as the *Gini*- M_{20} method or the *CAS* (Concentration-Asymmetry-Clumpiness) method (Lotz et al. 2004; Conselice et al. 2003). These methods are each individually limited by different merger initial conditions, such as mass ratio and gas fraction, and by merger stage. For instance, while identifying merging galaxies using asymmetry tends to be more sensitive to early-stage mergers, *Gini* - M_{20} tends to identify late-stage mergers. Additionally, *Gini* - M_{20} is slightly more sensitive to minor mergers (Lotz et al. 2010a,b).

In Chapter 4, I develop an imaging classification tool to identify merging galaxies that utilizes a combination of the above imaging tools (I introduce some of these imaging techniques in more depth in Section 1.4.3). The goal of Chapter 4 is to combine the strengths of these stand-alone methods to increase the precision and accuracy of the merger classification. A key aspect of this technique is my use of simulated galaxy mergers to better characterize the strengths and biases of the new identification tool.

Simulations of merging galaxies can be used to make predictions about the observability of galaxy mergers using different predictors, the merger fraction over cosmic time, and the importance of mergers to various evolutionary processes in galaxies. One approach is cosmological merger tree simulations, which study the merger rate over cosmic time (e.g., Rodriguez-Gomez et al. 2015). This type of approach also incorporates the fact that galaxies do not live in isolation; for instance, galaxies can be influenced by galaxy flybys (that do not culminate in a merger) or non-binary mergers. Also in cosmological simulations, galaxies can accrete gas from the inter-cluster medium. Cosmological simulations such as Illustris (Vogelsberger et al. 2014) or the Millenium simulations (Springel 2005) capture the frequency of false positives (galaxies that are passing by but not merging).

Another approach to simulating merging galaxies is binary mergers or ‘isolated’ merger simulations. Some examples of isolated galaxy simulations are the **GADGET-3/SUNRISE** simulations (Jonsson 2006; Jonsson et al. 2010), which I utilize in Chapters 4 and 5, or the **FIRE** simulations (Hopkins et al. 2014, 2018). This approach does have its limitations since

it is unable to place galaxy mergers in a cosmological context and/or examine the variety of morphologies that are available in a cosmological context. However, isolated simulations have high temporal and spatial resolution and more closely track the physics of the ISM of the merging galaxies. Both types of simulation are very useful in making different predictions about merging galaxies. They both also provide the opportunity to calibrate merger identification techniques since it is possible to know a priori if a galaxy is merging or not.

Here I focus primarily on past examples of work that has relied upon isolated merger simulations to make key predictions about observations of merging galaxies, since this is the direction pursued in Chapters 4 and 5 of this thesis. Lotz et al. (2008); Lotz et al. (2010a,b) demonstrate that the timescale over which a binary merger is observable (known in the field as the merger observability timescale) varies for different non-parametric tools. The observability timescale also depends most strongly on the merger parameters of mass ratio and gas fraction. Hung et al. (2016) also explore this in more depth for some kinematic signatures of merging galaxies in the star-forming gas of the same type of **GADGET-3/SUNRISE** simulations. They find that the observability timescale for the kinematic signatures of the mergers is $\sim 0.2 - 0.4$ Gyr, which is much shorter than for imaging predictors, and that this timescale is also sensitive to gas fraction and mass ratio.

I will introduce some of the kinematic signatures of mergers in Section 1.3.1 and will further discuss some imaging tools that can identify galaxy mergers in the wider context of galaxy morphology and structure in Section 1.4.3.

1.3.1 The Kinematics of Galaxy Mergers

In this section, I will go into detail about the observed kinematic characteristics of galaxies in general in order to introduce kinematic tools that are useful for identifying merging galaxies. This involves discussing the distinct kinematics of spiral and elliptical galaxies and further subdividing elliptical galaxies into two interesting classes of ‘fast rotators’ and ‘slow rotators’. I will mainly use the stellar velocity and velocity dispersion as tools to describe

the kinematics of a galaxy, occasionally deviating to discuss gas kinematics, which can be quite informative but are not covered as extensively in this thesis work (in the context of mergers). The stars (stellar kinematics) are the target of this thesis since they offer a more direct probe of the underlying gravitational potential of a galaxy and thus the assembly history of galaxies. As I show in Chapters 2 and 3, the gas kinematics of galaxies can be more affected by external processes such as outflows or inflows. Throughout this section, I will also discuss some recent simulations that are useful for making predictions about the kinematics of galaxies.

The kinematics of galaxies are primarily governed by the dark matter halos in which they reside, which is best demonstrated in the flat rotation curves of spiral/disk galaxies (e.g., Rubin & Ford 1970; Rubin et al. 1978). This was initially surprising in observations, since the light profiles of galaxies begin to fall off at ~ 10 kpc. However, light does not trace the overall mass of galaxies, which are dominated by the dark matter halos, so rotation curves became a method to characterize the overall mass distribution of a galaxy (light and dark matter). The rotation curves of spiral galaxies (Figure 1.5) tend to have ordered rotation, where the velocity increases towards a turnover radius at $\sim 1 - 5$ kpc. The maximum rotational velocity is $\sim 300\text{--}400 \text{ km s}^{-1}$ (Sparke & Gallagher 2000). Exterior to this turnover radius, the velocity curves do not decay as quickly as predicted by the light alone (Figure 1.5). In combination with their relatively fast and ordered rotation, spiral/disk galaxies also tend to have relatively small velocity dispersions, which is why they are commonly labeled ‘rotation-dominated’. They have large V/σ values, where V is the rotational velocity and σ is the velocity dispersion of the stars.

The rotation curves of spiral galaxies in Figure 1.5 are measured using longslit spectroscopy. When galaxies are observed with IFS, the rotational velocity of the galaxy can be modeled using full two-dimensional models. For instance, the motion of the stars in spiral galaxies is well described by circular motion, and if the inclination is known (or can be fit), the velocity profile can be described as:

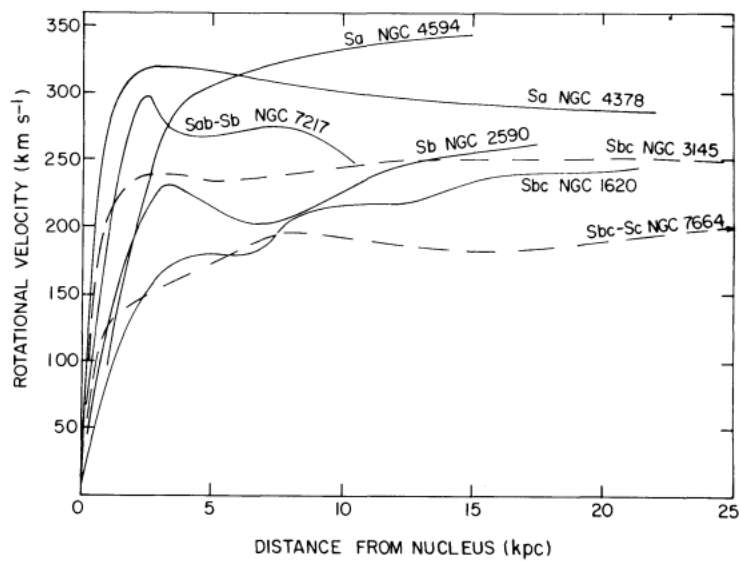


Figure 1.5: Rotation curves of spiral galaxies from Rubin et al. (1978), where the stellar disk dominates the kinematics of the inner part of the rotation curve and the dark matter halo dominates the outer regions, which explains why the rotational velocity does not rapidly decline with the light profiles of these galaxies.

$$V(R, \psi) = V_0 + V_c(R) \sin(i) \cos(\psi)$$

where R is the radius, V_0 is the systemic velocity, V_c is the circular velocity, i is the inclination, and ψ is the azimuthal angle (Krajnovic et al. 2006).

In this thesis, I use numerous methods that measure how ‘disk-like’ a galaxy’s rotation profile is. This includes **kinemetry** (Krajnovic et al. 2006), which is a disk-fitting code that uses a harmonic decomposition to fit the rotation curves of galaxies and can be useful to determine how an observed rotation field deviates from an ordered disk. I also utilize the Radon Transform, which was developed by Stark et al. (2018) for use on MaNGA stellar velocity maps. It is a non-parametric method that measures the kinematic position angle at different points in a galaxy.

The velocity dispersion of spiral galaxies can be another useful tool in the kinematic toolbox. The Milky Way is a spiral galaxy that has both a thick and thin disk, which are distinct in their velocity dispersion; the thick disk is made of older stars, which have a larger dispersion while the thin disk has a smaller dispersion. However, for most of the non-local disk galaxies, the resolution does not exist to separate these two components. The general picture is that spiral galaxies often have a bulge-like component towards the center, which has a higher velocity dispersion since it is often dominated by older stars and a decreasing velocity dispersion towards the exterior of the galaxy. Tools such as **kinemetry** can also characterize the relative order or disorder of the velocity dispersion of galaxies.

The other main type of galaxy in the local universe are elliptical galaxies. Often elliptical galaxies are thought of as a separate class from spirals due to visual morphology. However, they are also distinct in terms of their kinematics. Traditionally, before IFS and longslit spectroscopy provided spatially resolved kinematic maps (for more details, see Sections 1.4.1 and 1.4.2), ellipticals were characterized as having a low V/σ value; they had little rotation and were instead dominated by velocity dispersion (de Zeeuw & Franx 1991).

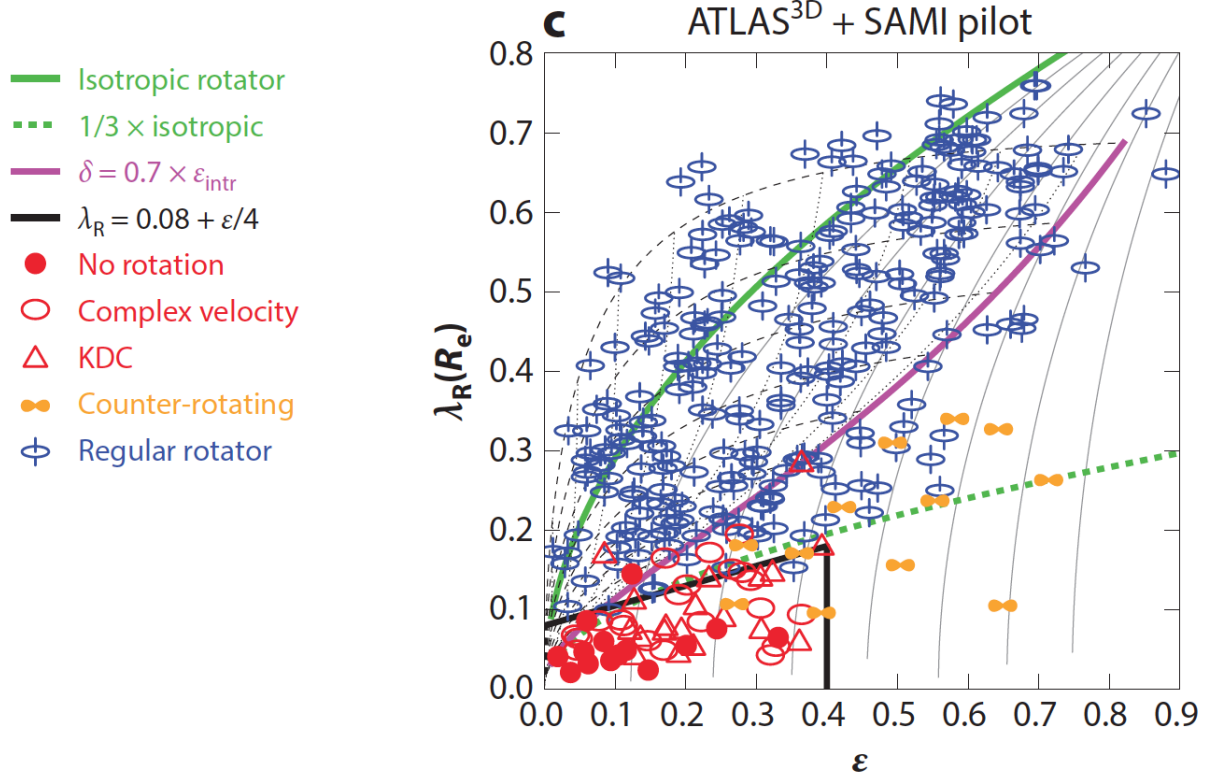


Figure 1.6: Classification of fast and slow rotators on the λ_{R_e} - ϵ parameter space, taken from Cappellari (2017). The black line shows the empirical divide between the two populations, where the individual galaxies are 340 ETGs from Emsellem et al. (2011) and Fogarty et al. (2015). The galaxies are also color-coded by regular (blue) or non-regular (red) rotation.

With the advent of IFS data it is now possible to more closely probe the angular momentum in a spatially resolved manner using the specific angular momentum (measured to the effective radius R_e), λ_{R_e} , as a stand-in for V/σ . By replacing V with the magnitude of the luminosity-weighted average projected angular momentum, $\langle \vec{L} \rangle = \langle \vec{R} \times \vec{V} \rangle$ and normalizing by $V_{rms} = \sqrt{V^2 + \sigma^2}$, we obtain the parameter λ_{R_e} (Emsellem et al. 2007):

$$\lambda_R \equiv \frac{\langle R|V| \rangle}{\langle R\sqrt{V^2 + \sigma^2} \rangle} = \frac{\sum_{n=1}^N F_n R_n |V_n|}{\sum_{n=1}^N F_n R_n \sqrt{V_n^2 + \sigma_n^2}}$$

where F_n is the flux in the n th spatial bin, R_n is the mean radius of the bin, V_n is the mean stellar velocity, and σ_n is the mean stellar velocity dispersion of the bin.

This tool is able to more cleanly separate populations of galaxies by their angular momentum content, and thus more directly probe their assembly histories. It has been used to huge success in IFS surveys of elliptical galaxies and shows that there are distinct populations of elliptical galaxies and that not all elliptical galaxies are ‘dispersion-dominated’. For instance, Emsellem et al. (2007, 2011) define a cutoff in (λ_R, ϵ) space, where ϵ is a galaxy’s ellipticity, and classify elliptical galaxies as fast or slow rotators based on a cut in this parameter space:

$$\lambda_{R_e} < 0.08 + \epsilon_e/4 \text{ with } \epsilon_e < 0.4 \text{ (for slow rotators)}$$

This classification of fast vs slow rotators was originally done using galaxies in the ATLAS^{3D} and SAURON surveys and later extended to surveys like CALIFA, SAMI, and MaNGA. I show an example of this classification for a set of galaxies from SAMI and ATLAS^{3D} in Figure 1.6. When these kinematic classes of elliptical galaxies are coupled with other properties from IFS surveys, it becomes clear that these two classes of elliptical galaxies are distinct in their assembly histories. For instance, slow rotators tend to be more massive and reside as the central galaxy in galaxy clusters (Cappellari et al. 2011; D’Eugenio et al. 2013), whereas fast rotators are smaller. Distinct differences in their star formation histories also point towards different assembly histories (e.g., Smethurst et al. 2018). There-

fore, fast and slow rotators offer an example of how classifying by the kinematic properties of galaxies can separate galaxies by their assembly histories. Naab et al. (2014) use cosmological simulations to assemble fast and slow rotators and find that slow rotators tend to assemble at early times through more rapid evolutionary processes such as major mergers and since then have been dominated by minor mergers. On the other hand, fast rotators can assemble in a variety of ways including gas rich/gas poor minor/major mergers as well as cold flow gas accretion.

There has recently been increased focus on the kinematics of high redshift merging galaxies. The merger fraction is much higher in the high redshift universe, meaning that mergers are more common. A host of issues accompany studying the kinematics of higher redshift mergers: nonmerging high redshift galaxies are inherently more disorganized and all high redshift galaxies suffer from lower spatial resolution, meaning that merging galaxies could be mistaken for rotating disks (Simons et al. 2019). While high redshift merging galaxies are inherently different from local mergers, the tools that are developed to study these higher redshift mergers can still be applied to local galaxies. For instance, Shapiro et al. (2008) and Hung et al. (2015) utilize the higher order kinematic moments from **kinemetry** to characterize the disorder of the kinematics of merging galaxies. These techniques have been extended to local ULIRGs and the kinematic tools show good agreement with imaging tools when applied to identify these galaxies as mergers (e.g., Bellocchi et al. 2012).

The scarcity of local mergers coupled with the paucity of IFS surveys (until recently) has led to a lack of work in the kinematics of local mergers. Given that the MaNGA survey will observe $>10,000$ local galaxies, I am motivated to focus on the kinematics of local mergers. The recent interest in high redshift systems further motivates this critical work focusing on the local merger systems, which we have yet to fully explore in order to trace the evolution of the kinematics of mergers over time.

Local, bright, major mergers are often studied individually in great detail and are found to have significantly disturbed gas kinematics (e.g., Bellocchi et al. 2012). However,

GADGET-3/SUNRISE simulations of merging galaxies have revealed that the kinematic tracers are much weaker than imaging tracers of local mergers and have a much shorter observability timescale (e.g., Hung et al. 2016). Additionally, the kinematic tracers change with the properties of the merger such as mass ratio or gas fraction.

A number of studies have investigated the kinematic misalignments of the stars and gas in galaxies. Many of these focus primarily on the kinematic misalignments of gas, which are more frequently observed in galaxies than that of the stars (e.g., Stark et al. 2018). The gas kinematics are sometimes found to be distinct from that of the stars, meaning that they could trace recent gas accretion events from new gas acquisition from either inflows or recent mergers (Jin et al. 2016). This is an interesting area, but this work focuses on stellar kinematics since it is thought to more closely trace the assembly history of galaxies. Stark et al. (2018) find that a significant fraction of galaxies in MaNGA show deviation from a constant kinematic position angle for the stars. There are different types of kinematic misalignments including warps (where the kinematic position angle is different in the outer disk and the inner disk), kinematically decoupled cores (KDCs), or oval distortions. These deviations from circular rotation can have a variety of physical origins and are much debated; these can include bar instabilities, major mergers, minor mergers, and recent gas accretion either by mergers or through ‘cold-mode’ accretion (e.g., Kereš et al. 2009; Masters et al. 2011; Tsatsi et al. 2015).

There are many promising avenues forward to characterize the kinematics of merging galaxies. Here I focus on the 2D kinematics from IFS which allow us to apply kinematic tools such as λ_{Re} , the higher order harmonic terms from **kinemetry**, and the position angle of the kinematic axis. In order to clarify the origin of some of these interesting kinematic features of galaxies and to fully understand the kinematic signatures of merging galaxies, it is necessary to use simulations of merging galaxies alongside observations, which I do in Chapter 5, where I create a classification technique for merging galaxies first using **GADGET-3/SUNRISE** simulations of mergers. The stellar kinematics of mergers are an intriguing and underexplored

path forward in identifying merging galaxies.

1.4 Tools of the Trade

The main focus of this thesis work is on the kinematics of galaxies and AGN. Therefore, I dedicate a section to explore the instruments and techniques that measure kinematics, focusing on longslit spectroscopy (Section 1.4.1) and integral field spectroscopy (Section 1.4.2). Additionally, Chapter 4 focuses exclusively on imaging techniques, so I explore some of these in Section 1.4.3. In this section, I also introduce the surveys and instruments that I use in this thesis.

1.4.1 Longslit Spectroscopy

The most basic form of astronomical spectroscopy is integrated spectroscopy, where a single aperture observes a source on the sky. This is known as one dimensional spectroscopy because there is only a spectral dimension and there is no spatial information. Longslit spectroscopy is referred to as two dimensional spectroscopy because the aperture is now a slit, which allows for two dimensions of information where one is spatial and one is spectral. It is often known as the workhorse of the spectroscopic techniques; it is relatively fast and efficient to use and provides an important dimension of spatial information. So while it is not as fast as using an integrated fiber, in our case it is useful as a follow-up technique to integrated fiber spectra, such as those from the Sloan Digital Sky Survey (SDSS).

I show an example of an observation I made of the central region of NGC6240 from Müller-Sánchez et al. (2018), centered on the [OIII] emission line, in Figure 1.7. This observation was made using the Apache Point Observatory’s (APO) Dual Imaging Spectrograph (DIS), which is mounted on the 3.5m ARC telescope. This instrument is a medium dispersion optical longslit spectrograph with a red and a blue channel. It has a spatial resolution of $0''.4$ per pixel and a variable spectral resolution based on grating (we use the high resolution blue channel B1200, which as has $1200 \text{ lines mm}^{-1}$ or $0.62 \text{ \AA pix}^{-1}$). APO/DIS is an

instrument that I use frequently throughout this thesis and additionally for various other papers I have collaborated on; it is extremely useful for follow-up of integrated fiber spectra because it further reveals the kinematics of the galaxy at different spatial positions. For example, in Figure 1.7, I line up the longslit along the position angle of an [OIII] prominence in NGC6240. I can then place the extended and high velocity [OIII] at the position of a biconical structure in *HST* imaging and additionally constrain the energetics of the [OIII] outflow (Müller-Sánchez et al. 2018).

In this work, I utilize longslit spectroscopy as a follow-up to localize the double-peaked emission lines in spectra of galaxies that host AGN (Chapter 2). I place two (long)slits at orthogonal positions for each galaxy, which enables me to separate the stellar kinematics from the ionized gas kinematics. I can then determine the kinematic nature of the ionized gas based on position, velocity, and velocity dispersion. Integrated spectroscopy combines all kinematic information into one profile, where the spatial details are washed out. I use longslit spectroscopy to measure the velocities of smaller Gaussian components of the galaxy kinematics at each position since they are not combined with emission lines from a different spatial position.

In this work I use a variety of optical longslit spectrographs that have similar specifications: Lick/Kast, Palomar/Double Spectrograph, MMT/Blue Channel Spectrograph, Keck/DEIMOS (Deep Imaging Multi-Object Spectrograph), and APO/DIS. All have a 1200 lines mm^{-1} grating that disperses the light in the spectral direction and all have similar spatial resolution on the order $0''.5$.

1.4.2 Integral Field Spectroscopy

Longslit spectroscopy is limited by efficiency, meaning that it is useful for one or two slit positions on a galaxy but would take too many slit positions to cover the entire face of a galaxy. This is where integral field spectroscopy (IFS) comes in. It is the natural extension of longslit to fully 3D spectroscopy, where every spaxel (spatial pixel) contains its

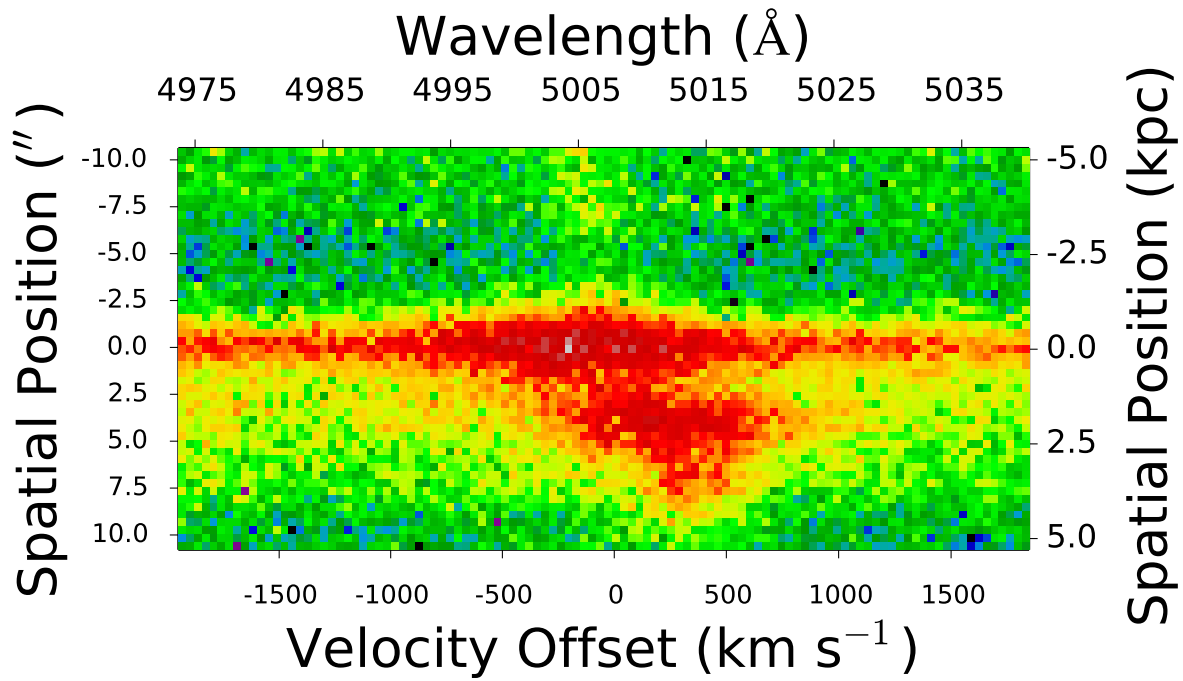


Figure 1.7: APO/DIS longslit observation of NGC6240 from Müller-Sánchez et al. (2018), which centers on the [OIII] emission at $\lambda 5007$. It reveals a spatially-resolved outflow that extends to the north (~ 5 kpc) of the stellar continuum and has a high velocity dispersion.

own spectrum. There are a couple of different techniques used to achieve IFS; this work focuses on fiber IFS. A disadvantage of fiber bundles is that there are gaps between the individual fibers, which must be filled in using techniques such as dithering.

IFS data can provide a wealth of information. For example, sampling galaxies at a variety of spatial positions allows the construction of spatially-resolved quantities such as the specific angular momentum of galaxies, which is a more informative tool than the rotation curves from longslit data. However, IFS data is much more complicated to handle and comes with a variety of challenges, such as practical limitations due to spatial sampling, dealing with adaptive binning schemes, and/or modeling wavelength-dependent PSFs to name a few. While some of these considerations are still relevant for integrated or longslit spectroscopy, many are made much more complicated by the 3D nature of IFS datasets. Handling IFS data requires a detailed knowledge of both spectroscopy and imaging simultaneously.

An example of the utility of IFS in comparison with longslit observations is shown in Appendix B, where I construct a pseudo-IFS observation using two orthogonal longslit position angles and then compare the kinematics from the pseudo-IFS to that of the full velocity field from IFS observations. With the IFS follow-up I am more easily able to model and constrain the position angle of the velocity field.

The field of IFS is changing rapidly due to many recent large IFS surveys of local galaxies. While there are exciting advances in higher redshift IFS surveys, I focus here on the local counterparts. The early local IFS surveys explored one galaxy at a time and were limited in the number of observed galaxies. They included the SAURON survey (de Zeeuw et al. 2002), the DiskMass survey (Bershady et al. 2010), the ATLAS^{3D} survey (Cappellari et al. 2011), and the CALIFA (the Calar Alto Legacy Integral Field Area) survey (Sánchez et al. 2012). The next generation of surveys have the ability to observe multiple galaxies simultaneously. They include the SAMI (Sydney-AAO Multi-object IFS) survey (Bryant et al. 2015) and the MaNGA (Mapping Nearby Galaxies at APO) survey (Bundy et al. 2015). Both SAMI and MaNGA provide the spatially-resolved equivalent of the SDSS survey, allowing the study of

spatially resolved galaxy properties for a wide variety of galaxies. MaNGA in particular is a focus of this work, since it will survey $>10,000$ galaxies from a carefully selected set of galaxies with a large dynamic range in galaxy properties, environment, and star formation rate. This dataset offers the unique opportunity to carry out detailed statistical work on the kinematics of galaxies.

The newest IFS surveys tackle many of the challenges of IFS data mentioned above in their data reduction and processing pipelines. For instance, the MaNGA survey’s data analysis pipeline (DAP) incorporates adaptive binning schemes that can be user-defined. Much of Chapter 5 of this thesis focuses on the detailed considerations to IFS data that are addressed by the DAP.

1.4.3 Imaging

Imaging is a very common tool in extragalactic astronomy and has been used for decades to understand galaxy morphologies and structures. It has also been utilized in a variety of ways to identify merging galaxies. Deep imaging surveys with CCDs have been around for many years and in this work I use imaging from the Sloan Digital Sky Survey (York et al. 2000). While imaging is not a new technique, the community continues to develop new tools to extract sources from images and to measure various imaging properties of galaxies (both parametric and non-parametric) that I will introduce in this section.

The individual imaging tools used to study galaxy evolution range from tools such as the visual (by-eye) classifications of galaxies in GalaxyZoo (Lintott et al. 2011) into morphological types by citizen scientists (these morphological types were originally identified by Edwin Hubble in the 1920s; Hubble 1926), to the extraction and modeling of the light profiles of galaxies using surface-brightness tools like **GALFIT** that rely upon parameterizing the light of the galaxy using exponential profiles (Sérsic 1963), to non-parametric techniques to determine the asymmetry of light in a galaxy (Conselice et al. 2003). Lately, it has additionally become popular to use machine learning techniques that use the light in each

individual pixel to classify and make conclusions about galaxies, using techniques such as random forests or convolution neural networks (CNN). These tools fall into four main categories: visual morphology, parametric tools to measure light profiles, non-parametric tools to measure light, and machine-learning. In Chapter 4, I primarily utilize non-parametric tools (and one parametric one), which I combine to identify merging galaxies under a machine learning tool.

It has become clear over time that all of these techniques are susceptible to different biases. For instance, many techniques are sensitive to the signal-to-noise (S/N) of a given observation; the lower surface-brightness regions of a galaxy could become undetectable if a galaxy is dimmer. Another concern is that galaxies look different in different wavelengths of light; for instance a galaxy observed in redder light in may have dimmer spiral arms. Yet another concern is that galaxies themselves as well as the imaging techniques change with redshift. This is a function of resolution, dimmer surface brightness, as well as the inherent evolution of galaxy properties over cosmic time. There are additional difficulties that accompany the use of complex machine learning tools; these tools can still be sensitive to S/N and require detailed attention to cleaning the input galaxy images. The results of machine learning are also difficult to interpret. All of these techniques can be useful for different applications and in order to use them correctly, it is necessary to consider the biases associated with each technique. Chapter 5 focuses on utilizing a machine learning technique that combines many different imaging tools (parametric and non-parametric), so I introduce these here.

Galaxy surface brightness can be quantified using integrated light profiles, which measure the intensity of light and fit this as a function of radius. Sérsic (1963) defines the surface brightness profile of a galaxy using the general exponential formula:

$$I(R) = I_0 \exp(-b(n) \times R/R_e^{1/n} - 1)$$

where the surface brightness at radius R is parameterized using an exponentially decaying profile with radius that depends on the effective radius (R_e) and the Sérsic index, n . $b(n)$ is a function of the Sérsic index and is determined such that R_e contains half of the light within the galaxy. $n = 1$ describes a disk galaxy and $n = 4$ describes an elliptical galaxy.

This parameterization of the surface brightness of a galaxy has been widely used and is also applied in the **GALFIT** code (Peng et al. 2002), which I use in this work. It models the image of a galaxy using various different types of exponential profiles and/or PSFs.

Non-parametric methods aim to measure the light in galaxies without assuming an underlying function. Challenges of this class of technique include that they can be sensitive to the noise in the galaxy, so many of these measurements include corrections for noise. One popular non-parametric technique is the *CAS* system (Conselice 2014), which includes measurements of concentration, asymmetry, and the clumpiness of galaxies. Measuring these quantities involves determining which spaxels belong to a galaxy which can be tricky in its own right; I employ various tools to carry out detailed aperture photometry on images of galaxies before measuring these quantities. This process is described in detail in Chapter 4, but in brief, tools such as **Source Extractor** are useful aperture photometry tools that identify galaxies within an image and can help determine which pixels belong to a given galaxy.

Other imaging tools include the *Gini* – M_{20} parameters, which have been used to determine how light is distributed within a galaxy. The *Gini* coefficient is actually borrowed from the field of economics to determine how wealth is distributed in a society. A higher *Gini* value indicates that all wealth/light is concentrated in one person/pixel and a lower *Gini* value means that the wealth/light is more spread out. M_{20} is the second order moment of the brightest 20% of the light in a galaxy and probes how light is distributed relative to the center of the galaxy. As with any statistical quantity, it is possible to invent other statistics to quantify the distribution of light in galaxies. Shape asymmetry, A_S , was invented with the goal of creating an asymmetry measurement that was equally sensitive to fainter features

of galaxies like tidal tails (Pawlik et al. 2016).

The imaging tools described above are used to study the structure and morphologies of galaxies in many different applications. Here, I utilize these tools to identify merging galaxies. There is precedent for using these specific imaging tools to identify merging galaxies, which I describe in more detail in Chapter 4.

1.5 Summary of the Following Thesis Work

In this introductory chapter, I have introduced some processes that drive galaxy evolution and have specifically identified two processes, AGN feedback and galaxy mergers, which are the primary focus of this thesis.

I have also identified some open questions about these two potential avenues for galaxy evolution. For instance, while AGN-driven outflows are theoretically important for driving feedback in galaxies, many details remain unclear such as:

- The size scale of the outflow
- The connections between different phases of observed outflows
- The amount of energy entrained in outflows
- How this energy couples to the ISM of the host galaxy

Additionally, since many outflows are observed only for the most luminous and extreme AGN, it is unclear how important AGN feedback is for the overall population of galaxies.

The topic of galaxy mergers also has many open questions. On one hand, the theoretical foundation of our understanding of how the universe assembles itself points towards the necessity of merging galaxy halos. However, observational studies of merging galaxies disagree on their importance for driving galaxy evolutionary processes such as star formation and AGN activity. Part of this difficulty stems from the fact that galaxy mergers come in a surprising diversity. Also, the literature disagrees on the evolutionary role of galaxy mergers

due to the many heterogeneous methodologies that have been employed to identify galaxy mergers; these different techniques, coupled with the diversity of types of merging galaxies, present a difficult problem.

I have presented a number of observational tools that are useful for addressing these open questions in AGN feedback and galaxy mergers. I have specifically focused on the kinematics of AGN outflows and of merging galaxies, introducing many different kinematic tools that are used to study the energetics of outflows and to identify merging galaxies. The kinematics of gas (for AGN outflows) and of the stellar component (for galaxy mergers) are crucial for directly addressing some of the posed problems in the field. In this thesis, I advance our understanding of galaxy evolution using a combination of these tools coupled with rigorous statistical techniques.

The kinematic techniques in this thesis include spatially resolved longslit observations of double-peaked AGN, which I use to resolve the nature of the double peaks by examining them at different positions in the galaxy. The kinematic classification I develop from this method is presented in Chapter 2. I then pair the longslit data with analytic Markov Chain Monte Carlo modeling in order to constrain the energetics of the biconical outflows among the sample of double-peaked AGN. I present this model and examine the potential for these biconical outflows to drive feedback in their host galaxies in Chapter 3.

In Chapter 4 I create a statistical learning technique that utilizes images from simulations of merging galaxies to improve the identification of merging galaxies. Then, in Chapter 5, I introduce another merger identification technique based on the kinematic maps of these simulated galaxies. The goal of this type of approach is to increase the observability timescale of galaxy mergers, to understand how different merger parameters like mass ratio or gas fraction affect the observability of mergers, and to increase the accuracy and precision (over that of existing merger identification techniques).

Finally, I summarize the main conclusions of this thesis and explore some future work in Chapter 6.

Chapter 2

The Origin of Double-Peaked Narrow Lines in AGN II: Kinematic Classifications for the Population at $z < 0.1$

We present optical longslit observations of the complete sample of 71 Type 2 active galactic nuclei (AGNs) with double-peaked narrow emission lines at $z < 0.1$ in the Sloan Digital Sky Survey. Double-peaked emission lines are produced by a variety of mechanisms including disk rotation, kpc-scale dual AGNs, and NLR kinematics (outflows or inflows). We develop a novel kinematic classification technique to determine the nature of these objects using longslit spectroscopy alone. We determine that 86% of the double-peaked profiles are produced by moderate luminosity AGN outflows, 6% are produced by rotation, and 8% are ambiguous. While we are unable to directly identify dual AGNs with longslit data alone, we explore their potential kinematic classifications with this method. We also find a positive correlation between the narrow-line region (NLR) size and luminosity of the AGN NLRs ($R_{\text{NLR}} \propto L_{[\text{OIII}]}^{0.21 \pm 0.05}$), indicating a clumpy two-zone ionization model for the NLR.

This chapter reproduces Nevin et al. (2016). Reproduced with permission of the AAS.

2.1 Introduction

A primary goal of modern astrophysics is to investigate how galaxies and their supermassive black holes (SMBHs) grow and coevolve. Correlations between the properties of the SMBH and the host galaxy suggest that the growth of galaxies and SMBHs are closely connected; for example, the $M-\sigma_*$ relation connects the mass of the SMBH to the velocity

dispersion of the stars in the galactic bulge (e.g., Merritt 2000; McConnell & Ma 2013). Active galactic nucleus (AGN) feedback and AGN feeding processes have been invoked by theory as possible methods to maintain this relationship between SMBH and the host galaxy (e.g., Croton et al. 2006; Di Matteo et al. 2005; Springel 2005).

‘Positive’ feedback, where the energy from the central AGN ignites star formation, has reproduced some observed relationships between the central AGN and the host galaxy (e.g., King 2005; Ishibashi & Fabian 2012; Silk 2013). The relative importance of positive or negative AGN feedback on the host galaxy remains unknown, as does the relative importance of different potential mechanisms for feedback (radiation, jets, or winds).

AGN-driven ‘negative’ feedback (henceforth, feedback) provides a method to evacuate gas from a galaxy and regulate star formation and the growth of the SMBH (e.g., Croton et al. 2006; Springel 2005; Hopkins et al. 2005). The bimodal color distribution of galaxies in the nearby universe and the lack of massive galaxies in the mass function of galaxies require quenching of massive galaxies via a feedback mechanism (e.g., Silk 2011; Faber et al. 2007; Bell et al. 2004; Brown et al. 2007). AGN feedback operates through a variety of mechanisms including relativistic plasma jets (e.g., Fabian 2012), direct radiation (e.g., Ciotti et al. 2010), and mass outflows of ionized gas (e.g., Crenshaw & Kraemer 2003). These types of feedback can impact material on different size scales from regions directly surrounding the central SMBH (Tombesi et al. 2013) to the Mpc-scale intergalactic medium (Malarecki et al. 2013). However, it is difficult to observe these different types of feedback in action. Additionally, the details of the efficiency of energy and momentum transfer to the interstellar medium (ISM) and how this feedback might affect the surrounding galaxy are largely unknown (Khalatyan et al. 2008; Hopkins et al. 2005). Observational studies often focus on relativistic AGN jets (e.g., Veilleux et al. 2005) or other highly energetic cases such as Broad Absorption Line QSO outflows as examples of feedback (e.g., Arav et al. 2013). In this series of papers, we instead focus on the much more numerous (but less luminous) AGN-driven ionized outflows in the nearby universe. These types of galaxies account for 90-95% of the total AGN population

(Rafter et al. 2009), and their ionized mass outflows, or AGN winds, operate on a spatial scale coincident with circumnuclear star formation (Crenshaw et al. 2015).

In addition to feedback, AGN feeding through stochastic processes such as bar-driven inflows (e.g., Coelho & Gadotti 2011; Ellison et al. 2011), or through merger-driven processes is important in SMBH-galaxy coevolution. Simulations of galaxy mergers indicate that during the merger, gas is driven to the center of the remnant galaxy (e.g., Hopkins et al. 2005; Springel 2005). These simulations predict AGN feeding and SMBH growth will occur in this post-merger phase and observational studies have found that the AGN fraction increases from separations of 100 kpc to 10 kpc between stellar bulges in a galaxy merger (e.g., Ellison et al. 2011; Koss et al. 2012; Ellison et al. 2013). However, little is known about fueling at kpc-scale separations of these active nuclei, which we refer to as ‘dual AGNs’.

Both feeding and feedback processes can be investigated using active galaxies that have a narrow line region (NLR) with disturbed kinematics. The NLR is a low density ($n_H \leq 10^6 \text{ cm}^{-3}$) spatially extended region (from a few hundreds of parsecs to $\sim 30 \text{ kpc}$) surrounding the central AGN that is characterized by forbidden narrow emission lines ($\Delta v < 1000 \text{ km s}^{-1}$, e.g., Osterbrock & Ferland 2006; Schmitt et al. 2003; Hainline et al. 2013). Disturbed kinematics manifest as double-peaked emission lines. These double-peaked narrow emission line profiles can be produced by dual AGNs, outflows, inflows, and disk rotation. Inflows and dual AGNs are associated with AGN feeding processes while outflows can probe AGN feedback.

In this paper we present a uniform sample of 71 double-peaked narrow emission line AGNs from the Sloan Digital Sky Survey (SDSS). Although this sample was originally selected with the purpose of identifying dual AGNs, this work is mostly concerned with the kinematics of single AGNs with disturbed NLRs. This sample of AGNs with disturbed NLR kinematics enables us to investigate the origin of the disturbed NLR and probe both feeding and feedback processes in these galaxies.

However, determining the origin of double-peaked emission lines has been historically

challenging since it is difficult to determine the spatial location of the emission in integrated spectra. For instance, ionized outflows have been identified based upon signatures in integrated spectra such as blue wings (e.g., Whittle 1985). This is problematic since gas kinematics can shift across the spatial extent of the NLR, becoming impossible to disentangle in an integrated spectrum. As a result, past work has associated double-peaked emission lines with a variety of origins and often is unable to unambiguously identify the origin of these double peaks. Double-peaked and asymmetric emission lines have long been associated with an outflowing biconical structure; the blueshifted component is identified as the front-facing wall of the bicone, and the redshifted peak of the double-peaked profile is the rear-facing wall (e.g., Heckman et al. 1981; Das et al. 2006; Crenshaw et al. 2015). Other work has also suggested that double-peaked NLR emission lines could also be associated with kinematic dual AGNs (e.g., Comerford et al. 2009b; Comerford et al. 2013; Barrows et al. 2013). Smith et al. (2012) suggest that equal flux double-peaked emission lines could be associated with rotating disks.

Using spatially-resolved spectra we can now study the double-peaked profiles at each spatial position. In this work we develop a longslit kinematic classification technique to determine if the NLR kinematics are outflow-dominated or rotation-dominated. Here we focus on the kinematic nature as well as the ionization structure of the NLR. We use our observations of moderate luminosity AGNs to study the size-luminosity relationship for the NLR. Although the exact ionization structure of the NLR is not well determined, there is an observed positive correlation between the size of the NLR and the luminosity of the AGN, which indicates that the NLR is photoionized by the central AGN (e.g., Hainline et al. 2014, 2013; Bennert et al. 2002; Schmitt et al. 2003; Liu et al. 2013b; Müller-Sánchez et al. 2015). The slope of this relationship reveals the ionization structure of the NLR; a steeper slope of $R_{\text{NLR}} \propto L_{[\text{OIII}]}^{0.5}$ corresponds to a simplistic NLR described by a constant density law and a constant ionization parameter, while a shallower slope of 0.34 corresponds to a two-zone clumpier ionization model (Baskin & Laor 2005; Dopita et al. 2002).

In this paper (Part 2 of a multiple paper series) we address the kinematic nature of the NLR for galaxies in the nearby universe for our sample of 71 Type 2 AGNs with double-peaked narrow emission lines at $z < 0.1$. We describe the sample selection and data reduction in Section 2.2. We describe our kinematic classification technique in Section 2.3.1, where we classify galaxies as different subclasses of outflow- or rotation-dominated. We discuss our results from the kinematic classification and the properties of each kinematic class of galaxies in Section 2.4. In Section 2.5, we discuss the implications of the classification method for identifying dual AGNs as well as our measurement of the size-luminosity relation and its implications for the ionization structure of the NLR. We present our conclusions in Section 2.6. A cosmology with $\Omega_m = 0.3$, $\Omega_\Lambda = 0.7$, and $h = 0.7$ is assumed throughout.

In this paper (Part 2 of a multiple paper

2.2 Methods

2.2.1 Sample Selection

The 71 galaxies in the uniform sample originate from a full sample of Type 2 AGNs with double-peaked [OIII] emission lines in SDSS (York et al. 2000). Three groups selected catalogues of double-peaked AGNs (Wang et al. 2009; Liu et al. 2010; Smith et al. 2010).

Wang et al. (2009) selected 87 Type 2 active galaxies using BPT emission-line diagnostics (Baldwin et al. 1981), then made a cut to eliminate galaxies with SDSS r -band magnitude $r > 17.7$. They selected for similar intensity peaks of the double-peaked profiles using a flux ratio cut of 1:10 between the intensity of each peak and required a wavelength separation between these two peaks of $\Delta\lambda \geq 1 \text{ \AA}$. Smith et al. (2010) selected a sample visually for active galaxies that exhibit double peaks. However, the Type 1 and Type 2 AGNs from Smith et al. (2010) are located at redshifts $0.1 < z < 0.7$, so they are not included in the sample selection for this paper. Since Smith et al. (2010) is the only catalog with Type 1 objects, by excluding these higher redshift objects we also restrict our sample to Type 2

objects. This avoids the influence of broad lines ($\Delta v > 1000 \text{ km s}^{-1}$) on the [OIII] profiles. Liu et al. (2010) selected 167 Type 2 AGNs by making a $S/N > 5$ cut for [OIII] $\lambda 5007$ and requiring that both [OIII] $\lambda 5007$ and [OIII] $\lambda 4959$ be best fit by two Gaussians. This excludes AGNs with more complex profiles, wings, and > 2 Gaussian components. These three groups selected 340 unique objects. We select the complete sample of 71 double-peaked Type 2 AGNs that are at $z < 0.1$ to ensure sub-kpc spatial resolution on all optical longslit instruments used in the follow-up observations.

To determine the nature of these objects and further characterize their properties, we observe them using two complementary follow-up methods: optical longslit spectroscopy and Jansky Very Large Array (VLA) radio observations.¹ We use the longslit spectroscopy to map the source of the double-peaked emission across the spatial extent of each galaxy; to do so we observe each galaxy at two position angles in order to constrain the orientation and spatial positioning of the NLR. For most galaxies, these two position angles are orthogonal with the exception of galaxies that have an intriguing disturbed feature or companion galaxy at a given position angle.

We choose one position angle to be the photometric major axis of the galaxy from the SDSS r -band photometry. This is motivated by one of our science goals, which is to determine if the NLR is rotational in origin. Galaxies in which the NLR is dominated by rotation will demonstrate the most extended emission along the photometric major axis, in the plane of the galaxy.

We use various spectrographs with similar pixelscales (Lick Kast Spectrograph, $0.78''/\text{pixel}$; Palomar Double Spectrograph, $0.39''/\text{pixel}$ (Oke & Gunn 1982); MMT Blue Channel Spectrograph, $0.29''/\text{pixel}$ (Schmidt et al. 1989); APO Dual Imaging Spectrograph, $0.42''/\text{pixel}$ in the blue channel, $0.4''/\text{pixel}$ in the red channel; and Keck DEep Imaging Multi-Object Spectrograph, $0.12''/\text{pixel}$ (Faber et al. 2003). We use a $1200 \text{ lines mm}^{-1}$ grating for

¹ Spatially-resolved imaging of X-ray sources (e.g., Komossa et al. 2003; Mazzarella et al. 2012; Barrows et al. 2016) that are coincident with emission-line peaks can also confirm the presence of dual AGNs. In this paper series we focus on radio observations as a method for confirming dual AGNs.

all spectrographs. Table A.1 lists the details of these observations.

The VLA observations are complementary to the optical longslit data and together they can fully constrain the source of the double peaks for a given galaxy; Müller-Sánchez et al. (2015) focus on this technique for a subsample of 18 double-peaked AGNs. In this paper we develop a novel technique using only the longslit data to characterize the NLR of this sample of 71 galaxies. In future work, we will combine our longslit observations with the VLA data for the full sample of 71 galaxies (Müller-Sánchez et al. in prep.).

2.2.2 Data Reduction

We reduce and extract both the 2 and 1-dimensional spectra at both position angles for each galaxy using the IRAF packages CCDPROC and APALL, respectively. The Keck/DEIMOS data were reduced using the DEEP2 pipeline (Cooper et al. 2012; Newman et al. 2013). We preserve the spatial information in the 2d spectra and use the aperture-extracted 1d spectra for wavelength solutions, which we use to produce the velocity maps. We obtain accurate systemic velocities using extinction corrected stellar absorption features from the OSSY SDSS DR7 value-added catalog (Oh et al. 2011; Abazajian et al. 2009) and the IDL code GANDALF (Sarzi et al. 2006).

2.2.3 Extracting and Characterizing OIII Profiles

With fully reduced data in hand, we use a variety of IDL and Python programs to fit the [OIII] λ 5007 line profiles at each spatial position along the slit and extract velocity and dispersion information. We determine the spatial center of emission for each 2d spectrum using the stellar continuum. We fit a one dimensional Gaussian across the continuum in two 10 pixel cutouts on either side of the wavelength center of the [OIII] λ 5007 profile, and determine its average center and full width at half maximum ($\text{FWHM}_{\text{cont}}$). We later apply this spatial center and width ($\text{FWHM}_{\text{cont}} \pm 1$ row) when we refer to the ‘resolved center’ of the emission. The positive spatial direction shown in all plots of the 2d spectra in this work

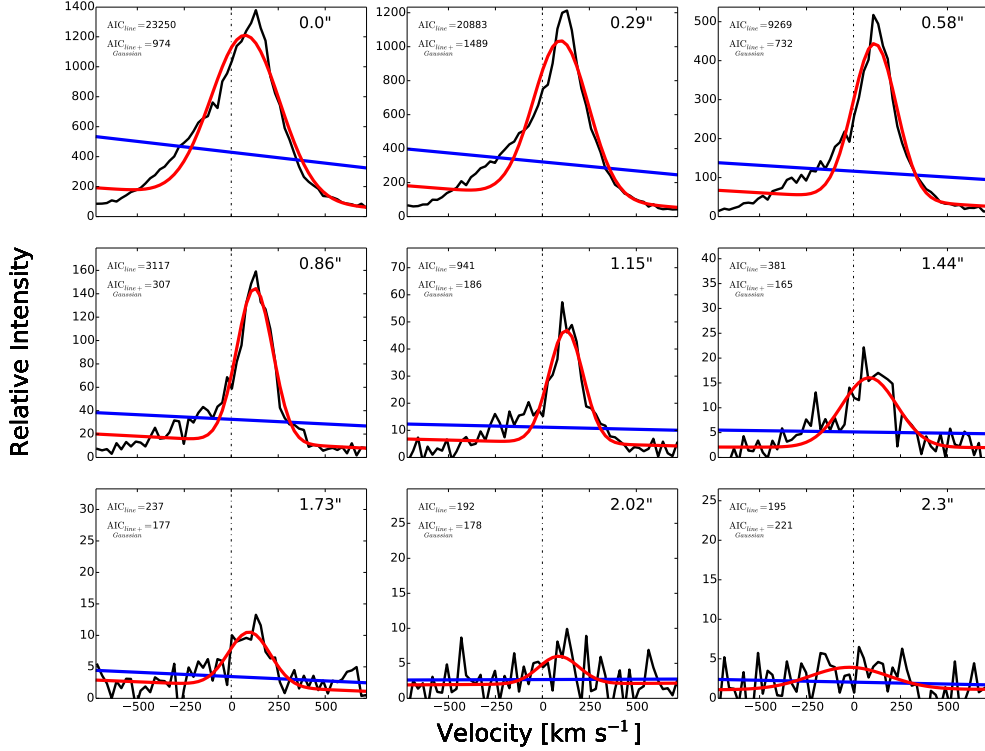


Figure 2.1: The Akaike statistics demonstrated for the [OIII]λ5007 emission for the example galaxy J0009-0036. For each spatial row of the example galaxy J0009-0036 (to the NE of the spatial center of the galaxy) we report the spatial position (in arcseconds, upper right). Each panel is spaced by angular distance 0.29'', which is the pixelscale of the MMT Blue Channel Spectrograph. We start the figure at spatial position 0.0'' to highlight the diminishing flux of the emission line to one spatial extreme (the NE) of the galaxy spatial center. Note that this is a symmetric NLR with flux also extending to the SW of the spatial center. We show the Akaike statistic for both a line (two parameter fit), plotted in blue, and a single Gaussian with an underlying line (five parameter fit), plotted in red. If $AIC_{line+Gaussian} < AIC_{line}$, then that spatial row is considered to have significant emission and lies within the Akaike width. Here, the 2.02'' row is the row of last significant emission, and the 2.3'' row no longer has significant emission. We repeat this process for both observed position angles of each galaxy.

corresponds to the NE direction on the sky.

We use an information criterion to determine both the extent of the emission and the number of Gaussian components to fit at each spatial position. The Akaike Information Criterion (AIC) is a least squares statistic that introduces a penalty for additional parameters, defined by Akaike (1974). Numerically, $AIC = \chi^2 + 2k$, where k is the number of parameters and χ^2 is the chi-square statistic:

$$\chi^2 = \sum_{i=1}^n \frac{(y_i - f(x_i; \hat{\theta}))^2}{\hat{\sigma}_i^2}$$

where n is the number of data points in the sample, y_i is the measured flux, $f(x_i; \hat{\theta})$ is the Gaussian model for the emission line flux, x_i is the input wavelength of the Gaussian model, $\hat{\theta}$ are the parameter values of the Gaussians, and $\hat{\sigma}_i^2$ is the measurement uncertainty on the measured flux. We utilize the corrected AIC (AIC_c) due to our finite number of data points: $AIC_c = AIC + 2k(k+1)/(n-k-1)$ where n is the sample size and k is the number of parameters. When comparing two models with a different number of parameters, the model that produces the smallest value for the above statistic represents the better fit.

We apply this statistic to each row in the spatial direction to determine the extent of the emission. We establish if the row is better fit with a two parameter linear fit or a five parameter Gaussian + linear fit (Figure 2.1). This provides what we define as the ‘Akaike width’ of the emission, which is measured in both arcseconds and pixels, and encompasses all the rows that are best fit by a five parameter Gaussian + linear fit. We then derive errors on this measurement from a Monte Carlo simulation. We construct 100 realizations of the spectrum by adding Gaussian noise with flux according to the inverse variance error image, and repeat the measurement of the Akaike width for each realization. The mean value of the Akaike width and its standard deviation are derived from the properties of the resulting distribution (Table A.2).

We also apply the Akaike statistic to determine the appropriate number of Gaussians

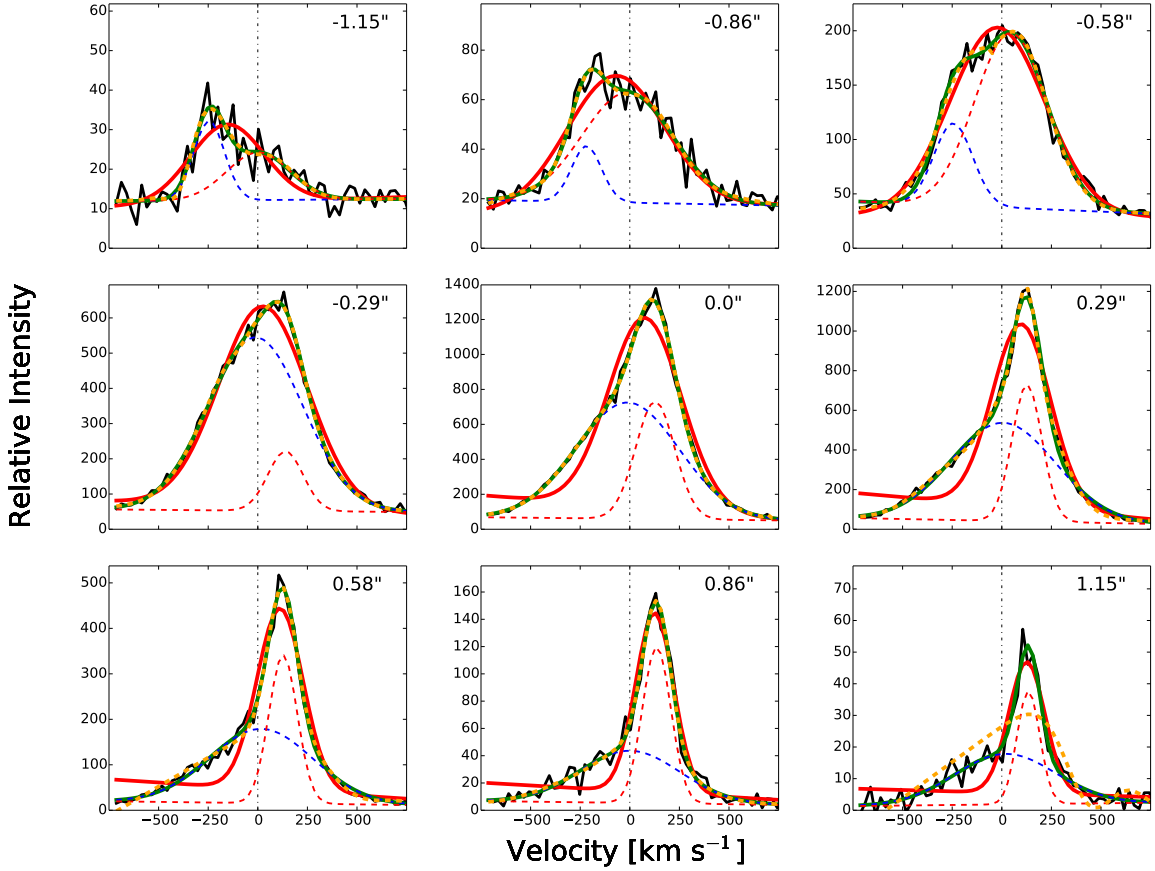


Figure 2.2: Fitting multiple Gaussians across the spatial extent of J0009-0036 to the $[\text{OIII}]\lambda 5007$ profile. The galaxy and position angle of the observation are the same as Figure 2.1 but now we change the spatial coverage to $1.15''$ on either side of the spatial center of the galaxy to highlight the fitting of multiple Gaussian components. The data are shown as solid black lines. For each spatial row, we show the integrated one, two, and three Gaussian fits in red solid, green solid, and yellow dashed lines, respectively. We also display the individual Gaussians from the two Gaussian fit in blue and red dashed lines, where the blue represents the blueshifted component and the red is the redshifted component of the two Gaussian fit. The black dashed vertical line is the systemic velocity of the galaxy. Intensity is displayed in units of relative intensity. This plot demonstrates the AIC_c applied to determining the number of Gaussians to fit to each significant spatial row ('significant' implies that the emission line is already better fit by one than zero Gaussians and is therefore within the Akaike width, Figure 2.1).

to fit to each spatial row (Figure 2.2). We use the AIC_c to determine how many Gaussians are the best fit for each row within the resolved center of the galaxy ($FWHM_{\text{cont}} \pm 1$ row). We classify a galaxy as having > 2 Gaussian components only if more than half of these interior rows are better fit by three or more components. This approach is used in the kinematic classification scheme.

We extract velocity information for each row within the Akaike width by fitting both one and two Gaussians. The velocity offsets of each of the one and two Gaussian profiles are calculated relative to the systemic velocity of the galaxy. The center of each of these Gaussians in velocity space is mapped across the spatial extent of the galaxy. Similarly, we map the dispersion of each of these Gaussian profiles across the galaxy (reported as σ for the one Gaussian fit and σ_1 and σ_2 for the two Gaussian fit). We derive errors on these calculations from the Monte Carlo method described above. The uncertainty on velocity measurements increases as the distance from the galaxy center increases because the S/N for these rows drops dramatically.

Outflows and NLRs with disturbed kinematics have asymmetric emission line profiles and often blue wings. We utilize a nonparametric diagnostic for profile asymmetry. In order to avoid excluding profiles that have low flux wings or other non-traditional types of asymmetry, we choose not to assign parametric Gaussian metrics of asymmetry. Instead, we employ the nonparametric measurement for line profile asymmetry from Liu et al. (2013c):

$$A \equiv \frac{(v_{90} - v_{\text{med}}) - (v_{\text{med}} - v_{10})}{W_{80}}$$

where v_{10} and v_{90} are the velocities that encompass 10% and 90% of the integrated flux across the profile, respectively, v_{med} is the velocity that corresponds to the median value of the integrated flux profile, and W_{80} is defined as $W_{80} \equiv v_{90} - v_{10}$. The sign of asymmetry is negative if the profile has a blue wing and positive for red wings.

This statistic (Figure 2.3) is sensitive to double-peaked profiles that have unequal flux ratios; specifically the absolute value of asymmetry is large if the profile has what can be

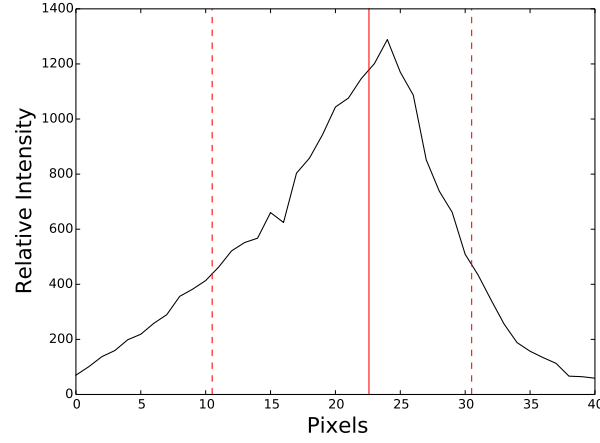


Figure 2.3: The asymmetry measurement reveals a blue wing for J0009-0036. Here, the $[\text{OIII}]\lambda 5007$ profile of the central spatial row is plotted in black for a 40 pixel cut (20 pixels on either side of the systemic velocity). The red solid line represents the median velocity (v_{med}) for the profile; this is the velocity that corresponds to a summed 50% of the integrated flux profile at this spatial position. The left red dashed line is v_{10} , or the velocity that corresponds to 10% of the integrated flux profile, and the right dashed line corresponds to v_{90} . For this galaxy, $A = -0.146$, indicating the presence of a blue wing.

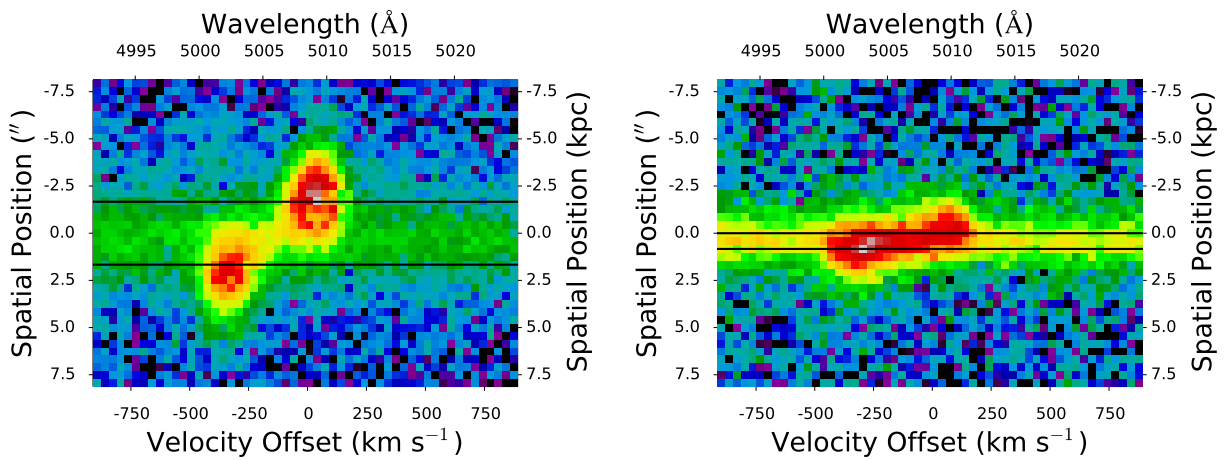


Figure 2.4: Spatial centroiding technique for J1516+0517. $[\text{OIII}]\lambda 5007$ images centered vertically on the spatial center of J1516+0517 for both position angles (top: $\text{PA}=81^\circ$ East of North, and bottom: $\text{PA}=171^\circ$). The black lines show the fitted spatial position for each of the two spectral components ($\lambda > 5007$ and $\lambda < 5007$ here). $\text{PA}=81^\circ$ displays a greater separation. Using both of these individual PAs, we are able to reconstruct the separation on the sky as well as the position angle on the sky of maximal separation of the double emission components.

better described as a shoulder as opposed to an equal flux double-peaked profile. We only use the measurement to classify rotation-dominated profiles as disturbed or obscured. We discuss this aspect of kinematic classification in Section 2.3.1.

In addition, we measure the position angle of the NLR [OIII] λ 5007 emission ($\text{PA}_{[\text{OIII}]}$) on the sky. This allows us to determine if the [OIII] emission is rotational in origin. We fit position centroids at each peak of the double-peaked profile and calculate a separation in spatial position (Figure 2.4). By iterating at each position angle while introducing Gaussian noise from the inverse variance image, we calculate an angle of maximal separation of these spatial centroids with an associated error.

Formally, the true position of maximal separation is given by $\text{PA}_{[\text{OIII}]}$:

$$x_1 \cos(\text{PA}_{[\text{OIII}]} - \theta_2) = x_2 \cos(\text{PA}_{[\text{OIII}]} - \theta_1)$$

where x_1 and x_2 are the spatial separations at the observed position angles (Figure 2.4), θ_1 and θ_2 , respectively.

2.2.4 The Luminosity of the NLR

To investigate the ionization structure of the NLR, we measure both the size and the [OIII] λ 5007 luminosity of the region. To determine the radius (in parsecs) of the NLR, we use half the Akaike width, defined in Section 2.2.3. We then convert to a physical distance using the Python `astropy.cosmology` utility.

To determine the luminosity of the NLR, we use the SDSS DR7 OSSY value-added catalogue (Oh et al. 2011). We use a dereddened luminosity, $L_{[\text{OIII}]}^c$, which is calculated from the observed [OIII] luminosity, $L_{[\text{OIII}]}$, based upon a two component reddening correction (Oh et al. 2011). This includes a galaxy-wide dust correction as well as a nebular correction using the Hydrogen Balmer decrement:

$$L_{[\text{OIII}]}^c = L_{[\text{OIII}]} \left(\frac{(\text{H}\alpha/\text{H}\beta)_{\text{obs}}}{3.0} \right)^{2.94}$$

where $H\alpha/H\beta$ is the line ratio for the Balmer lines (Osterbrock & Ferland 2006).

The bolometric luminosity is calculated from $L_{[\text{OIII}]}$:

$$L_{\text{bol}} = CL_{[\text{OIII}]}$$

where the correction, C , depends upon the $[\text{OIII}]$ luminosity. C is 87, 142, or 454 for $L_{[\text{OIII}]}$ in the respective bins $L_{[\text{OIII}]}^c (\text{erg s}^{-1}) < 10^{40}$, $10^{40} < L_{[\text{OIII}]}^c (\text{erg s}^{-1}) < 10^{42}$, and $10^{42} < L_{[\text{OIII}]}^c (\text{erg s}^{-1}) < 10^{44}$ (Heckman et al. 2004; Lamastra et al. 2009). We report $L_{[\text{OIII}]}$, $L_{[\text{OIII}]}^c$, the bolometric luminosity, and the radius of the NLR in parsecs in Table A.2 for all galaxies.

2.3 Analysis

2.3.1 Kinematic Classification

We develop a novel technique for quantitative classification of the double-peaked $[\text{OIII}]\lambda 5007$ profiles using the spatially-resolved kinematics of the NLR. Our primary goal is to determine the nature of the double peaks and assess the relative importance of their various spectral features in the kinematic classification scheme. This technique depends on the longslit data alone. In future papers, the radio data will be independently analyzed and the two data sets will be synthesized.

We design the classification method to isolate rotation-dominated spectra from outflow-dominated spectra. Müller-Sánchez et al. (2015) use a subsample of 18 galaxies to demonstrate that the majority (75%) of double-peaked NLR galaxies are caused by ‘gas kinematics’ (includes 70% outflows and 5% rotating NLR kinematics), 15% are caused by dual AGNs or outflows produced by dual AGNs, and 10% are ambiguous. Shen et al. (2011) and Fu et al. (2011) used resolved spectroscopy to show that the majority of double-peaked NLR galaxies are produced by ‘gas kinematics’ from a single AGN, including extended emission-line nebulae, jet-cloud interactions, or peculiar narrow-line.

Since Müller-Sánchez et al. (2015), Shen et al. (2011), and Fu et al. (2011) identify a statistical majority of outflow-dominated spectrum with the double-peaked selection tech-

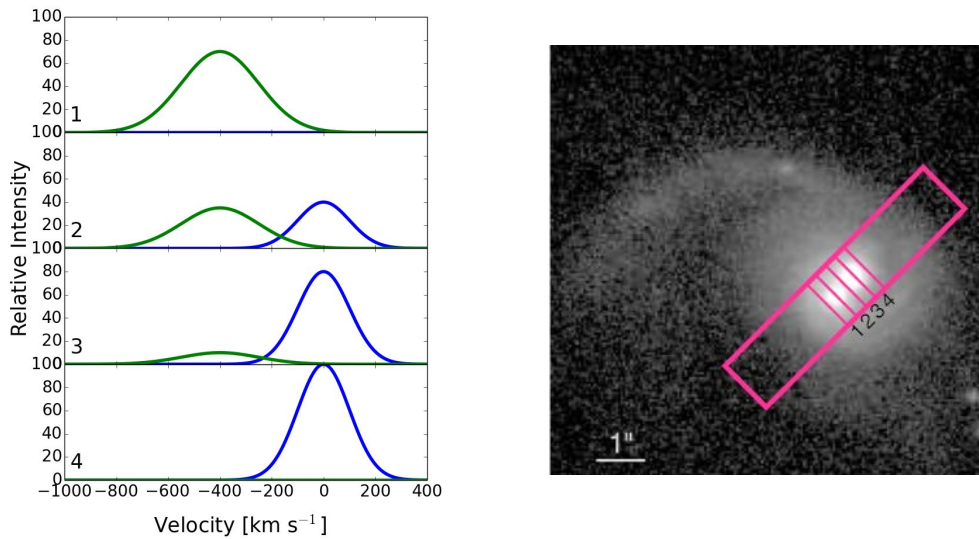


Figure 2.5: The spectrum of a toy model of a dual AGN that is characterized by the rotation-dominated NLRs of the dual AGNs with no outflow components. The x axis of the spatially-resolved spectrum (left) is in velocity space (km s^{-1}). On the right is the theoretical galaxy that hosts a dual AGN. The magenta box is the slit position (aligned SW to NE). We would expect to observe the longslit profiles as two distinct rotation-dominated NLRs with only one shifted peak at each spatial extremum and a double-peaked profile at the center. Note that based on the relative luminosity of the dual AGNs, the peaks may not be equal in flux as in this example. (Image taken from Comerford et al. 2009a).

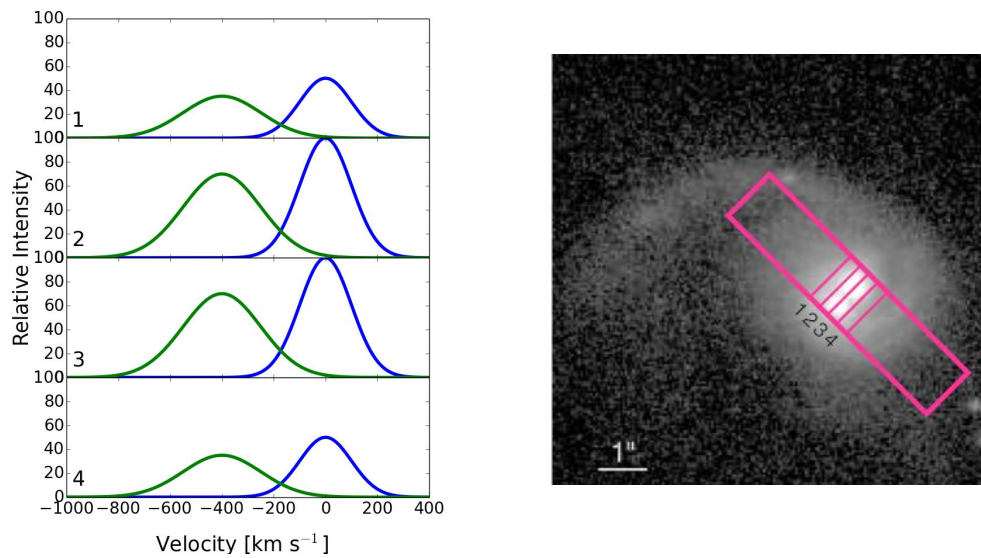


Figure 2.6: Same as Figure 2.5 but for the orthogonal slit position. At this PA we would observe the NLRs as overlapping because they are spatially coincident at all slit positions. Note that based on the relative luminosity of the dual AGNs, the peaks may not be equal in flux. The NLRs would be located at velocities centered at the relative velocities of the AGNs. (Image taken from Comerford et al. 2009a).

nique, we create a classification technique that classifies a spectrum as outflow-dominated or rotation-dominated and then focuses on the kinematic nature of each broad classification. For instance, we further classify outflows as ‘Outflow Composite’ if they have more than two Gaussian components or ‘Outflow’ if they are best fit by two components. The ‘Outflow Composite’ classification identifies outflows with complicated emission knots observed moving at distinct velocities. We further classify rotation-dominated spectra as containing a disturbance or an obscuration.

Note that dual AGNs may exist in our classification scheme but fall into multiple different categories (Section 2.5.1)². In this work, we explore the kinematic classifications for the complete sample of $z < 0.1$ double-peaked AGNs. Within this sample, there are no confirmed dual AGNs from the combination of radio and longslit data yet.

In this work we will instead focus on the possible kinematic classifications of dual AGNs that will be confirmed in future work in which we synthesize the VLA radio data and the longslit kinematic data (Müller-Sánchez et al. in prep.). In Figures 2.5 and 2.6 we explore the kinematic properties of a toy model of a dual AGN with no outflow components that is instead dominated by rotating NLR components. Each dual AGN has a rotating disk and both are orbiting in the potential of the host galaxy. We determine that one of the galaxies in the sample matches this observational prediction of a spectral profile of a rotation-dominated dual AGN. This galaxy, J1018+5127, is classified as ‘Rotation Dominated + Disturbance’. Figure 2.7 shows the spatially-resolved profiles at both PAs for this candidate dual AGN. However, since this candidate lacks confirmation of dual radio cores, we do not create a separate kinematic classification for ‘dual AGNs’ and instead allow candidate dual AGNs to fall under different kinematic classifications that describe the nature of the dual AGNs. Additionally, other work has predicted that dual AGNs such as the toy model presented

² The three dual AGNs from Müller-Sánchez et al. (2015) are classified as Outflow Composite and Outflow, and are at higher redshifts ($z > 0.1$). They are classified as dual AGNs in Müller-Sánchez et al. (2015) because they have two radio cores but these dual AGNs also have a powerful outflow component and their double-peaked profiles are well described as outflow-dominated.

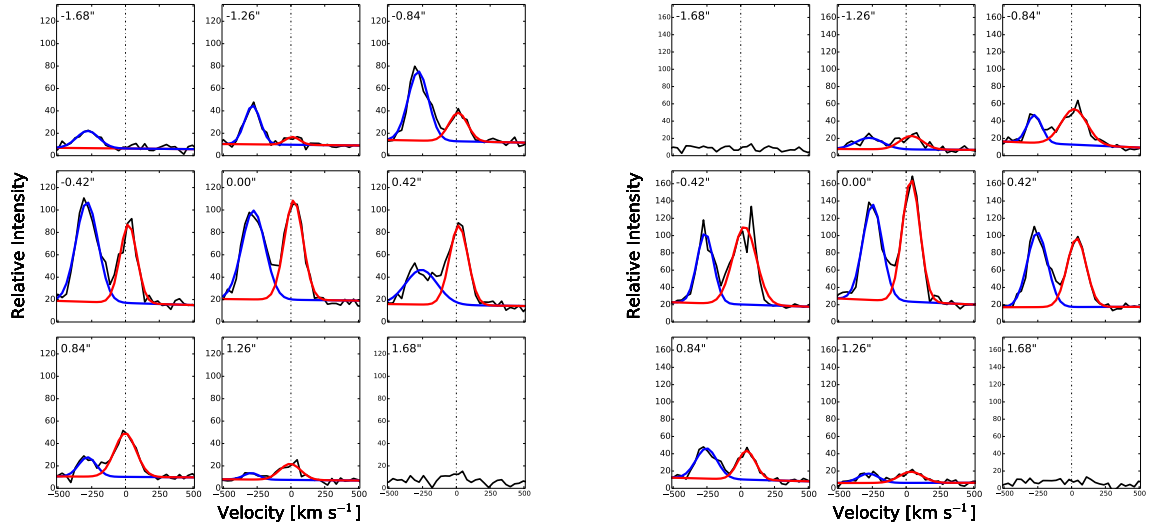


Figure 2.7: Spatial profiles of emission for J1018+5127 at both PAs. We plot the spatial profiles for PA 22° (left) and 112° (right). On the left, the narrow components alternate in flux, matching the predictions for an outflow-free dual AGN at maximum spatial separation (Figure 2.5). On the right, the narrow components do not alternate in flux, which is consistent with the prediction for a rotation-dominated dual AGN in Figure 2.6.

here that are characterized purely by rotation-dominated NLRs are not as common as dual AGNs with outflow components (Blecha et al. 2013).

We find that the most powerful quantitative properties for identifying the kinematic nature of a spectral profile are the velocity dispersion of each of the individual Gaussians in a two Gaussian fit (σ_1 and σ_2), the radial velocity of a one Gaussian fit (V_r), the number of kinematic components, and the alignment of the [OIII] λ 5007 emission with the major axis of the galaxy. Figure 2.8 demonstrates the classification scheme based upon these parameters, Table A.3 shows the values of these properties for both observed position angles of each galaxy, and Table A.4 produces the final classification for the entire sample of 71 galaxies.

Using these four properties of the [OIII] λ 5007 profiles, we first separate rotation-dominated profiles from outflow-dominated profiles. This elimination-based technique is useful because the observational properties of rotating structure have more stringent constraints. For instance, rotating structure behaves according to Keplerian physics, which place limits on the line of sight velocity ($V_r < 400 \text{ km s}^{-1}$) and velocity dispersion (σ_1 and $\sigma_2 < 500 \text{ km s}^{-1}$, Osterbrock & Ferland 2006). These observationally-defined velocity limits are used to divide outflow-dominated from rotation-dominated kinematics.

We identify outflow-dominated profiles as galaxies with velocity dispersions and line of sight velocities that are in excess of the limits given above for rotation-dominated profiles. The presence of a broad component (σ_1 or $\sigma_2 > 500 \text{ km s}^{-1}$) demonstrates the presence of an outflow (Müller-Sánchez et al. 2011). Likewise, line of sight velocities that exceed 400 km s^{-1} ($V_r > 400 \text{ km s}^{-1}$) for a single Gaussian fit identify an outflow because discrete knots of emission have been observed at these velocities in outflows (e.g., Das et al. 2006, Fischer et al. 2013, Crenshaw et al. 2015). These outflow-dominated galaxies are then further classified into ‘Outflow’ or ‘Outflow Composite’ according to the number of kinematic components. For instance, a profile with > 2 kinematic components is designated ‘Outflow Composite’ (determined using Akaike statistics described in Section 2.2). Outflows can show > 2 components because they have distinct clouds of gas that move at a variety of discrete

velocities dominated by a central engine. For a diagram of an outflow-dominated galaxy, see Figure 2.9.

Galaxies that are not classified as outflow-dominated continue along the quantitative classification scheme; we next determine if a galaxy is rotation-dominated or ambiguous according to the alignment. Alignment of the ionized gas with the stellar disk is a property of rotation-dominated galaxies. We measure alignment by comparing PA_{gal} , the position angle of the photometric major axis of the galaxy from the SDSS r -band, to $PA_{[\text{OIII}]}$ (measured in Section 2.2). As discussed in Comerford et al. (2012), a rotationally dominated double-peaked NLR should be aligned with the plane of the galaxy because the galaxy’s potential dominates the kinematics; thus for these galaxies, $PA_{[\text{OIII}]} \sim PA_{\text{gal}}$ within a 20° error (as in Müller-Sánchez et al. 2015). If the $[\text{OIII}]\lambda 5007$ emission is aligned with the plane of the galaxy, the emission is classified as rotation-dominated.

If the emission is not aligned with the plane of the galaxy and the emission has not already been classified as an outflow according to the value of radial velocity or the individual velocity dispersions, the emission could be a counter-rotating disk, an outflow, an inflow, or some combination of these kinematic origins. We could further tie the gas kinematics to an inflow origin if the galaxy were undergoing a merger since mergers funnel gas to the center of the galaxy (e.g., Hopkins et al. 2006). However, these gas kinematics could be also be explained by an outflow or counter-rotating disk in a merger. If the galaxy is not undergoing a merger, we can rule out merger-driven inflows for the kinematic origin of the disturbed NLR kinematics. However, it would still be difficult to distinguish between an outflow-dominated kinematic origin to the NLR or a counter-rotating disk. We classify these galaxies as ‘Ambiguous’ since we do not have the ability to fully determine the presence of a merger in these galaxies based upon SDSS imaging alone. Additionally, in either case, this type of galaxy is still ambiguous in its classification.

We use alignment as a classification tool once we have already classified the outflow-dominated galaxies; therefore, galaxies with outflows may also have emission that is aligned

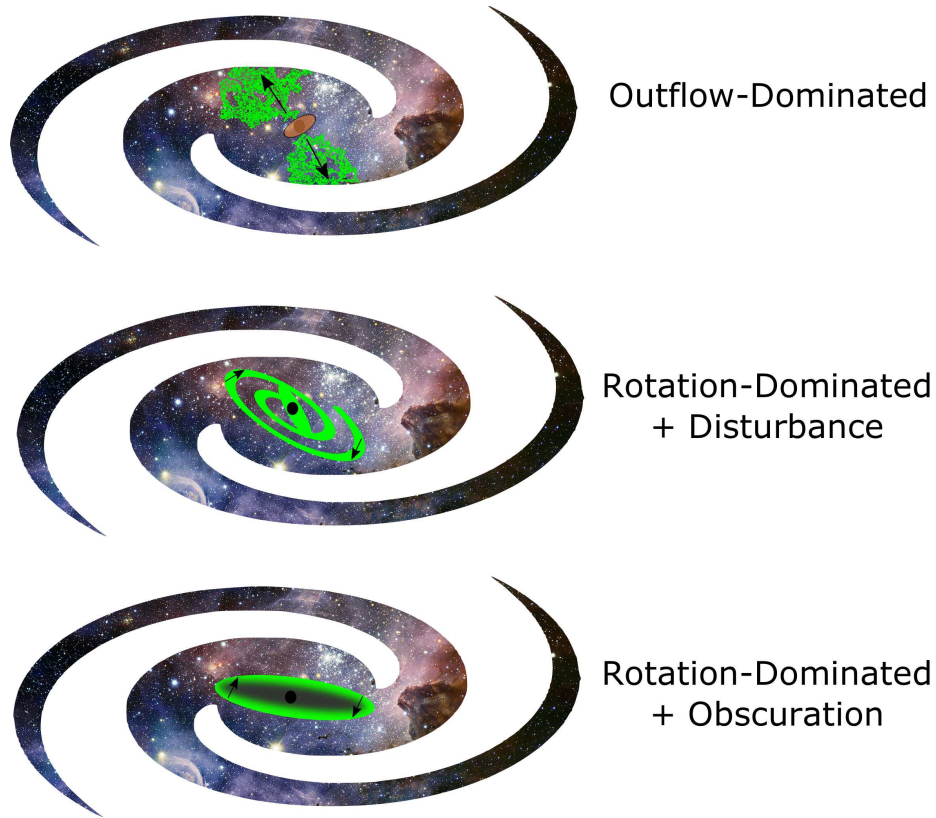


Figure 2.9: Cartoon diagrams of three of the main kinematic classifications. Here we show the origin of the $[\text{OIII}]\lambda 5007$ kinematics in green for an outflow-dominated classification and the two rotation-dominated classifications. We demonstrate the kinematic components that are responsible for the velocity shifts in the $[\text{OIII}]\lambda 5007$ profiles using black arrows. Top: An outflow-dominated galaxy, ‘Outflow’ or ‘Outflow Composite’, is characterized by outflowing $[\text{OIII}]\lambda 5007$ emission. Middle: A Rotation Dominated + Disturbance galaxy may have rotating spiral structure or a bar structure. Bottom: A Rotation Dominated + Obscuration galaxy is characterized by a rotating disk that has a co-rotating obscuring structure such as a dust lane that produces a double-peaked profile at each spatial position.

with the photometric major axis of the galaxy. This will be important in later work where we discuss the implications of the geometry of the outflow-dominated galaxies (Nevin et al. in prep.). Likewise, the number of Gaussian components is not used to further classify rotation-dominated galaxies. A rotation-dominated galaxy may have more than two Gaussian components, but we do not use this to further classify rotation-dominated galaxies into subcategories.

Within the category of rotation-dominated spectra, we further classify galaxies as ‘Rotation Dominated + Obscuration’ or ‘Rotation Dominated + Disturbance’ (such as a bar or spiral). If a galaxy has all of the kinematic properties of a rotation-dominated galaxy, the $[\text{OIII}]\lambda 5007$ emission is aligned with the kinematic major axis of the galaxy, and the galaxy has a symmetric profile (compared to both the full sample and the rotation-dominated galaxies), we classify it as Rotation Dominated + Obscuration. Smith et al. (2012) suggest that equal flux double-peaked symmetric profiles are rotating disks. We classify one galaxy (J0736+4759) from the sample of 71 galaxies as Rotation Dominated + Obscuration due to its high degree of symmetry. Radiative transfer effects from a central dust lane could account for a single peaked Gaussian with a decrease in flux at zero velocity at both observed position angles, which would produce a double-peaked profile. Figure 2.9 shows a diagram of this type of kinematic origin of a double-peaked profile.

Dynamic disturbances in the plane of the galaxy could also account for a rotation-dominated spectrum with a double-peaked profile. We classify asymmetric rotation-dominated profiles where the $[\text{OIII}]\lambda 5007$ emission is aligned with the kinematic major axis as ‘Rotation Dominated + Disturbance’. These galaxies could host nuclear bars, spiral arms, or a kinematically disturbed dual AGN that causes asymmetric double-peaked profiles (Davies et al. 2009; Hicks et al. 2009; Schoenmakers et al. 1997; Blecha et al. 2013). Bars or spirals accelerate the zero velocity gas through infall or chaotic motion (Müller Sánchez et al. 2009). This enhances the wings of the single peaked rotation-dominated profile and produces a double peaked profile that is asymmetric in flux. Again, Figure 2.9 shows a diagram of

a disturbed rotation-dominated galaxy. Note that distinguishing between a disturbed and obscured rotation-dominated NLR is the only category of classification that requires the asymmetry parameter. We discuss the quantitative determination of relative asymmetry for the rotation-dominated galaxies in Section 2.4.1.2.

For each position angle of each galaxy, we measure radial velocity, velocity dispersion, number of kinematic components, and alignment for each spatial row within the Akaike width (Table A.3, for PA 1 and PA 2). Then, we calculate the number of rows that have > 2 kinematic components within the spatial center (as measured by the stellar continuum) of the galaxy. We classify a galaxy as having > 2 kinematic components if more than half of the rows of the Akaike width are best fit with > 2 components (Table A.4). We record velocity dispersion for both the one Gaussian fit (σ) and the individual components of the two Gaussian fit (σ_1 and σ_2). In Table A.4 we determine if the dispersion of the single Gaussian fit is less than or greater than 500 km s^{-1} . We repeat this for each individual velocity dispersion of the two Gaussian fit. Next, in Table A.3 we list the position angle of the galaxy (photometric major axis in SDSS r -band) and the position angle of the $[\text{OIII}]\lambda 5007$. The photometric major axis measurements are reported in Müller-Sánchez et al. (2015), originating from Comerford et al. (2012). These position angles each have an error of $\sim 7^\circ$ associated with the measurement, thus they are classified as aligned if these position angles are within 3σ (20°). After recording the quantitative measurements, we classify the galaxies in Table A.4. We present a cartoon diagram of the kinematic origin of the $[\text{OIII}]\lambda 5007$ double peaks for three of the main classification categories (‘Outflow’, ‘Rotation Dominated + Disturbance’, and ‘Rotation Dominated + Obscuration’) in Figure 2.9. We show an example of the profiles of the five main classifications, ‘Outflow’, ‘Outflow Composite’, ‘Rotation Dominated + Obscuration’, ‘Rotation Dominated + Disturbance’, and ‘Ambiguous’ in Figures 2.10 and 2.11. We show the SDSS images to demonstrate the power of the alignment classification tool to separate ‘Ambiguous’ from rotation-dominated classifications in Figure 2.12.

We take the error on each measured quantity into consideration. We use a superscript

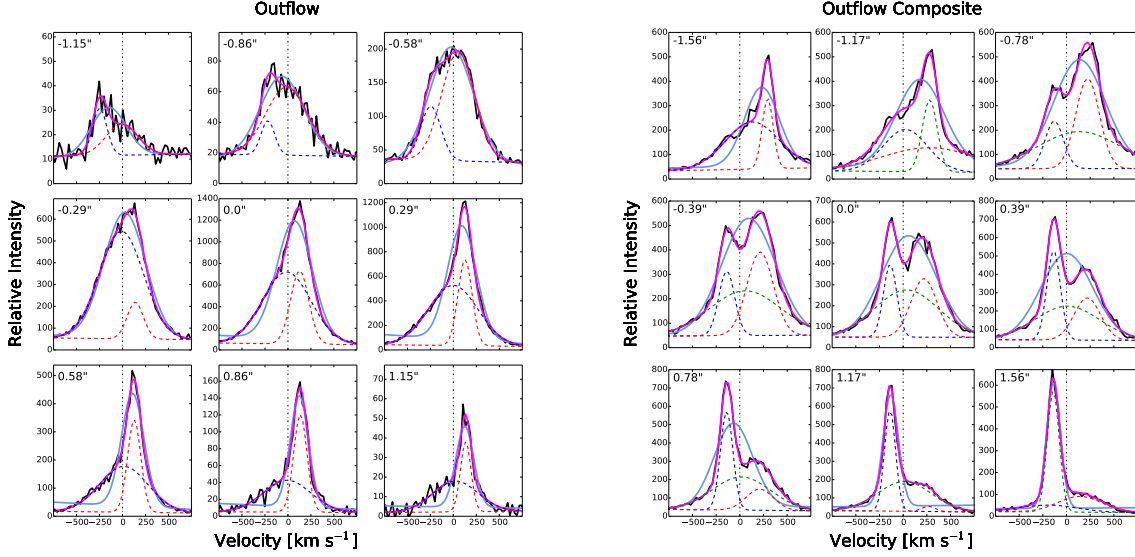
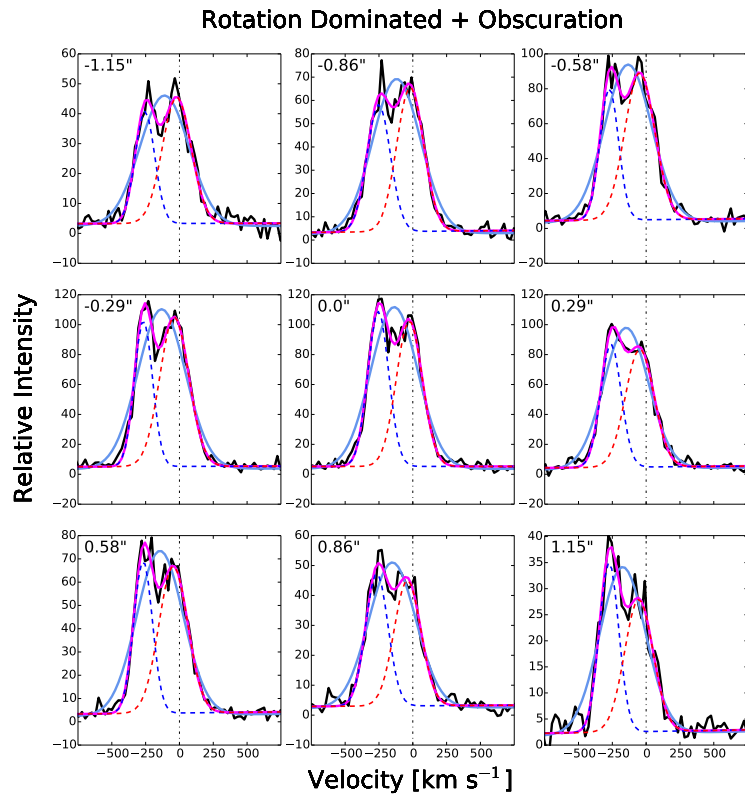
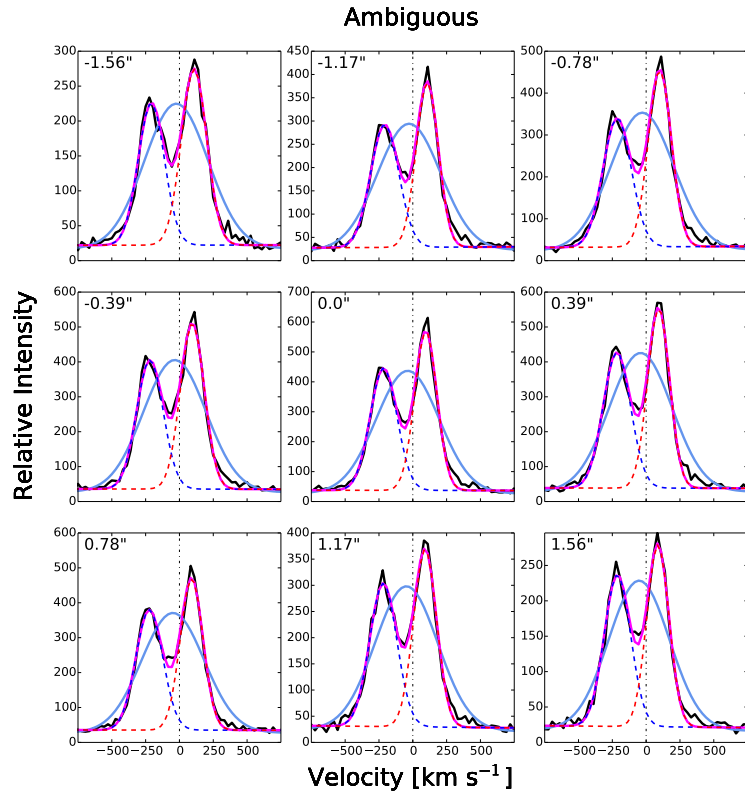


Figure 2.10: Examples of galaxy profiles for galaxies classified as ‘Outflow’ (left) and ‘Outflow Composite’ (right). We plot the profiles for the nine central spatial rows, with the spatial position shown in arcseconds in the upper left corner of each panel. The data are in black and the integrated one Gaussian fit is a blue solid line. Here we plot a two Gaussian fit for the galaxy classified as ‘Outflow’ (left), where the red and blue dashed lines are the individual Gaussian components and the solid magenta line is the integrated two Gaussian fit. For the ‘Outflow Composite’ galaxy, if a given spatial row is better fit by a three Gaussian fit, we plot the integrated fit for the three Gaussian fit where the dashed red, green, and blue lines are the individual Gaussian component fits and the solid magenta line is the integrated three Gaussian fit. For rows where two Gaussians are a better fit, we plot the individual and integrated profiles from the two Gaussian fit. We plot the three Gaussian fits for the ‘Outflow Composite’ galaxy to demonstrate that three components are sometimes necessary to fit the low flux wider wings of this type of profile. Here, we identify these galaxies as outflow-dominated due to the velocity dispersions (σ_1 or $\sigma_2 > 500 \text{ km s}^{-1}$) of the individual components of the two Gaussian fit. We then further classify one galaxy as ‘Outflow Composite’ because three Gaussian components are a better fit for more than half the spatial rows. Conversely, the ‘Outflow’ galaxy is better fit with two Gaussian components.



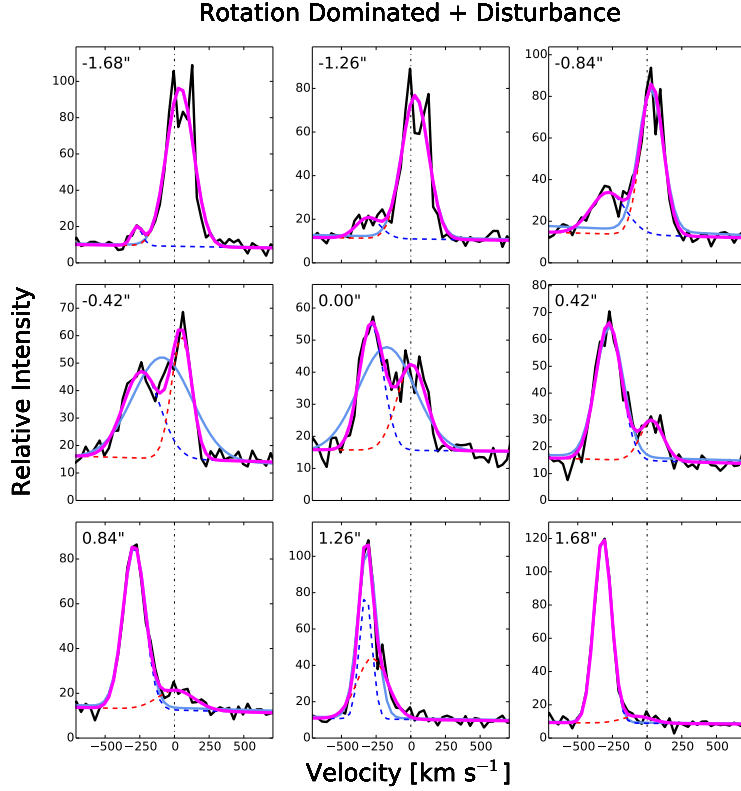


Figure 2.11: Same as Figure 2.10, but for the classifications of ‘Ambiguous’, ‘Rotation Dominated + Obscuration’, and ‘Rotation Dominated + Disturbance’. We show the individual Gaussian components of the two Gaussian fits to demonstrate our classification technique’s ability to identify the velocity dispersion and velocity offset of each of these components. All three galaxies are excluded from our outflow-dominated classification because the individual velocity dispersions are low (σ_1 and $\sigma_2 < 500 \text{ km s}^{-1}$) and the line of sight velocity is low ($V_r < 400 \text{ km s}^{-1}$). These three galaxies are then classified based upon their asymmetry or the alignment of the [OIII] emission (Section 2.4.1.2). The galaxy classified as ‘Ambiguous’ has profile characteristics that are consistent with a rotation-dominated galaxy; the only characteristic that sets it apart is the fact that the [OIII] emission is not aligned with the photometric major axis of the galaxy. See Figure 2.12 for a visualization of the [OIII] alignment of the galaxies classified here as ‘Ambiguous’ and ‘Rotation Dominated + Obscuration’. The galaxy classified as ‘Rotation Dominated + Obscuration’ has [OIII] emission that is aligned with the photometric major axis of the galaxy and a symmetric profile. The galaxy classified as ‘Rotation Dominated + Disturbance’ has aligned [OIII] emission and an asymmetric profile.

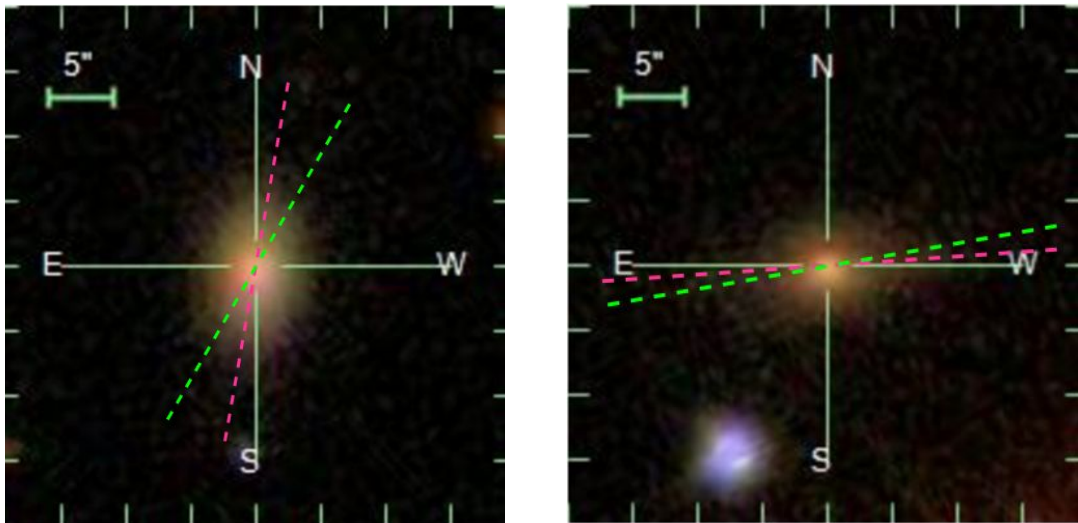


Figure 2.12: The SDSS images of the galaxies classified as ‘Ambiguous’ (J0802+3046, left) and ‘Rotation Dominated + Obscuration’ (J0736+4759, right) in Figure 2.11. The pink dashed line marks the photometric major axis of the galaxy as measured from SDSS r -band photometry. The green dashed line marks the position angle of the [OIII] emission as measured in this work. The [OIII] emission for J0802+3046 is not aligned with the photometric major axis of the galaxy, so we classify it as ‘Ambiguous’ even though in this case all other characteristics of the emission profiles are consistent with a rotation-dominated NLR. Conversely, the [OIII] emission for J0736+4759 is aligned with the photometric major axis, so we classify it as rotation-dominated. Alignment is an important classification tool in distinguishing between rotation-dominated and ambiguous classifications.

to identify galaxies that fall into a given category but based upon the error bars are on the edge of this classification (within 1σ) in Table A.4. We include these galaxies in their respective categories for later statistical analysis in Section 2.4.1.

This quantitative classification system allows us to use the spatial information from longslit spectra to determine the origin of the disturbed kinematics that produce a double-peaked profile. We track the emission lines across the spatial extent of the galaxy and use the behavior of the ionized gas both at each individual position and across the galaxy as a whole to determine the structure responsible for the integrated double peaks. For the first time, we are able to make a distinction between rotation-dominated spectra and outflow-dominated spectra. Additionally, we are able to separate rotation-dominated and outflow-dominated spectra into further kinematically descriptive categories that explain the origin of the double peaks. After classifying the full sample, we find 26/71 Outflow Composite galaxies, 35/71 Outflow galaxies, 4/71 Rotation Dominated galaxies (1/71 Rotation-Dominated + Obscuration, 3/71 Rotation-Dominated + Disturbance), and 6/71 Ambiguous galaxies in this sample. We comment on the distribution of properties and the success of the classification for our kinematic classification technique in Section 2.4.1.

2.4 Results

2.4.1 Kinematic Classification

We are able to successfully classify 92% of the galaxies as either outflow- or rotation-dominated using our stand-alone longslit classification technique. This technique utilizes the spatially-resolved spectra to probe individual locations in the NLR and successfully identifies the nature of the NLR based upon this spectral information alone. We find from the 71 galaxy sample that 6% of the galaxies (4/71) are Rotation Dominated (1/71 has an obscuration and 3/71 are disturbed), 49% (35/71) are Outflows, 37% (26/71) are Outflow Composites, and 8% (6/71) are Ambiguous (having some combination of outflow, inflow, or

rotation-dominated kinematic components).

Shen et al. (2011) conduct a similar classification with optical slit spectroscopy and near-infrared (NIR) imaging of 31 double-peaked AGNs and find 50% of their sample are classified as having a single NLR, 10% are candidate dual AGNs, and the remaining 40% are ambiguous. Fu et al. (2011) use resolved spectroscopy to show that a single AGN with disturbed ‘gas kinematics’ can produce 70% of the double-peaked profiles. Müller-Sánchez et al. (2015) find that 75% of the double-peaked profiles are produced by ‘gas kinematics’ (including 70% outflows and 5% rotating NLRs), 15% are dual AGNs, and 10% are ambiguous. Blecha et al. (2013) find from their hydrodynamic simulations that only a minority of double-peaked NLRs result directly from two distinct NLRs associated with two AGNs orbiting a central potential. Most are associated with complex gas kinematics or rotating gas disks.

Our results agree with these findings, produce fewer ambiguous cases, and further separate complex gas kinematics into rotation-dominated and outflow-dominated categories. The majority (86%) of our sample is dominated by outflow signatures and only a small minority of the subsample is dominated by rotation. We conclude that selecting Type 2 AGNs by double peaks in integrated SDSS spectra is the most successful at selecting outflows.

We note that we are not fully able to confirm dual AGNs using this technique in isolation without radio data. We discuss the placement of a candidate dual AGN in the Rotation Dominated + Disturbance category in Section 2.5.1.

We discuss the properties of the galaxies classified as outflow-dominated in Section 2.4.1.1 and the implications for NLR outflow theory. We analyze the properties of the rotation-dominated galaxies in Section 2.4.1.2 and compare to predictions from the literature.

2.4.1.1 Kinematic properties of the Outflow and Outflow Composite galaxies

We find that the majority (86%) of the uniform sample of double-peaked NLR galaxies are dominated by outflows. Double-peaked emission lines in SDSS are far more successful at selecting AGN outflows than two kinematically distinct rotating NLRs associated with a dual AGN. Here we discuss the kinematic properties of Outflows and Outflow Composite galaxies and we compare these findings to the current theory of the structure of NLR outflows.

Roughly half of the outflow-dominated galaxies are classified as Outflow. We add the caveat that the classification of Outflow or Outflow Composite is sensitive to S/N; for galaxies with lower S/N, we often do not have enough flux to distinguish the low flux wings of the profiles from the background. We therefore find that these lower S/N galaxies are often better fit with two Gaussians than three. To confirm that the number of Gaussian components is sensitive to S/N, we perform an experiment. We introduce Gaussian noise at a level equivalent to 10% of the flux to spectra that are best fit with a 3 Gaussian component fit. We complete 100 iterations of this random noise introduction and find that 37% of the time we recover a three component fit. The rest of the time we find that a 2 Gaussian component fit is better. Figure 2.13 shows an example simulation of decreased S/N and its effects on the number of Gaussian components that provide the optimal fit for a spatial row.

We note that although using the number of Gaussian components as a classification tool is sensitive to S/N, we still find it useful as a method of constraining the number of emission knots observed in an outflow. Although S/N can influence this classification, galaxies may intrinsically have only two kinematic components and be true Outflows. However, due to the S/N sensitivity, in some cases the number of components fit is a lower limit, so the galaxies that are classified as Outflow could be classified as Outflow Composites if they were observed with longer integration times. Due to these considerations, we choose to analyze Outflow Composites and Outflows together and refer to this combined category as outflow-dominated in our discussion.

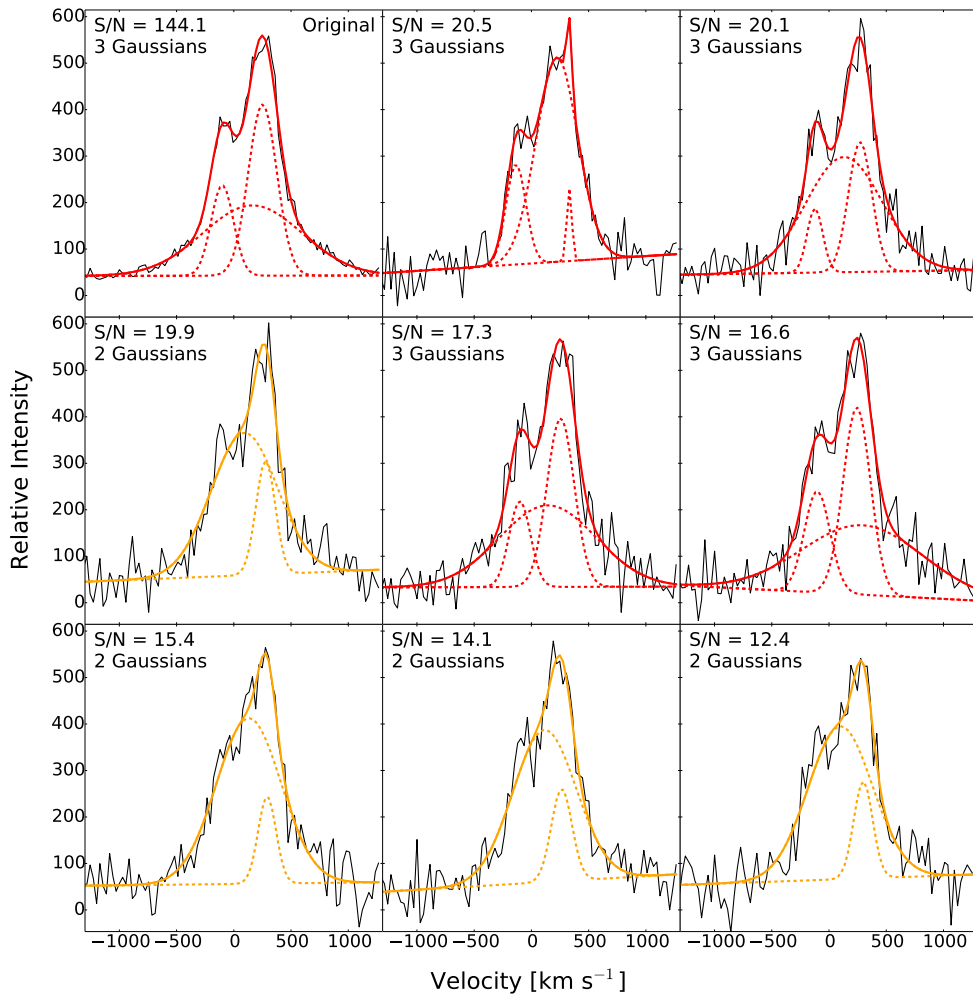


Figure 2.13: An example of introducing simulated Gaussian noise into a spatial row of the spectrum of J0803+3926. The original spectrum (upper left) is best fit by three Gaussians. All other panels list the S/N after adding different realizations of simulated and the number of Gaussians that give the optimal fit. If three Gaussian components are the best fit, the fit is shown in red, where the solid red line is the integrated fit and the dashed red lines are the individual component fits. If two Gaussian components provide the best fit, the fit is shown in orange. This galaxy is classified as Outflow Composite. However, when Gaussian noise is introduced into the spectrum, decreasing the S/N, we find that the spectrum is sometimes best fit by two components. Thus, S/N affects the classification of Outflow or Outflow Composite. Note that the effect shown here is not linear; there is no S/N threshold above which a given galaxy will always be classified as Outflow Composite.

We present the kinematic properties of all of the classification categories in Table A.5. We focus here on the properties of the outflow-dominated galaxies. We find that 18% of the outflow-dominated galaxies have a single Gaussian radial velocity in excess of 400 km s^{-1} , 77% have an overall velocity dispersion greater than 500 km s^{-1} , and 100% have a single component with a velocity dispersion in excess of 500 km s^{-1} . Some profiles show the discrepancy where a single Gaussian velocity dispersion is less than the two individual velocity dispersions for the two Gaussian fit. This is because these are double-peaked profiles that are often separated significantly in velocity space. When we fit a single Gaussian component, it sometimes encompasses only one of the two components, while the two Gaussian fit is more sensitive to underlying high velocity dispersion low flux wings.

We find that velocity dispersion of the individual components of the two Gaussian fit, σ_1 or σ_2 , is the most powerful tool in identifying outflow-dominated galaxies. In a few galaxies, radial velocity is also important in identifying knots of emission moving at velocities in excess of a rotation-dominated NLR. However, all of the outflow-dominated galaxies that have a radial velocity in excess of 400 km s^{-1} also have individual components of the two Gaussian fit with velocity dispersions in excess of 500 km s^{-1} . We determine that σ_1 and σ_2 are more useful as a probe of the bulk motion of the outflow than V_r . The knots of emission that achieve velocities in excess of 400 km s^{-1} could be the faintest components of the outflow, and remain unidentified in our Gaussian fitting and classification method for galaxies with lower S/N. Velocity dispersion is a more consistent identifier of outflow-dominated galaxies because it describes the bulk properties of the walls of the outflow as opposed to being related to extremely low surface brightness knots of fast-moving gas.

We found that although we did not directly use the velocity dispersion of a single Gaussian fit (σ) in our classification, 77% of the outflow-dominated galaxies had overall velocity dispersions in excess of 500 km s^{-1} . However, 75% of the rotation-dominated galaxies also had this property. This is unsurprising since rotation-dominated galaxies with a disturbance should have an overall velocity dispersion that exceeds the value for an undisturbed rotat-

ing disk. The single velocity dispersion σ was not as useful as σ_1 and σ_2 in discriminating between rotation-dominated and outflow-dominated galaxies.

2.4.1.2 Properties of the rotation-dominated galaxies

We identify four galaxies as rotation-dominated. The origin of the double peaks is disturbed kinematics from a bar, spiral, or a possible dual AGN in 3/4 cases and an obscuration in 1/4 cases. In other words, the category ‘disturbed’ accounts for all kinematic deviations of a rotation-dominated profile from a single rotating disk. We distinguish between an obscured rotation-dominated galaxy and a disturbed rotation-dominated galaxy using the relative nonparametric asymmetry values of the profiles of each galaxy. Although we measure the relative asymmetry parameter for all galaxies, we only use it as a classification tool to distinguish between different kinematic origins of rotation-dominated galaxies.

We use a statistical quantitative method to classify rotation-dominated galaxies as asymmetric or symmetric. We determine the asymmetry values for each galaxy by measuring an asymmetry value for all spatial positions of each position angle. We then take the asymmetry value to be the maximum asymmetry value from either PA. We show this maximum asymmetry value for the four rotation-dominated galaxies in Figure 2.14. The rotation-dominated galaxies have asymmetry values of 0.12 (J0736+4759), 0.57 (J1018+5127), -0.43 (J1250+0746), and -0.72 (J1516+0517). Note that we compare the absolute value of the asymmetry value because a negative or positive value indicates if the profile has blue or red wings, respectively. Using the values of asymmetry for the rotation-dominated galaxies, we can compare the population mean of the entire sample of 71 galaxies (0.43). Given the sample standard deviation (0.15) for this measurement, we can initially conclude that J0736+4759 is about two standard deviations below the mean and the remaining three rotation-dominated galaxies are consistent with the mean (J1250+0746), one standard deviation greater than the mean asymmetry (J1018+5127) and about two standard deviations above the mean (J1516+0517).

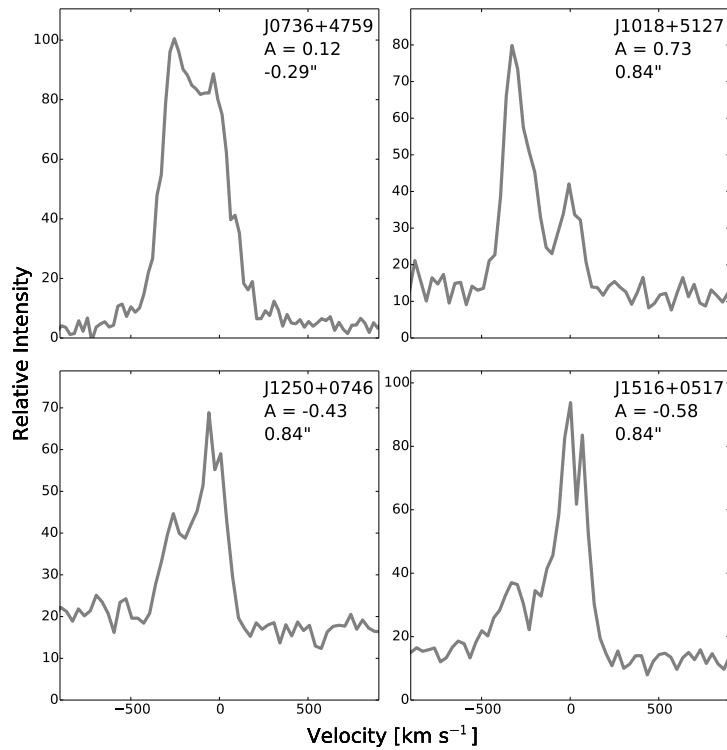


Figure 2.14: The maximum nonparametric asymmetry values (A) and their corresponding spatial row for each of the four rotation-dominated galaxies. We classify the first as symmetric (J0736+4759) and the final three (J1018+5127, J1250+0746, and J1516+0517) as asymmetric based upon a statistical analysis of the asymmetry values.

We build upon these initial conclusions using the Analysis of Means (ANOM) statistical test. ANOM allows us to set a confidence interval and test for differences in means between subsamples. We plan to group J1018+5127, J1250+0746, and J1516+0517 together and prove that the mean asymmetry of this group is statistically different than the asymmetry of the galaxy J0736+4759, which we have preliminarily demonstrated has a relatively symmetric profile when compared to the other rotation-dominated galaxies. We define the confidence interval and population mean used in ANOM as:

$$\bar{X} \pm h_{c,n_j} \sqrt{\frac{\sigma_p^2(c-1)}{n}}$$

where \bar{X} is the mean of the full sample (71), c is the number of groups between which we wish to compare means (2), n_j is the sample size for group j , h_{c,n_j} is the critical value for Nelson's h statistic with c groups and n_j observations per group, σ_p^2 is the pooled variance of the overall sample, and n is the total number of observations. Note that n_j is set by the smallest sample size of the groups (1). The smallest group sample size is set by J0736+4759 with one measurement. Thus, in our case, $h_{2,1} = 12.7$ for a 95% confidence value.

We obtain a 95% confidence interval around the sample mean of [0.19, 0.66]. We find that the A value of J0736+4759 (0.12) is significantly less than the mean of the overall sample and that the mean of the A values for the group including J1018+5127, J1250+0746, and J1516+0517 (0.58) is consistent with mean of the overall sample. J1018+5127, J1250+0746, and J1516+0517 are classified as asymmetric rotation-dominated galaxies quantitatively according to sample statistics. We classify them as Rotation Dominated + Disturbance. We classify J0736+4759 as Rotation Dominated + Obscuration.

Liu et al. (2013c) use an identical definition of nonparametric asymmetry and find values of asymmetry with a maximum around 0.4 for their energetic outflows. Therefore, our quantitative asymmetry cut is even higher, meaning that our rotation-dominated galaxies with a disturbance are even more asymmetric when compared to other work.

We can also confirm that the three galaxies that we classify as asymmetric under our nonparametric measurement would be classified as asymmetric by Smith et al. (2012) using an alternate definition of asymmetry. Smith et al. (2012) use a ratio of the red and blue flux components of their double-peaked profile fits to quantify asymmetry for their sample of “equal-peaked” AGNs (EPAGNs). Specifically, they classify a symmetric EPAGN as one with a value of $0.75 \leq F_r/F_b \leq 1.25$, where F_r is the flux of the redder Gaussian component and F_b is the flux of the bluer component. Their quantitative classification involves fitting two Gaussians. We prefer the nonparametric method of asymmetry quantification because it accounts for features such as low flux wings in complicated profiles that are best fit by more than two Gaussians.

Smith et al. (2012) conclude that symmetric EPAGNs from the double-peaked sample are most likely to originate from a single rotation-dominated NLR. Our clearest example of this type of a rotation-dominated galaxy is the galaxy J0736+4759, which is rotation-dominated with a central obscuration due to its high degree of symmetry. The peaks are of equal flux for both position angles across the entire slit. This galaxy is consistent with the EPAGNs discussed in (Smith et al. 2012). However, the results of our classification reveal that rotation-dominated objects with double-peaked profiles are more likely to be asymmetric due to disturbances such as spirals, bars, or dual AGNs. Three of our four rotation-dominated galaxies have asymmetric peaks.

We also investigate the $H\alpha$ kinematics of the four rotation-dominated galaxies. We refrain from investigating the $H\alpha$ kinematics of all the galaxies in this sample because it is beyond the scope of this work. However, it is a useful exercise to compare the $H\alpha$ kinematics to the $[OIII]\lambda 5007$ kinematics for the rotation-dominated profiles because ionized gas dominated by rotation should exhibit gas kinematics that are identical to the stellar kinematics of the stars in the disk. Note that although $H\alpha$ traces both the NLR and stellar kinematics, in the case of a rotation-dominated NLR both the stellar kinematics and gas ionized by the AGN should be consistent with rotation. In other words, if the ionized gas is coincident with

the stellar disk, the $H\alpha$ and $[OIII]\lambda 5007$ kinematics should be identical.

We find for the four rotation-dominated galaxies that the $H\alpha$ emission is aligned with the $[OIII]\lambda 5007$ emission and that the velocity offsets, velocity dispersions, and relative asymmetry values of the profiles are consistent within the errors (to 3σ). We present velocity separations (ΔV) between the red and blue Gaussian components of each profile in Table A.6 and demonstrate the consistency of the profiles visually in Figure 2.15 for J1018+5127. The results verify that the kinematics of these galaxies are indeed dominated by rotation.

2.5 Discussion

2.5.1 What are the expected kinematic classifications of dual AGNs?

This kinematic longslit technique was originally conceived as a method for positively identifying candidate dual AGNs. We cannot exclude dual AGNs from any of the classification categories with this work, but we can offer insight into which categories they could fall.

A compelling candidate dual AGN could be classified as Outflow or Outflow Composite. Both NLRs will only be visible during the latest kpc and sub-kpc separation stages of dual AGN evolution while both AGNs are accreting simultaneously (Blecha et al. 2013; Van Wassenhove et al. 2012; Steinborn et al. 2016). Since observable dual AGNs are by definition in an actively accreting phase of evolution, they can drive outflows and be classified as outflow-dominated. Observationally, past work has found that the optical spectra of confirmed dual AGNs have signatures of disturbed kinematics (outflows and shocks, e.g., Mazzearella et al. 2012; Engel et al. 2010). Even if one or both distinct NLRs can be described as rotation-dominated, the two AGNs might have unequal luminosities. We would observe this type of galaxy as one narrow component with an associated outflow that dominates a smaller flux second narrow rotation-dominated component from the second AGN. This case of a fainter NLR would be categorized as Outflow Composite or Outflow based upon the

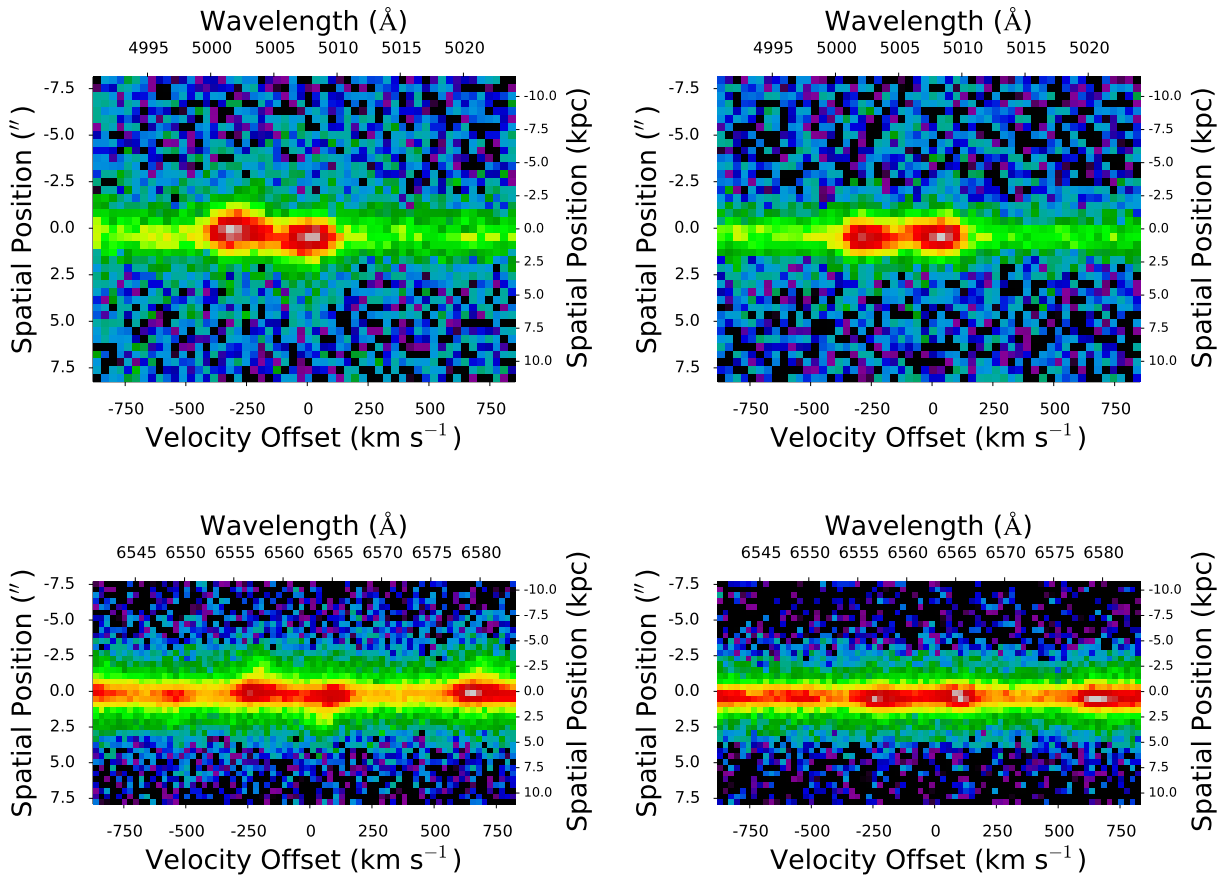


Figure 2.15: The two dimensional longslit spectra for J1018+5127 for each PA (PA 1, left, PA 2, right). The top row shows the [OIII] $\lambda 5007$ profiles and the bottom row shows the H α profiles. The dispersion direction is the x axis in all spectra, with both a velocity axis in km s^{-1} offset from systemic (bottom) and rest frame wavelength axis in \AA (top). The y axis is the spatial direction along the slit reported in both arcseconds (left) and kiloparsecs (right) with the spatial center defined as the center of the galaxy continuum. Note that the line profiles of H α and [OIII] $\lambda 5007$ are similar and consistent in orientation, velocity offset, and velocity dispersion with a gas disk that is coincident with a rotating stellar disk.

number of kinematic components in the outflow and the brightness of the dimmer AGN.

Blecha et al. (2013) demonstrate that either rotation-dominated NLR of the pair of AGNs could be disturbed by the secondary AGN and appear rotation-dominated with a disturbance. In fact, dual AGNs are more likely to appear observationally as NLRs characterized by disturbed kinematics rather than kinematics dominated by the motion of two SMBHs. We would classify this type of profile as Rotation Dominated + Disturbance. Returning to the picture of the toy model of a dual AGN with two rotation-dominated NLRs, recall that even a theoretical dual AGN with no disturbed kinematics would be classified as Rotation Dominated + Disturbance (e.g., J1018+5127). This theoretical dual AGN would have NLRs that alternate in flux at the position angle of maximum spatial separation (Figure 2.5). This causes the profile of this type of dual AGN to appear asymmetric for at least one position angle. Lastly, dual AGNs could be classified as Ambiguous because they may demonstrate a lower velocity offset or dispersion, which are properties that are consistent with either an inflow or a less energetic outflow (σ_1 or $\sigma_2 < 500 \text{ km s}^{-1}$ or $V_r < 400 \text{ km s}^{-1}$).

Even if both rotation-dominated NLRs are visible, Blecha et al. (2013) show that these NLRs would most likely demonstrate a large velocity separation between individual components of order $\Delta V > 500 \text{ km s}^{-1}$ due to enhanced velocity separation during pericentric passage. These objects would most likely be classified as outflow-dominated by our kinematic classification because the velocity offset between the individual components is so large. This large velocity offset would cause the single Gaussian V_r to be greater than 400 km s^{-1} and this type of galaxy would be classified as an outflow. While the velocity offset limits were derived with the purpose of identifying fast moving outflow components, narrower dual components could also fall into this category. At present, we have no galaxies that fall into this category of being classified as an Outflow due to the velocity offset of two narrow lines with a large velocity separation.

The only category that is unlikely to include dual AGNs is Rotation Dominated + Obscuration. The high degree of symmetry required for this classification is statistically

unlikely to be associated with two NLRs producing an outflow or either rotating NLR being disrupted by a secondary AGN. Blecha et al. (2013) predict that equal flux symmetric profiles are most likely associated with an obscured rotating disk, and Smith et al. (2012) support this prediction observationally.

None of the galaxies in this sample are yet confirmed as radio-detected dual AGN, but one galaxy presents a compelling longslit spectrum where each NLR appears to be rotation-dominated. This galaxy, J1018+5127, is undetected in the VLA radio data, so we can place an upper limit on the radio luminosity but cannot reject the presence of a double radio core (Müller-Sánchez et al. in prep.). The longslit [OIII] λ 5007 profiles of J1018+5127 (Figure 2.16) are consistent with two distinct rotation-dominated NLRs, and this galaxy is classified as Rotation Dominated + Disturbance. One of the rotation-dominated NLRs is centered at zero velocity and one has a blueshift $\sim 450 \text{ km s}^{-1}$ at all spatial positions. The flux ratio of the NLRs switches along the first PA and the NLRs are roughly equal in flux at the second PA. This is consistent with a dual NLR system with maximal separation nearest the first PA; we measure $\text{PA}_{[\text{OIII}]} = 22^\circ$, which is nearly aligned with $\text{PA}_{\text{gal}} = 27^\circ$. This object is most extended in the plane of the galaxy, and this is consistent with a dual AGN interpretation (Comerford et al. 2012). Although we can conclude that the longslit kinematic information is consistent with a dual AGN explanation, we stress that this is not a confirmed dual AGN without the complementary double radio core confirmation.

2.5.2 A size-luminosity relationship for the NLR reveals the nature of the photoionized region

In the study of the structure of AGNs, the nature of the NLR is still uncertain. In this work, we investigate how the extent of the NLR scales with the luminosity of the central source ($R_{\text{NLR}} \propto L_{[\text{OIII}]}^\alpha$). If we can investigate this relationship over a large range of AGN luminosities (by combining our sample with other studies), we can use the strength of this correlation to constrain the ionization structure (ionization parameter) and density structure

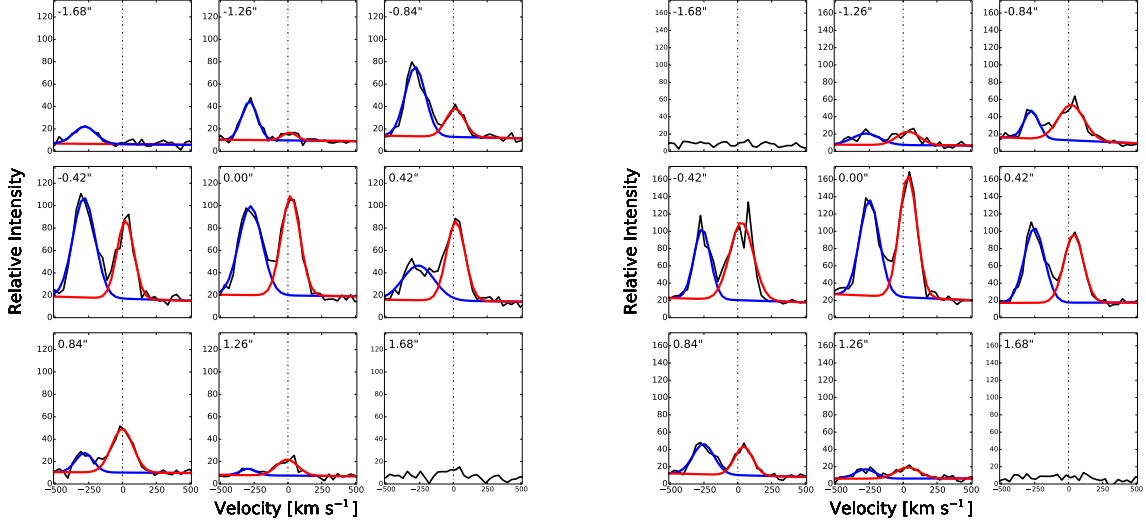


Figure 2.16: The spectral profiles of J1018+5127 at both PAs. We show the PA observed at 22° (left) and the PA observed at 112° (right). The spatial center of the galaxy ($0.0''$) is the central panel, and the spatial position is indicated in the upper right of each panel. We plot the data in black and the two Gaussian fit in blue and red lines for the blueshifted and redshifted Gaussian components of the fit, respectively. Although this galaxy is not confirmed as a dual AGN in the radio data, we demonstrate that the NLRs appear to alternate in flux (left) as expected for the most spatially extended PA of a rotation-dominated dual AGN. On the right, the NLRs could be spatially coincident rotation-dominated NLRs. This galaxy is kinematically classified as Rotation Dominated + Disturbance.

of the NLR.

The [OIII] luminosity is an accurate probe of the ionization structure and density of the NLR because it is a collisionally excited transition; the line emissivity of [OIII] λ 5007 is set by the electron density n_e and ionization state. Note that although [OIII] λ 5007 can also be produced by stars, BPT diagnostics suggest an AGN origin for the emission in this sample. We use the observed [OIII] luminosity ($L_{\text{[OIII]}}$; Section 2.2.4) in this work as a probe of the intrinsic luminosity of the NLR.³

A positive slope is expected in the size-luminosity relationship if the AGN's radiation is responsible for the photoionization of the NLR. The slope of the relationship, α , is influenced by the density structure of the NLR and the ionization parameter, U , which is defined as the ratio of the number density of ionizing photons to the number density of electrons:

$$U = \frac{n_\gamma}{n_e} = \frac{1}{4\pi R_{\text{NLR}}^2 c n_e} \int_{\nu_0}^{\infty} \frac{L_\nu}{h\nu} d\nu$$

where n_γ is the number density of ionizing photons, R_{NLR} is the radius of illumination by a central source (Section 2.2.4), L_ν integrated is the bolometric luminosity of the central source over all frequencies, ν is frequency, and ν_0 is the ionization edge.

Therefore, the relationship between the estimated integrated ionizing luminosity (L_{ion} , in this work we use $L_{\text{[OIII]}}$ as a proxy for L_{ion}) and radius can be written:

$$R_{\text{NLR}} = K L_{\text{[OIII]}}^{0.5} (U n_e)^{-0.5}$$

where $K = (4\pi c < h\nu >)^{-0.5}$. Determining the slope of the size-luminosity relationship is a direct investigation of both the ionization structure U and the density structure n_e of the NLR, both of which are poorly determined.

Our sample of 71 moderate-luminosity ($40 < \log L_{\text{[OIII]}} (\text{erg s}^{-1}) < 43$) AGNs represents

³ We have measured the size-luminosity relationship for our data for both the extinction corrected luminosity ($L_{\text{[OIII]}}^c$) and the observed luminosity ($L_{\text{[OIII]}}$) and find that the slope is identical within errors. Note that since other work uses the observed luminosity, we also use $L_{\text{[OIII]}}$ of our sample of AGNs in the discussion when we compare the luminosity range of our study to other work.

a unique opportunity to investigate this size-luminosity relationship for a uniform sample of moderate luminosity AGNs with resolved NLRs. Our measurement of R_{NLR} (Section 2.2.4) is a lower limit since we only have spatial data along two dimensions of the galaxy. If neither position angle is exactly aligned with the position angle of maximal extent of the NLR, we are unable to measure the true extent of the NLR (R_{NLR} ; Section 2.2.4). However, we note that other studies of the size-luminosity relationship are also limited by resolution and surface brightness considerations (Hainline et al. 2013; Schmitt et al. 2003; Bennert et al. 2002; Fraquelli et al. 2000; Liu et al. 2013b).

Here we review the slope of the size-luminosity relationship measured by other studies. In a simplistic one-zone model of the NLR, the NLR is described by an isotropic distribution of gas where n_e and U are constant. In this case, the size-luminosity relationship will have a positive correlation and slope of $\alpha = 0.5$ (Baskin & Laor 2005). Bennert et al. (2002) find a slope of $\alpha = 0.52 \pm 0.06$ for their sample of seven Seyfert 2 galaxies and seven quasars ($41 < \log L_{[\text{OIII}]}(\text{erg s}^{-1}) < 43$) and conclude that a constant density law and a constant value for the ionization parameter describe the NLR. Hainline et al. (2013) predict a limit to the correlation at the higher luminosity extreme of AGNs ($42 < \log L_{[\text{OIII}]}(\text{erg s}^{-1}) < 43$). This is confirmed by Hainline et al. (2014); they observe quasars at the high luminosity limit of AGNs and observe a flattening in the size-luminosity relationship. They attribute this flattening to a limit in the amount of gas in the gas reservoir of the NLR that is available for ionization. Liu et al. (2013b) confirm this effect and find a flatter slope of 0.25 ± 0.02 for a sample of 11 luminous obscured quasars ($42 < \log L_{[\text{OIII}]}(\text{erg s}^{-1}) < 44$).

However, the flattening at the high luminosity end of the relationship is not the only interesting conclusion from previous work. Schmitt et al. (2003) find a slope of 0.33 ± 0.04 for their sample of moderate luminosity ($39 < \log L_{[\text{OIII}]}(\text{erg s}^{-1}) < 42$) Seyfert 1 and Seyfert 2 galaxies, which is much shallower than the slope of $\alpha = 0.5$ predicted for a constant density law and ionization parameter. They conclude that a single-zone model with a constant density and ionization parameter is not an appropriate representation of the NLR and that

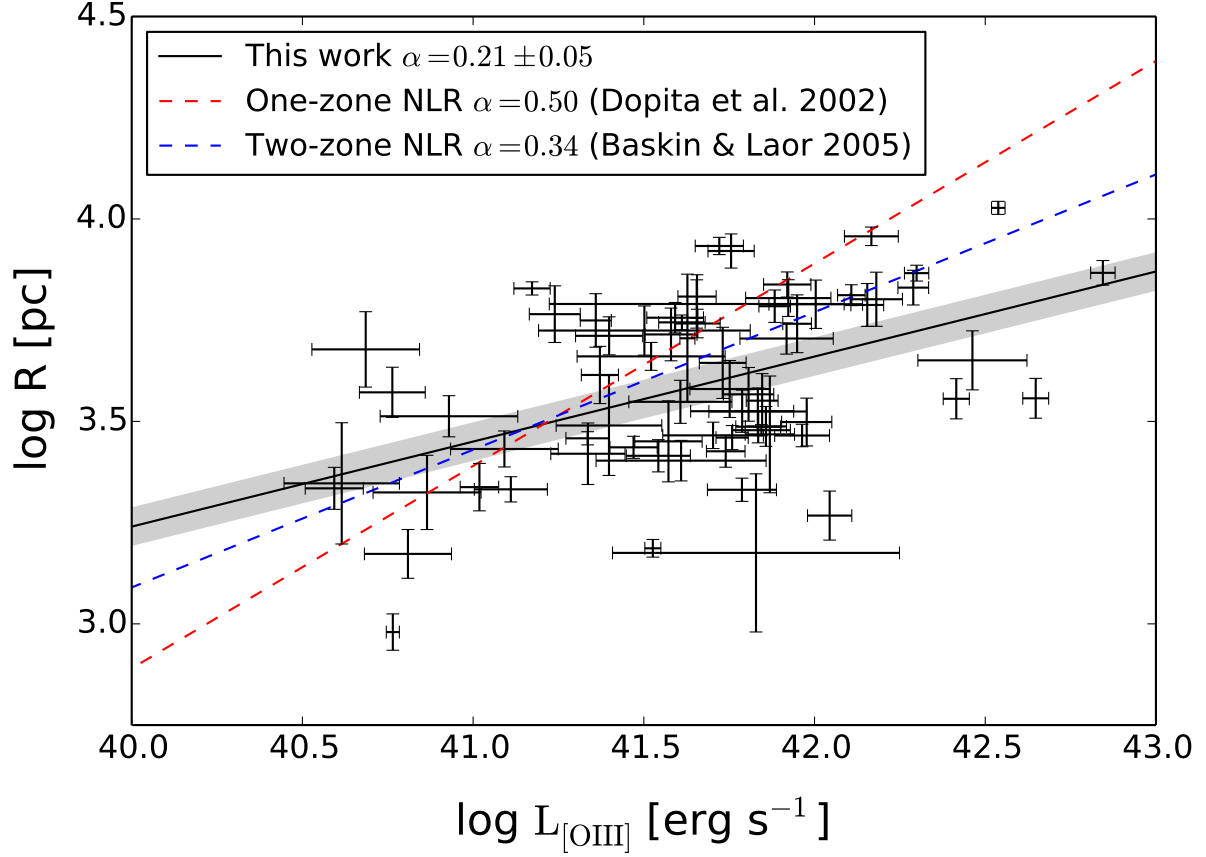


Figure 2.17: Size-luminosity ($L_{\text{[OIII]}}$) relationship for the NLR for the observed luminosity. We plot the 71 galaxies from this sample in black. We overplot the best fit line in solid black and find a value of $\alpha = 0.21 \pm 0.05$ for the slope of the log-log relationship. We include the confidence interval for this slope in the shaded region. We also plot the predicted slope for a one-zone NLR model in red and a two-zone NLR model in blue.

a two-zone ionization model for the NLR is a better explanation (Baskin & Laor 2005; Dopita et al. 2002).

In a two-zone ionization model, the NLR can be described by both a matter-bound zone and an ionization-bound zone, where the ionizing photons are pre-processed by passing through a ionization-bound zone. The ionization-bound zone is characterized by a lower ionization parameter and a higher density. The ionization-bound regime is thus optically thick to ionizing radiation. In the most simplistic two-zone models, the ionization-bound zone is confined to a smaller radius and the matter-bound zone exists at spatial positions exterior to this. We will also discuss a more complicated two-zone model where these two zones exist in a clumpier and/or mixed state but note that Baskin & Laor (2005) model the radially confined case where denser NLR clouds are confined to a smaller radii and all NLR material is distributed continuously. Most work deals with this simplistic model. Baskin & Laor (2005) assume that the majority of emission originates from the outer matter-bound zone where the size-luminosity relationship can be modeled with a slope of $\alpha = 0.34$. Thus, a NLR with mixed matter-bound and ionization-bound zones could be described by a slope between the extremes of $\alpha = 0.34$ and $\alpha = 0.5$. Likewise, a NLR with a clumpier distribution of matter-bound material than the continuous assumption would have a slope shallower than $\alpha = 0.34$.

Observations support this idea of a changing ionization parameter; the ionization parameter can decrease with radius (e.g., Fraquelli et al. 2000), which could be a signature of a matter-bound region at a larger radius of a galaxy. Liu et al. (2013b) confirm that beyond 7 kpc for their quasars sample, the ionization diagnostic $[\text{OIII}]/\text{H}\beta$ declines. They argue that the NLR is entering a matter-bound regime at these radii, which explains the shallower slope they fit to their size-luminosity relationship (0.25 ± 0.02). Consequently, arguing for a two-zone ionization model where an outer matter-bound zone is characterized by a lower density is similar to arguing that the gas reservoir is depleted at these extreme radii.

Shocks may also influence the size-luminosity relationship for AGNs. Müller-Sánchez

et al. (2015) find a steeper slope of 0.52 ± 0.14 for a sample of 18 double-peaked AGNs that includes three confirmed dual AGNs. We note that shocks may steepen this slope by introducing higher-ionization zones. Dual AGNs, which host two interacting NLRs, are most likely to produce shocks that are enhancing this relationship, thus enhancing the $[\text{OIII}]\lambda 5007$ emissivity.

From our sample of moderate luminosity AGNs, we confirm a linear correlation with a Pearson correlation coefficient of 0.48 and find a log-log slope of 0.21 ± 0.05 (Figure 2.17).⁴

Our results for a fitted slope are inconsistent with the predicted slope of $\alpha = 0.5$ for a one-zone ionization model to 3σ confidence. Our results cannot be explained by a constant density profile with a constant ionization parameter. Our slope is closer to the predicted slope of 0.34 (within 3σ confidence) for the two-zone ionization model of the NLR (Baskin & Laor 2005). However, our slope is still shallower than $\alpha = 0.34$ at a confidence level of 1σ . We suggest two possible explanations for this discrepancy.

First, the filling factor of the NLR is not well determined, so if the clouds are sparsely distributed, this would flatten the relationship to values less than the $\alpha = 0.34$ slope derived for a simple two-zone ionization model. This simple model assumes a smooth density distribution of the NLR gas and a radial distribution of the two zones. This implies that the simplistic two-zone model may not be adequate to explain our data and we may require a clumpier or mixed NLR that is not well described by a simplistic radial density profile as in Baskin & Laor (2005).

Alternatively, we measure larger than average NLR extents when compared to NLR size measurements for AGNs with a similar luminosity range ($40 < \log L_{[\text{OIII}]}(\text{erg s}^{-1}) < 43$); see Hainline et al. (2013) and references therein. We find a mean R_{NLR} of 4.3 kpc, which

⁴ We also fit this relationship for the intrinsic (corrected) $[\text{OIII}]$ luminosity, $L_{[\text{OIII}]}^c$, and find a slope of 0.24 ± 0.05 . Our two measurements are consistent within error. We choose to use the observed luminosity value of slope in our discussion to compare with other work (Bennert et al. 2002; Schmitt et al. 2003; Hainline et al. 2013, 2014; Liu et al. 2013b). We can reject the null hypothesis that $\alpha = 0$ to a 1% confidence level. We plot the results of our linear fit in Figure 2.17 with the slopes of the one-zone and two-zone ionization models for comparison. We discuss our linear correlation coefficient, fitted slope, and confidence interval on this value both in the context of the one and two-zone ionization models.

is comparable to studies of more luminous AGNs (e.g., Bennert et al. (2002) find a mean R_{NLR} of 4.3 kpc for their $41 < \log L_{[\text{OIII}]}(\text{erg s}^{-1}) < 43$ AGNs and Hainline et al. (2013) find a mean R_{NLR} of 3.8 kpc for their $42 < \log L_{[\text{OIII}]}(\text{erg s}^{-1}) < 43$ AGNs) and our value of R_{NLR} is greater than studies of AGNs with a similar luminosity range (e.g., Schmitt et al. (2003) find a maximum R_{NLR} of 1.6 kpc for their $39 < \log L_{[\text{OIII}]}(\text{erg s}^{-1}) < 42$ AGNs).

Although we refer to our sample as moderate luminosity AGNs, note that some of them have observed luminosities in a range described as higher luminosity ($42 < \log L_{[\text{OIII}]}(\text{erg s}^{-1}) < 43$). We may be probing regions of the NLR where the gas reservoirs available for ionization are limited and the material is better characterized as matter-bound. Baskin & Laor (2005) derive the expected slope of 0.34 for a two-zone ionization model for galaxies with a maximum spatial extent of the NLR of 1.3-1.7 kpc and a constant density. Our sample of galaxies may have a relatively larger and/or sparsely populated (less dense) matter-bound region. These effects could lead to a shallower slope for the relationship. We note that while we cannot fully distinguish between these two scenarios, our results are more consistent with a two-zone rather than a one-zone picture of the NLR. We refer to some combination of a non-constant density or non-radially distributed matter-bound region as a ‘clumpy two-zone model’.

The positive correlation of this relationship indicates that the AGN itself is the mechanism responsible for ionization of the NLR. The Pearson correlation coefficient for the data (0.48) reflects scatter in the data. This could be a consequence of the lower limit nature of the R_{NLR} measurement. The error bars show significant uncertainty in both the luminosity measurement and the spatial extent measurement for some galaxies in the sample. Another source of the scatter in our data could be the nature of a two-zone ionizing model for the NLR. While studies mostly describe the matter-bound zone as the outer zone of a galaxy, the matter-bound and ionization-bound zones could exist at different locations in a galaxy, forming a “clumpier” picture of an intermixed two-zone NLR. Therefore, individual galaxies in our large sample could have different ionization structures and this could intrinsically

produce the scatter.

2.6 Conclusions

Based on optical longslit spectroscopy of the complete sample of 71 double-peaked AGNs at $z < 0.1$ in SDSS, we create and implement a classification system for double-peaked NLR emission lines. Our method determines the kinematic origin of the emission at different spatial positions for each galaxy. We present the following conclusions based upon this technique:

- Of the sample of 71 galaxies, 6% have kinematics dominated by rotation, 86% of the galaxies are dominated by outflows, and 8% of the galaxies are dominated by some combination of outflows, inflows, and rotation. Our kinematic classification determines that the majority of double-peaked emission lines originate from outflows and succeeds at further determining the properties of the gas outflows and the rotating disks.
- While we cannot confirm (or exclude) dual AGNs using the kinematic classification method in isolation, we find that dual AGNs can be classified under any category other than rotation-dominated with an obscuration.
- We find that the 71 AGNs in this sample demonstrate a positive correlation between NLR size and luminosity ($R_{\text{NLR}} \propto L_{[\text{OIII}]}^{0.21 \pm 0.05}$). This suggests a two-zone clumpy ionization model for the NLR.

The full sample of double-peaked AGNs at $z < 0.1$ have been observed in the radio. Future work will combine the optical and radio data to investigate the orientation of the radio emission and its relationship to the ionized gas. To further investigate the direct effects of feedback on the host galaxies in this sample, we will also introduce an analytic model for the structure of the biconical outflow for the galaxies classified kinematically as outflow-dominated galaxies. Using these models, we will constrain the energetics and momentum

entrained in these ionized outflows and discuss their effect on star formation in the host galaxies.

Chapter 3

The Origin of Double-Peaked Narrow Lines in Active Galactic Nuclei III: Feedback from Biconical AGN Outflows

We apply an analytic Markov Chain Monte Carlo model to a sample of 18 AGN-driven biconical outflows that we identified from a sample of active galaxies with double-peaked narrow emission lines at $z < 0.1$ in the Sloan Digital Sky Survey. We find that 8/18 are best described as asymmetric bicones, 8/18 are nested bicones, and 2/18 are symmetric bicones. From the geometry and kinematics of the models, we find that these moderate-luminosity AGN outflows are large and energetic. The biconical outflows axes are randomly oriented with respect to the photometric major axis of the galaxy, implying a randomly oriented and clumpier torus to collimate the outflow, but the torus also allows some radiation to escape equatorially. We find that 16/18 (89%) outflows are energetic enough to drive a two-staged feedback process in their host galaxies. All of these outflows geometrically intersect the photometric major axis of the galaxy, and 23% of outflow host galaxies are significantly redder or have significantly lower specific star formation rates when compared to a matched sample of active galaxies.

This chapter reproduces Nevin et al. (2018). Reproduced with permission of the AAS.

3.1 Introduction

The tight observational correlations between stellar bulge properties such as mass and velocity dispersion and supermassive black hole (SMBH) mass indicate that SMBHs can be

powerful drivers of galaxy evolution (e.g., Merritt 2000; McConnell & Ma 2013). Since the sphere of influence of the SMBH’s gravity is minuscule, a physical coupling between the host galaxy and the energy of active galactic nuclei (AGNs), which are the active phase of SMBHs, must explain these scaling relations. This coupling is known as AGN feedback.

Both theoretical models and observations have investigated the role of AGN feedback in galaxy evolution. Observationally, the bimodal color distribution of galaxies in the nearby universe and the lack of massive galaxies in the galaxy mass function require quenching of star formation in galaxies via a feedback mechanism (e.g., Bell et al. 2004; Brown et al. 2007; Faber et al. 2007; Silk 2011). In models, AGN-driven feedback provides a mechanism to evacuate gas from a galaxy and quench star formation and the growth of the SMBH (e.g., Di Matteo et al. 2005; Hopkins et al. 2005; Springel 2005; Croton et al. 2006). Despite the utility of AGN feedback in regulating galaxy and SMBH growth, there is limited direct evidence for feedback operating on host galaxies. Additionally, despite many proposed mechanisms to deliver energy from the AGN to the interstellar medium (ISM) of the host galaxy, little is known about the energy, geometry, and efficiency of these mechanisms.

Recent work has focused on a handful of very energetic AGN-driven outflows and winds, such as UV and X-ray Broad Absorption Line (BAL) QSO outflows (e.g., Crenshaw & Kraemer 2012; Arav et al. 2013; Crenshaw et al. 2015) as well as narrow line region (NLR) outflows (e.g., Müller-Sánchez et al. 2011; Fischer et al. 2013; Crenshaw et al. 2015; Müller-Sánchez et al. 2016; Fischer et al. 2017). This work has carefully measured the outflow velocity, and therefore, kinetic energy, of these objects. Theoretical studies predict a 0.5% threshold as the ratio of kinetic luminosity, or L_{KE} , associated with an outflow to the AGN bolometric luminosity, or L_{bol} , of the AGN outflows necessary to drive a powerful two-staged feedback process (Hopkins & Elvis 2010). Some high energy outflows exceed this energy threshold (e.g., Crenshaw & Kraemer 2012; Arav et al. 2013; Borguet et al. 2013; Liu et al. 2016).

While some energetic outflows have the potential to disrupt the molecular gas in the

disk of the host galaxy, these are extreme cases, and it remains difficult to find direct evidence for feedback in most of these galaxies. To fully address how the overall population of AGNs drive feedback in their host galaxies, it is necessary to characterize the amount of energy entrained in outflows, determine the efficiency of energy delivery using the geometry of the outflow, and find direct evidence for the effects of feedback on the host galaxy.

It is important to determine both the geometry of the outflow and how the outflow is oriented with respect to the star forming disk of the galaxy to establish how and where the energy is delivered to the ISM. Some authors find that a spherical geometry with a 180° opening angle describes NLR outflows while others measure narrower opening angles associated with a biconical outflow (e.g., Müller-Sánchez et al. 2011; Liu et al. 2013a). A bicone model for the NLR of an outflow is expected from the unified model of AGNs; a thick torus provides the collimation necessary to produce a biconical outflow (Antonucci & Miller 1985). Fischer et al. (2013) find a homogeneous distribution of orientations for their sample of Seyfert galaxies with ionized outflows, suggesting that AGN outflows may have a random orientation with respect to the star forming disk of the galaxy. The AGNIFS group also finds that ionized gas outflows are oriented at random angles to the galactic plane (Storchi-Bergmann et al. 2010; Riffel & Storchi-Bergmann 2011a,b; Riffel et al. 2013, 2015; Schönell et al. 2014). Other observational studies of ionized outflows suggest outflows that are aligned with the photometric major axis of the galaxy (e.g., Elitzur 2012).

Our sample of AGN outflows from Nevin et al. (2016) are moderate-luminosity ($42 < \log L_{\text{bol}} \text{ (erg s}^{-1}\text{)} < 46$) AGN outflows in the local universe. They were originally selected from the Sloan Digital Sky Survey (SDSS) as $z < 0.1$ Type 2 AGNs with double-peaked narrow emission lines. Moderate-luminosity AGNs such as these account for 10% of the total AGN population at low redshifts ($z < 0.1$) (e.g., Silverman et al. 2006; Ueda et al. 2014); they are more ubiquitous than high-luminosity AGNs (1% of the total AGN population), which includes the BAL QSO population. In addition to representing a larger fraction of the AGN population, moderate-luminosity outflows also operate on kpc-scales, coincident

with circumnuclear star formation. This enables us to directly assess the effects of outflows on the ISM of the host galaxies (Crenshaw et al. 2015). If moderate-luminosity AGNs are capable of driving feedback, they are so common that they could contribute significantly to the explanation for observed galaxy-SMBH scaling relations.

The remainder of this paper is organized as follows. We describe the sample selection, biconical models, and Markov Chain Monte Carlo analytic modeling technique in Section 3.2. In Section 3.3 we calculate sample statistics for orientation of the outflows and energy diagnostics of the outflows. We discuss the implications of the best fit biconical outflow models, energy diagnostics, and geometry in Section 3.4. We present our conclusions in Section 3.5. A cosmology with $\Omega_m = 0.3$, $\Omega_\Lambda = 0.7$, and $h = 0.7$ is assumed throughout.

3.2 Methods

The 71 Type 2 AGNs with double-peaked narrow emission lines at $z < 0.1$ in the SDSS were introduced and classified in Nevin et al. (2016). We observed each galaxy at two position angles with optical longslit spectroscopy (Comerford et al. 2012; Nevin et al. 2016). For each galaxy, we reduced the 2d spectra and extracted the [OIII] λ 5007 profiles. We calculated the velocity offset of the [OIII] λ 5007 emission line relative to the systemic velocity derived in the SDSS DR7 value-added catalogues (OSSY) from absorption lines (Oh et al. 2011). The 71 galaxies were classified as Outflow, Outflow Composite, Rotation-Dominated + Obscuration, Rotation-Dominated + Disturbance, or Ambiguous. Here we focus only on the 61 galaxies that were classified under the outflow-dominated classifications of Outflow and Outflow Composite.

3.2.1 Selection Criteria for Analytic Modeling

We initially model all of the 61 outflow-dominated AGNs as biconical outflows. We are motivated to use a biconical outflow model because each of the double-peaked emission lines are kinematically described as outflows on all spatial scales (Nevin et al. 2016). We apply

the kinematic classification method from Nevin et al. (2016) to the velocity dispersions and velocity offsets of both components on all spatial scales. We find that unlike in some nearby Seyfert galaxies, where the NLR kinematics are best described by a small-scale outflows and large-scale illuminated disk rotation (Fischer et al. 2017), both components can only be described by outflow kinematics for our sample. We analyze the lack of rotation-dominated structure further in Appendix B.1. Therefore, we rule out illuminated rotating structure as the origin for the double peaks at all positions observed along the slit and ensure that we are physically motivated to model the two components as the walls of a biconical outflow.

Then, we establish selection criteria to determine which galaxies are well-modeled, and identify 18 galaxies for further analysis in this paper. We present these 18 galaxies with their PAs, spatial apertures, spatial resolution, and spectral resolution in Table A.7. We select these 18 galaxies based upon three requirements for the spatially resolved spectra as described in the following paragraphs.

First, we include only rows in the longslit spectra in which the Akaike statistic from Nevin et al. (2016) demonstrates that a two Gaussian fit is significantly better than a one Gaussian fit. This ensures that our goal of producing an analytic model of a cone for a two Gaussian profile is met. Second, we require that the kinematic model directly model the two Gaussian centroids as the two walls of a cone. We assign a joint velocity and dispersion tracking method to associate each single Gaussian component of the two Gaussian fit with a physical wall of the cone.

Second, in previous work, groups have used a dispersion association method to track components that belong to a given wall of a bicone. In Westmoquette et al. (2011), the component with the larger dispersion always corresponds to the same wall of the bicone. For example, one wall of the bicone has a larger velocity dispersion and is the redder emission component at one spatial position. If at a different spatial position, the emission components switch relative velocity dispersions, where the bluer component now has a larger dispersion, suddenly the bluer component is now associated with the wall with the larger velocity dis-

persion.

We choose to use a stricter tracking method than Westmoquette et al. (2011). In addition to the dispersion tracking method, we restrict our modeling to galaxies where the components with similar dispersion across the slit are also related in velocity. This combination of velocity and dispersion tracking restricts our physical model to a model of bulk motion of the biconical outflow. For instance, the dispersion tracking method in Westmoquette et al. (2011) allows material from a given wall of the bicone to suddenly move at a new velocity that may be $\sim 1000 \text{ km s}^{-1}$ different from the bulk motion of that wall. In contrast, we require that both of the walls of the cone move at the velocity set by the velocity law (Section 3.2.2), and we choose to model only galaxies whose spectra match this physical explanation.

We eliminate rows of data that violate the velocity and dispersion association requirements. For example, if a narrower emission component is the blueshifted component in one row but then in a subsequent row becomes the redshifted component, we eliminate the exterior rows by truncating the data at the last row of dispersion association. The justification is that the flux in these exterior rows is low enough to confuse emission components, and we may not be associating components with their proper physical wall of the cone.

An additional motivation for eliminating rows of data based upon the Akaike statistic and the velocity and dispersion tracking method is to ensure model convergence. Since we use a likelihood maximization technique, rows with large error bars on the velocity centroids do not lead to the convergence of the best-fit model. Spatial rows that do not pass the two requirements discussed above often have very low S/N and therefore large error bars.

Third, we select only the galaxies with $n > 2k$, where k is the number of parameters in the bicone fit and n is the number of spatial rows of data (from each individual PA) that satisfy the other two requirements described above. Typical values for k and n are 5-6 and 10-20, respectively. Given an average pixelscale of $0''.3 \text{ pix}^{-1}$ and an average redshift of 0.05, this corresponds to emission profiles with a typical radius of 1.5-3 kpc.

This last requirement discourages false convergence for data sets that are too small to truly constrain the geometry of a cone. We find that 18 galaxies meet these criteria. Therefore, the biconical outflows discussed in this work represent the best quality data (top 30%) from the full sample of 61 outflow-dominated galaxies. We discuss the implications of our selection criteria in Section 3.4.1, but in general we find that by requiring these three selection criteria, we select for galaxies that are nearby, more luminous, and more extended from the full sample of 61 outflows-dominated galaxies.

3.2.2 Analytic Outflow Models

We model the 18 galaxies selected in Section 3.2.1 as biconical outflows. A biconical model for AGN outflows is well motivated by observations and theory. From theory, a bicone model for the NLR of an outflow is expected from the unified model of AGNs; a thick torus provides the collimation necessary to produce a biconical outflow (Antonucci & Miller 1985). Observationally, Schmitt & Kinney (1996) found biconical geometry in Seyfert 2 galaxies. Barbosa et al. (2014) confirm this biconical geometry for NGC 1068 with IFS. Crenshaw & Kraemer (2000) also find that the NLR kinematics of NGC 1068 observed with STIS longslit data are well-described by a radial biconical outflow. Other work followed to model biconical outflows with kinematic longslit and IFS data (e.g., Crenshaw et al. 2000; Das et al. 2006, 2007; Müller-Sánchez et al. 2011; Fischer et al. 2013; Crenshaw et al. 2015; Müller-Sánchez et al. 2016). Although some groups model AGN outflows using a quasi-spherical geometry (e.g., Liu et al. 2013a; Harrison et al. 2014), our double-peaked velocity centroids are not consistent with a spherical geometry and instead suggest the inclined geometry of a bicone. Additionally, spherical shell models for bicones tend to overestimate the surface area of the outflow, and one of our main goals is to provide an accurate estimate of this parameter since it is used to estimate the kinetic energy of the outflow.

The bicone model builds off of the evacuated two-walled bicone with a front and rear wall where material begins to decelerate at a given turnover radius from Das et al. (2006).

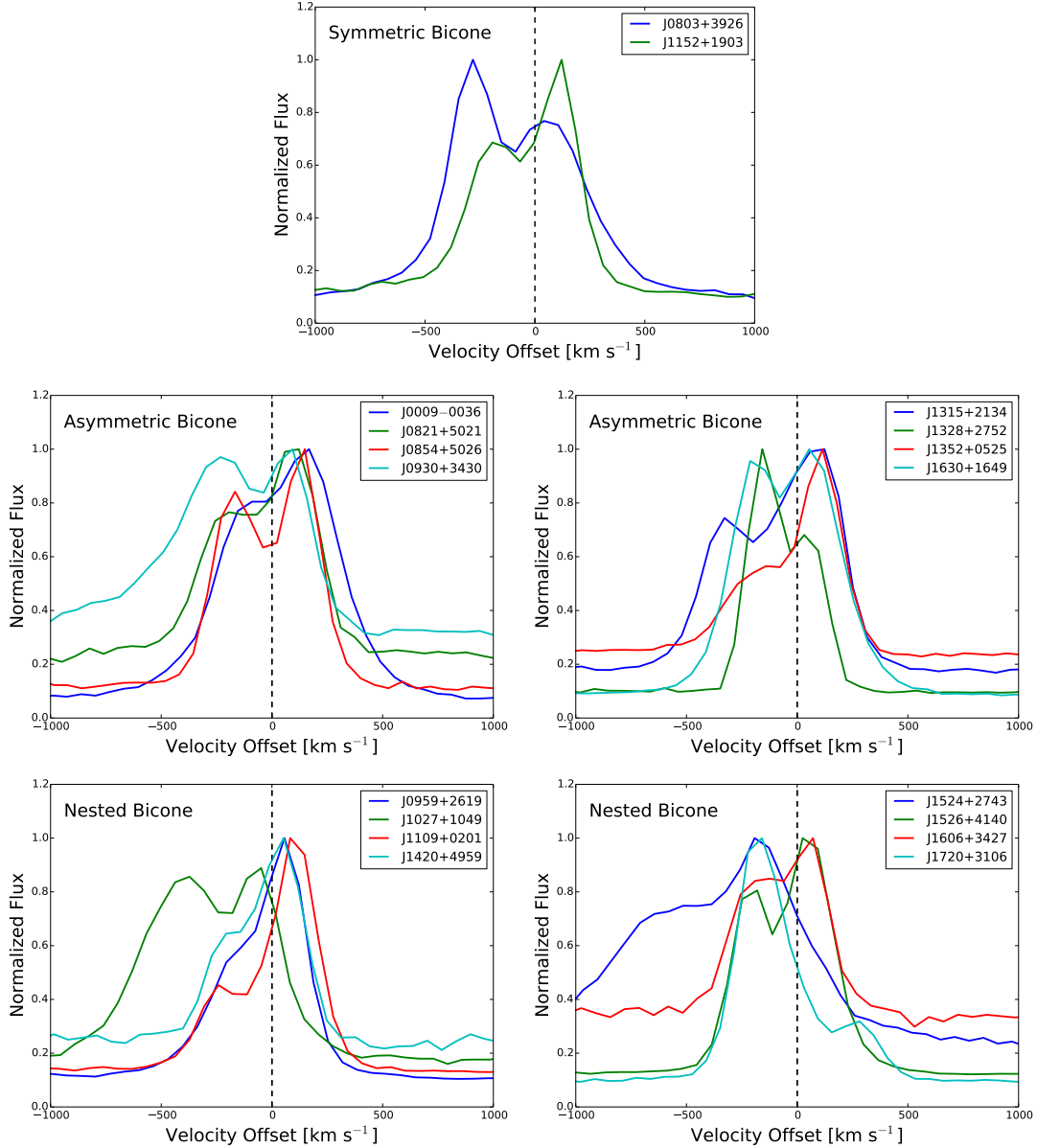


Figure 3.1: The integrated [OIII] $\lambda 5007$ SDSS profiles of the 18 galaxies modeled as biconical outflows in this work. The velocity offsets are measured relative to the host galaxy stars. Here we separate the galaxies according to the biconical outflow model that is the best fit. The symmetric bicone model with symmetric velocity centroids is the best fit model for the two galaxies in the top panel. The asymmetric bicone is the best model to describe the eight galaxies in the middle row. The nested bicone is the best model for the eight galaxies in the bottom row. Note that outflows possess distinct knots of emission that move at random velocities; therefore, profiles such as J0959+2619 (bottom left, nested bicone) may be best modeled as a nested bicone even though the redder velocity centroid is shifted redward of zero velocity in the integrated profiles. These types of profiles are better explored using spatially-resolved longslit spectra.

In Das et al. (2006), the two-walled structure is filled in between the walls. In this work, we evacuate the volume between the walls (Section 3.4.3 presents the motivation for this fully evacuated bicone). The parameters for the bicone are inclination (i), position angle on the sky ($\text{PA}_{\text{bicone}}$), turnover radius for the velocity law of the outflow (r_t), the maximum velocity of the outflow at this turnover radius (V_{max}), the inner half opening angle of the bicone ($\theta_{1,\text{half}}$), and the outer half opening angle ($\theta_{2,\text{half}}$). The height of the bicone is determined by the turnover radius (r_t), specifically $h = 2r_t$. We measure the kinetic energy at r_t to capture the bulk of the energy since the outflow decelerates beyond r_t .

The velocity law for the material along the wall of a biconical outflow has two phases. Exterior to r_t , the material decelerates linearly due to drag forces associated with the ISM (e.g., Das et al. 2006, 2007). Interior to r_t , the bicone velocity law can be modeled with either an accelerating or constant velocity law.

In nearby Seyferts with pc-scale resolution, observations have revealed the linear acceleration phase of AGN outflows with a turnover radius around 100 pc (e.g., Crenshaw et al. 2000, 2003; Das et al. 2006; Müller-Sánchez et al. 2011; Fischer et al. 2013; Crenshaw et al. 2015). In contrast, other work with pc-scale resolution fails to find this acceleration (e.g., Storchi-Bergmann et al. 2010). Yet other work with larger resolution (kpc-scale) fails to find an accelerating phase and uses a constant velocity law to describe the outflowing gas (e.g., Liu et al. 2013a; Harrison et al. 2014).

Since we are probing AGN outflows with kpc-scale resolution and also fail to observe an accelerating phase to the wind, we are well motivated to use a constant-velocity law to describe the interior regions of the outflow (prior to the deceleration phase). We note that we cannot distinguish between being unable to resolve this small-scale acceleration phase and the non-existence of this phase. We now turn to the theory of the accelerating mechanism for an outflow and how it fails to explain this acceleration phase.

It is unclear how and where NLR winds are produced and accelerated to their observed maximum velocities of 100 to 1000 km s⁻¹ (Crenshaw & Kraemer 2005; Fischer et al. 2013;

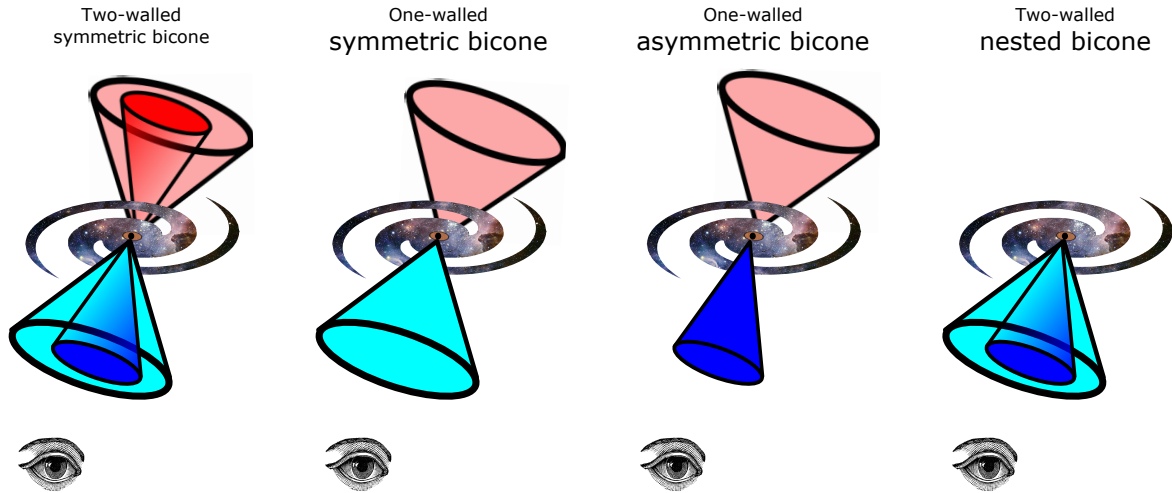


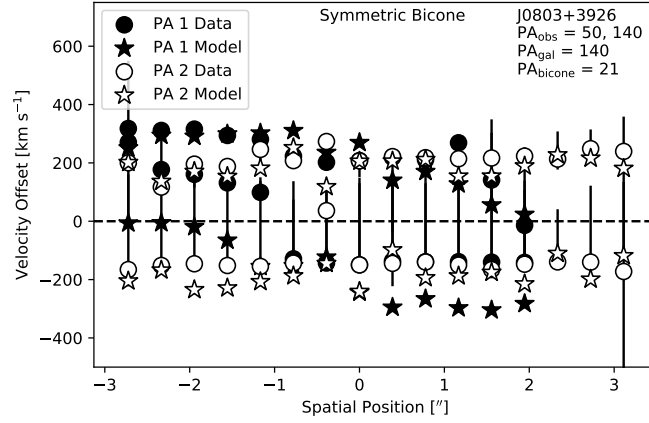
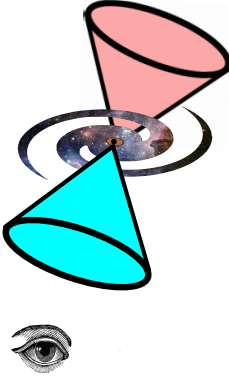
Figure 3.2: The general structure and variations of the symmetric bicone. Only observed walls are shown, where darker colors indicate larger line of sight velocities. Here we make no distinction between illumination, obscuration, or selection effects leading to the absence of walls relative to the two-walled symmetric bicone. The general structure (left) has four total walls, all of which are aligned and described by two different opening angles. The symmetric bicone (second from left) has two cones of the same opening angle that touch apex to apex. The asymmetric bicone (second from right) has two cones of different opening angles, where the larger opening angle cone illustrates the receding emission component. We find that a larger opening angle receding cone is the case for all of the galaxies that are best modeled as an asymmetric bicone. The nested bicone (far right) has two cones, both of which are blueshifted.

Fischer et al. 2014). Possible proposed mechanisms for accelerating an AGN wind include thermal winds, magnetic fields, and radiative pressure (e.g., Matzner & McKee 1999; Lada & Fich 1996; Das et al. 2007). However, these mechanisms fail to explain the acceleration phase out to 100 pc observed by some work (e.g., Everett 2005; Das et al. 2007). Everett & Murray (2007) demonstrate that Parker winds (thermal winds) cannot reproduce the observed range of velocities observed. They also find that radiative pressure and magnetic fields can launch powerful winds, but these are small-scale winds that reach their terminal velocities ~ 10 pc from the central source, the 100 pc distance as observed.

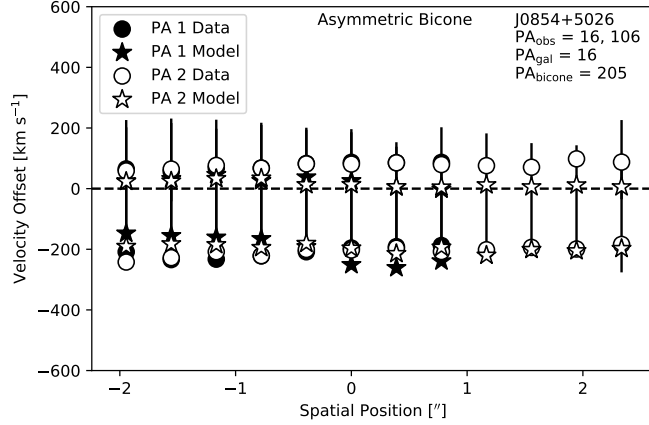
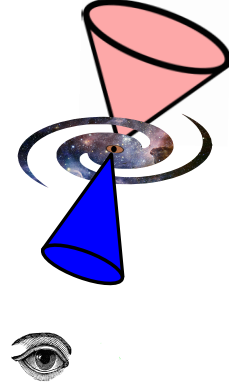
Everett & Murray (2007) propose that since the various wind models fail to reproduce the observation, an already accelerated wind could be interacting with the surrounding medium. Storchi-Bergmann et al. (2010) investigate the accelerating velocity profile of the outflow in NGC 4151 observed by Das et al. (2006) and explain that since the velocity centroids probe the brightest emission, the observed accelerating structure could be produced by bright lower velocity gas entrained in the disk closer to the nucleus. Then, at greater radii in the outflow in NGC 4151, the outflowing component dominates the flux and produces the observed deceleration phase. Therefore, the observed acceleration could be attributed to a rotation-dominated component at small spatial scales.

We model the 18 AGN outflows using three biconical outflow models: the symmetric bicone, the asymmetric bicone, and the nested bicone. We are motivated to expand our models beyond that of the classical symmetric bicone due to asymmetries in the measured velocity centroids for the bluer and redder components of the two Gaussian fits to the spectra. This is apparent in both the SDSS integrated profiles (Figure 3.1) and the spatially resolved longslit profiles. We find that 15/18 outflows have integrated profiles that have a blueshifted overall velocity centroid. When we fit two Gaussians to the profile, 15/18 also have a mean velocity (averaging the two centroids) that is blueshifted. Motivated by the failure of a symmetric bicone model to uniformly describe the velocity centroids of all of the galaxies, we introduced the two additional analytic models.

One-walled
symmetric bicone



One-walled
asymmetric bicone



Two-walled
nested bicone

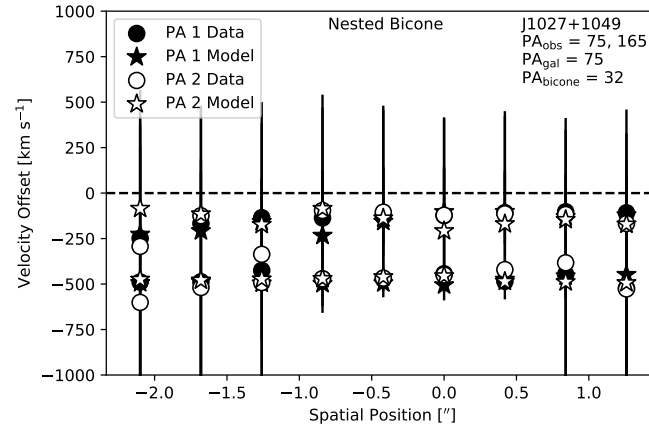


Figure 3.3: Three variations of bicone models (left) with associated velocity profiles for example galaxies that are best fit by each model (right). We plot the velocity data in points and the best fit models with stars. The positive spatial direction corresponds to the NE direction of the slit. We plot a horizontal dashed line at zero velocity to fully demonstrate the origin of the names of the bicone models. For instance, the asymmetric bicone has velocity centroids in the spectrum that are asymmetric about zero velocity.

Each of the three bicone models can be described as a variation of a two-walled symmetric bicone; each model a total of two cone structures that are aligned with one another and produce double-peaked emission lines. We refer to a one-walled structure when there is one wall on either side of the galaxy (the one-walled symmetric bicone and one-walled asymmetric bicone). The two-walled bicones have two walls on one or both sides (the nested bicone and the general two-walled symmetric bicone, respectively). We use the same physical structure in all three model variations of the bicone, and the distinct models simply select different walls of a two-walled symmetric bicone structure. Figure 3.2 shows diagrams of these three models.

In addition to the simple case of the symmetric bicone, the asymmetric bicone and nested bicone are also motivated by observations. In a sample of SDSS Type 2 AGNs, Woo et al. (2016) find that inclination, dust obscuration, and velocity are the dominant parameters that control the modeled velocity and velocity dispersion profiles of AGNs. Their flux-weighted models demonstrate that dust can obscure the receding cone entirely when the inclination of the bicone is high, producing an observed profile similar to that of the nested bicone.

Additionally, if the receding side of the bicone is larger than the dust plane, Woo et al. (2016) find that an asymmetric biconical structure can appear in the integrated spectrum because a wider opening angle receding cone is more favored in the flux-weighted profile. Storchi-Bergmann et al. (2010) observe very weak emission from the more inclined walls (relative to the disk) of the AGN outflow in NGC 4151. They explain that more gas is entrained at low angles to the galactic disk; an asymmetric bicone profile could originate from a wider opening angle receding cone that is close to the disk of the galaxy. Müller-Sánchez et al. (2013) find that an asymmetric bicone model is the best fit for the outflow in the Seyfert galaxy NGC 3081 with a wider opening angle receding cone.

The general symmetric two-walled bicone has a total of four cones (two receding and two approaching along the line of sight; Figure 3.2). For each of the three models, we select

two cones from the symmetric two-walled bicone. Here we do not make a distinction between the existence and non-existence of various walls, obscuration effects, or illumination effects. We discuss obscuration effects, illumination effects, and lack of gas effects that may lead to these different models in Section 3.4.3.

The symmetric one-walled bicone has two symmetric conical structures that can be described with the same opening angle on either side of the galaxy. A symmetric biconical model is constrained by five parameters (i , $\text{PA}_{\text{bicone}}$, r_t , $\theta_{1,\text{half}}$, and V_{max}) and produces two velocity centroids that are symmetric about zero velocity. The asymmetric bicone consists of two cones that are aligned. However, these cones can be described by two different opening angles. This model is constrained by six parameters (i , $\text{PA}_{\text{bicone}}$, r_t , $\theta_{1,\text{half}}$, $\theta_{2,\text{half}}$, and V_{max}). Likewise, the nested bicone has six parameters (i , $\text{PA}_{\text{bicone}}$, r_t , $\theta_{1,\text{half}}$, $\theta_{2,\text{half}}$, and V_{max}). It consists of two cones that are aligned but nested inside one another. The velocity centroids of the nested cone are both blueshifted. We show an example of a velocity profile from each of the three types of bicones in Figure 3.3.

Due to our $n > 2k$ constraint, we are unable to assign 10 free parameters (i , $\text{PA}_{\text{bicone}}$, r_t , $\theta_{1,\text{half}}$, V_{max} , i_2 , $\text{PA}_{2,\text{bicone}}$, $r_{2,t}$, $\theta_{2,\text{half}}$, and $V_{2,\text{max}}$) for the nested and asymmetric bicone models. However, past observations and asymmetric bicones in this work justify allowing just six free parameters in the nested and asymmetric bicone models, where we allow the opening angles of the two cones to vary.

First, either two different intrinsic velocities or two different opening angles could explain the asymmetric velocity centroids in the asymmetric bicone model. Observations of asymmetric bicones indicate that the redshifted wall often has a larger opening angle (e.g., Müller-Sánchez et al. 2013; Woo et al. 2016). Additionally, all the velocity centroids of galaxies in this work that can be described as asymmetric have a higher velocity blueshifted component and a lower velocity redshifted component. There is no physical motivation for 100% of AGN outflows having an intrinsically lower velocity to the redshifted cone, so we favor the geometry explanation for this effect.

We find in Section 3.2.3 that the choice of two distinct opening angles was merited, since the models converge on two different opening angles that are unique. Additionally, after completing the modeling, we assess the sensitivity of the parameters in Section 3.2.3 and find that the opening angles are the best-determined parameters. We find that the other parameters have large error bars and fitting two separate parameters for each model yields two values that are consistent with one another and therefore meaningless as separate parameters. For instance, when we fit two inclinations for each of the two sides of the asymmetric bicone, we find two values for each cone’s inclination that are consistent with one another within errors. Therefore, our choice of the six free parameters for the asymmetric and nested bicones is justified by past observations of bicones as well as the limitations of our data and the sensitivity of our model (Section 3.2.3 and 3.2.4).

We create a three dimensional model of each of these three cone structures. We project the velocities of our three dimensional models onto the plane of the sky and extract a line of sight velocity for all points along the observed PAs of the two slits (Figure 3.4). The model accounts for the pixelscale and the slitwidth of each observation. We use a Markov Chain Monte Carlo process (described in Section 3.2.3) to model all 18 galaxies using each of these three models. We find that 2/18 galaxies are best modeled as a symmetric bicone, 8/18 galaxies are best modeled as an asymmetric bicone, and 8/18 galaxies are best modeled as a nested bicone.

3.2.3 Markov Chain Monte Carlo parameter estimation

For each of the three outflow models for each galaxy, we perform a multi-parameter Markov Chain Monte Carlo (MCMC) iterative modeling process to determine the best fit model and combination of parameters for the velocity data. In this section, we briefly outline the MCMC sampling, present the results of our modeling, discuss the methods we use to verify convergence, and discuss implications of the parameters using practical identifiability and sensitivity analysis.

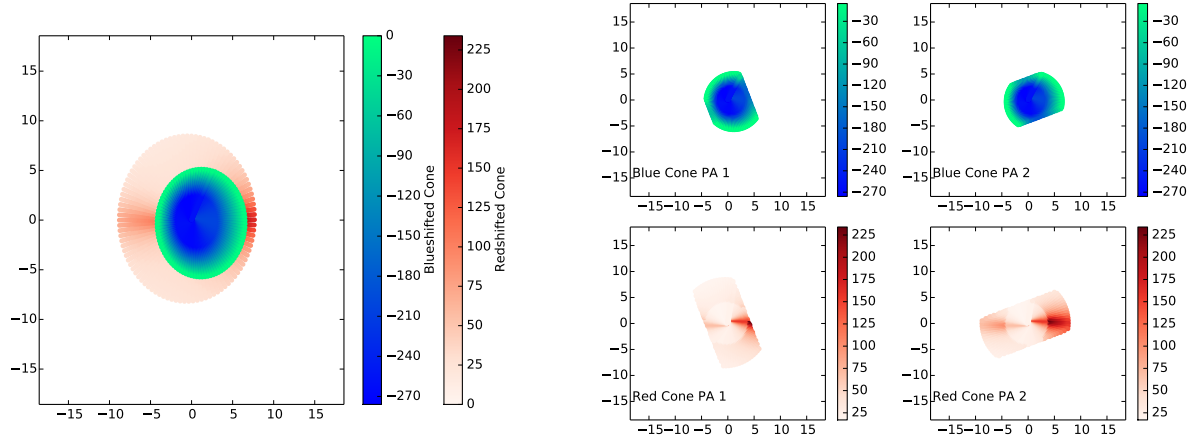


Figure 3.4: The best fit asymmetric bicone model for the galaxy J0930+3430. Spacing on all axes corresponds to pixels (here, the pixelscale is $0''.389\text{pix}^{-1}$). Left: model of the bicone. The bicone is very inclined and the two colorbars show the line of sight velocities for both the redshifted (wider opening angle) cone and the blueshifted (smaller opening angle cone). Right: the cuts we make to the model (left) along the two observed PAs of the longslits on the sky (PA1 = 21° , PA2 = 111°). This takes pixelscale and slitwidth into account. We extract modeled velocity centroids for the blueshifted cone (top) and redshifted cone (bottom). Velocity color bars are in units of km s^{-1} .

We utilize the affine-invariant MCMC Ensemble sampler from Goodman & Weare (2010), conveniently packaged in the Python code `emcee` (Foreman-Mackey et al. 2013). The MCMC method takes advantage of parallel processing to sample the posterior probability density function (PDF) for a multi-parameter space efficiently on multiple cores. Computing the PDF of a biconical outflow is computationally expensive, so we run our parallel sampling for the bicone models on the University of Colorado supercomputer JANUS. An affine-invariant sampler also performs well under all linear transformations; the sampler is insensitive to covariance between parameters. Parameters demonstrate covariance within our parameter set, so this is an advantage.

In the case of uniform priors (which applies here), the MCMC technique maximizes the log-likelihood of the parameter space. Gaussian log-likelihood is defined as:

$$\log \mathcal{L} = -0.5 \left(\sum \ln(2\pi\sigma_i^2) + \sum \frac{(y_i - x_i)^2}{\sigma_i^2} \right)$$

where y_i is the data, x_i is the model, and σ_i is the associated error with each data point. Here, σ_i includes both error on the measurement of the Gaussian centroid of each velocity component and the error inherent to the instrumental dispersion (e.g., for the instruments used in this sample, the typical error is 2.5 km s⁻¹). The Gaussian log \mathcal{L} is related to a χ^2 value, since in the Gaussian case with a normal error assumption, they are directly proportional. To compare goodness of fit between different models, we use a reduced chi-square defined as:

$$\chi_\nu^2 = \chi^2 / (n - k - 1)$$

where n is the number of data points and k is the number of free parameters.

Due to the simplistic nature of the outflow model, the χ_ν^2 values are relatively high. Although we could add more parameters to make a more realistic model, the number of data points do not justify it. These models assume a continuous distribution of NLR emission along the walls of the outflow and are too simplistic for a structure with many complicated discrete knots of emission, but model the overall morphology well. Therefore, we do not

expect χ^2_ν values to be ~ 1 for these models, and we are unable to assess the absolute “goodness of fit” of a given model in isolation. Instead, we use the χ^2_ν values only to compare between different models for an individual galaxy; the χ^2_ν values are not intended to be used to compare the outflows of two different galaxies.

We find that 2/18 (11.1%) galaxies are best modeled as a symmetric bicone, 8/18 (44.4%) galaxies are best modeled as an asymmetric bicone, and 8/18 (44.4%) galaxies are best modeled as a nested bicone. The χ^2_ν values are reported in Table A.8 and the parameters for the best fit model along with 1σ error bars are reported in Table A.9, A.10, and A.11 for the galaxies that are best fit by a symmetric bicone, asymmetric bicone, and nested bicone, respectively. We also include the mean modulus of the residuals between the observed velocities and the modeled velocities to quantify the goodness of fit. We find that this quantity is comparable to the uncertainty of the observed velocities, which indicates that the models are a good fit.

We confirm convergence of the MCMC fit to the global maximum by assessing the acceptance fraction of the walkers and the autocorrelation function. We use the acceptance fraction of the walkers as one method to assess if the walkers have fallen into a local maximum. We ensure that the walkers are in the range of acceptance fraction (0.2-0.5) suggested by Foreman-Mackey et al. (2013). If the acceptance fraction is less than 0.2, this implies that the walkers have fallen into a local maximum and are unable to walk their way out, and instead reject every step. An acceptance fraction that is too high would imply that the PDF is featureless, and walkers are accepting random steps across the entirety of parameter space. Our average acceptance fraction is in the 0.2-0.5 range due to our careful selection of data that are high enough in quality and quantity as discussed in Section 3.2.1.

Another method for quality assurance of the fit is to determine the “burn-in” period and ensure that the MCMC process iterates for at least this long. The code `emcee` provides an estimation of the autocorrelation time, which is defined as the time lag that drives the value of the autocovariance function of a time series to zero. When the autocovariance is

zero, the chain has fully sampled the probability space. For our parameters, the typical autocorrelation time is 50-60 steps, indicating that it takes 50-60 steps for the walkers to converge upon the true value. We run all chains for 200 steps to ensure that the runs extend for at least twice the maximum autocorrelation time. On average, our chains run for four autocorrelation times.

We next investigate the relative sensitivity of the six outflow parameters and their practical identifiability. We determine the best fit parameter values and their associated 1σ errors from the marginalized distributions (Figure 3.5). The PDF of each parameter is constructed from the final position of all 100 walkers in parameter space. One advantage of MCMC sampling is that the final parameter distributions are not restricted to symmetric errors. Instead, we use the shape and width of these distributions to determine how the various parameters affect the modeling process.

The first parameter-related check that we perform is a test of practical identifiability. Rothenberg (1971) define lack of identification as the lack of sufficient information to distinguish between alternative structures or models based upon the data. There are different types of identifiability; here we discuss practical identifiability. Lack of identifiability where the data may not uniquely identify a model could either be a structural problem with the model itself or a problem that arises due to noisy data (Campbell & Lele 2013). We assess the practical identifiability of the model by constructing a synthetic data set based upon the symmetric bicone model with a pixelscale and spectral resolution typical of the longslit data for the 18 galaxies. We then create two different realizations of this synthetic data; one where the error is equal to that of the data ($\sigma \approx 10\%$) and one where the error is inflated ($\sigma \approx 100\%$).

The synthetic bicone has parameters typical of the galaxies we model here: $i = 0$; $\text{PA}_{\text{bicone}} = 15^\circ$; $r_t = 5$ (pixels); $\theta_{1,\text{half}} = 55^\circ$; and $V_{\text{max}} = 500 \text{ km s}^{-1}$. We run the synthetic model through **emcee** starting at an intentionally incorrect starting point for the parameters. The goal is to determine if the **emcee** process returns the correct set of parameters and

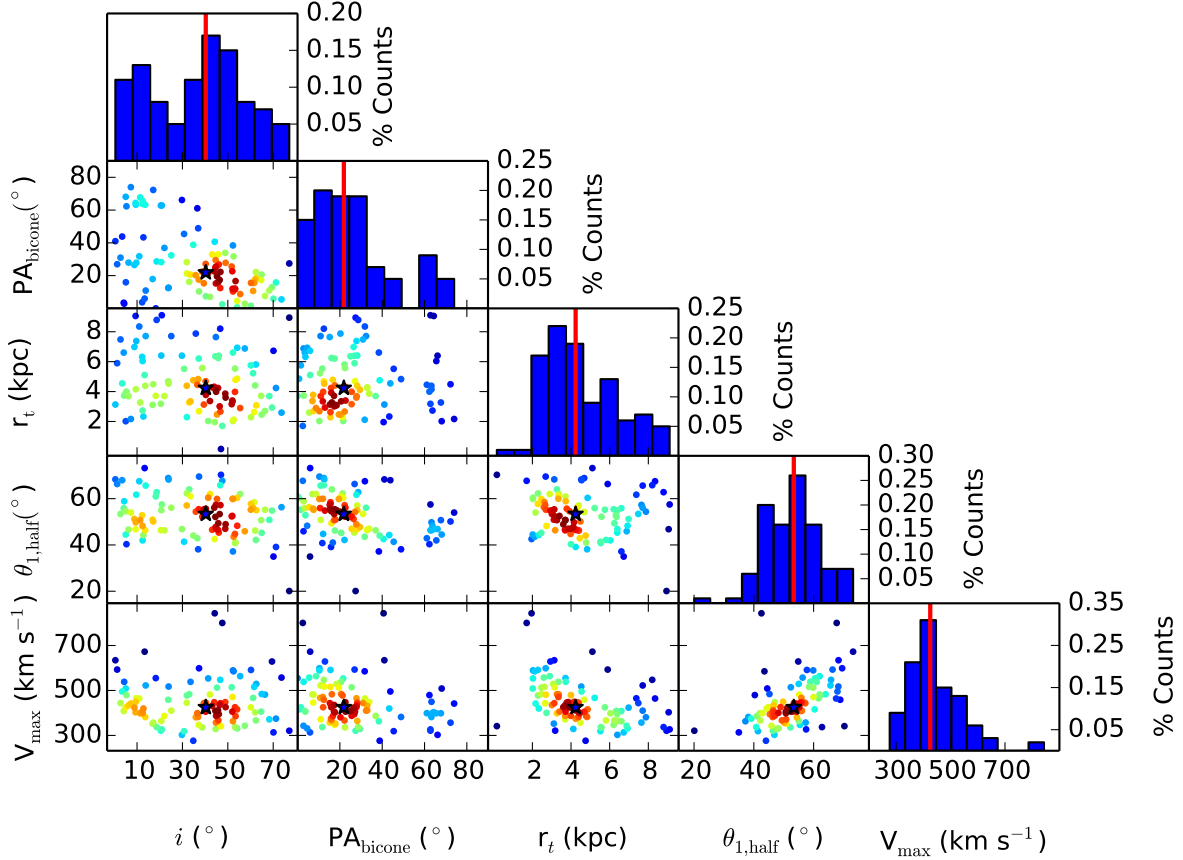


Figure 3.5: Triangle plot for the best fit model parameters for the symmetric bicone model for the galaxy J0803+3926. Each column and row represents one of the five parameters for which the MCMC method estimates a best value. From left to right these parameters are: Inclination i , position angle on the sky (PA_{bicone}), turnover radius r_t , half opening angle of the cone ($\theta_{1,\text{half}}$), and maximum velocity (V_{max}). The top plot of each column gives the histogram of final values for each parameter, where the red line represents the median value. We demonstrate that our method successfully returns normally-distributed histograms for the value of each parameter. In the interior plots, walker final locations are colored according to point density on each plot, where red represents the densest clustering of points. The black star illustrates the best fit values provided by the median value of each parameter histogram.

examine the posterior probability of the output.

When examining the walkers from both runs, it becomes apparent that the walkers better converge upon the true parameter values for the run with smaller, more representative error bars. This is unsurprising, as it indicates that the probability space is well-defined for the smaller errors. For the larger errors the likelihood is smooth and featureless (less conducive to convergence). We have demonstrated practical identifiability for our data, which has errors of order 10%. However, extreme caution should be taken when attempting to identify models with velocity measurement errors on the order of 100% of the value of the velocity.

We also assess the sensitivity of the six parameters involved in the biconical outflow models. For instance, from the parameter error bars reported in Tables A.9, A.10, and A.11, it is apparent that $\text{PA}_{\text{bicone}}$ is not well determined; the modeling process is not particularly sensitive to this parameter. We use one-factor-at-a-time (OFAT) sensitivity analysis to investigate the relative sensitivity of all parameters. We keep all parameters but the one in question at their baseline (nominal) values and compute the change in likelihood produced by varying the parameter in question through the full range of allowed values. For example, for an OFAT sensitivity analysis of the inclination, we vary the inclination between 0 and 90°. We quantify the change in likelihood by computing $\Delta\chi_\nu^2$ between the best fit χ_ν^2 value and the largest χ_ν^2 value within this parameter range.

As an example, we discuss the OFAT sensitivity analysis for J0930+3430, which is best fit by an asymmetric bicone. We find the following $\Delta\chi_\nu^2$ values for the parameters listed in order of increasing sensitivity: (1.2, 256.2, 262.3, 613.2, 1051.1, 1335.3) for ($\text{PA}_{\text{bicone}}$, V_{max} , r_t , i , $\theta_{1,\text{half}}$, $\theta_{2,\text{half}}$). As expected from the large error bars on $\text{PA}_{\text{bicone}}$, $\text{PA}_{\text{bicone}}$ is the least sensitive parameter. This is explained by our finding that the AGN outflows are biased to have large inclinations in Section 3.4.1. A large inclination outflow is face-on, which causes the line of sight velocities to only change slightly over a range of values of $\text{PA}_{\text{bicone}}$. We calculate energy diagnostics for each outflow (Section 3.3.2) using V_{max} , r_t , $\theta_{1,\text{half}}$, and $\theta_{2,\text{half}}$,

which are among the most well-determined parameters in our models.

3.2.4 Verifying the Models

We note that we are limited to two PAs of longslit data, with a limited number of data points for each. Therefore, we use two tests to verify that the models are converging and that we have enough longslit data points to converge upon the parameters of the bicone. For the first test, in this section we examine a galaxy for which we have obtained additional longslit data. We are motivated by Fischer et al. (2017), who find that their original longslit observations of the biconical outflow in Mrk 573 (Fischer et al. 2010) were insufficient to return the correct parameters for their bicone and disk models for the kinematics of the galaxy. Returning to gather IFS observations in Fischer et al. (2017), they find a different model for Mrk 573 that indicates an outflow is occurring on small scales and that rotation-dominated kinematics dominate at large scales. We will address the concern of rotation-dominated kinematics in Appendix B.1. Here, we examine the limitations of our longslit data.

To address this concern for the longslit observations in this paper, we present additional observations for the galaxy J0930+3430. We choose to further investigate this galaxy because the best-fit PA for the bicone is between the two originally observed PAs. Additionally, the original best-fit model was one of the largest and most energetic of the 18 galaxies. The original two PAs observed and presented in Nevin et al. (2016) are 21 and 111 degrees, and we found that the best-fit bicone model is oriented along PA 75. These two position angles were observed with the Palomar Blue Channel Spectrograph (pixelscale $0''.389 \text{ pixel}^{-1}$). We obtain two new PAs at 66 and 156 degrees with the Dual Imaging Spectrograph at APO (pixelscale $0''.42 \text{ pixel}^{-1}$). In Figure 3.6 we overplot all of the observed PAs.

We have modified our bicone modeling code to incorporate four PAs. We have rerun the the `emcee` code for all possible combinations of two PAs as well as the four PA run (pseudo-IFS) in Table A.12. We use the asymmetric bicone model for J0930+3430, and we

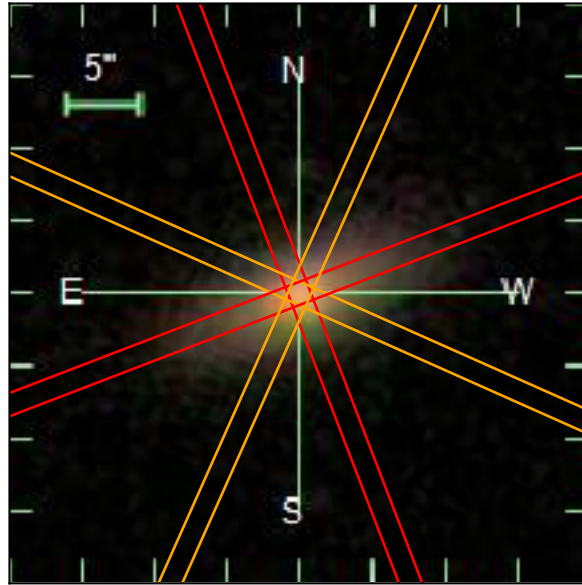


Figure 3.6: Four observed PAs for J0930+3430 overplotted on the SDSS *gri* image. We combine them to construct a pseudo-IFS map. The PAs are E of N: 21, 66, 111, and 156 degrees. PA 66 and 156 are the new observations, shown in orange, obtained from APO. The original two PAs of 21 and 111 degrees, shown in red, were obtained from Palomar (Nevin et al. 2016). The slitwidth is $1.5''$.

find that all parameters agree within the 1σ error interval for each run. Additionally, the model with four PAs does not significantly reduce the error interval although it provides better spatial coverage (Figure 3.6).

For the second test, in Appendix B.1 we examine a galaxy for which we have IFS data. This galaxy was not included in the 18 galaxy sample for this work. It was classified as an ‘Outflow Composite’ in Nevin et al. (2016) but excluded from the modeling in this paper due to a third component at small scales and the lack of data points at one PA.

3.3 Results

3.3.1 Bicone and Disk Orientation

For each of the 18 galaxies, we compare the orientation of the bicone with the orientation of the photometric major axis of the galaxy. The orientation statistics for this sample of modeled outflows enable us to comment both on biconical outflow theory with the orientation of a theoretical collimating structure and on how the ionized outflows may affect the ISM and therefore drive feedback in the host galaxy; Section 3.4.4 and Section 3.4.6.

The position angle of the photometric major axis of the galaxy (PA_{gal}) is the photometric major axis of the galaxy in the SDSS r -band. In this work, we determine the alignment of the bicone axis and the opening angle of the bicone structure from the analytic models ($\text{PA}_{\text{bicone}}$ and $\theta_{2,\text{half}}$, respectively). We use $\theta_{1,\text{half}}$ for the galaxies that are best fit with a symmetric bicone. We report these two position angles and the half opening angles in Table A.13 and determine if the biconical structure is aligned with the photometric major axis, if it intersects the photometric major axis, and if it is perpendicular to the photometric major axis for all 18 galaxies. Alignment is defined as $\text{PA}_{\text{gal}} = \text{PA}_{\text{bicone}}$ within a 1σ error margin.

We find that a significant portion of outflows are aligned with the photometric major axis of their host galaxy (10/18, 55.6%). However, we also find that a significant portion of outflows are aligned with a position angle that is perpendicular to the photometric major

axis of the galaxy (10/18, 55.6%). We find that six galaxies are included in both of these groups and that this is a reflection of the uncertainty of the $\text{PA}_{\text{bicone}}$ parameter. When we remove these overlapping galaxies we find that 4/18, or 22.2% of the outflows are aligned with the photometric major axis of the galaxy. The 95% binomial confidence interval on the measured alignment fraction is 3.0% to 41.4%.

The typical 1σ error margin on the measurement of the position angle of the bicone is $\sim 20^\circ$. If the bicone axes were randomly oriented, 22.2% of all outflows should be measured to be within 20° of the photometric major axis. We derive the 22.2% random orientation percentage from the total error margin, 40° , divided by the total possibility of orientations on the sky (180°). As a result, the percentage of outflows that have a biconical outflow axis that is aligned with the photometric major axis of the host galaxy is consistent with the percentage expected for a randomly oriented bicone. We discuss the implications of this result in Section 3.4.4.

3.3.2 Energy Diagnostics

After constraining the geometry of the NLR outflows in the analytic modeling process, we derive energy diagnostics for the biconical outflows. By constraining the kinetic luminosity of the momentum-driven outflows, we can determine the ratio of the kinetic luminosity to the total radiated luminosity. This diagnostic enables us to make observational comparisons to the theoretically predicted 0.5% threshold, which has been quoted as the ratio of $L_{\text{KE}}/L_{\text{bol}}$ necessary to evacuate cold molecular gas from the inner regions of a galaxy and suppress star formation in the ISM (Hopkins & Elvis 2010).

To determine the mass outflow rate of the wind and the kinetic luminosity, we use the best fit parameters from our biconical models as well as density and temperature diagnostics from emission line ratios in the integrated SDSS spectra. We use the SDSS DR7 value-added catalogues (OSSY) to obtain information on integrated spectral lines (Oh et al. 2011).

The mass outflow rate is defined as:

$$\dot{M} = m_p n_e V_{\max} f (A_1 + A_2)$$

where m_p is the proton mass, n_e is the electron density of the NLR, V_{\max} is the maximum velocity of the outflow, f is the filling factor, and A_1 and A_2 are the lateral surface areas of each cone in the bicone. A_1 is the smaller opening angle cone and A_2 is the larger opening angle cone.

To calculate the electron density, n_e , we calculate the intensity ratios of $[\text{OII}]\lambda 3729/[\text{OII}]\lambda 3726$ and $[\text{SII}]\lambda 6716/[\text{SII}]\lambda 6731$, which are sensitive to density (Osterbrock & Ferland 2006). We find mean values of ~ 0.82 and ~ 1.18 , respectively, for these intensity ratios for the 18 galaxy sample. Typical temperatures are in the range $(1 - 2) \times 10^4$ K in the NLRs of AGNs (Osterbrock & Ferland 2006), and thus the corresponding electron density is $\sim (1 - 5) \times 10^2 \text{ cm}^{-3}$. Thus, we verify that $10^2 < n_e (\text{cm}^{-3}) < 10^3$, which is typical for the NLR (Taylor et al. 2003). We use a density of 100 cm^{-3} in our calculations. This assumption is consistent with previous work that finds an electron density of 100 cm^{-3} exterior to 1 kpc from the AGN (Karouzos et al. 2016). With our spatial resolution, we always resolve gas at > 1 kpc.

The filling factor represents the proportion of the bicone surface that contains ionized NLR clouds. It scales inversely with the electron density, n_e : $n_e \propto f^{-1/2}$ (Oliva 1997) and has values in the range of $0.01 < f < 0.1$ for the NLR (Storchi-Bergmann et al. 2010). We adopt a value of 0.01, which is a conservative lower limit based upon the literature. Some authors choose to adopt $f = 0.1$, but we choose to be conservative in our calculation of outflowing energy and adopt $f = 0.01$, representing a bicone in which 1/100 of the bicone surface contains ionized NLR clouds.

The lateral surface area, A , which is the generalized form of A_1 and A_2 , is:

$$A = \pi r \sqrt{h^2 + r^2}$$

where h is the height, which we define as the turnover radius for energy calculation purposes,

and r is the deprojected radius, determined by the half opening angle of the cone:

$$r = r_t \sin(\theta_{\text{half}})$$

where r_t is the turnover radius.

We determine the turnover radius, the opening angle, and the maximum velocity for the 18 galaxies using the best fit analytic models (Section 3.2.3). As we discuss in Section 3.4.3, various additional walls of these three biconical outflow models could be obscured or not illuminated so this calculation is a lower limit for energy outflow rate.

Once we have derived the mass outflow rate of the biconical outflows, we calculate the kinetic luminosity:

$$L_{\text{KE}} = \frac{1}{2} \dot{M} V_{\text{max}}^2$$

We compare the kinetic luminosity to the AGN bolometric luminosity, which is calculated from the dereddened [OIII] λ 5007 luminosity from the SDSS DR7 value-added catalogues in Nevin et al. (2016).

We report the lateral surface area, mass outflow rate, kinetic luminosity, maximum outflow velocity, half opening angle, turnover radius, AGN bolometric luminosity, and ratio of kinetic to AGN bolometric luminosity for the 18 galaxies in Table A.14.

We find that 16/18 (88.9%) of the galaxies have a $L_{\text{KE}}/L_{\text{bol}}$ ratio that is above the 0.5% threshold value to drive two-staged feedback. Of these galaxies, 100% have a bicone that intersects the photometric major axis of the host galaxy. We discuss the implications of these results in Section 3.4.6.

3.4 Discussion

3.4.1 This sample of biconical outflows is biased to be very large and energetic

Before we analyze the energetics of our outflows, we first must understand the observational biases. In this section, we discuss the selection criteria that bias our sample towards larger and more energetic outflows. We also discuss a theoretical ‘minimum energy bicone’ that corresponds to a bicone with the smallest possible surface area that it is possible to recover from our sample given the sample biases.

First, the galaxies in this sample were selected from the SDSS for their double-peaked emission lines. The average velocity separation of the double peaked narrow lines of the integrated spectra of the 18 galaxy sample is $\sim 300 \text{ km s}^{-1}$. Second, these 18 galaxies also have large spatial extents of emission (the average extent of emission is 6.8 kpc) by our selection criteria that requires that the number of rows of statistically significant emission be greater than twice the number of parameters. Third, the average pixelscale of the instruments in this sample is $0''.3 \text{ pix}^{-1}$ which biases our sample towards larger (kpc-scale) outflows.

These three factors have several effects on the best fitting bicone models. First, the large separation in velocity space produces biconical outflows with preferentially large opening angles and higher intrinsic velocities. A higher intrinsic velocity along the walls of the cone produces a larger observed velocity separation between the velocity centroids, regardless of the orientation of the structure, while a larger opening angle cone’s geometry can produce this same effect.

Second, the requirement of many statistically significant rows of emission produces bicone structures with larger turnover radii, larger inclinations, and/or larger opening angles. The average pixelscale of the instruments ($0''.3 \text{ pix}^{-1}$) corresponds to a physical distance of $\sim 0.3 \text{ kpc}$ at $z = 0.05$, which is the typical redshift. If we require that the observed bicone structure cover 5 spatial rows from the center of the galaxy (10 total; $n = 2k$ where $k = 5$

for the symmetric bicone) at each PA, for example, the bicone structure will extend out to a radius of 1.5 kpc. This distance is the full extent of the measured bicone in our data and the turnover radius is interior to this point. However, for our sample the turnover radius is close to the full extent because we observe very little deceleration in the bicones modeled here. Therefore, we are biased towards finding larger bicone structures that tend to also have a larger turnover radius. The spatial row selection also ensures that we observe double peaked emission at both position angles. This selects for more inclined bicones with larger opening angles that can open up along both position angles, producing the full spatial coverage of both orthogonal position angles.

We are therefore selecting for AGN outflows that are more energetic (larger sizes, opening angles, and velocities) and that have a greater chance of intersecting the photometric major axis of their host galaxies with their larger opening angles.

We create a theoretical minimum energy bicone using the limitations of the sample to characterize the selection biases towards higher energy bicones. This helps us place a lower limit on the mass outflow rates of the galaxies in this sample. To produce the minimum energy bicone, we minimize the turnover radius, opening angle, and maximum velocity. We first use the smallest resolvable turnover radius of one pixel at a representative pixelscale of $0''.3\text{pix}^{-1}$ (the average pixelscale of the collection of instruments used here). We use the typical redshift for this sample of 0.05 which corresponds to a conversion factor of $\sim 1 \text{ kpc}''$. This yields a turnover radius of 0.3 kpc. This is slightly smaller than the smallest modeled turnover radius in the sample, which is 0.48 kpc for J1630+1649.

We use the representative separation of double peaks of 300 km s^{-1} from our sample. This is an observed velocity and does not directly correspond to intrinsic velocity. However, for a randomly oriented sample of outflows where inclinations and half opening angles are distributed between 0 and 90° , the observed velocity could range between 0 and 600 km s^{-1} for an intrinsic velocity of 300 km s^{-1} . Therefore, 300 km s^{-1} is a fair average intrinsic velocity. It is also slightly larger than the smallest measured intrinsic velocity from our

sample, which is 281.5 km s^{-1} for J0959+2619.

The fact that we observe velocity separations at both observed orthogonal PAs places limits on the possible range of values for the combination of opening angles and inclination. For example, if the inclination is zero, the half opening angles are constrained to be at least 45° so that the bicone is observable at both orthogonal PAs. For the nested bicone, the inclination must be high so that the bicone walls are observed across the plane of the sky. When we consider inclination and opening angle at the same time, this requires that the combination of inclination and $\theta_{1,\text{half}}$ be greater than 90° . For instance, if the nested bicone axis is inclined at 45° , the half opening angle of the inner cone must be at least 45° so we observe it at all spatial positions. For the asymmetric bicone, the same rules apply.

For all three models it is possible that the bicone structure is inclined exactly 90° relative to the line of sight with a small opening angle bicone. However, this is very unlikely given that our sample selects for high inclinations but few are greater than 80° . We choose to use the average inclination of 66° , which requires that the half opening angle be $> 24^\circ$ for the bicone to intersect both observed PAs at all spatial positions. We use an inclination of 66° and a half opening angle of 24° .

Using the combination of these minimized parameters, we find a kinetic luminosity of $5.1 \times 10^{40} \text{ erg s}^{-1}$ for our minimum energy bicone case. This is roughly an order of magnitude below our lowest measured kinetic luminosity ($2.7 \times 10^{41} \text{ erg s}^{-1}$ for J1630+1649). The corresponding minimum mass outflow rate is $1.8 \text{ M}_\odot \text{ yr}^{-1}$. We use a horizontal line in Figure 3.7 to compare the mass outflow rate of the minimum energy bicone to the rest of our sample.

3.4.2 The biconical outflows in this sample are large and energetic

For the 18 galaxies we model, we find that the average intrinsic maximum velocity is $370 \pm 146 \text{ km s}^{-1}$, the average inner half opening angle is $44.5 \pm 11.8^\circ$, the average outer half opening angle (for those galaxies that were best fit as nested bicones or asymmetric

bicones) is $69.5 \pm 12.4^\circ$, and the average turnover radius is 3.4 ± 1.8 kpc. Our sample of moderate-luminosity AGNs ($42 < \log L_{\text{bol}} \text{ (erg s}^{-1}\text{)} < 46$) have large surface geometries due to their large half opening angles and turnover radii. This leads to large mass outflow rates ($1 < \log \dot{M} \text{ (M}_\odot \text{ yr}^{-1}\text{)} < 3$), large kinetic luminosities ($41 < \log L_{\text{KE}} \text{ (erg s}^{-1}\text{)} < 45$), and therefore large kinetic to total AGN bolometric luminosity ratios ($0.001 < L_{\text{KE}}/L_{\text{bol}} < 1.0$). In this section we compare these findings to previous work and examine assumptions made in mass outflow rate estimates in the literature.

In Figure 3.7, we plot the mass outflow rates and AGN bolometric luminosities of the galaxies in this sample against other estimated mass outflow rates from AGN-driven outflows in the literature. We also compile the mass outflow rates from the literature in Table A.15.

Our galaxies span a wide range of AGN bolometric luminosities, overlapping with low-luminosity local Seyfert galaxies (e.g., Müller-Sánchez et al. 2011; Schnorr-Müller et al. 2014) as well as high-luminosity quasars (e.g., Liu et al. 2013a; Mcelroy et al. 2015). The average mass outflow rate for the 18 galaxies modeled in this work is $\sim 10^{2.7} \text{ M}_\odot \text{ yr}^{-1}$. The mass outflow rates we derive agree with the mass outflow rates of high-luminosity AGNs and have some overlap with the mass outflow rates of moderate-luminosity AGNs. They are greater than that of samples of low-luminosity AGN outflows.

Liu et al. (2013a) and Mcelroy et al. (2015) measure the mass outflow rates of samples of high-luminosity AGN outflows and find averages of $10^{3.2}$ and $10^{2.5} \text{ M}_\odot \text{ yr}^{-1}$, respectively. Both of these studies use non-kinematic estimation techniques; they use a spherical shell assumption and $\text{H}\beta$ and $\text{H}\alpha$ luminosities to estimate a total mass outflow rate. Although they assume similar number densities for the NLR ($\sim 100 \text{ cm}^{-3}$), the non-kinematic technique can underestimate the mass entrained in the outflow. However, the use of $\text{H}\beta$ and $\text{H}\alpha$ could lead to an overestimate of the mass outflow rate, since $\text{H}\alpha$ and $\text{H}\beta$ can also trace gas associated with the disk of the galaxy. Karouzos et al. (2016) find that 60% of the kinetic energy calculated using $\text{H}\alpha$ may be unrelated to the outflow. It is unclear if the combined effect of hydrogen tracers and a luminosity-based technique result in an overestimate or an

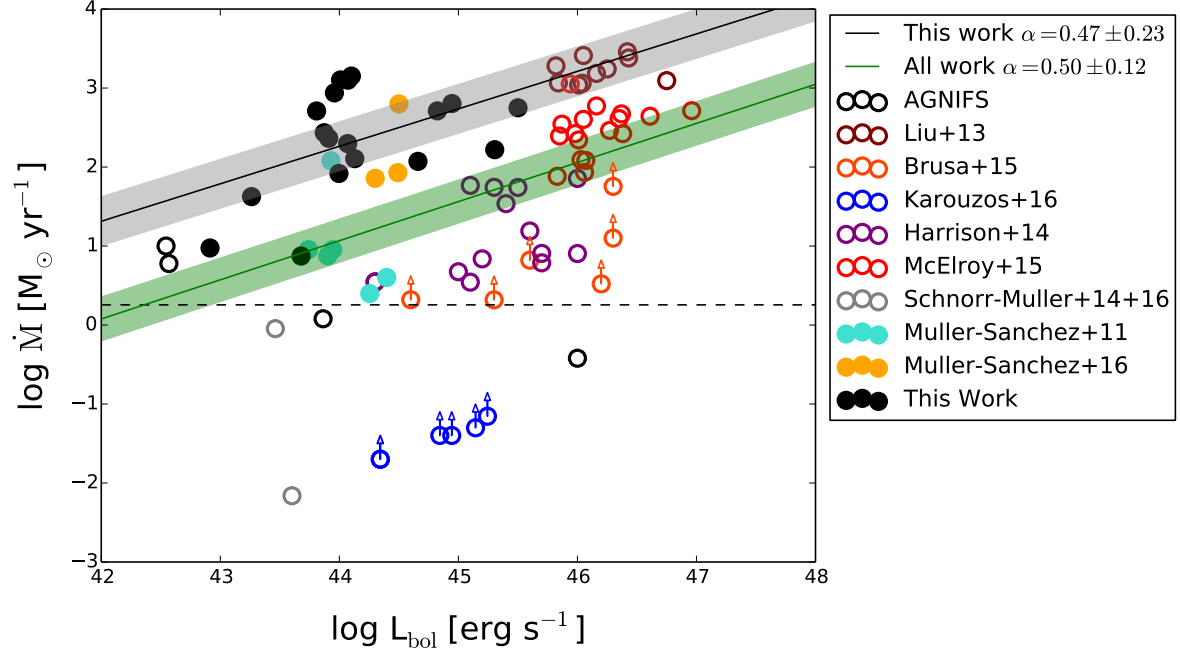


Figure 3.7: The measured mass outflow rates for AGN outflows in the literature and this work plotted against AGN bolometric luminosity. The filled circles utilize biconical kinematic models to constrain the parameters to measure mass outflow rate. The open circles assume either a spherical geometry or a biconical geometry for their outflow and emission line fluxes to estimate the material swept up in the shell. These geometries for the open circles are not kinematically constrained. We include arrows to indicate underestimation of the mass outflow rates according to the discussion in Section 3.4.2. We plot a horizontal line representing the mass outflow rate ($\sim 1.8 M_{\odot} \text{ yr}^{-1}$) associated with the minimum energy bicone discussed in Section 3.4.1. We plot a black line ($\alpha = 0.47$) and a green line ($\alpha = 0.50$) for the best fit slopes associated with this sample and all data points plotted, respectively. We overplot the confidence intervals on both lines. References include: AGNIFS (Storchi-Bergmann et al. 2010; Riffel & Storchi-Bergmann 2011a,b; Riffel et al. 2013, 2015; Schönell et al. 2014); Liu et al. 2013b,a; Brusa et al. 2015; Karouzos et al. 2016; Harrison et al. 2014; McElroy et al. 2015; Schnorr-Müller et al. 2014; Schnorr-Müller et al. 2016; Müller-Sánchez et al. 2011, 2016.

underestimate of the mass outflow rate.

Harrison et al. (2014), Brusa et al. (2015), Karouzos et al. (2016), and Müller-Sánchez et al. (2016) measure the mass outflow rates for moderate-luminosity AGN outflows and find averages of $10^{1.4}$, $10^{1.1}$, $10^{-1.4}$, and $10^{2.4} \text{ M}_{\odot} \text{ yr}^{-1}$, respectively. Again, the majority of these samples (Harrison et al. 2014; Brusa et al. 2015; Karouzos et al. 2016) use non-kinematic models. Müller-Sánchez et al. (2016) use the same kinematic technique as this work and therefore agrees most closely with the mass outflow rates estimated here. Harrison et al. (2014), Brusa et al. (2015), and Karouzos et al. (2016) use a spherical geometry and the luminosity of the $\text{H}\beta$, $[\text{OIII}]$, and $[\text{OIII}]$ emission lines, respectively. Again, a luminosity-based technique in combination with a hydrogen tracer as in Harrison et al. (2014) has an unknown effect on the estimate mass outflow rate. Karouzos et al. (2016) and Brusa et al. (2015) use a luminosity-based technique with $[\text{OIII}]$ as a tracer. This significantly underestimates the mass outflow rate of the outflow. Additionally, Karouzos et al. (2016) use an electron density of $200\text{--}800 \text{ cm}^{-3}$, which further drives down the estimate of the mass outflow rate. We calculate a mass outflow rate using the $[\text{OIII}]$ luminosities of the galaxies in our sample as in Karouzos et al. (2016) and find a rate that is a large underestimate of the mass outflow rate.

The AGNIFS group (Storchi-Bergmann et al. 2010; Riffel & Storchi-Bergmann 2011a,b; Riffel et al. 2013, 2015; Schönell et al. 2014), Schnorr-Müller et al. (2016), and Müller-Sánchez et al. (2011) find mass outflow rates for their samples of low-luminosity AGN outflows of $10^{0.5}$, $10^{-0.3}$, and $10^{1.4} \text{ M}_{\odot} \text{ yr}^{-1}$, respectively. Schnorr-Müller et al. (2016) use a biconical geometry, a higher electron density of 1350 cm^{-3} , and $\text{H}\alpha$ tracers, which have an unknown combined effect on the estimate of the mass outflow rate. Müller-Sánchez et al. (2011) use lines with higher ionization potential in the CLR to trace a fast outflow in a higher ionization phase. They also find the same ionization cones for the NLR outflows. The AGNIFS group use an electron density of 500 cm^{-3} and a similar biconical geometry to this work with HII gas to trace the outflow. This has an unknown effect on the mass outflow rate.

Interestingly, some of the AGN outflows in other work with high mass outflow rates also have double-peaked narrow emission line profiles. For instance, 19% of the galaxies in Harrison et al. (2014) and 41% of the galaxies in Mcelroy et al. (2015) have double-peaked profiles. Additionally, Liu et al. (2013a) fit multiple Gaussian components to their [OIII] λ 5007 profiles. Müller-Sánchez et al. (2016) also find significant velocity offsets in the emission lines of the three AGN outflows in their sample, so while these profiles cannot be characterized as double-peaked, they are also selected to be highly energetic outflows by selecting for a significant velocity offset in the spectral lines. While these AGN outflows are selected in a variety of ways, double-peaked or offset line profiles indicate a wide separation in velocity space and select for highly energetic outflows with large mass outflow rates as discussed in Section 3.4.1.

Despite the potpourri of different estimation techniques and therefore the large scatter in mass outflow estimates, overall, the mass outflow rate of AGN outflows increases with AGN bolometric luminosity. Therefore, the ratio of $L_{\text{KE}}/L_{\text{bol}}$ remains constant over a large range of AGN luminosities. We fit a line to all the data and find a log-log slope of $\alpha = 0.50 \pm 0.12$. When we fit a line to only the 18 galaxies from this work, we find a consistent slope of $\alpha = 0.47 \pm 0.23$. We confirm that this relationship is statistically significant using the t-statistic. We find a p-value for this statistic of 0.05, which indicates that we can reject the null hypothesis that the slope is equal to zero at 95% confidence.

This positive slope indicates a trend of increased mass outflow rate with increased AGN bolometric luminosities. An additional danger of using a non-kinematic AGN outflow model to measure mass outflow rate is that this creates an artificial positive correlation for this relationship if $L_{[\text{OIII}]}$ is included in both the calculation of mass outflow rate and L_{bol} . We repeat the slope measurement by excluding the two studies from the sample that use this technique and find a consistent slope of $\alpha = 0.50 \pm 0.10$. Therefore, since only two studies included in Figure 3.7 use [OIII] as a probe of mass outflow rate, the measured positive correlation is real and unrelated to artificial correlations from this technique.

Overall, while we find that the mass outflow rates of the galaxies in our sample are biased towards larger values (Section 3.4.1), they are broadly consistent with other AGN outflows in the literature and follow the same trend of increased mass outflow rates with increased AGN bolometric luminosities. An implication of this trend is that lower luminosity AGNs still have the potential to exceed the critical value of the energy ratio required to expel gas. This is reflected in this work; we find that the majority of biconical outflows in our work, regardless of AGN bolometric luminosity, exceed the 0.5% threshold.

3.4.3 Selection, illumination, and obscuration effects explain the best fit models

We find that 2/18 (11.1%) galaxies are best modeled as a symmetric bicone, 8/18 (44.4%) galaxies are best modeled as an asymmetric bicone, and 8/18 (44.4%) galaxies are best modeled as a nested bicone. The relative percentages of best fit models as well as the nature of the bicone walls in each model can be explained by invoking a combination of obscuration, illumination, lack of gas, and selection effects. First, we discuss that very few biconical outflows are best fit by the symmetric bicone model. Second, we consider the nature of the observed walls in the asymmetric and nested models and the implications for the structure of the general bicone model.

Only two of the 18 total galaxies are best fit by a symmetric bicone model. The lack of symmetric bicone models in this work could be explained by a more general interpretation of biconical outflows as four-walled structures with two opening angles. Some studies model a biconical outflow using a four-wall filled structure where the outer and inner walls can be described by distinct opening angles (e.g., Das et al. 2006; Müller-Sánchez et al. 2011; Crenshaw et al. 2015). Our bicones may be better described with a four-walled evacuated structure with different amounts of gas and/or illumination on various walls. We first describe the evidence for an evacuated general model of a bicone in this work. Then, we discuss other work that provides evidence of illumination and/or obscuration effects that could explain

the lack of symmetric bicone models in this work.

Das et al. (2006), Müller-Sánchez et al. (2011), and Crenshaw et al. (2015) model the bicone using an averaging process to approximate the velocity of material between the two different opening angle walls. In other words, they use a filled bicone structure. This is an acceptable approximation because the outer and inner opening angles seldom differ by more than $\sim 10\text{-}15^\circ$, so the average velocity is always close to the velocity of material along the walls of the bicone. However, in our case, $\theta_{1,\text{half}}$ and $\theta_{2,\text{half}}$ often differ by $> 20^\circ$, so this approximation is no longer valid. Instead, although the four-walled structure may exist, the selection bias that leads to large opening angle outflows and the double-peaked profiles that trace two walls necessitate a different overall model of a bicone. Therefore, we created individual models to describe bicones that have illuminated material along distinct opening angle walls. It is no longer adequate to describe a ‘filled bicone’ structure by averaging the velocity of the two opening angles because the opening angles now differ considerably.

The location of the filled material within the walls has never been investigated, although it has been hypothesized that it is very clumpy and sparsely distributed (e.g., Nenkova et al. 2008; Mor et al. 2009). Our models indicate that although the material still has a large velocity dispersion, the material is not evenly distributed between the two walls (Nevin et al. 2016). Instead, it seems to be clumped in distinct velocities around various walls of the more general four-walled structure. Additionally, since this sample includes large opening angle cones, the material is positioned at distinct lines of sight from the ionizing source (the AGN) and therefore can experience different amounts of illumination. These effects can lead to alternate bicone structures such as an asymmetric or nested bicone.

In many studies, a symmetric geometry has been preferred for kinematic modeling (e.g., Das et al. 2006; Müller-Sánchez et al. 2011; Crenshaw et al. 2015). However, other work indicates that the canonical symmetric biconical outflow structure may not be the best description for all AGN-driven outflows. For instance, Müller-Sánchez et al. (2013) find that an asymmetric bicone model is the best fit for the outflow in NGC 3081. Storchi-Bergmann

et al. (2010) model NGC 4151 using a two-walled cone structure with weaker emission from the steeply inclined wall of the cone and stronger emission from the walls that are closer to the photometric major axis. This produces an asymmetric bicone structure if the wider opening angle posterior wall is brighter. Woo et al. (2016) use a larger sample of 39,000 Type 2 AGN outflows and find that the amount of dust extinction is a main driver of the observed velocity profile. They use models of outflows with obscuration effects in the photometric major axis of the galaxy and produce a large fraction of nested and asymmetric types of biconical outflows with asymmetric integrated line profiles.

The illuminated walls in the asymmetric and nested biconical outflows can be explained by selection effects, different amounts of illumination, lack of gas, and obscuration effects. First, by selecting for double-peaked narrow emission line profiles in the SDSS spectra, we are selecting for two walls of illumination at two distinct velocities in our bicone structure. Although the general structure of a symmetric biconical outflow (Figure 3.2) has four illuminated surfaces, we are only able to select for cones in which two of these are illuminated and/or not obscured. This selection effect does not eliminate the possibility of a structure inherently having more than two walls. For instance, the third and fourth walls could be much fainter due to illumination or obscuration effects. These lower flux components are much harder to detect and could be swamped out by the emission of the brighter walls. We are therefore limited to a model of a two-walled structure due to the flux limit of the longslit data.

Second, we can analyze the best fit models to make conclusions about the obscuration of walls in our biconical outflows. Since we observe only nested cones with blueshifted walls (we observe no nested cones with two redshifted walls), this indicates that obscuration plays a key role in the observed walls of the bicone. Obscuring dust in the disk of the galaxy could be preferentially allowing us to observe the anterior walls while obscuring the two posterior walls. While it is difficult to distinguish between this obscuration scenario and a complete absence of the posterior two-walled structure associated with the general structure of a

bicone (four total walls), we find evidence that the obscuration scenario is most likely. If the absence of a side of the bicone is the better explanation, then we would expect to see equal numbers of redshifted and blueshifted nested bicones. Since we see only blueshifted bicones, obscuration is a likelier explanation than preferential illumination or lack of structure in one direction.

Third, we observe asymmetric bicones with a preferential orientation. The posterior cone always has a larger opening angle; we observe this for all eight asymmetric bicones. We can rule out obscuration effects as solely responsible for this observation. If obscuration effects were involved, we would expect to see the anterior wider opening angle wall and not the posterior wider opening angle wall.

Illumination effects explain the relative brightnesses of the velocity components of our biconical outflows but they are not the complete explanation. We expect the material in walls with lower inclinations relative to the galaxy to be brighter. Storchi-Bergmann et al. (2010) witness this illumination effect in the outflow in NGC 4151 and hypothesize that the bicone walls with high inclination relative to the line of sight are fainter. By examining the relative fluxes of the two emission components in our asymmetric bicones, we find that the majority (7/8) have a brighter integrated redshifted component. Additionally, 7/8 of the nested bicones have a brighter velocity component nearer to zero velocity (the wall with a lower inclination relative to the line of sight). Therefore, since the blueshifted wider opening angle wall has a low inclination relative to the line of sight, it is expected to be very bright. However, since we do not observe this to be the case, different illumination of various walls relative to the line of sight is not the full explanation for the lack of a blueshifted wider opening angle wall.

We can also rule out a lack of material in this blueshifted wall as the sole explanation since it is unlikely that the material is preferentially more clumpy on the side of the galaxy facing us. Therefore, the most probable explanation is a combination of an obscuration effect, an illumination effect, a lack of material effect, and a selection effect. First, the lower

inclination walls are the brightest. Second, the faint high inclination redshifted wall is most likely to be totally obscured by dust in the plane of the galaxy. Third, we select for galaxies with only two velocity peaks. This explains why we observe equal numbers of asymmetric and nested bicones. Fourth and finally, the anterior and posterior low inclination walls must be absent to observe both nested and asymmetric bicones.

Overall, by selecting for double-peaked narrow emission line profiles, we eliminated the possibility of observing more than two distinct velocity peaks corresponding to more than two walls. The presence of various walls of a general four-walled structure can be explained by obscuration effects, illumination effects, and/or lack of material in various walls.

3.4.4 The outflows have random orientations

We determine that 4/18 (22.2%) of the galaxies have a bicone axis that is aligned with the photometric major axis of the galaxy in Table A.13. The bicones are randomly oriented with respect to the photometric major axis of the galaxy. We also determine that 100% of galaxies have a bicone structure that intersects the photometric major axis of the galaxy; this measurement takes into account the large half opening angles of the bicones, which is on average 68° . A bicone with a half opening angle of 68° will cover 272° , which is 76% of the plane of the sky. Therefore, the 100% intersection percentage is unsurprising and we discuss its effect on feedback in Section 3.4.6. Here we focus instead on the implications of the orientations of the bicones in this sample both in terms of previous observations and the theory of a collimating torus.

Observations of biconical NLRs necessitate an optically thick, collimating torus that exists at parsec scales (e.g., Antonucci & Miller 1985; Mulchaey et al. 1996), but the orientation and structure of this theoretical torus remain uncertain. If Type 1 and Type 2 AGNs are to be explained by the orientation of the torus alone, the relative fraction of observed Type 1 and Type 2 AGNs require that the torus be geometrically thick ($H/R \sim 1$, H is the height and R is the radius of the torus), covering an angle of 65° as seen from the central

source (Risaliti et al. 1999). However, theory has shown that it is difficult to maintain a geometrically thick cold rotating structure even if the torus is clumpier (e.g., Krolik & Begelman 1988; Krolik 2007). Alternately, Ramos Almeida et al. (2011) fit a model of a clumpy torus to the spectral energy distributions (SEDs) of seven Seyfert galaxies and find that the torus has no preferential orientation with respect to Seyfert 1s and Seyfert 2s. Additionally, they find that a clumpy, or somewhat transparent torus is the only explanation for the observations of a BLR in NGC 7469, which has an edge-on torus. The parsec extent of the torus makes it difficult to resolve, but we can probe both the degree of clumpiness and the orientation of the torus using the alignment and opening angles of our large-scale outflows.

Observational and theoretical work has found a range of NLR outflow alignments; they are not preferentially aligned with the photometric major axis, aligned with the photometric major axis, and aligned perpendicular to the photometric major axis. For instance, some theoretical work has shown that AGN-driven outflows tend to follow the ‘path of least resistance’, emerging perpendicular to the photometric major axis of the host galaxy (e.g., Gabor & Bournaud 2014). However, other work finds no preferential orientation. Müller-Sánchez et al. (2011) and Fischer et al. (2013) find no alignment between the inclinations of a sample of Seyfert galaxies with biconical outflows and the photometric major axes of their host galaxies. Other work finds equatorial outflows that are aligned parallel to the photometric major axis of the host galaxy (e.g., Elitzur & Shlosman 2006; Riffel et al. 2014; Ricci et al. 2015).

Our findings agree with Müller-Sánchez et al. (2011) and Fischer et al. (2013), which is one of the only other large statistical studies of AGN outflows. A randomly oriented bicone structure has important implications for the theory of a collimating torus. If the torus is fully collimating and optically thick, this implies that the torus is randomly oriented with respect to the photometric major axis of the galaxy. We cannot rule out this possibility. However, since our biconical outflows have such large opening angles, this would imply a very wide opening angle for the thick molecular torus. The widest half opening angle is 82°

which implies $H/R \sim 1/7$. This is an unphysically thin torus or a torus with an unphysically large radius, so this implies that it is more likely that the torus is clumpy as opposed to thin.

3.4.5 Type 1 vs Type 2 AGNs

In addition to the orientation of the bicones with relation to the plane of the host galaxies, we also discuss the orientation of the bicone structures with relation to the line of sight (LOS) and the implications for the unification of Type 1 and Type 2 AGNs. Since the 18 bicones modeled in this sample have large inclinations and opening angles (Section 3.4.1), 100% satisfy the condition $|i| + \theta_{1,\text{half}} > 90^\circ$. We choose $\theta_{1,\text{half}}$ as opposed to the larger $\theta_{2,\text{half}}$ because the walls of the smaller inner cone more tightly constrain the LOS to the BLR. If the classification of Type 1 and Type 2 AGNs depends only on the orientation of the collimating torus, and therefore the bicone inclination and opening angle, this would imply that these are all Type 1 objects with a direct view to the BLR. However, these objects are all classified as Type 2 AGNs in SDSS and have no observed BLRs. We discuss three possible explanations for this apparent discrepancy.

If we account for the large errors on the half opening angles and inclinations measured for these bicones (the uncertainties of the parameters are discussed in Section 3.2.3), within a 3σ error margin, 50% of the bicones are consistent with $|i| + \theta_{1,\text{half}} < 90^\circ$, and therefore the bicone and/or collimating torus obscure the BLR from view. The entire sample is consistent with $|i| + \theta_{1,\text{half}} < 106^\circ$, which means that the bicone walls are consistent with being within $\sim 10^\circ$ of the LOS (90°) for the entire sample. Since we assume optically thick walls for the bicone that have a finite thickness, a LOS along the edge of a wall could obscure the BLR. It is realistic to assume that both of these parameters (i and $\theta_{1,\text{half}}$) are overestimated in the modeling for 76% and 60% of galaxies, respectively, due to asymmetric error bars. The lower limit is larger for the inclination for 76% of the 18 galaxies and 60% of the inner opening angle. However, it is unrealistic to assume that the large error bars are solely responsible for the lack of visible BLRs for all of the galaxies, so we turn towards physical explanations.

The classification of Type 1 or Type 2 objects may depend more on the intrinsic properties of the torus rather than on orientation effects related just to inclination and opening angle. Ramos Almeida et al. (2009) do not find a clear trend in the inclination of the torus with Seyfert 1s and Seyfert 2s with their SED models and find that the intrinsic properties of the torus for Type 1 and Type 2 AGNs may be different. Ramos Almeida et al. (2011) find that the Type 2 torii in their sample have larger geometric covering factors, and therefore a smaller probability of having a direct view of the BLR. They also find that Type 2 torii are intrinsically clumpier with a higher density of clouds closer to the nucleus. The clumpy torus model is supported by other work (e.g., Krolik & Begelman 1988; Krolik 2007) as well as our finding that a clumpy torus is required for the large opening angles of the bicones in this work. With a clumpy torus model, there is a finite possibility of seeing the central source at any inclination through the clumpy material (Netzer 2015). As a result, some Type 1 AGNs might have high inclination angles (edge-on line of sight to the central source), while obscuration by a large cloud could lead to a Type 2 AGN classification (e.g., Ramos Almeida et al. 2011).

Some work finds that different areas of the torus require different physical models for their structure. Davies et al. (2015) find that the inner boundary of the geometrically thick torus may be decoupled from the outer regions. The region that provides collimation of the outflow may be distinct from the region that allows a direct LOS to the BLR. This is similar to the findings of Ramos Almeida et al. (2011) that there is a higher density of clouds towards the center of the torus structure.

Finally, obscuration of the BLR can occur at a variety of spatial scales. The obscuration of the BLR need not come only from pc-scale structures such as the torus. Bianchi et al. (2012) and references therein discuss that obscuration on ~ 100 pc scales in a host galaxy can contribute to AGN obscuration. For instance, optically selected AGN samples are biased against edge-on galaxies due to dust in the plane of the galaxy (e.g., Maiolino & Rieke 1995; Lagos et al. 2011). Additionally, interferometric maps of molecular gas show evidence of a

large amount of dense gas in the 100 pc regions surrounding the AGN (e.g., Schinnerer et al. 2000; Boone et al. 2011; Krips et al. 2011). Other work has confirmed larger-scale obscuring structures that are aligned with the host galaxy plane (e.g., Gelbord et al. 2004).

While it is beyond the scope of this work to fully explore AGN unification by delving into physical modeling of the torus, BLR variability, and/or intrinsic Type 2 AGNs, it is apparent that the large half opening angles and inclinations of the biconical outflows in the sample are not consistent with a thick fully collimating torus alone (e.g., Antonucci & Miller 1985). Instead, we find that a combination of large uncertainties on our modeled parameters as well as physical structures (a clumpier torus with obscuring material on a variety of spatial scales) can explain why our galaxies are classified as Type 2 AGNs.

3.4.6 The outflows are energetic enough to drive feedback

We find that 16/18 of the biconical outflows in this sample are above the 0.5% energy threshold necessary to drive a two-staged feedback process in their host galaxy (Section 3.3.2). To investigate the implications of this further, we first discuss their outflow geometry and how they may interact with the ISM, and then we discuss indications of positive or negative feedback in the host galaxies.

As discussed in Section 3.4.4, 100% of the galaxies have a biconical structure that intersects the photometric major axis of the host galaxy. This has important implications for outflow interactions with the ISM and feedback in the host galaxy. Since these outflows have the geometrical alignment to interact with the gas in the galactic disk, the Hopkins & Elvis (2010) threshold has more physical implications. To determine if these outflows actually affect star formation in the host galaxies, we examine the star formation rates and colors of the host galaxies.

To place these galaxies in the context of AGNs in the local universe, we compare each outflow host galaxy to a control sample of SDSS galaxies that are matched in stellar mass, redshift, and AGN bolometric luminosity using the MPA-JHU (Kauffmann et al. 2003) and

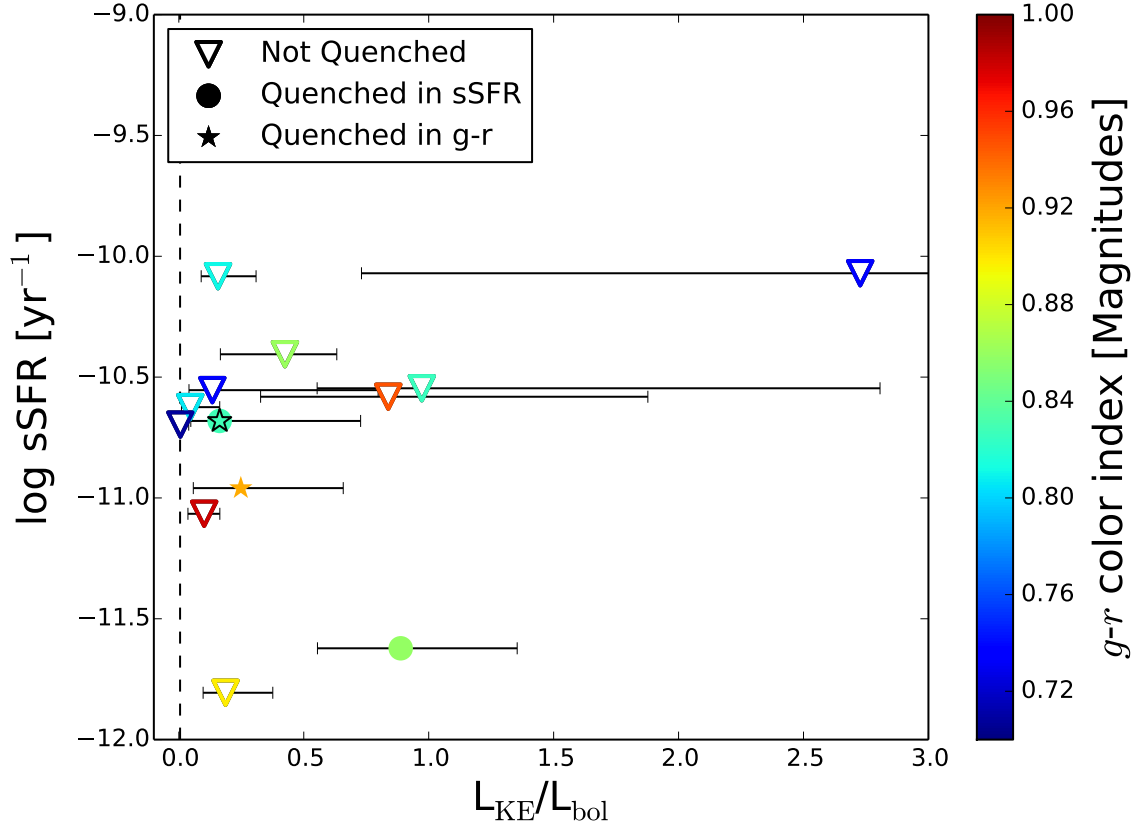


Figure 3.8: sSFR compared to kinetic to AGN bolometric luminosity ratio for 13 outflow host galaxies that have >10 comparison galaxies matched in stellar mass, redshift, and AGN bolometric luminosity (Table A.16). Filled stars denote galaxies that are quenched according to $g-r$ color, while filled circles denote galaxies that are quenched according to sSFR. Open triangles represent galaxies that are not quenched. The colorbar is the $g-r$ color index. The vertical dashed line is the 0.5% energy threshold from Hopkins & Elvis (2010) that is required to drive a two-stage feedback process.

OSSY (Oh et al. 2011) value-added catalogs. To build statistically significant (>10) control samples for most of our AGNs, we use thresholds of 20%, 20% and 50%, respectively, for stellar mass, redshift, and AGN bolometric luminosity matching. We remove four outflow host galaxies (J0009-0036, J0803+3926, J1352+0525, and J1526+4140) from this analysis due to matching control samples that were too small (<10 matches) and one galaxy (J1720+3106), for which the specific star formation rate (sSFR) could not be measured, due to artifacts in the SDSS spectrum. When we adjust the comparison thresholds by 10% in either direction to test for consistency with changing sample sizes of the comparison sample, we find the same results. Only when we increase all thresholds by more than 10% do we find that a single galaxy changes its classification from not quenched to quenched. We list the 13 galaxies that we use for the matched sample comparison of sSFR and $g-r$ color index in Table A.16.

We define a galaxy as quenched if its $g-r$ color is more than one standard deviation above the mean $g-r$ color of the comparison sample, and/or if its sSFR is more than one standard deviation below the mean sSFR of the comparison sample. We find that 3/13 (23.1%) galaxies are quenched according to either $g-r$ color or sSFR. One of these galaxies is also quenched according to both of these criteria. Of the 13 galaxies, 12 have an energy ratio that exceeds 0.5%, so 3/12 of the galaxies with an energy ratio that exceeds the threshold value are quenched in this sample. We plot the energy ratio and sSFR of these 13 galaxies in Figure 3.8 and find that there is no correlation between energy ratio and quenching. Nine galaxies have a high energy ratio but have colors and sSFRs that are consistent (within 1σ) with those of the comparison samples. Importantly, none of the galaxies in this sample have enhanced sSFR or bluer color indices relative to their comparison samples. Therefore, our analysis favors the negative feedback scenario over the positive feedback scenario for these galaxies.

For comparison, Wylezalek et al. (2016) find a negative correlation between outflow strength and sSFR for a sample of 132 AGN. This is consistent with AGN feedback operating on the host galaxies in the sample, and is most apparent for galaxies that are gas rich with

high SFRs. None of the galaxies in this work have a $\text{SFR} > 100 \text{ M}_{\odot} \text{ yr}^{-1}$, which is the cutoff for the galaxies with the most detectable negative correlation in Wylezalek et al. (2016). Since the galaxies in this work have less star formation and therefore less gas to couple with the AGN outflow, the effects of feedback may be less pronounced for the galaxies in this sample.

Overall, we find preliminary evidence for negative feedback in the galaxies in this sample. However, to fully confirm the negative feedback in these galaxies, we require detailed star formation histories or maps of the gas, e.g., with ALMA.

3.5 Conclusion

We model 18 SDSS galaxies with double-peaked narrow emission lines as AGN-driven biconical outflows using three models: a symmetric bicone, an asymmetric bicone, and a nested bicone. We find that 8/18 are best fit as asymmetric bicones, 8/18 are best fit as nested bicones, and 2/18 are best fit as symmetric bicones. These results inform us that obscuration, illumination, and our sample selection of double-peaked NLR profiles dictate the type of bicone structure observed. The results of the analytic modeling also yield the geometry and energetics associated with the ionized outflows. Based upon these results, we find that:

- (1) Our bicones have large opening angles (average $\theta_{1,\text{half}} = 44.5^{\circ}$ and average $\theta_{2,\text{half}} = 69.5^{\circ}$), large turnover radii (average 3.4 kpc), and fast intrinsic velocities (average 370 km s^{-1}). Since these galaxies have double-peaked narrow emission lines, they are biased to have larger opening angles than similar moderate-luminosity AGN outflows, and as a result they also have larger kinetic energies.
- (2) Using the geometry of the bicone structures, we find that the bicone axes have random orientations with respect to the photometric major axis of the galaxy. This implies that the torus responsible for producing the bicone structure is randomly

oriented and clumpy, where clumpiness enables radiation to escape along the plane of the torus.

- (3) We find that 16/18 (88.9%) of galaxies exceed the kinetic luminosity to AGN bolometric luminosity threshold value from Hopkins & Elvis (2010) of 0.5%, which means that they have the potential to drive a two-staged feedback process.
- (4) Of the outflows that exceed the 0.5% energy threshold, 100% intersect the photometric major axis of the galaxy on kpc-scales coincident with the location of circumnuclear star formation. They have the potential to directly deliver energy to the ISM of the galaxy.

While we can make tentative conclusions that these galaxies are quenched and thus potentially experiencing negative feedback as a result of the AGN-driven outflows, we cannot make any definitive conclusions without observations of the molecular gas. In the future, we could pursue ALMA as a means to observe the direct effect of feedback in these galaxies.

The sample of AGN outflows in this work demonstrates that moderate luminosity AGNs have the potential to drive feedback in their host galaxies. Since moderate luminosity AGNs are common in the local universe (10% of the AGN population, whereas high-luminosity AGNs are only 1% of the population), this indicates that they may play an important role in driving galaxy-SMBH co-evolution as well.

Chapter 4

Accurate Identification of Galaxy Mergers with Imaging

Merging galaxies play a key role in galaxy evolution, and progress in our understanding of galaxy evolution is slowed by the difficulty of making accurate galaxy merger identifications. We use **GADGET-3** hydrodynamical simulations of merging galaxies with the dust radiative transfer code **SUNRISE** to produce a suite of merging galaxies that span a range of initial conditions. This includes simulated mergers that are gas poor and gas rich and that have a range of mass ratios (minor and major). We adapt the simulated images to the specifications of the SDSS imaging survey and develop a merging galaxy classification scheme that is based on this imaging. We leverage the strengths of seven individual imaging predictors (*Gini*, M_{20} , concentration, asymmetry, clumpiness, Sérsic index, and shape asymmetry) by combining them into one classifier that utilizes Linear Discriminant Analysis. It outperforms individual imaging predictors in accuracy, precision, and merger observability timescale (> 2 Gyr for all merger simulations). We find that the classification depends strongly on mass ratio and depends weakly on the gas fraction of the simulated mergers; asymmetry is more important for the major mergers, while concentration is more important for the minor mergers. This is a result of the relatively disturbed morphology of major mergers and the steadier growth of stellar bulges during minor mergers. Since mass ratio has the largest effect on the classification, we create separate classification approaches for minor and major mergers that can be applied to SDSS imaging or adapted for other imaging surveys.

This chapter reproduces Nevin et al. (2019). Reproduced with permission of the AAS.

4.1 Introduction

In the current Λ cold dark matter (Λ CDM) framework for structure formation in the universe, galaxies form as gas cools at the center of dark matter halos (e.g., White & Rees 1978; White & Frenk 1991; Cole et al. 2008). These galaxies then grow through gas accretion and mergers from small, irregular galaxies with high rates of star formation to large, quiescent galaxies with lower rates of star formation in the local universe (e.g., Glazebrook et al. 1995; Lilly et al. 1995; Giavalisco et al. 1996).

Simultaneously, supermassive black holes (SMBHs), which are found at the centers of all massive galaxies, have accumulated mass over time. Both SMBHs and galaxies grow through the accretion of gas; SMBHs that are actively accreting gas are known as active galactic nuclei (AGNs) and can be among the most luminous objects in the universe. Observational correlations suggest a co-evolution between SMBHs and their host galaxies (Magorrian et al. 1998; Ferrarese & Merritt 2000; Gebhardt et al. 2000), but it remains unclear which processes are most important for triggering AGNs and star formation.

Observational work has identified three main processes that drive evolution, but disagrees on the relative import of each process. Tidal torques from major mergers (where the mass ratio of the galaxies is less than 1:4) can drive gas accretion; some work indicates that these tidal torques from major mergers are primarily responsible for fueling both star formation (Mihos & Hernquist 1994, 1996) and rapid SMBH growth (Di Matteo et al. 2005; Hopkins et al. 2005; Ellison et al. 2011; Koss et al. 2012; Treister et al. 2012; Satyapal et al. 2014). Other work suggests that minor mergers or continuous ‘cold flow’ gas accretion are the most important mechanism for shaping the morphologies of galaxies, driving star formation, and contributing to the mass growth of SMBHs (e.g., Noeske et al. 2007; Daddi et al. 2007; Cisternas et al. 2011; Kocevski et al. 2012; Kaviraj 2013; Villforth et al. 2014). Yet other studies find that secular instabilities driven by disks and spiral arms in the local universe, as well as highly irregular morphologies and high gas fractions in the high redshift universe,

can dominate galaxy evolution. These secular instabilities can grow pseudo-bulges locally and contribute to significant gas inflows and disk and bulge growth in high redshift galaxies (e.g., Bournaud 2016 and references therein). Many details of these processes that could drive evolution remain unclear, such as when and how these processes operate on AGNs and galaxies.

One main reason these details are unknown is that it is difficult to build a clean observational sample of galaxy mergers (major and minor). Imaging studies that rely upon one or a couple of imaging predictors can fail to accurately identify mergers, which leads to inconclusive results (e.g., Conselice 2014 and references therein). Recent work has relied increasingly upon non-parametric tools to identify merging galaxies from imaging surveys, such as the *Gini*- M_{20} method or the *CAS* (Concentration-Asymmetry-Clumpiness) method (Lotz et al. 2004; Conselice et al. 2003). These methods are each individually limited by different merger initial conditions, such as mass ratio and gas fraction, and by merger stage. For instance, while identifying merging galaxies using asymmetry tends to be more sensitive to early-stage mergers, *Gini*- M_{20} tends to identify late-stage mergers. Additionally, previous simulations of galaxy mergers have demonstrated that the merger observability timescale varies strongly for different non-parametric tools (e.g., Lotz et al. 2008; Lotz et al. 2010a,b).

We combine the sensitivities of different imaging predictors to create an imaging classification method that is better able to identify merging galaxies over a larger range of merger initial conditions and merger stages. In Nevin et al. (2019, in prep), we will incorporate kinematic predictors as well.

It is challenging to identify galaxy mergers directly from observations because each merger is observed at only a single viewing angle and moment in time, whereas the full duration of a merging event is several Gyr. Since the observational signatures of a merger depend so heavily on the merger initial conditions and stage of the merger, we create our classification scheme from hydrodynamics simulations that cover a range of merger initial conditions. In this way, we determine the fundamental capabilities of different imaging

predictors. We utilize the **GADGET-3** smooth-particle hydrodynamical code coupled with the **SUNRISE** dust radiative transfer code to construct mock observations of the simulated galaxies. From these mock observations, we create the imaging classification and determine its accuracy and precision for identifying galaxy mergers of different gas fractions, mass ratios, and merger stages. We tailor our classification for SDSS imaging, although the code will be publicly available and can be easily modified for different imaging surveys.

The remainder of this paper is organized as follows. We describe the hydrodynamics and radiative transfer simulations, techniques for matching the simulated galaxies to SDSS’s specifications, and merger classification scheme in Section 4.2. In Section 4.3 we describe the performance of the classification scheme and the sensitivities of the individual imaging predictors. We compare the technique to previous imaging methods for merger identification and discuss the implications for merging galaxy identification in imaging surveys in Section 4.4. We present our conclusions in Section 4.5. A cosmology with $\Omega_m = 0.3$, $\Omega_\Lambda = 0.7$, and $h = 0.7$ is assumed throughout.

4.2 Methods

We create the imaging classification scheme from simulated galaxy mergers, which we introduce in Section 4.2.1 and 4.2.2. In order to develop the classification for SDSS imaging data, we ‘SDSS-ize’ the simulations to create mockup images matching SDSS specifications in Section 4.2.3. Next, we determine the separation of the stellar bulges to assign galaxy merger stage in Section 4.2.4. Finally, we develop the imaging classification scheme using LDA (Linear Discriminant Analysis) in Section 4.2.5.

4.2.1 N-body/Hydrodynamics Merger Simulations

To develop our imaging classification scheme, we begin with a suite of simulated merging and isolated galaxies. Specifically, we use two of the high-resolution simulations from Blecha et al. (2018), to which we have added three new simulations to cover a larger param-

eter space of initial conditions. We also have a set of isolated galaxies that is matched by stellar mass and gas fraction to each merger simulation.

These simulations were carried out with **GADGET-3** (Springel & Hernquist, 2003; Springel, 2005), a smoothed-particle hydrodynamical (SPH) and N-body code that conserves energy and entropy and includes sub-resolution models for physical processes such as radiative heating and cooling, star formation and supernova feedback, and a multi-phase interstellar medium (ISM). All simulations have a baryonic mass resolution of $2.8 \times 10^4 M_\odot$ and a gravitational softening length of 23 pc. SMBHs are modeled as gravitational "sink" particles that accrete via an Eddington-limited Bondi-Hoyle (Bondi & Hoyle, 1944) prescription. AGN feedback is also incorporated by coupling 5% of the accretion luminosity ($L_{\text{bol}} = \epsilon_{\text{rad}} \dot{M} c^2$) to the gas as thermal energy. We assume a radiative efficiency $\epsilon_{\text{rad}} = 0.1$ for accretion rates $\dot{M} > 0.01 \dot{M}_{\text{Edd}}$ (where \dot{M}_{Edd} is the Eddington limit); below this we assume radiatively inefficient accretion following Narayan & McClintock (2008). **GADGET** has been used for many studies concerning merging galaxies (e.g., Di Matteo et al. 2005; Snyder et al. 2013; Blecha et al. 2011; Blecha et al. 2013).

The merger progenitor galaxies include a dark matter halo, a disk of gas and stars, a stellar bulge in some cases, and a central SMBH. The initial conditions for each simulated galaxy merger are given in Table A.18, and the initial conditions for the matched isolated galaxy simulations are given in Table A.19. In this work, we focus primarily on the effects of varying the merger mass ratio and initial gas fraction, since these two parameters have been shown to have the largest effect on the morphology and star formation rates of merging galaxies in previous work (Cox et al. 2008; Lotz et al. 2008; Lotz et al. 2010a,b; Blecha et al. 2013). We include three major merger simulations (q0.5_fg0.3, q0.333_fg0.3, and q0.333_fg0.1) with mass ratios 1:2, 1:3, and 1:3, respectively. The initial progenitor gas fractions in these simulations (defined as $M_{\text{gas,disk}}/(M_{\text{gas,disk}} + M_{*,\text{disk}})$), which are identical for both merging galaxies in a given simulation, are 0.3, 0.3, and 0.1. These major merger simulations have a bulge-to-total mass (B/T) ratio of 0. We design the two 1:3 major merger

simulations to have different gas fractions but identical mass ratios to investigate the effects of varying gas fractions on the morphology of mergers. We also create two minor merger simulations (q0.2_fg0.3_BT0.2 and q0.1_fg0.3_BT0.2), both of which have a B/T ratio of 0.2. These two minor mergers have initial gas fractions of 0.3 and mass ratios of 1:5 and 1:10, respectively. We design these two minor mergers to have a gas fraction of 0.3 so that we can directly compare mass ratios of 1:2, 1:3, 1:5, and 1:10 across simulations with identical gas fractions. We further justify our choice of initial conditions in Appendix B.3.

4.2.2 Radiative Transfer Simulations

In order to directly compare the simulated galaxies with observations, we use the 3D, polychromatic, Monte-Carlo dust radiative transfer code **SUNRISE** (Jonsson 2006; Jonsson et al. 2010) to produce resolved UV to IR spectra and broadband images.

It has been used extensively in combination with **GADGET** galaxy merger simulations (e.g., Lotz et al. 2008; Lotz et al. 2010b,a; Wuyts et al. 2010; Narayanan et al. 2010).

Age- and metallicity-dependent spectral energy distributions for each star particle are calculated using the **STARBURST99** stellar population synthesis models (Leitherer et al. 1999). Emission from HII regions (including dusty photodissociation regions) around young stars is calculated by applying **MAPPINGSIII** models (Groves et al. 2008) to newly formed star particles, based on their age, metallicity, and surrounding gas pressure. The AGN spectrum is determined using the SMBH accretion rate and the luminosity-dependent templates of Hopkins et al. (2007).

To calculate the dust distribution, we use the Draine & Li (2007) Milky Way dust model with $R_V = 3.1$ and assume that 40% of gas-phase metals are in dust (Dwek 1998). A 3D adaptively-refined grid is placed on the simulation domain to map the gas-phase metal distribution. Following Snyder et al. (2013) and Blecha et al. (2018), we assume that gas in the cold phase of the **GADGET-3** multi-phase ISM model has a negligible volume filling factor and therefore does not contribute to the attenuation of radiation. While this may not be

an appropriate choice for extremely gas-rich, high-redshift galaxies that produce extreme IR and sub-mm luminosities (e.g., Hayward et al., 2011; Snyder et al., 2013), it is a reasonable assumption for the low-redshift analog galaxy simulations in our suite.

SUNRISE performs Monte Carlo radiative transfer through this grid, computing emission from stars, HII regions, and AGN, as well as energy absorption (including dust self-absorption) to obtain the emergent, attenuated resolved SEDs for seven different isotropically distributed viewing angles.

For each merger simulation, we perform **SUNRISE** calculations on snapshots at $\sim 50 - 100$ Myr intervals during the merger. The spatial resolution of all images and resolved spectra is 167 pc, which exceeds the resolution of the SDSS survey (see Section 4.2.3). We divide each merger simulation into early-stage, late-stage, and post-coalescence snapshots based on the projected separations of the stellar bulges in the images. We describe this process in more depth in Section 4.2.4. Briefly, early-stage mergers are defined as the snapshots with average stellar bulge separations $\Delta x \geq 10$ kpc. Late-stage mergers are defined to have stellar bulges with separations of $1 \text{ kpc} < \Delta x < 10 \text{ kpc}$. Post-coalescence snapshots are those in which two stellar bulges are no longer resolvable in SDSS ($\Delta x \leq 1 \text{ kpc}$) since the spatial resolution of SDSS is 1-2 kpc. For each merger simulation, we run **SUNRISE** at ~ 100 Myr intervals in the early stage of the merging galaxies, at ~ 50 Myr intervals in the late stage, and at ~ 100 Myr intervals for the post-coalescence stage. This creates a roughly equal number of $\sim 5 - 10$ **SUNRISE** snapshots per merger stage. In Figure 4.2, we show r -band images for early-stage, late-stage, and post-coalescence snapshots from the 1:2 major merger gas-rich simulation q0.5_fg0.3.

We also simulate isolated galaxies with matched stellar mass and gas fraction for each merger simulation (Table A.19). Additionally, because the progenitor galaxies are still isolated and undisturbed in the very early stages of the merger simulations, we include snapshots prior to first pericentric passage in our sample of isolated galaxy snapshots as well. We confirm, using the supplemental outputs of **SUNRISE**, that the star formation rate and

AGN luminosity have yet to be affected by the merger in these snapshots. Additionally, the imaging predictors are not yet significantly different than the matched sample of isolated galaxies.

We also include merger snapshots at times > 0.5 Gyr after final coalescence as isolated galaxies. Our motivation for this is twofold. First, after > 0.5 Gyr following final coalescence, the simulated galaxies begin to lose tidal features but remain centrally concentrated when compared to the isolated matched sample of galaxies. If we include these post-coalescence galaxies in the analysis as mergers, the technique becomes overly sensitive to the central concentration of galaxies and is most efficient at identifying early-type galaxies. Second, since we wish to develop a tool that best identifies galaxy mergers in the early, late, and beginning of the post-coalescence stage, we terminate the merger period at 0.5 Gyr after final coalescence for all simulations. We find that this choice of cutoff time allows the sensitivity of our merger detection technique to decay smoothly during the post-coalescence stage. We include an isolated galaxy snapshot in Figure 4.2 as well as several isolated snapshots prior to first pericentric passage and 0.5 Gyr following final coalescence.

Broadband images for each snapshot are produced for seven isotropically-distributed viewpoints. We focus on the SDSS r -band filter, since the r -band is a good tracer of stellar populations in low redshift galaxies. Since we next plan to incorporate kinematic predictors into the analysis (Nevin et al. (2019, in prep)), we will apply the classification technique to the MaNGA (Mapping Nearby Galaxies at Apache Point) survey, which is an integral field spectrograph (IFS) survey of a subsample of $\sim 10,000$ SDSS galaxies. We therefore place the simulated galaxies at the average redshift of the MaNGA survey ($\langle z \rangle \sim 0.03$) and extract the r -band images, which we process further to match the specifications of the SDSS survey in Section 4.2.3.

To understand the range of redshift and surface brightness for which our merger classification can return consistent classifications, we experiment with adjusting the surface brightness and redshift of the simulated images. The consistency of the classification is

closely tied to the behavior of the imaging predictors, which are sensitive to both resolution and the average S/N per pixel ($\langle S/N \rangle$). For instance, Lotz et al. (2004) find that *Gini*, M_{20} , C , A , and S are reliable to 10% for $\langle S/N \rangle \geq 2$ and systematically decrease with $\langle S/N \rangle$ below this level. We implement a $\langle S/N \rangle$ cutoff of 2.5 (which is calculated for all pixels within the segmentation mask) because the measurements of the imaging predictors (especially A and S) from **statmorph** are unreliable below this threshold (Vicente Rodriguez-Gomez, private communication). For instance, A systematically decreases to negative values below this threshold. We also use this $\langle S/N \rangle$ cutoff value to assess the magnitude limit of the method (described below).

We find that the surface brightness of the simulated galaxies changes over the course of each simulation. This happens as the galaxies brighten and dim with star formation and AGN activity as the merger proceeds. This corresponds to a range in r -band apparent magnitude from 14 – 16 (at $z = 0.03$). We convert from surface brightness to r -band magnitude using the conversion in Section 4.2.3 to convert to units of nanomaggies, which we then convert to apparent magnitude using the Petrosian radius as the aperture. We experiment with dimming the images to determine how the r -band Petrosian magnitude of a mock image relates to the S/N per pixel. The classification becomes significantly different (since the mock images begin to drop below a $\langle S/N \rangle$ value of 2.5) when the r -band Petrosian magnitudes are ≥ 17 . In other words, the classification only works for r -band magnitudes ≥ 17 and it should not be used for fainter galaxies. For context, typical SDSS galaxies from this paper (in Section 4.13) have $\langle S/N \rangle$ values between 5-10, which corresponds roughly to r -band magnitudes of ~ 16 . Since SDSS imaging has flux limit of 17.77 in the r -band, the LDA classification technique applies to the majority of galaxies in the SDSS photometric catalog (Strauss et al. 2002).

Likewise, we move the simulated galaxies to higher redshifts while maintaining the same surface brightness and find that the predictor coefficients in the classification change significantly at $z \sim 0.5$. The average redshift of the SDSS photometric survey is $z \sim 0.4$,

so the LDA technique should still function well for the majority of SDSS galaxies (Sheldon et al. 2012).

4.2.3 SDSS-izing images from the simulations

In order to construct a classification scheme that can be applied directly to SDSS galaxies, we first ‘SDSS-ize’ or degrade the simulated images to match the specifications of the SDSS survey. In this section, we describe the relevant SDSS imaging properties and data products. Then, we provide a detailed description of the process of SDSS-izing the simulated images. Finally, we detail how we determine the stage of the merger snapshots.

The process of SDSS-izing the simulated images to create mock images that match the specifications of the SDSS imaging involves the following steps (Figure 4.1):

- (1) Clip the images.
- (2) Convolve and rebin to the spatial resolution and pixelscale of SDSS imaging.
- (3) Introduce residual background noise.
- (4) Create an error image.

To complete these steps, we utilize the imaging properties (i.e., noise, instrumental gain, sky levels, etc) of SDSS imaging, which are described in Albareti et al. (2017) and Blanton et al. (2011). The SDSS imaging procedure involves producing large field images that are composed of six long rectangular images of the sky called ‘camcols’. The camcols are then further split into individual filters (u , g , r , i , and z) and six smaller ‘frame’ images. Frame images are the basic data product of SDSS; these images are background subtracted and include an extension with background sky levels, instrumental gain, dark variance, and a calibration factor to convert between flux and photoelectrons. The frame images can be further cut to postage stamp images (in our case, with a field of view of $80''0 \times 80''0$). The most recent SDSS data release (DR13) uses a specific NASA-Sloan Atlas (NSA) reprocessing

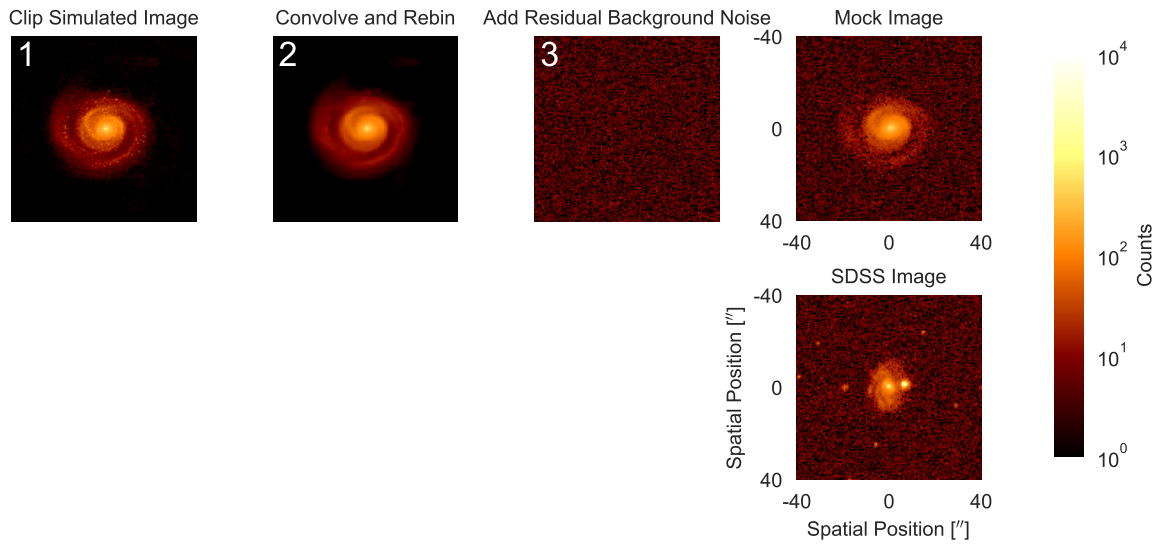


Figure 4.1: Steps of the process to create mock images from the simulated images (1-3). We first clip the simulated image to the $80''.0$ field of view (1). We then convolve the image with the $1''.43$ FWHM PSF and rebin to the $0''.396$ pixelscale of SDSS imaging (2). Finally, we add residual background noise that is characteristic of SDSS imaging (3) to create a mock image (upper right panel). We compare to a SDSS image (lower right panel) that has been centered on a galaxy and cut to the same $80''.0$ field of view as the mock image.

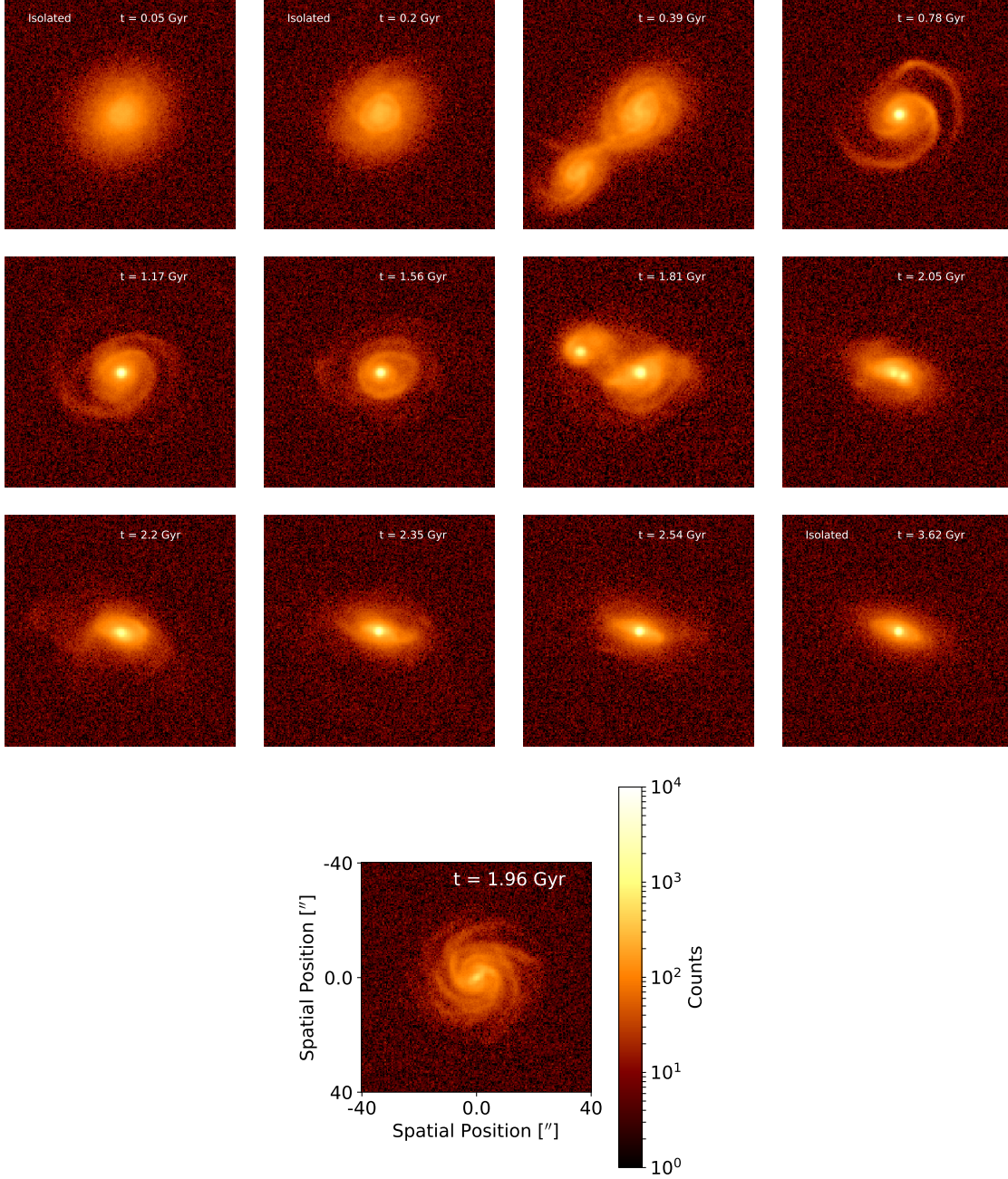


Figure 4.2: Time series of r -band ‘SDSS-ized’ images from the q0.5_fg0.3 merger simulation (mass ratio 1:2, gas fraction 0.3). To SDSS-ize simulated images, we convert to counts, convolve to the seeing limit of the survey, rebin to the SDSS imaging pixelscale, and add background noise typical of SDSS imaging. All images are centered on the brightest **Source Extractor** selected source and cut to the $80''0$ (~ 50 kpc) SDSS imaging camera field of view. The merger images at $t = 0.05$, 0.2 , and 3.62 Gyr are included as isolated galaxies in the analysis. The merger images at $t = 0.39$, 0.78 , 1.17 , and 1.56 Gyr are early-stage mergers, the images at $t = 1.81$ and 2.05 Gyr are late-stage mergers, and the images at $t = 2.2$, 2.35 , and 2.54 Gyr are post-coalescence mergers. The bottom middle image is an isolated galaxy snapshot that is matched to the q0.5_fg0.3 simulation for mass and gas fraction.

of the original SDSS DR7 imaging data, which includes a new background subtraction that improves the photometry of large galaxies (Blanton et al. 2011). We use DR13 imaging properties to compare to SDSS-ized images below. The median seeing, which is the effective width (FWHM) of the PSF, for SDSS imaging is $1''.43$ and the pixel scale is $0''.396 \text{ pix}^{-1}$ (Ivezić et al. 2004; Blanton et al. 2011).

We start with the imaging output of **SUNRISE** for the five broadband SDSS filters (u , g , r , i , z). Here, we focus on the SDSS r -band images since they best capture light from stellar bulges for nearby galaxies. To best mimic the placement of the imaging camera from SDSS, we use aperture photometry to identify the brightest pixels over which to center the camera. We identify the brightest source using **Source Extractor**, which is a useful tool to extract sources through aperture photometry on astronomical images (Bertin & Arnouts 1996). **Source Extractor** separates an object from the background noise, applies a convolution filter to separate low surface brightness sources from spurious detections, and deblends sources. We use a detection threshold of 1.5σ above the local sky background and a minimum group number of two pixels to trigger a detection. We use a normal convolution kernel with size 3×3 pixels, a FWHM of two pixels, and a deblending threshold of 32 (the recommended value for **Source Extractor**). The output from **Source Extractor** includes x and y positions of sources and aperture photometry, which includes Petrosian radii and corresponding fluxes. We determine the brightest source from these fluxes and then clip the image in a $80''.0$ square around this source. We select an $80''.0$ square cutout because it allows us to accurately determine the image background for the extraction of the imaging predictors. Some of our simulations snapshots have smaller fields of view (down to $50''.0$) since the simulated galaxies are in the edge of the simulation field of view. We include these smaller snapshots in interest of maximizing the temporal resolution of our method. We find that very few mock images have a smaller field of view than $80''.0$ and that this does not affect the imaging predictors for these snapshots.

After clipping the mock images, we convolve them with a PSF with FWHM $1''.43$, which

is the median PSF for the r -band (Ivezić et al. 2004). Then, we rebin the images to the pixelscale of SDSS ($0''.396 \text{ pixel}^{-1}$).

We then convert to flux units typical of SDSS, introduce residual background noise, and produce an error image, as outlined below. The units of the simulated image are surface brightness ($\text{W/m/m}^2/\text{sr}$). We convert to flux density in nanomaggies:

$$\text{nanomaggy} = \text{Janskys} \times 3.631 \times 10^6$$

where we first convert to Janskys using the pixelscale and angular diameter distance of a simulated galaxy at the average redshift of the MaNGA survey, $z \sim 0.03$. Again, we use the average redshift of the MaNGA survey since we plan to further develop the kinematic technique for MaNGA IFS in Nevin et al. (2019, in prep).

Then, we extract a nanomaggy to data number (dn) conversion rate from each frame image (c). This conversion rate is used to produce a mock image in units of counts (from here on dn is synonymous with counts). We find an average c value of 0.005 with a standard deviation of 0.0002. The conversion rate varies little across the frames and camcols.

In order to introduce background noise to the mock images, we characterize the residual background of the SDSS frame images using bilinear interpolation. We also determine other imaging properties such as background sky levels (prior to background subtraction), instrumental gain, and dark variance from the frame images. Since the gain and background sky levels vary in complicated ways across the frames and camcols (Michael Blanton, private communication), we characterize these values based upon several locations from the larger frame images.

For instance, we use 50 postage stamps (from the frame images) that are selected to belong to all six camcols and locations on the frame images. We extract a region from the background and characterize its mean and standard deviation. The postage stamp images have already been background-subtracted, so this region is characteristic of the residual background of SDSS images following the sky subtraction step. We find that the typical

residual background has a mean of 0.33 dn (counts) with a standard deviation of 5.63 dn. After conducting an improved background subtraction for the SDSS-III DR8 imaging data (which is the same imaging reduction used for DR13), Blanton et al. (2011) find a residual standard deviation of 0.02 nanomaggies in the r -band photometry. This is ~ 4 dn, so our standard deviation of 5.63 dn is a good approximation of the residual noise.

We reintroduce this background into our images by adding a standard normal with a mean of 0.33 and a standard deviation of 5.63 dn to each pixel. This mock image is used in the calculation of the imaging predictors in Section 4.2.5.1. We use both the conversion factor, c , and the residual background value, bg_{resid} , to produce an image that is representative of a SDSS image (in counts):

$$\text{dn} = \text{nanomaggies}/c + \text{bg}_{\text{resid}}$$

We use the images in units of dn for display purposes and for the extraction of the imaging predictors.

Finally, we create an error image. To calculate the photometric uncertainty, we use the average gain and dark variance from the r -band frame images (4.7 photoelectrons per dn and 1.2 dn^2 , respectively) in combination with the simulated galaxy image to produce an error image in dn:

$$\sigma_{\text{dn}} = \sqrt{(\text{dn} + \text{bg}_{\text{sky}})/\text{gain} + \text{darkvar}}$$

where we also include the background counts prior to background subtraction (bg_{sky}). The photometric uncertainty is dominated by the galaxy flux except for low surface brightness features such as tidal tails, where the background sky dominates. To determine the background sky level, we extract a region from each sky image and measure the average value. We find that this value varies between frame images and that the mean background value is 121.2 dn with a standard deviation of 37.4.

Figures 4.1 and 4.2 show examples of simulated images after the image has been spa-

tially convolved, rebinned, and the residual background has been introduced to match the specifications of the SDSS survey.

4.2.4 Measuring Stellar Bulge Separations

We use **Source Extractor** and **GALFIT** (Bertin & Arnouts 1996; Peng et al. 2002) to identify, pinpoint, and measure the separation of stellar bulges from the SDSS-ized r -band images. Using **Source Extractor**, we first determine if there are one or two stellar bulges within the field of view and pinpoint their locations. We eliminate spurious detections from **Source Extractor** using the above prescription for a detection threshold (1.5σ above sky) combined with a normal convolution kernel (a 3×3 pixel mask with a FWHM of 2 pixels). We avoid the detection of star forming regions by requiring that the flux within the measured Petrosian radius of the secondary source be greater than 10% of the primary source.

Under these prescriptions **Source Extractor** performs well, detecting the primary and secondary stellar bulges for four of the merger simulations without spurious detections or detections of star forming regions. To ensure that **Source Extractor** is not detecting star forming regions, we require that the location of the regions identified by **Source Extractor** correspond to the locations of the SMBHs tracked by **GADGET**.

Source Extractor fails to accurately identify the secondary source for the q0.1-fg0.3-BT0.2 simulation. Since we require that the flux of the secondary source detected by **Source Extractor** be greater than 10% of the flux of the primary source, the 1:10 minor merger often falls below this level. We do not lower the 10% detection cutoff since we wish to avoid star forming region detection, so we use the locations of the SMBHs for the q0.1-fg0.3-BT0.2 simulation to identify the secondary sources in order to determine merger stage.

Then, we use **GALFIT**, which is a two-dimensional fitting algorithm that extracts structural components from images of galaxies. It can fit one or more two-dimensional models such as exponential disks, Sérsic profiles, Gaussian profiles, or Moffat functions to the light

profile of a galaxy. We use **GALFIT** to fit a Sérsic profiles to each source identified by **Source Extractor** and extract the projected separations of the stellar bulges (if there are two). With the **GALFIT** output in hand, we average the projected separation of the stellar bulges for all viewpoints of a given snapshot of a merger and use this average to determine the merger stage. Again, if the average separation is $\Delta x \geq 10$ kpc the merger is early-stage, if the separation is $1 \text{ kpc} < \Delta x < 10 \text{ kpc}$ the merger is late-stage, and separations $\Delta x \leq 1 \text{ kpc}$ are post-coalescence.

4.2.5 Creating the Classification Scheme

Using the simulated galaxies, we know a priori whether a galaxy is a merging or nonmerging galaxy. In this section, we discuss the preparation of the imaging parameters that we use as an input to a supervised Linear Decomposition Analysis (LDA). We refer to these imaging parameters as ‘predictors’ from here on because they help predict whether a galaxy is undergoing a merger. We also describe the LDA technique, which allows us to determine which imaging predictors are critical for best separating the classes of merging and nonmerging galaxies for each simulation.

4.2.5.1 Imaging Predictors

In this section, we first describe the imaging predictors and then the methods used to extract them from the SDSS-ized galaxy images. We discuss their weaknesses and strengths; no one imaging predictor is the best determination of a merging galaxy. Instead they are sensitive to different orientations, merger stages, and mass ratios. The statistical power of the LDA methodology allows us to select the most successful predictors for various types of merging systems. We discuss these results in Section 4.3.

There are two main approaches to identifying a galaxy merger from imaging: parametric and nonparametric modeling of the surface brightness of the galaxy image. The parametric approach requires modeling the surface brightness of the galaxy using integrated

light profiles such as bulges, disks, or Sérsic profiles. Since parametric modeling tends to assume a symmetric profile for the surface brightness of a galaxy, it fails for irregular galaxies as well as those with structures such as compact nuclei, spiral arms, or bars (Lotz et al. 2004). More recent work on merger identification has focused on nonparametric modeling of the surface brightness of galaxies. Nonparametric tools can be applied to irregular galaxies as well as the more standard early or late Hubble-type galaxies. We employ two widely used nonparametric approaches as imaging predictors: the *CAS* (concentration (C), asymmetry (A), and clumpiness/smoothness (S)) morphological classification technique and the *Gini* - M_{20} method. We also use a binary variation of A , shape asymmetry (A_S) from Pawlik et al. (2016). Finally, we incorporate one parametric approach, the Sérsic index (n). Overall, we utilize seven different imaging predictors, defined below: *Gini*, M_{20} , C , A , S , n , and A_S .

Concentration is defined by Lotz et al. (2004) as the ratio of light within circular radii containing 80% and 20% of the total flux of the galaxy:

$$C = 5 \log\left(\frac{r_{80}}{r_{20}}\right)$$

where r_{80} is the circular radius that contains 80% of the total flux, and r_{20} is the circular radius that contains 20% of the total flux. We use the approach from Conselice et al. (2003) that defines the total flux as that within 1.5 Petrosian radii (r_p) of the galaxy's center. We measure the Petrosian radius using **Source Extractor**.

A galaxy with a higher value for C has more light contained within the central regions of the galaxy and is therefore more likely to be an early-type galaxy.

The imaging rotational symmetry predictor, A , is from Conselice et al. (2000):

$$A = \sum_{ij} \frac{|I(i,j) - I_{180}(i,j)|}{|I(i,j)|} - \sum_{ij} \frac{|B(i,j) - B_{180}(i,j)|}{|I(i,j)|}$$

where asymmetry is summed over all pixels (i,j) , $I(i,j)$ is the image, $I_{180}(i,j)$ is the image rotated by 180° about the center, $B(i,j)$ is the background image (the background image is described in Section 4.2.3 and includes only the residual background typical of SDSS imaging

following background subtraction), and B_{180} is the background image rotated by 180° about the same center. We define the center of the galaxy as the location that minimizes the value of asymmetry as in Lotz et al. (2008). Again, the galaxy image and background image are both masked to $1.5 r_p$.

A galaxy with a higher value of A has disturbed structure and/or bright tidal tails and is therefore more likely to be a galaxy undergoing a merger. A is particularly good at identifying early-stage merging galaxies (following first pericentric passage) when the structure of a merging galaxy is most disturbed and tidal tails are most prominent.

The shape asymmetry, A_S is measured using the same procedure as the asymmetry, but with a binary detection mask. The technique is described in detail in Pawlik et al. (2016) and Rodriguez-Gomez et al. (2018). Since it is measured using a binary mask, A_S is more sensitive to low surface brightness tidal features than A .

Clumpiness or smoothness (S) is defined by Conselice et al. (2003) and Lotz et al. (2004) to be the fraction of light within clumpy distributions in a galaxy:

$$S = \frac{\sum_{ij} |I(i, j) - I_S(i, j)|}{|I(i, j)|} - B_S$$

where $I(i, j)$ is the image and $I_S(i, j)$ is the smoothed image which is smoothed using a boxcar of width $0.25 r_p$. B_S is the average smoothness of the background calculated in a 10×10 pixel box using the same $0.25 r_p$ boxcar. S is summed over all pixels (i, j) within $1.5 r_p$ of the galaxy's center. However, the pixels within $0.25 r_p$ of the galaxy center are excluded for the calculation of S because the central regions of galaxies are highly concentrated and this elevates the value of S (see Conselice et al. 2003).

Since S measures the fraction of light from a galaxy that can be found in clumpy distributions, it identifies merging galaxies that have recently undergone star formation (e.g., Conselice et al. 2003). For instance, galaxies with a low value of S tend to be elliptical galaxies and galaxies with a high value of S are either undergoing mergers (with star formation) or

undergoing bursty star formation without experiencing a merger event.

The *CAS* morphological classification system was put forth as a method for cleanly separating galaxies based on their morphologies using their location in *CAS* space. However, it is limited in several ways. First, concentration assumes circular symmetry and therefore fails for some irregular galaxies (Lotz et al. 2004). For instance, Conselice et al. (2003) find that the average value of C for ULIRGs (ultraluminous infrared galaxies; $L_{\text{IR}} > 10^{12} L_{\odot}$) is not significantly different from that of Hubble sequence galaxies. This is problematic for merger identification since a significant fraction of ULIRGs (at least in the local universe) are gas rich major mergers (e.g., Veilleux et al. 2002; Draper & Ballantyne 2012). Second, not all mergers are asymmetric, and not all asymmetric galaxies are mergers (Thompson et al. 2015). Third, clumpiness is very dependent on the choice of boxcar width (smoothing length) used to smooth the image (Andrae et al. 2011), which has not been studied in detail. In this work, we find that clumpiness is most sensitive to viewing angle and therefore a poor merger predictor, so while we include it in the analysis, we focus more on concentration and asymmetry. This decision is supported by previous findings that focus on C and A alone from the *CAS* morphology (e.g., Lotz et al. 2008).

The *Gini* coefficient is used to describe the relative concentration of light in a galaxy and is insensitive to whether the light lies at the center of the galaxy. *Gini* is sensitive to major and minor mergers and is most sensitive for face-on systems (Thompson et al. 2015). *Gini* is defined by Abraham et al. (2003) and Lotz et al. (2004) as:

$$Gini = \frac{1}{|\bar{f}|n(n-1)} \sum_i^n (2i - n - 1) |f_i|$$

where \bar{f} is the average flux value, n is the number of total pixels in the image, and f_i is the flux value for each pixel where the n pixels are ordered by brightness in the summation.

Gini is high for galaxies with very bright single or multiple nuclei and low for galaxies with more distributed light, such as late-type disk galaxies. Therefore, a higher value of

Gini will select for merging galaxies during late stage mergers (with multiple bright nuclei) as well as post-coalescence merging galaxies.

The M_{20} coefficient is often combined with *Gini* to identify merging galaxies. It measures the relative concentration of the light in a galaxy and also does not assume a central concentration. The second-order moment of the light in a galaxy (M_{tot}) is the sum of the flux in each pixel, f_i , multiplied by the distance squared to the center of the galaxy:

$$M_{\text{tot}} = \sum_i^n M_i = \sum_i^n f_i [(x_i - x_c)^2 + (y_i - y_c)^2]$$

where M_i is the flux in a single pixel multiplied by the distance squared to the center of the galaxy. The center (x_c, y_c) is chosen to minimize the value of M_{tot} . M_{tot} is a tracer for the spatial distribution of any bright areas in the galaxy. M_{tot} is then used to compute M_{20} , which is defined by Lotz et al. (2004) to be the normalized second order moment of the brightest 20% of the galaxy's flux:

$$M_{20} = \log_{10} \left(\frac{\sum_i M_i}{M_{\text{tot}}} \right), \text{ while } \sum_i f_i < 0.2 f_{\text{tot}}$$

where f_{tot} is the total flux of all of the pixels that are identified by the segmentation map (defined below), and f_i are the fluxes rank ordered from brightest to faintest. The division by M_{tot} removes all dependence on the total galaxy flux.

M_{20} is similar to C but the center of the galaxy is a free parameter, allowing it to be more sensitive to spatial variations of light. Also, M_{20} is always a negative value due to the logarithm. Clear mergers with multiple bright nuclei have higher values of M_{20} ($M_{20} > -1$) and early-type galaxies have lower values ($M_{20} \leq -2$; Lotz et al. 2008). Therefore, higher values of M_{20} select for merging galaxies.

Since *Gini* and M_{20} are sensitive to the ratio of low surface brightness pixels to high surface brightness pixels, we use a segmentation map to measure both of these predictors, as in Lotz et al. (2008). The segmentation map assigns pixels to the galaxy that are above the threshold value given by the surface brightness at the Petrosian radius. We use a seg-

mentation map instead of making S/N cuts, because galaxies with the same morphologies but different intrinsic luminosities will have different *Gini* values if the cut is made based on S/N.

In addition to the *CAS* and *Gini*– M_{20} nonparametric predictors, we measure the shape asymmetry (A_S) for each galaxy. Shape asymmetry is similar to the imaging asymmetry we also describe above; it is calculated using the same method, but with a binary detection mask instead of the image itself. This weights all parts of the galaxy equally regardless of relative brightness, making it a useful probe of morphological asymmetry (as opposed to the asymmetry of the light distribution). It has proven useful for detecting faint asymmetric tidal features that are suggestive of a merger (Pawlik et al. 2016).

Our final imaging predictor is the Sérsic index, which is used to define the exponential surface brightness profile of a galaxy:

$$I(R) = I_e \exp\left(-b_n \left[\left(\frac{R}{R_e}\right)^{1/n} - 1\right]\right)$$

where $I(R)$ is the intensity within a given circular radius, I_e is the intensity at the effective radius (R_e), which is the radius that contains half of the total light, and b_n is a constant that depends on the Sérsic index, n (Sérsic 1963).

A Sérsic index of $n = 1$ denotes an exponential disk, indicative of a spiral galaxy, while $n = 4$ denotes a de Vaucouleurs profile, indicative of an elliptical galaxy. In general, higher n indicates light that is more centrally concentrated. A division between morphologies has been standardized as $n \lesssim 2.5$ for spirals and $n \gtrsim 2.5$ for ellipticals (van der Wel et al. 2008). Fisher & Drory (2008) predict that values of $n > 2$ (steeper surface brightness profiles) are produced by major mergers.

To extract the values of *Gini*, M_{20} , C , A , S , and A_S for each galaxy, we utilize the galaxy morphology tool **statmorph** (Rodriguez-Gomez et al. 2018). Within this tool, we invoke the segmentation map defined from the surface brightness at $1.5r_p$, which is measured using **Source Extractor**. We measure the value of n for each galaxy with **GALFIT**.

4.2.5.2 Identifying Mergers with Imaging Predictors

We seek a classifier that can separate merging and nonmerging galaxies of various merger mass ratios, gas fractions, viewing angles, and merger stages. We also need to incorporate multiple different imaging predictors. LDA is uniquely suited for these purposes. LDA is able to maximize the separation between multiple classes (in our case, we only need to separate two classes, ‘merging’ vs ‘nonmerging’ galaxies). In this work, we use LDA as a classifier. Here, we train LDA on our SDSS-sized simulation data to determine the most important imaging predictors for each simulation. Then, we combine all simulated galaxies to prepare an LDA classifier. In a subsequent paper, we will apply the LDA classifier to the SDSS galaxies.

Past work on simulated galaxies has shown that the effectiveness of the imaging predictors depends strongly on merger stage, the initial mass ratio, and the gas fraction of the merging galaxies (Lotz et al. 2008; Lotz et al. 2010a,b). We therefore run LDA for each simulation individually so that we can compare the LDA outputs from different merger initial conditions. In this way, we are able to compare the sensitivity of different imaging predictors for minor and major mergers with low and high gas fractions at three different merger stages (early, late, post-coalescence). For each iterative LDA run, we use simulated nonmerging galaxies that are matched for gas fraction and stellar mass to the merging galaxies, since Lotz et al. (2010b) find that gas fraction can alter the performance of *CAS* and *Gini* – M_{20} . We therefore approach the LDA classification with a set of galaxies for which we know a priori if a galaxy belongs to the nonmerging (0) or merging (1) class. We include enough nonmerging galaxies to roughly balance the number of merging galaxies. Our motivation is to achieve an accurate LDA classification by ensuring that the isolated galaxies cover a realistic range of imaging predictor space and roughly balance the number of galaxies in the merging class. We later account for the lack of merging galaxies in nature with a prior (described below). We use disk-dominated simulated galaxies to create the LDA, so it is important to note that

this classification technique is most applicable to galaxies with similar properties.

The purpose of LDA is to use Bayesian likelihood to calculate a posterior probability that a galaxy belongs to a given class (for a review of LDA, see James et al. 2013):

$$p(\pi_0|x) = \frac{e^{\hat{\delta}_0(x)}}{e^{\hat{\delta}_0(x)} + e^{\hat{\delta}_1(x)}} \quad (4.1)$$

where π_0 is the prior probability of the nonmerging class (described below), $\hat{\delta}_0$ is the score of the nonmerging class, and $\hat{\delta}_1$ is the score of the merging class. The score is the relative probability that the galaxy belongs to a class, so a galaxy will be classified into the class that has the maximum score. This classifier is nonbinary; instead of classifying galaxies as simply nonmerging or merging, we will assign a probability that a galaxy belongs to each class.

When there is only one input predictor, the discriminant score for the nonmerging class is defined as:

$$\hat{\delta}_0(x) = x \cdot \frac{\hat{\mu}_0}{\hat{\sigma}^2} - \frac{\hat{\mu}_0^2}{2\hat{\sigma}^2} + \log(\hat{\pi}_0)$$

where $\hat{\delta}_0(x)$ is the discriminant score for class 0 (the nonmerging class) for a set of galaxies, x is the list of the one measured predictor value for all simulated galaxies, $\hat{\mu}_0$ is the mean vector for the predictor for the nonmerging class, $\hat{\sigma}^2$ is the variance of the predictor for the nonmerging class, $\log(\hat{\pi}_0)$ is the prior probability of belonging to the nonmerging class, and $\hat{\delta}_1(x)$ is defined the same way but for mergers.

For the priors of the two classes for the major mergers, we use $\hat{\pi}_0 = f_{nonmerg} = 0.9$ and $\hat{\pi}_1 = f_{merg} = 0.1$ based on the fraction of nonmerging and merging galaxies from observations and simulations (e.g., Rodriguez-Gomez et al. 2015; Lotz et al. 2011; Conselice et al. 2009; López-Sanjuan et al. 2009; Shi et al. 2009). We use $\hat{\pi}_0 = f_{nonmerg} = 0.7$ and $\hat{\pi}_1 = f_{merg} = 0.3$ for the minor mergers since minor mergers are 3-5 times more frequent in the local universe (e.g., Bertone & Conselice 2009; Lotz et al. 2011). We find that the LDA analysis is relatively insensitive to the chosen priors within a range of values ($0.1 < f_{nonmerg} < 0.9$). For a full discussion of priors see Appendix B.4.

For multiple predictor variables (seven in our case), the LDA score can be generalized:

$$\hat{\delta}_0(x) = x^T \Sigma^{-1} \hat{\mu}_0 - \frac{1}{2} \hat{\mu}_0^T \Sigma^{-1} \hat{\mu}_0 + \log(\hat{\pi}_0)$$

where x , Σ , and $\hat{\mu}_0$ are now vectors for the values of the predictors, covariance matrix, and mean value of each predictor, respectively. LDA assumes that the data are normally distributed, that the input predictors are independent, and that each class has identical covariance matrices. The homogeneity of covariance matrices assumption leads to the simplification: $\Sigma_0 = \Sigma_1 = \Sigma$. We examine these statistical assumptions in more detail in Appendix B.5.

We classify a galaxy as ‘nonmerging’ if $\hat{\delta}_0 > \hat{\delta}_1$ and ‘merging’ if $\hat{\delta}_1 > \hat{\delta}_0$. Since we are working in a multi-dimensional space, this is equivalent to searching for the dividing hyperplane that satisfies:

$$x^T \Sigma_0^{-1} \hat{\mu}_0 - \frac{1}{2} \hat{\mu}_0^T \Sigma_0^{-1} \hat{\mu}_0 + \log(\hat{\pi}_0) = x^T \Sigma_1^{-1} \hat{\mu}_1 - \frac{1}{2} \hat{\mu}_1^T \Sigma_1^{-1} \hat{\mu}_1 + \log(\hat{\pi}_1)$$

The terms with the covariance matrices can be expanded fully out to yield a quadratic classifier, as is done in Quadratic Discriminant Analysis (QDA). We assume the equality of covariance matrices, which means the covariances between predictors are roughly equivalent for the nonmerging and merging class ($\Sigma_0 = \Sigma_1$). This assumption yields a linear classifier (LDA):

$$\Sigma^{-1}(\mu_0 - \mu_1) + \frac{1}{2} \mu_0^T \Sigma^{-1} \mu_0 + \frac{1}{2} \mu_1^T \Sigma^{-1} \mu_1 + \log\left(\frac{\hat{\pi}_0}{\hat{\pi}_1}\right) = 0$$

We solve for the hyperplane that satisfies the above equation, LD1:

$$\text{LD1} = \hat{w}^T \vec{x} + \hat{w}_0 = 0$$

where the slope, \hat{w} , is the weight vector:

$$\hat{w} = \Sigma^{-1}(\mu_0 - \mu_1)$$

and the intercept is given by \hat{w}_0 :

$$\hat{w}_0 = \frac{1}{2}\mu_0^T \Sigma^{-1} \mu_0 + \frac{1}{2}\mu_1^T \Sigma^{-1} \mu_1 + \log\left(\frac{\hat{\pi}_0}{\hat{\pi}_1}\right)$$

LD1 is also known as the first discriminant axis. Since we have only two classes (merging and nonmerging) to separate in this analysis, the second, third, and so on discriminant axes are unnecessary. Instead, we are able to focus only on one hyperplane to separate the populations.

We run the LDA on the imaging input predictors, which are the *Gini*, M_{20} , C , A , S , n , and A_S . We specifically utilize the python package `sklearn` for this analysis. By focusing on the imaging predictors, our goal is to produce a result that is useful for observational samples of galaxies with imaging only. Since the imaging predictors are cross-correlated, meaning that combinations of two of the predictors have a linear relationship with one another (Appendix B.5), we also include ‘interaction’ terms which are multiples of all combinations of the imaging predictors (e.g., $Gini * M_{20}$, $Gini * C$, $Gini * A$, etc). We refer to these as ‘interaction’ terms, but they can be better thought of as multiplicative terms that allow us to explore the synergistic effects of combining predictors. These interaction terms allow us to remove cross-correlation effects from the original ‘primary’ (*Gini*, M_{20} , C , A , S , n , and A_S) imaging predictors. We can then directly explore how these primary imaging predictors affect the classifier in Section 4.3.1.

Including the interaction terms, we have 34 input terms for each run of LDA. Therefore, we first use forward stepwise selection with k –fold cross-validation to select the best input variables for each simulation. In brief, forward stepwise selection proceeds by introducing one predictor at a time; we choose the number of predictors that minimizes the number of misclassifications determined with cross-validation. We specifically implement k –fold cross-validation, which is a method to divide the full sample of merging and nonmerging galaxies (for each run) into k equally sized subsamples, where $k = 10$. We then train the LDA on nine of the subsamples, and test on the tenth sample. We repeat this procedure ten times,

and the mean number of misclassifications all ten test samples allows us to decide which set of input predictors to select. We proceed, adding one predictor at a time, until the minima of the misclassifications is determined. We describe this process in more detail in Appendix B.6.

The input predictors that are selected by the forward stepwise selection are given in Tables A.20 and A.21, along with their coefficient values and standard errors from the LDA run. The standard errors are obtained using k -fold cross-validation (Appendix B.6). If a predictor is selected by the forward stepwise selection but the 3σ standard error indicates that it is consistent with zero, we eliminate it from the selected predictors. We refer to the remaining imaging predictors and imaging predictor interaction terms as ‘required’ predictors henceforth because they are necessary to separate the merging galaxies from the nonmerging galaxies along LD1 for each simulation. LD1 is a linear combination of the selected input imaging predictors and interaction terms, with weights \hat{w} and intercept term \hat{w}_0 . Each element of \hat{w} corresponds to an imaging predictor or interaction term, and their relative absolute values represent their degree of importance to the classification. We report and interpret these coefficients, their relative signs, and their order of importance in Section 4.3.

After running LDA on each simulation individually, we assess their differences in Section 4.4.3 and 4.4.4. Since the major and minor merger LDA runs are significantly different, we caution against combining all runs into one overall classifier. We do attempt, however, to combine all simulations into one classifier and find that it does not adequately separate merging from nonmerging galaxies for all merger simulations. Instead, we create two classifiers, one from the combined major merger simulations and one from the combined minor merger simulations, that will be used to classify the SDSS galaxies. They could also function as a diagnostic tool to determine the mass ratio of the merging galaxies.

In subsequent work, we will calculate the value of LD1, or the score of a given galaxy, using the linear combination of the terms from \hat{w} and the input predictors and \hat{w}_0 given in Section 4.3. For example, LD1 for the combined overall run for major mergers is:

$$\begin{aligned}
\text{LD1}_{\text{major}} = & 0.69 \text{ Gini} + 3.84 C + 5.78 A + 13.14 A_S \\
& - 3.68 \text{ Gini} * A_S - 6.5 C * A_S - 6.12 A * A_S \\
& - 0.81
\end{aligned} \tag{4.2}$$

where all predictor inputs must be standardized before using this equation. To standardize, we subtract the mean and divide by the standard deviation of the set of all predictor values.

Likewise, LD1 for the minor merger combined simulation is:

$$\begin{aligned}
\text{LD1}_{\text{minor}} = & 8.64 \text{ Gini} + 14.22 C + 5.21 A + 2.53 A_S \\
& - 20.33 \text{ Gini} * C - 4.32 A * A_S \\
& - 0.87
\end{aligned} \tag{4.3}$$

The decision boundary for LD1 for the major merger combined run is 1.16 and 0.42 for the combined minor merger run; all galaxies with values of LD1 greater than this value will be classified as merging. This decision boundary is the halfway mark between the mean of the merging and nonmerging galaxy distributions. From here on, we use ‘LD1’ to describe the linear combination of predictor coefficients for each run of LDA.

LD1 is a hyperplane, so it is unable to capture complicated non-linearities in the imaging predictors. For instance, there is some migration for different merger stages that occurs for predictors such as M_{20} , where merging galaxies occupy different regions of predictor space for different phases of the merger. Since the LDA captures the bulk behavior of each imaging predictor, it searches for the overall trend for all stages within each merger simulation and is unable to describe these non-linearities.

LDA adequately separates nonmerging from merging galaxies. For instance, Figure 4.3 presents the histograms for the imaging predictors for all simulations, and it is clear that the imaging predictors are each individually unable to separate the populations of merging and nonmerging galaxies. After performing LDA, we find that we are able to more cleanly

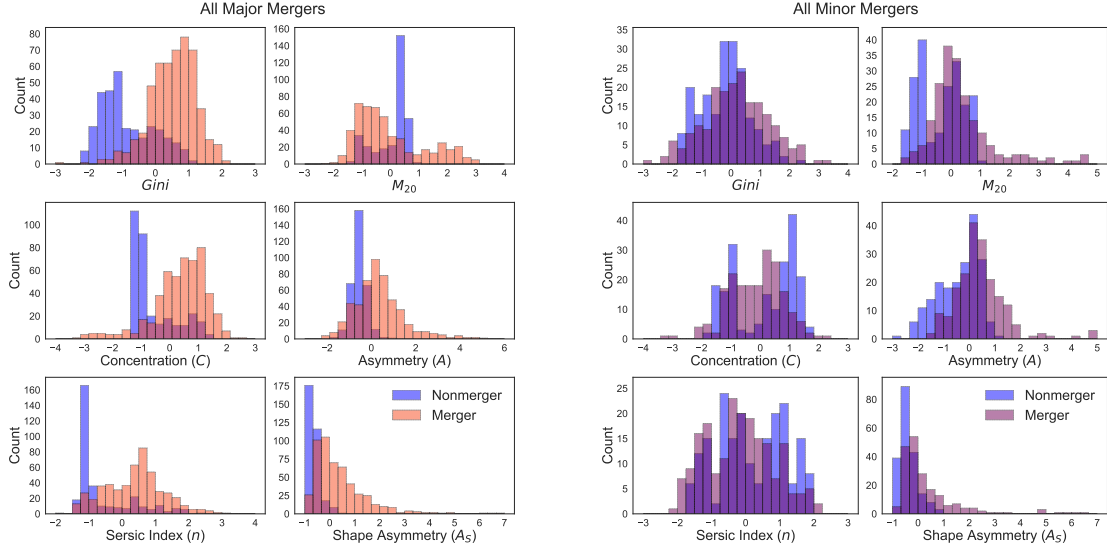


Figure 4.3: Individual histograms for each imaging predictor for the combined major merger simulations (left) and combined minor merger simulations (right). We show for all the simulations combined that we are unable to cleanly separate the nonmerging (blue) and merging (pink and purple for major and minor mergers, respectively) galaxies using any individual imaging predictor. The y-axis is the ‘Count’ or number of merger simulation snapshots in each bin. The x-axis of each subplot is the standardized predictor value for the seven imaging predictors, where the mean of the combined merging and nonmerging populations for each predictor is 0 and the standard deviation is 1. Standardizing the input predictor values acts to stabilize the LDA but has no effect on the relative value of each predictor; for example, a greater value of *Gini* corresponds to an increased likelihood that a given galaxy is a merger. This statement is valid both for the measured *Gini* value and the standardized *Gini* value given here.

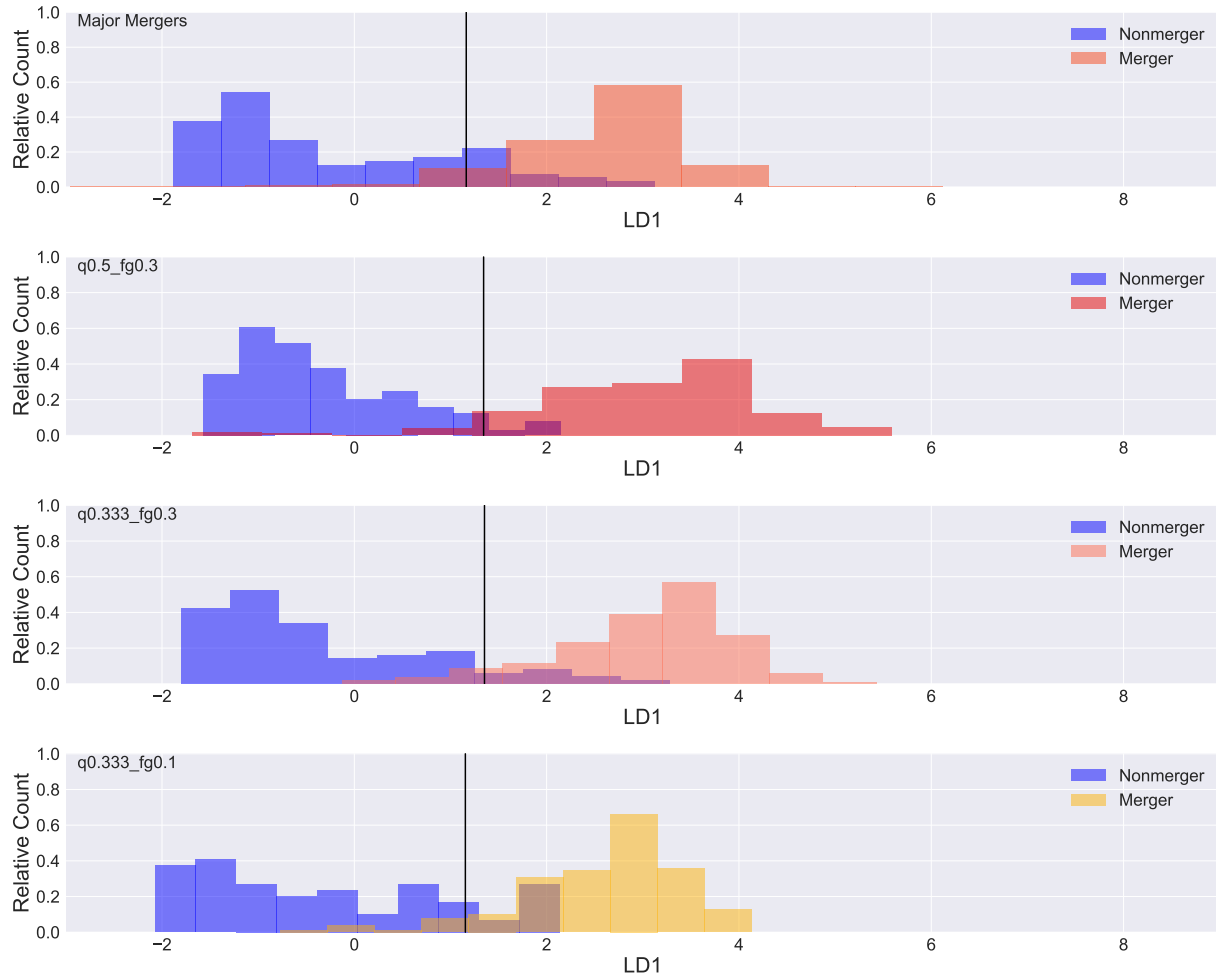


Figure 4.4: Histograms of the distribution of score values for galaxies in the nonmerging and merging class for all of the major merger simulations and the combined major merger run (top). The vertical black line marks the decision boundary - the halfway mark between the mean of the nonmerging and merging distributions. A galaxy with a score above (to the right) of this value has a higher probability of being a merging galaxy and a galaxy with a score to the left of this value has a higher probability of being a nonmerging galaxy. The decision boundaries are in similar locations for all major merger runs of LDA because the separation of the merging and nonmerging populations is so similar. The histograms have different colors to distinguish different LDA runs and the blue bars are the matched nonmerger sample for each run.

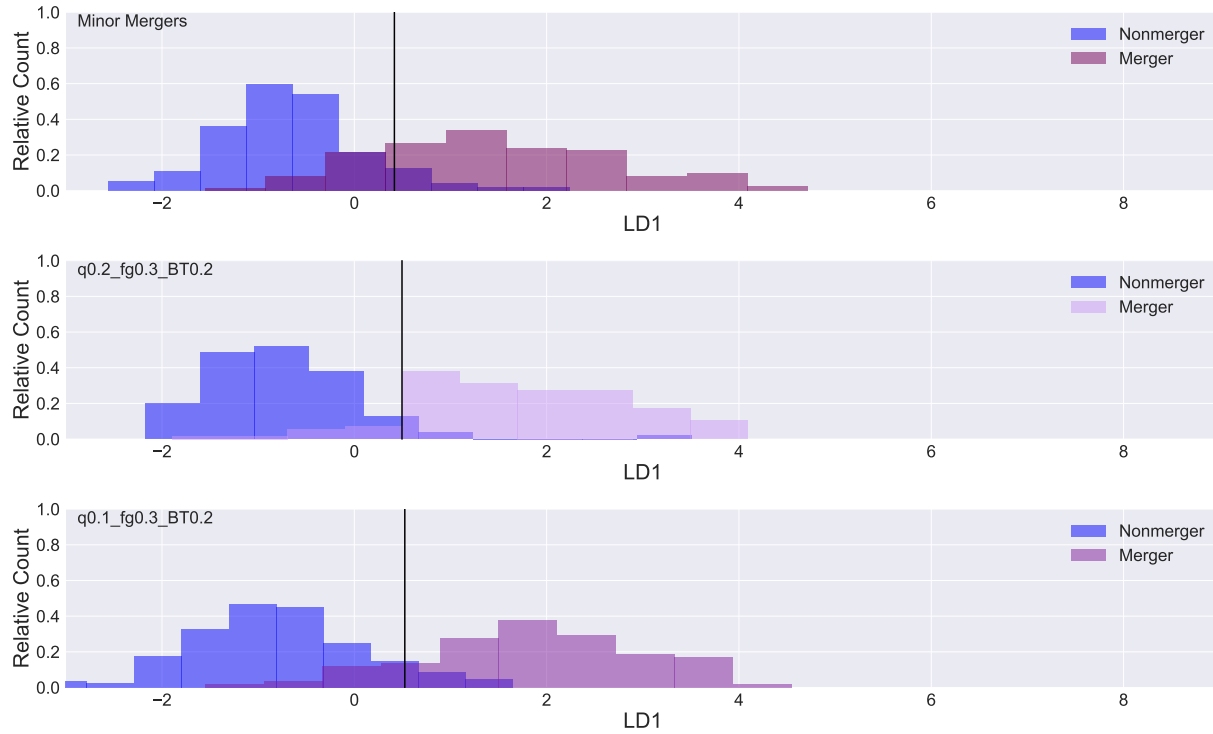


Figure 4.5: Same as Figure 4.4 but for all of the minor merger runs of LDA and the combined minor merger run (top). The decision boundaries for these simulations are lower than for the major merger runs because the separation between classes is not as extreme for the minor mergers.

separate the two classes using the first discriminant axis LD1 (Figures 4.4 and 4.5).

While it is possible to classify a galaxy as merging or nonmerging given a decision boundary and a value of LD1, we use the posterior probability that a galaxy belongs to a given class from Equation 4.1. Since we standardize the input predictors to train the LDA, classifying galaxies after the determination of LD1 is complicated. Instead of simply plugging in measured values of predictors into LD1, it is necessary to apply the same standardization used in this work prior to classification.

We discuss the statistical assumptions made by LDA in Appendix B.5. We discuss the coefficients of LD1 in Section 4.3.1 and the implications for each run and the combined run. Finally, we demonstrate in Appendix B.7 that LDA classification is able to accurately separate the classes of merging and nonmerging galaxies.

4.3 Results

After running LDA for each galaxy merger, we compare the results. We describe our methodology to compare the LDA classifications from different simulations in Section 4.3.1. Finally, we compute the observability timescales for $Gini - M_{20}$, A , A_S , and the LDA technique in Section 4.3.2. We describe the LDA classification in more statistical detail in Appendices B.4, B.5, B.6, and B.7, where we include an investigation of the merging galaxy priors used, a multivariate analysis of the assumptions of LDA, a description of the k-fold error estimation, and an examination of the accuracy and precision of the tool, respectively.

4.3.1 Analyzing the LD1 Coefficients

Since we run LDA on each merger simulation individually, and LD1 is a vector, we produce different values for each coefficient of LD1. An advantage of LDA is that we are able to directly interpret the relative weights of each individual predictor (Tables A.20 and A.21) for each simulation. We focus on the primary predictors, which are in Table A.20, since they are a more straightforward way to interpret the influence of the imaging predictors than the

interaction terms in Table A.21. We compare the values of these primary coefficients of LD1 for each simulation. The coefficients have positive or negative values; since a larger value of LD1 indicates that a galaxy is a merger, a positive coefficient indicates that increasing the corresponding predictor increases the likelihood that the galaxy is a merger. Our goal is to determine if the classification is significantly different for different simulations and if it differs for different merger initial conditions.

We use stratified k -fold cross-validation (Appendix B.6) to determine the standard error on the coefficients of LD1 that are selected by forward stepwise selection. Briefly, we randomly split the sample into ten parts, where nine parts are the training sample and the tenth part is the test sample. Stratified k -fold cross-validation ensures that the percentage of merging and nonmerging galaxies in the test set matches that of the full sample. We perform this operation ten times and then calculate the mean value and standard deviation (standard error) for the LD1 coefficients and intercept (\hat{w} and \hat{w}_0) from the ten iterations of training and test sets.

For both Table A.20 and Table A.21, include the predictors that are selected by the forward stepwise selection. Additionally, we bold the input predictors that are significant (to 3σ above zero) according to their errors provided by k -fold cross-validation. We use both of these predictor selection techniques to determine which predictors are selected and significant (we exclude all other predictors from our analysis and discussion). We show a visualization in Figure 4.6 of the order of importance of the individual primary imaging predictors for each simulation. Overall, we can only discard the clumpiness (S) primary predictor from our analysis; it is always either excluded by the forward stepwise selection of predictors or $< 3\sigma$ above zero.

There are significant differences between the rankings of imaging predictors for each simulation. For instance, we find that the major merger simulations (q0.5_fg0.3, q0.333_fg0.3, and q0.333_fg0.1) have different rankings of predictor importance; A_S and A are more important for the major mergers. For minor mergers, A_S is unimportant, while C and *Gini*

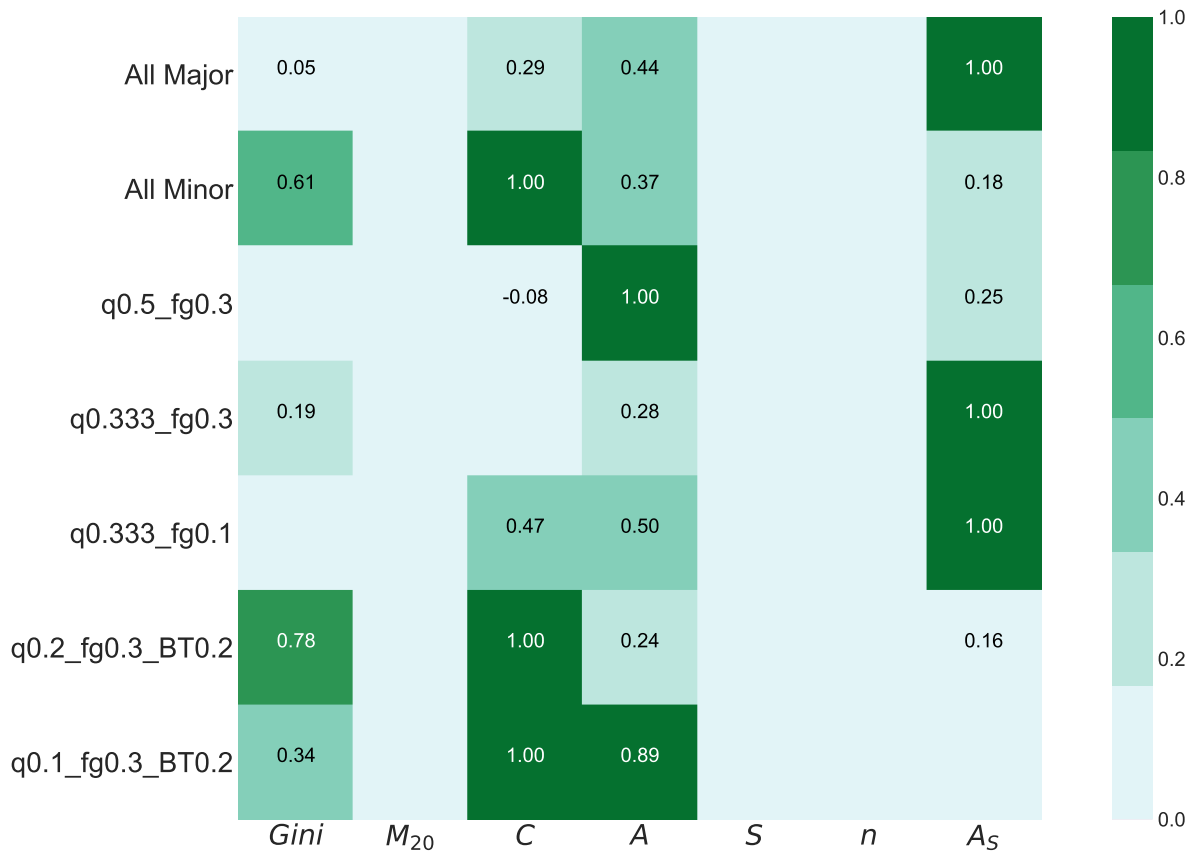


Figure 4.6: Visualization of the LD1 coefficient values of each predictor, weighted relative to the maximum primary predictor for each run. This includes each LDA run for each individual simulation and all of the major merger simulations combined (first row) and all of the minor merger simulations combined (second row). We find that the relative importance of predictors changes between all simulations.

become very important.

We interpret the sign of each coefficient individually for each simulation in Section 4.4, comparing to previous work. We further interpret the relative importance of the coefficients for different merger initial conditions and discuss that the value of the predictors evolve as the merger progresses in Section 4.4.

4.3.2 Observability Timescales

To compare our new LDA technique to previous work that identifies merging galaxies, we calculate the observability timescales of $Gini - M_{20}$, A , A_S , and the LDA technique for the simulated galaxies. We focus on these particular predictors because past work has defined cuts for $Gini - M_{20}$, A , and A_S , and classified galaxies lying above these thresholds as merging. Likewise, the observability timescale of $Gini - M_{20}$, A , and A_S are measured from these cuts in predictor space, where a simulated galaxy is ‘identifiable’ as a merger for the duration of the time it spends above these thresholds. For $Gini - M_{20}$, Lotz et al. (2008) use:

$$Gini > -0.14 M_{20} + 0.33$$

where everything above the line is defined as a merger. The asymmetry cut is defined by Conselice et al. (2003):

$$A > 0.35$$

where galaxies with A values above 0.35 are mergers. The shape asymmetry cut is from Pawlik et al. (2016):

$$A_S > 0.2$$

where galaxies with A_S values above this cut are mergers.

We show these cuts in predictor space in Figures 4.7, 4.8, and 4.9, respectively, for the combined major and minor merger simulations. We plot C with A in Figure 4.8 to include

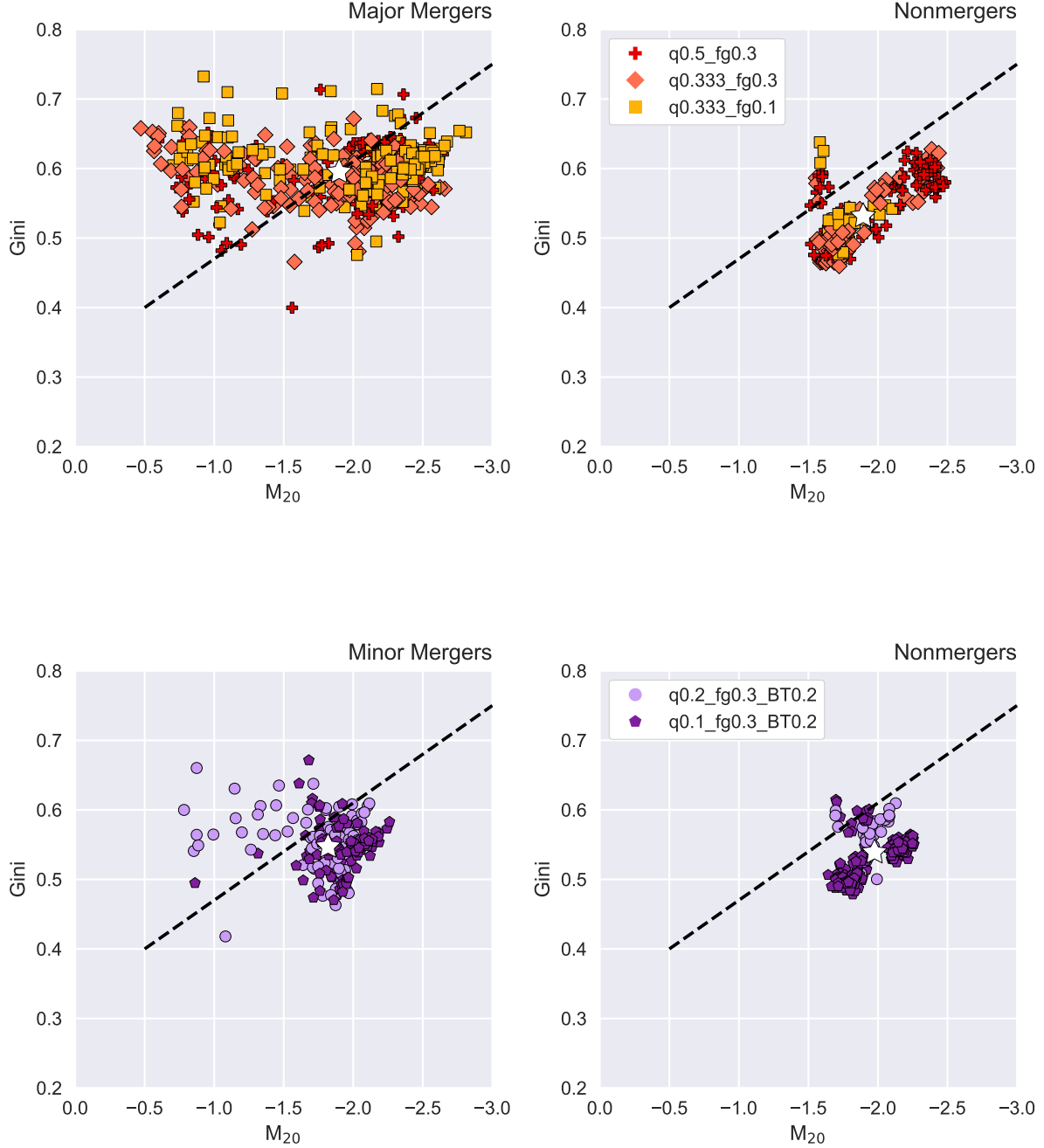


Figure 4.7: Viewpoint-averaged values at each snapshot of a merger for the three major merger simulations (top) and two minor merger simulations (bottom) in the $Gini - M_{20}$ two-dimensional predictor space. Red is q0.5_fg0.3, pink is q0.333_fg0.3, yellow is q0.333_fg0.1, light purple is q0.2_fg0.3_BT0.2, and dark purple is q0.1_fg0.3_BT0.2. The stars mark the mean of the data presented on each plot. We show the merging galaxies in the left plots and the matched nonmerging isolated galaxies on the right. We include the cuts in predictor space from Section 4.3.2 used to identify merging galaxies in other work. The cut in $Gini - M_{20}$ is $Gini > 0.14 M_{20} + 0.33$; all galaxies above this cut are identified as mergers in other work (e.g., Lotz et al. 2008).

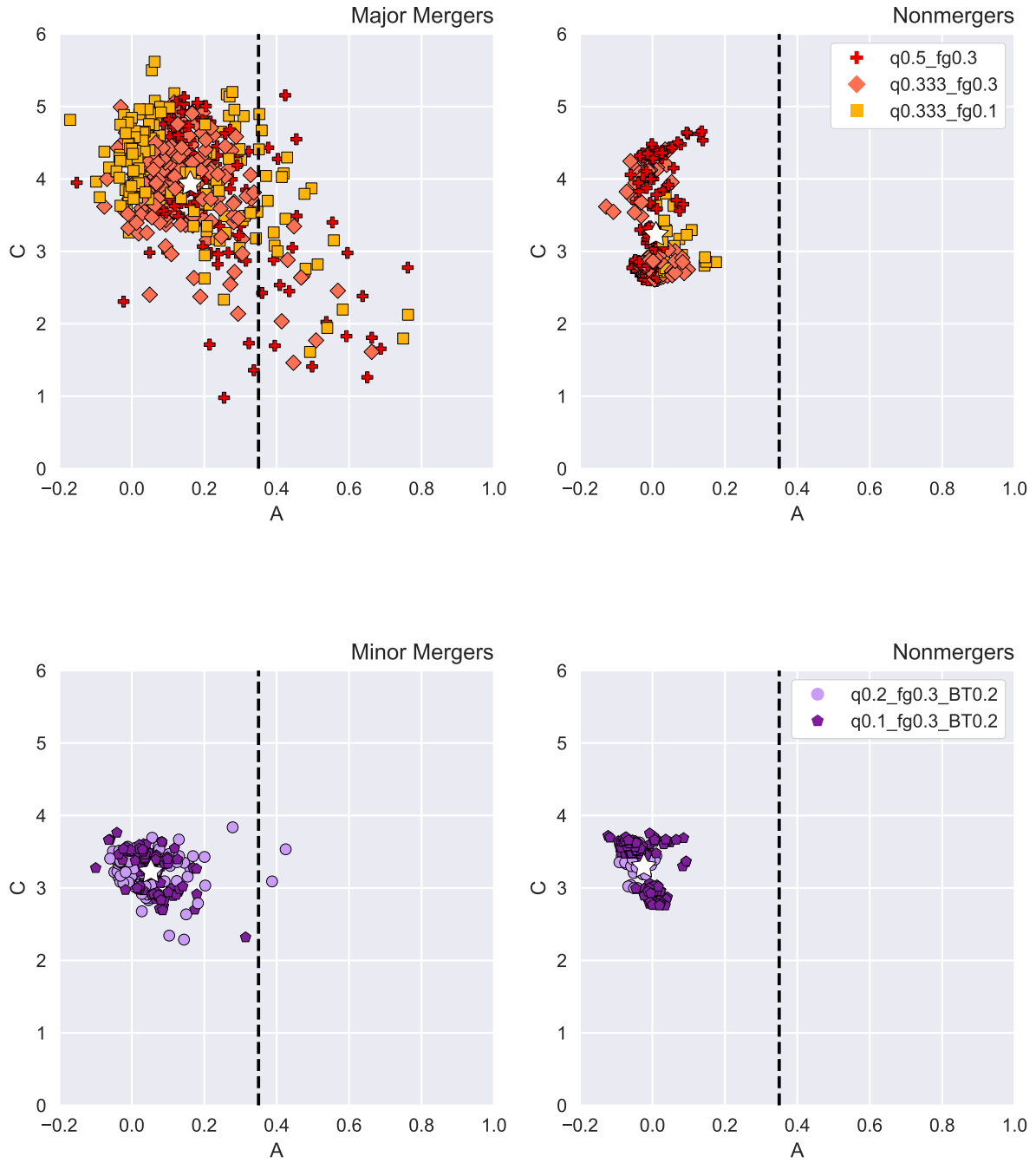


Figure 4.8: Same as Figure 4.7 but for the CA predictor space. The cut in CA space is $A > 0.35$; all galaxies to the right of this line are identified as mergers (e.g., Conselice et al. 2003).

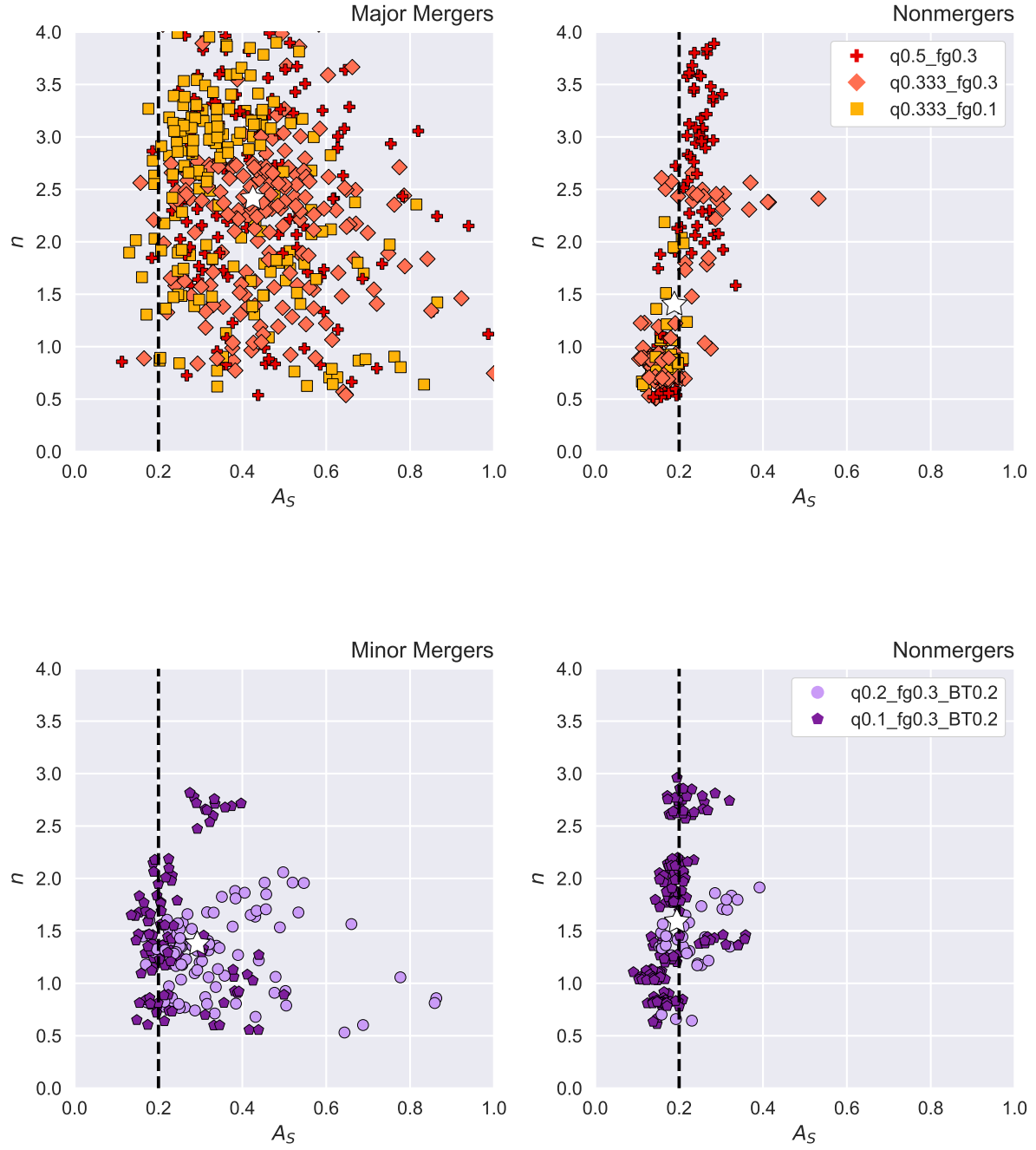


Figure 4.9: Same as Figure 4.7 but for the $n - A_S$ diagrams. The dashed line for the $n - A_S$ diagram is for $A_S > 0.2$; all galaxies to the right of this cut are identified as mergers in Pawlik et al. (2016).

the evolution of C although there is no formal cut in predictor space for this predictor. For the same reason, we plot n against A_S in Figure 4.9. In these three predictor space plots, we are able to show all of the predictors (we only exclude S because it is unimportant to the analysis).

For each snapshot in each merger simulation, we determine the viewpoint-averaged value for $Gini - M_{20}$, A , and A_S . If a given snapshot exceeds the cut threshold for a merging galaxy, we designate that snapshot as ‘identifiable’. By combining all identified snapshots, we determine the observability timescale, which we list in Table A.22. If zero snapshots were successfully identified, the observability timescale is less than the time resolution (i.e., < 0.1 Gyr). The timescale of observability from the LDA technique is shown in Figure 4.10; we label a snapshot of a merger as identifiable if the viewpoint-averaged mean of LD1 is above the decision boundary (shown with a horizontal black line).

For all simulations, we find that the timescale of observability for the LDA technique is longer than the individual $Gini - M_{20}$, A , and A_S timescales of observability. The overall trend is $\sim 0.2 - 0.8$ Gyr observability timescales in $Gini - M_{20}$, very short timescales of observability for A (< 0.1 Gyr), and longer observability timescales in A_S that are > 1 Gyr. The observability window for LDA comprises $\sim 80 - 90\%$ of the total length of the merger event, which translates to $2.0 - 2.5$ Gyr timescales for the major mergers and $3.5 - 8.8$ Gyr timescales for the minor mergers.

Overall, the LDA observability timescale dominates because it relies upon multiple different imaging predictors that are sensitive to the merging galaxies at different stages of the merger. However, for the major mergers, the A_S timescale is comparable to the LDA observability timescale. We discuss these trends, how observability timescales scale with the merger initial conditions, and how these timescales compare to previous work in Section 4.4.2.

4.4 Discussion

We explore the behavior of the individual predictors in the LDA technique. Since we remove correlations between predictors with the interaction terms, we are able to discuss the positive or negative signs of the primary predictors (we refer to *Gini*, M_{20} , C , A , S , n , and A_S as the ‘primary predictors’) in Section 4.4.1. We also compare these results to past work with these imaging predictors and discuss how their values change for merging and nonmerging galaxies. Then, we discuss the strengths of the LDA technique. First, we focus on the increased observability timescale of the LDA technique in Section 4.4.2 and how it is sensitive to different stages of the merger. We also discuss how different imaging predictors change in sensitivity throughout the timeline of a merger. Second, we focus on how the classification changes for different mass ratios and gas fractions in Section 4.4.3 and Section 4.4.4, respectively. Finally, we assess the overall accuracy and precision of the LDA technique in Section 4.4.5 and test it on a subsample of SDSS galaxies in Section 4.4.6.

4.4.1 The signs of the LD1 coefficients are consistent with previous work

One of the strengths of LDA is that we can independently interpret the behavior of each predictor. We compare the primary coefficients of LD1 to previous work by Conselice et al. (2003), Lotz et al. (2008), and Lotz et al. (2010a,b) in terms of the signs (positive or negative) of the predictor coefficients.

In Figures 4.4 and 4.5, a higher value of LD1 indicates that a galaxy is more likely to be identified as a merger. Since LD1 is linear, we can interpret the individual signs of the coefficients in a similar way. If a coefficient is positive, this indicates that a higher value of the coefficient will increase the probability that a galaxy is classified as a merger and vice versa. We provide Figures 4.7, 4.8, and 4.9 to visually compare the location in predictor space of the population of merging galaxies relative to the population of nonmerging galaxies. Figures 4.11 and 4.12 examine the time evolution of the values of individual predictors for the

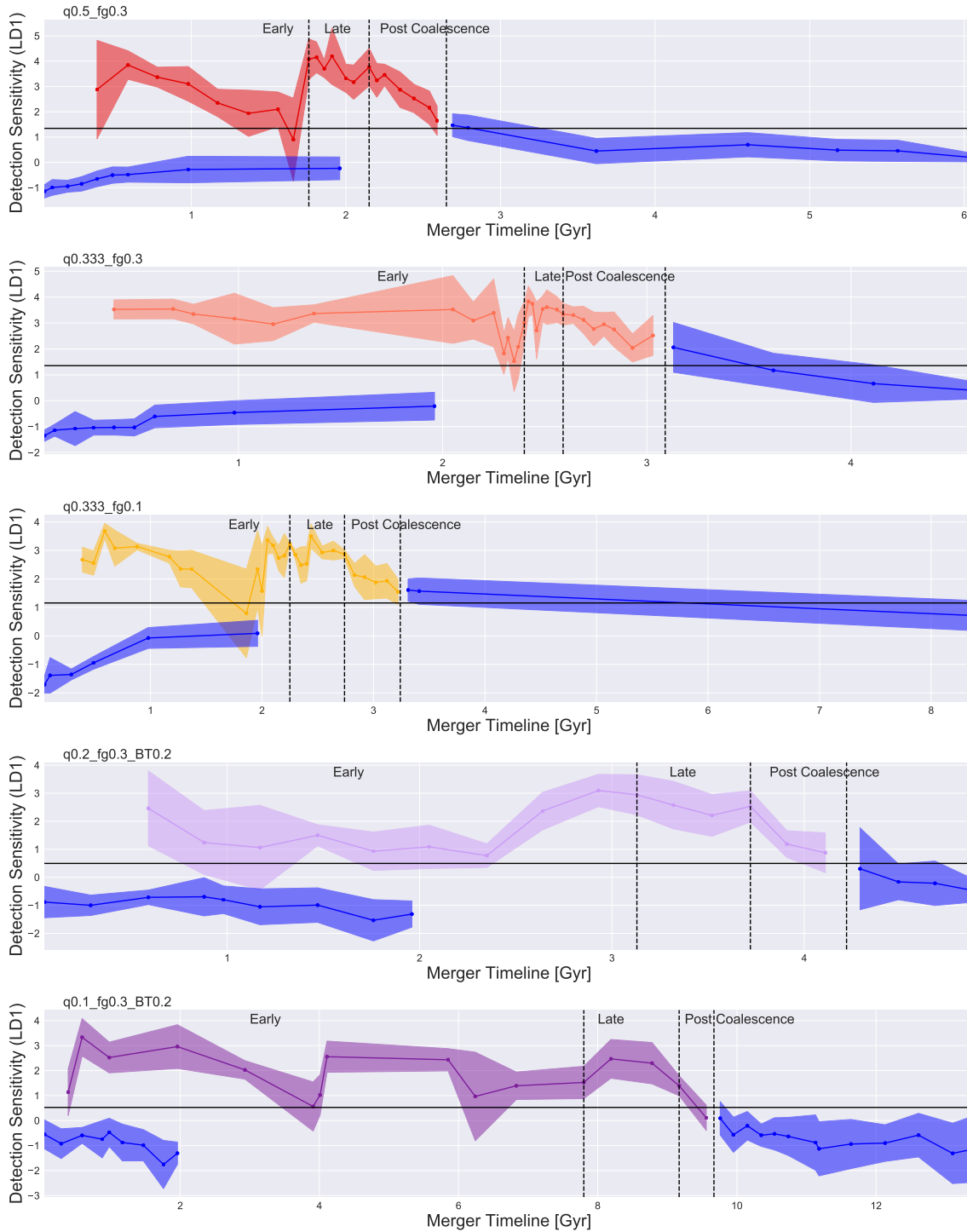


Figure 4.10: Average value of LD1 (mean for all viewpoints) of each snapshot of a merger for all galaxy merger simulations with confidence intervals 1σ above and below the mean. The horizontal black line is the decision boundary; galaxies above this line are classified as mergers and galaxies below this line are nonmergers. The blue line and confidence intervals are for the matched samples of nonmerging galaxies for each simulation. LD1 provides sensitive identification of merger morphology at many stages throughout the merger.

q0.5_fg0.3 and q0.2_fg0.3_BT0.2 runs, respectively. We select these two runs since they are representative of the predictor evolution for a typical major and minor merger simulation.

Since this discussion relies upon the time evolution of predictors, we quickly recap the definitions of merger stage. A merger begins at first pericentric passage and ends 0.5 Gyr following the final coalescence of the nuclei. An early-stage merger is one where the separation of the stellar bulges is $\Delta x \geq 10$ kpc, a late-stage merger is $1 \text{ kpc} < \Delta x < 10 \text{ kpc}$, and a post-coalescence merger is $\Delta x \leq 1 \text{ kpc}$.

Overall, we conclude that the positive/negative signs of the individual predictor coefficients are as expected from past studies of merger identification. We discuss the predictor coefficients in more detail and how they change for different mass ratios and gas fractions in Sections 4.4.3 and 4.4.4.

4.4.1.1 *Gini*

The *Gini* coefficients are significant and positive for the combined major and minor merger simulations, as well as q0.333_fg0.3, q0.2_fg0.3_BT0.2, and q0.1_fg0.3_BT0.2, which is unsurprising because a higher *Gini* index has been shown to identify merging galaxies with one or more bright nuclei (e.g., Conselice 2014 and references therein).

4.4.1.2 M_{20}

The M_{20} coefficient is insignificant for all runs. Interestingly, the value of M_{20} for the mergers evolves with time; this behavior can be examined in Figure 4.11, which shows the evolution of all the imaging predictors with time for the q0.5_fg0.3 simulation. This time evolution is especially apparent for the major merger simulations. Early stage mergers evolve to the left towards the merger region of the *Gini* – M_{20} diagram as their concentration decreases early in the merger (recall, M_{20} is similar to C but does not depend on the location of the center of the galaxy). This leftward migration towards the merger domain would correspond to a negative value for the M_{20} coefficient.

Then, in the post-coalescence stages, the merging galaxies evolve away from the merger region on the $Gini - M_{20}$ diagram, to the right. Lotz et al. (2008) also find this trend in which galaxies evolve away from the merger region of the $Gini - M_{20}$ diagram for the later stages of a merger. This rightward migration makes sense because post-coalescence galaxies begin to lose visually disturbed features such as tidal tails and appear more concentrated in their light distributions. This evolution of M_{20} in both directions for major mergers leads to a washing out of any dominant trend of M_{20} for the major merger simulations.

4.4.1.3 Concentration

The central concentration of light, C , is important for all LDA runs except q0.333_fg0.3, where it is insignificant. The value of the C coefficient is positive for all runs except q0.5_fg0.3, where it is negative. A positive C coefficient indicates that mergers tend to have a higher value of C . We first discuss the overall behavior of C and then focus on the nuances of C , such as the decrease of C during the early stages of major mergers.

Since C is positive for the majority of merger simulations, we can conclude that, in general, merging galaxies have more centrally concentrated light than isolated galaxies. Lotz et al. (2008) find that concentration is not a strong predictor of a merger but that it is higher for the later stages of a merger. This is expected given that mergers tend to build elliptical galaxies, which has been shown in detail for major mergers (e.g., Bendo & Barnes 2000; Bournaud et al. 2005). It has additionally been shown that minor mergers can contribute to stellar bulge growth and drive a less dramatic transformation of galaxy morphology (e.g., Walker et al. 1996; Cox et al. 2008). We discuss C in more detail for different mass ratios in Section 4.4.3.

We observe a gradual increase of C with the progression of the merger from the beginning of the early stage to the end of the post-coalescence stage. We examine Figure 4.11 for the time evolution of the C predictor for the q0.5_fg0.3 run. The value of C for q0.5_fg0.3 demonstrates an increase with a slight decrease during the early and late stages of

the merger. It remains heightened for the nonmerging snapshots following final coalescence. This overall increase is typical behavior for the rest of the merger simulations and happens for the minor merger simulations, without the dip during the end of the early and beginning of the late stages (Figure 4.12). The increase of C throughout the lifetime of each individual merger simulation leads to positive coefficients of the C predictor in the LDA technique. However, the dip in C values for q0.5_fg0.3 is pronounced during the early stages and results in a negative coefficient of C in the LDA.

4.4.1.4 Asymmetry and shape asymmetry

The LD1 coefficients for the asymmetry (A) and shape asymmetry (A_S) predictors both have positive values for all simulations (A_S is insignificant only for q0.1_fg0.3_BT0.2). This indicates that the more asymmetric a galaxy, the more likely we are to identify it as a merger. Asymmetry shows this same relationship in Lotz et al. (2008) and Conselice et al. (2003), where the value increases for mergers.

4.4.1.5 Clumpiness

Clumpiness (S) is insignificant for LD1 for all simulations. This result is anticipated given that Lotz et al. (2008) find clumpiness to be a less powerful predictor, but disagrees with Conselice et al. (2003), who find that clumpiness is higher for merging galaxies. However, the sample of merging galaxies from Conselice et al. (2003) is built from local luminous and ultraluminous infrared galaxies (LIRGs and ULIRGs), both of which are inherently very high in clumpiness. Thus, it is expected that we do not see the same importance of S for the merging galaxies in this work.

4.4.1.6 Sérsic index

The Sérsic index, n , is also unimportant for all simulations. If n is higher for merging galaxies, this indicates that merging galaxies have steeper light profiles. The evolution of n

is closely tied to that of C , which is unsurprising given that these predictors are correlated (Appendix B.5). n evolves towards higher values for later stages in the merger, where only a single nucleus is present. The key difference between C and n is that n has a smaller separation in value between merging and nonmerging galaxies for most simulations, so it is an unimportant coefficient for the classification.

4.4.2 LDA lengthens the timescale of observability of merging galaxies

The various LDA predictors evolve with time over the course of a galaxy merger. By incorporating seven different imaging predictors, we are able to capture a longer timeline for merging galaxies with the LDA technique than with individual predictors. In this section we discuss the time evolution of the imaging predictors and how this limits their observability timescales. We also compare the estimates of observability time of different imaging predictors to past work.

We show the time evolution of the individual predictors (and LD1) in Figures 4.11 and 4.12 for the q0.5_fg0.3 and q0.2_fg0.3_BT0.2 simulations, respectively. We include the cutoff values of A and A_S ; if a galaxy exceeds these values it is ‘identifiable’ as a merger as in Section 4.3.2. We show one major and one minor merger simulation to demonstrate the main differences between the time evolution of the predictors for different mass ratios.

Using the $Gini - M_{20}$ cut in predictor space from Section 4.3.2, most of the simulated merging galaxies would be identified as merging by the cut in $Gini - M_{20}$ during the early and late stages of merging, but for a shorter total time than with the LDA technique. The $Gini - M_{20}$ 0.59 Gyr timeframe (indicated by the spike in M_{20} values) for the q0.5_fg0.3 major merger is shown in Figure 4.11. The q0.333_fg0.3 and q0.333_fg0.1 simulations are also identified by this cut during the early and late stages of merging for a similar timeframe. However, as the mass ratio begins to increase for minor mergers, the observability timescale of the merger from the $Gini - M_{20}$ technique decreases. For instance, the q0.2_fg0.3_BT0.2 merger is identified by this cut during the early and late stages of merging, but only for a

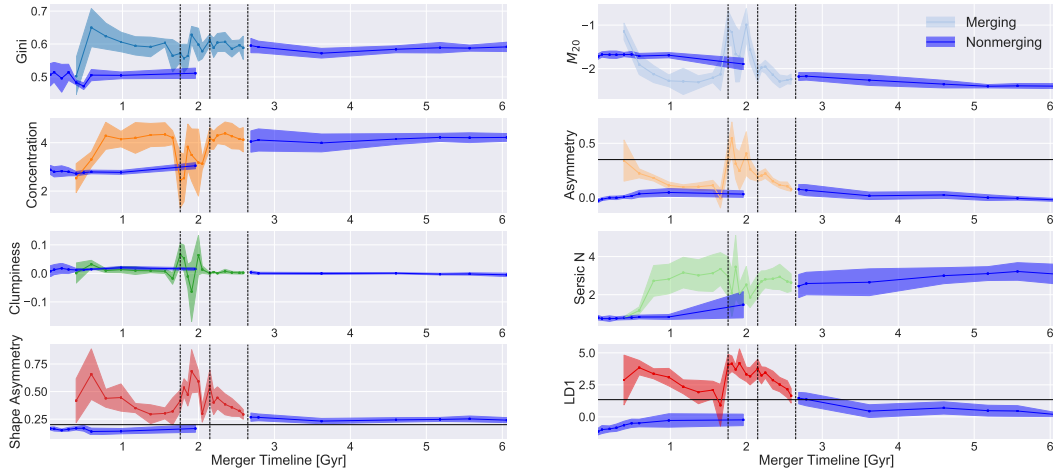


Figure 4.11: Time evolution of the imaging predictors for the q0.5_fg0.3 simulation. The LD1 sensitivity is shown in the bottom right panel for comparison; the dashed vertical lines mark the beginning of the late stage, beginning of the post-coalescence stage, and end of the merger. We plot the nonmerging galaxies in dark blue for comparison purposes. We also plot horizontal lines for the A_S and A cutoffs in the literature (0.2 and 0.35, respectively) and for the decision boundary for LD1. The dark blue lines are for the matched sample of isolated galaxies. The most powerful predictors for the q0.5_fg0.3 simulation are A_S , A , and C .

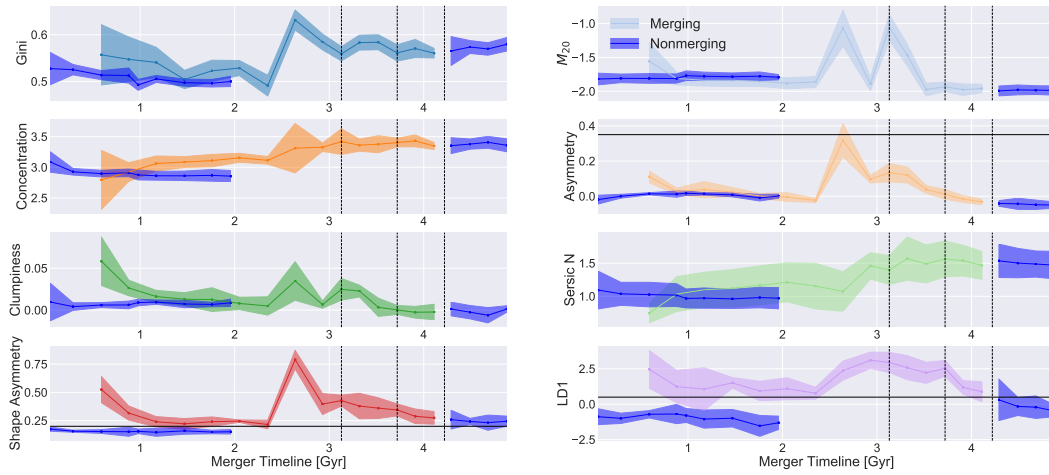


Figure 4.12: Same as Figure 4.11 but for the q0.2_fg0.3_BT0.2 simulation. The most powerful predictors for the q0.2_fg0.3_BT0.2 simulation are C , $Gini$, A , and A_S .

0.19 Gyr timeframe (also indicated by a spike in M_{20} values in Figure 4.12). These results are consistent with previous work; Lotz et al. (2008) find that $Gini - M_{20}$ is most sensitive to mergers during the first pass (early stage) and the final coalescence of the nuclei (late stage), and Lotz et al. (2010a) show that $Gini - M_{20}$ is sensitive to merger mass ratios less than 1:9. Also, our 0.2 – 0.8 Gyr $Gini - M_{20}$ timescale of observability for the simulations with a mass ratio $> 1:9$ is consistent with the 0.2 – 0.6 Gyr timescale of observability from Lotz et al. (2008).

The A cutoff identifies some of the early and late stages of the major mergers, but has an even shorter timescale of observability than $Gini - M_{20}$. This behavior is apparent in Figure 4.11 when the A value exceeds the 0.35 cutoff value during the beginning of the early stage and in a spike during the late stage of the merger. This is consistent with Lotz et al. (2008), where the first passage and final coalescence (during the late stage) show the largest asymmetries. While the A value exceeds 0.35 for more snapshots in the major merger simulations, we find a < 0.1 Gyr timescale for both major and minor mergers. This < 0.1 Gyr timescale for minor mergers can be seen in Figure 4.12, where the A value only approaches the cutoff value for one snapshot. Lotz et al. (2010a) find an A timescale of 0.2 – 0.4 Gyr for major mergers and then less than 0.06 Gyr for minor mergers. While we have a shorter timescale of continuously heightened A values for the major merger simulations, we find that the major mergers result in more snapshots where the value of A exceeds 0.35, which is consistent with the longer observability timescale of A for major mergers from Lotz et al. (2010a).

A_S has a longer timescale of observability than A and $Gini - M_{20}$ for both major and minor mergers. The merging galaxies evolve to have large values of A_S at various times throughout the early, late, and post-coalescence stages of the merger. A_S identifies the major mergers at nearly all points throughout the simulation, expanding the sensitivity of the LDA technique in time. It only fails to identify the major mergers at some post-coalescence stages. A_S is notably much better at identifying the minor mergers as mergers than both A and

$Gini - M_{20}$ and it is most sensitive to the early and late stages of these mergers. Overall, A_S shows less dependence on time in the merger and is a more consistent identifier of merging galaxies during the early, late, and early post-coalescence stages. This makes sense because A_S is sensitive to faint tidal features; it should therefore be more successful than A at identifying disturbed structures at all times.

Finally, we focus on the time evolution of C , which is not assigned a cutoff value in the literature but which has significant importance within the LDA technique. We find that all mergers show elevated values of C , especially for the post-coalescence stages, meaning that C is critical within the LDA technique for capturing the post-coalescence snapshots in time. $Gini$ exhibits a similar behavior to C for the minor mergers, becoming most enhanced during the late and post-coalescence stages.

Snyder et al. (2018) apply a random forest classifier to the Illustris galaxies and find that features that rely on concentration are more important for selecting recent mergers while features that rely on asymmetries are more important for selecting galaxies that are about to merge. While the Illustris simulation is a cosmological merger tree simulation, it is informative that the results are consistent with the time sensitivities of various imaging predictors in this work.

Unlike the individual imaging predictors, we find that the sensitivity of the LDA depends only minimally on merger stage. It is slightly less sensitive for the very early stages and very late post coalescence stages of the merger; this is expected since the galaxies often appear visually to be isolated galaxies prior to first pericentric passage and after coalescence. As discussed in Section 4.2.1, we use the very early and very late stages of the merger (prior to first passage and > 0.5 Gyr following final coalescence) as isolated galaxies in this analysis, so these galaxies are very similar in imaging to galaxies at an adjacent point in time. This explains why the 1σ confidence intervals overlap with the decision boundary for many of these very early-stage and very late-stage snapshots in Figure 4.10.

The individual imaging classification techniques are sensitive to different stages of a

merger. For instance, A and $Gini - M_{20}$ identify early and late-stage mergers, A_S identifies early-stage, late-stage, and some post-coalescence mergers, and C is most sensitive to post-coalescence mergers. LDA is able to combine these imaging techniques into one more complete classifier that maintains sensitivity throughout the lifetime of a merger.

4.4.3 The coefficients of LD1 change with mass ratio

When we examine the relative importance of various predictors for merger simulations with varying mass ratios, we determine that A_S and A are relatively more important for the major mergers and that C and $Gini$ are relatively more important for the minor mergers. A is important for all merger simulations.

First, we address the major mergers, where A_S and A are both important coefficients and indicators of disturbed visual morphology. The A coefficient has a normalized value of $0.28 - 1.0$ for the three major mergers and the combined major merger runs, indicating that it is one of the most important primary predictors. It is less important for the minor mergers and the combined minor merger simulation, but its relative importance is still high $\sim 0.24 - 0.89$ (Figure 4.6). This result agrees with Lotz et al. (2010a), who finds that A is a good probe of major mergers with mass ratios between 1:1 and 1:4. This is because the major mergers have more disturbed morphologies, especially during the early stages of the merger. However, the A predictor remains important for the minor mergers, where the visual morphology is less disturbed.

A_S is more sensitive (than A) to faint tidal tails in galaxies. The A_S coefficient ranges in normalized values from $0.25 - 1.0$ for the major mergers and $0.16 - 0.18$ for the minor mergers. Since both A and A_S track visual morphology, it is significant that while A is important for all runs, A_S is less important for the minor mergers. This suggests that the more disturbed visual morphology of major mergers is best identified with both measures of asymmetry. On the other hand, minor mergers rely more on measures of concentration like C and $Gini$, so while A is still an important predictor for them, it is less dominant.

Next we address C and $Gini$, where the importance to the minor mergers can be attributed to two main factors: scatter and necessity. The major mergers show more scatter in C values while the minor mergers show a general trend of C enhancement as the mergers progress. In Figure 4.8, the major mergers range from values of $1 - 5.5$ while the minor mergers only span $2 - 4$ in C . Upon examination of the predictor values with time (Figures 4.11 and 4.12), we verify that C increases steadily with time for the minor mergers and reaches a peak value of $\sim 3 - 3.5$. For major mergers, C shows a general increase with time but also decreases during the most visually disturbed epochs of the merger (early and late stage). However, the major mergers do ultimately build more concentrated remnants than the minor mergers, with C values peaking at $4 - 4.5$.

$Gini$ is heightened for both major and minor mergers in Figures 4.11 and 4.12. The LDA for the major mergers was able to rely upon stronger predictors such as A and A_S to fully separate the populations of merging and nonmerging galaxies. However, the minor mergers are less distinguishable from nonmerging galaxies using these predictors. Therefore, $Gini$ becomes more important for the minor mergers. This result is consistent with Lotz et al. (2010a), who find that $Gini - M_{20}$ remains effective for identifying minor mergers down to mass ratios of 1:9.

Figure 4.6 also shows an important difference between the 1:2 major merger and the 1:3 major mergers. Between the two mass ratios, measurements of concentration (C and $Gini$) become slightly more important in the 1:3 major mergers, initiating the trend towards minor mergers.

Our findings regarding C make sense given the current understanding of galaxy morphological evolution. To first order, equal mass ratio major mergers build large elliptical galaxies (e.g., Bendo & Barnes 2000; Bournaud et al. 2005) while intermediate mass ratio mergers (down to 1:10) are predicted to build galaxies with spiral-like morphologies and elliptical-like kinematics (e.g., Jog & Chitre 2002; Bournaud et al. 2004). Very high mass ratio mergers (minor mergers, $\geq 1:10$) build disturbed spiral-like galaxies (e.g., Naab et al.

2014 and references therein). However, some work has found that multiple minor mergers can still build elliptical surface brightness profiles in the remnant galaxy (Bournaud et al. 2007; Jesseit et al. 2009; Bois et al. 2011) and that even one merger of a very minor mass ratio can build stellar bulges in the remnant (Cox et al. 2008).

Statistically, minor mergers are much more common than major mergers, accounting for three times as many mergers (e.g., Bertone & Conselice 2009; Lotz et al. 2011). The ubiquitous nature of minor mergers increases their relative importance for galaxy evolution. For example, Ownsworth et al. (2014) find that the majority of stellar mass is added to galaxies by star formation (24% of stellar mass) and minor mergers (34% of stellar mass), whereas major mergers only account for 17% of the total galaxy stellar mass at $z = 0.3$. Other observations of local elliptical galaxies and the dearth of major mergers indicates that minor mergers may be more important than previously thought for building local elliptical galaxies with more concentrated light profiles (Trujillo et al. 2009; Taylor et al. 2010).

The above picture of galaxy morphological evolution is consistent with the differences between C for the major and minor merger simulations. C is more important for the minor mergers because it exhibits less scatter than for the major mergers, where the dip in C weakens the overall strength of the coefficient in the LDA technique. The major merger remnants show a greater overall enhancement of C by the end of the merger, building galaxies with $C \sim 4 - 5$ that are more consistent with the classical picture of large elliptical galaxies. Visually, the galaxy remnants for major and minor mergers still have disk profiles with a more concentrated center, indicative of an enhancement of the stellar bulge. This means that by the end of the merger, minor and major mergers have both enhanced the concentration of the light profile of the galaxy and therefore contributed to the morphological evolution of galaxies.

4.4.4 The coefficients of LD1 do not change (significantly) with gas fraction

Next, we examine differences between the gas rich and gas poor simulations. We specifically compare q0.333_fg0.3 to q0.333_fg0.1, which are both 1:3 mass ratio major mergers matched for all properties except gas fraction. The important predictors for the gas poor merger are A_S , A , and C , while A_S , A , and $Gini$ are important for the gas rich merger. Overall, these coefficients are very similar between the gas rich and gas poor simulations. Both rely upon measurements of asymmetry (A and A_S). Both simulations also rely upon measurements of concentration ($Gini$ and C). While C is more important for the gas poor merger, $Gini$ is more important for the gas rich merger.

Lotz et al. (2010b) establish that $Gini - M_{20}$ is weakly dependent on gas fraction whereas A is relatively enhanced for gas rich mergers. Since A and A_S are relatively important for both gas rich and gas poor simulations, we conclude that the dominant initial condition must be mass ratio for A to remain important for the gas poor major merger.

While there is little difference in A_S in terms of the coefficients for the gas rich and gas poor simulations, there is a small difference in the observability timescales for A_S and $Gini - M_{20}$. The observability times for A_S is shorter for the gas poor major merger in Table A.22. The timescale of observability for A_S for q0.333_fg0.1 is 2.34 Gyr while it is 2.64 Gyr for q0.333_fg0.3. Since the overall merger timescales are so similar for these two simulations, the A_S observability timescale is significantly longer for the gas rich major merger. The $Gini - M_{20}$ timescale is also significantly different for the gas rich and gas poor simulations; it is longer for the gas poor major merger (0.78 Gyr) and shorter for the gas rich major merger (0.34 Gyr). This result is consistent with Lotz et al. (2010b), where the result is that the $Gini - M_{20}$ observability timescale decreases slightly with increasing gas fraction while the A observability timescale increases with gas fraction. The $Gini - M_{20}$ timescale may be decreasing slightly with gas fraction here for similar reasons as stated in Lotz et al. (2010b), that the increased dust obscuration at the central nuclei lowers the $Gini$ values for gas rich

simulations. The gas poor simulation has the longest $Gini - M_{20}$ observability timescale of all the simulations.

Kormendy et al. (2009) suggest that both dry and wet mergers (gas poor and gas rich, respectively) build up the bulge mass of a galaxy, contributing to its elliptical morphology (or an increased value of C). Overall, dry mergers are more important for building elliptical galaxies but wet mergers can also increase the central concentration of a galaxy since they drive starbursts that contribute to bulge growth. The C value for the gas rich major merger increases with time to a peak value of ~ 4.3 while the gas poor major merger increase to a peak value of ~ 4.7 . The gas poor major merger seems to have a slightly higher concentration, possibly reflecting the tendency for dry mergers to build galaxies with elliptical morphologies. However, these values are not significantly different when we take into consideration the viewpoint-averaged standard deviation for these snapshots. Therefore, the difference in gas fraction is not producing a significant difference in the concentration of the remnant.

Overall, while the timescale of observability for A_S is longer for the gas rich major merger and the timescale of observability of $Gini - M_{20}$ is longer for the gas poor major merger (which is consistent with Lotz et al. (2010b)), the differences in LDA coefficients are most pronounced for mergers of different mass ratios (Section 4.4.3). This is why we choose to separate the combined runs by mass ratio as opposed to gas fraction.

4.4.5 The LDA technique is accurate and precise at identifying merging galaxies

The accuracy and precision of the LDA technique are very high (the accuracy is 85% and 81% and precision is 97% and 94% for the major merger and minor merger combined simulations, respectively; Table A.23 in Appendix B.7). We use accuracy to determine the relative number of true detections (TP, true positives, and TN, true negatives) to all detections (includes FP, false positives, and FN, false negatives); the accuracy is defined as $(TP + TN)/(TP + TN + FP + FN)$. If the accuracy is high, this means that our method

does a good job of minimizing the number of false positives and false negatives. We use precision to determine the relative number of true positives (TP) to all positive detections, including false positives (FP); the precision is defined as $(TP/(TP+FP))$. If the precision is high, then there are a low percentage of false positives, which is desirable because false positives are nonmerging galaxies that are incorrectly included as mergers. We want to avoid contamination in the sample of merging galaxies when we apply the technique to real imaging.

In this section we compare the accuracy and precision of the LDA technique to that of past work, which utilizes pair studies or cuts in $Gini - M_{20}$ space, A , or A_S . We also compare to other work that has utilized machine learning tools to identify merging galaxies.

First we compare the LDA accuracy and precision to that of close pair studies with SDSS. Darg et al. (2010) compare Galaxy Zoo classifications of major mergers to all SDSS galaxy pairs with a projected separation of < 30 kpc and a line of sight velocity offset < 500 km s $^{-1}$. After visually examining all 2308 close pair objects, they find that 28% of objects are chance superpositions and/or have no signs of interaction. While this is an imperfect comparison to our work since close pair studies only capture a brief snapshot of a merger, the overall result is that 28% of the close pairs are false positives. Darg et al. (2010) also estimate that only 20% of advanced mergers identified in Galaxy Zoo are pairs in SDSS, which is a small fraction of true positives. In comparison to the LDA technique, pair studies have low accuracy since many mergers are missed by the technique and low precision since there is also a significant fraction of false positives.

Next, we directly compare the accuracy and precision of the LDA technique to that of the cuts in predictor space introduced in Section 4.3.2. We measure the accuracy and precision of the $Gini - M_{20}$, A , and A_S cuts for the simulations and find that precision remains high. This means that these methods do not incorrectly identify nonmergers as mergers. In fact, they have the opposite problem and fail to identify merging galaxies as such, leading to low accuracies. We find that $Gini - M_{20}$ has accuracies from 60% to 70%, A

has accuracies from 40% to 60%, and A_S has accuracies from 70% to 90%. The low accuracy of the A predictor agrees with Conselice et al. (2003) who find that the fraction of mergers (defined to be a sample of ULIRGs) that are correctly identified by A is $\sim 50\%$.

We also find that there is a difference in accuracy for different mass ratios. For example, the minor mergers fall at the bottom of the accuracy ranges given above. This is worrisome because the cuts in predictor space are preferentially selecting major mergers, which are much less numerous than minor mergers. In contrast, the LDA accuracy changes by less than 10% between all simulations, ranging from $\sim 85 - 90\%$ accuracy for all simulations. Using $Gini - M_{20}$, A , or A_S in isolation is not sensitive enough to correctly and consistently identify mergers of all mass ratios at all merger stages.

Our LDA technique is more accurate and precise than individual imaging predictor classifiers and is comparable to other techniques that combine many different imaging predictors. For instance, Snyder et al. (2018) and Goulding et al. (2018) use random forest classifiers with a collection of similar parametric and nonparametric imaging predictors to classify merging and nonmerging galaxies and find similar accuracies and precisions.

Snyder et al. (2018) use the Illustris cosmological simulation to produce synthetic deep Hubble Space Telescope images of merging galaxies at 12 timesteps over a range of redshifts ($0.5 < z < 5$). While Snyder et al. (2018) work with dissimilar galaxies to our low redshift SDSS galaxies, we are able to roughly compare the two methods because both rely upon similar imaging predictors. For instance, Snyder et al. (2018) use a binary classification that relies upon $Gini$, M_{20} , A , and C as inputs (among other imaging predictors). They find a similar accuracy and precision of their classifier when they test it using the simulated Illustris galaxies. The result is a classifier that relies on different imaging predictors for different merger stages, similar to the LDA technique in our work. The random forest has a completeness of $\sim 70\%$ and a purity of 10% at $z = 0.5$ and 60% at $z = 3$. Completeness is defined as $TP/(TP+FN)$, which is defined as recall in our work, and purity is $TP/(TP+FP)$, which is defined as precision here.

Since the isolated galaxy sample in Snyder et al. (2018) is different than the sample of isolated disks used in this work, we are unable to directly compare the false positive and false negative rates. We instead discuss one relative strength of the LDA technique. Some of the false negatives in Snyder et al. (2018) result from the failure of the method to detect some minor mergers and some of the false positives result from a narrow temporal definition of the duration of the merger, which is restricted to 500 Myr. One relative strength of the LDA technique is that it is built from high temporal resolution simulations and is therefore able to use a more complete definition of merging galaxies. It also extends the definition of merging galaxies beyond the 500 Myr timeframe used in Snyder et al. (2018). This is a general strength of high temporal resolution isolated simulations over large cosmological simulations.

Goulding et al. (2018) use a random forest to create a non-binary classifier that separates their sample of Hyper Suprime-Cam (HSC) galaxies into subsamples of major mergers, minor mergers and irregulars, and non-interacting galaxies. The input imaging predictors include $Gini$, C , A , S , and n for the galaxy images as well as the residual images after subtracting a GALFIT surface brightness model. They visually classify galaxies in the HSC sample to test the performance of the classifier and find that the major mergers suffer from mild contamination ($\sim 10\%$) with an overall completeness for the merger samples of 75%. The LDA technique has a comparable result with 4% contamination and 79% completeness for major mergers. The minor mergers are more difficult to distinguish from isolated and major mergers in Goulding et al. (2018) and therefore have increased contamination and decreased completeness. The LDA technique on the other hand only suffers from 6% contamination and 66% completeness for minor mergers. It should be noted that Goulding et al. (2018) create and test the random forest method on real galaxy images, so this is an imperfect comparison, simply meant to roughly compare the accuracy and precision of different imaging merger identification methods. Additionally, since the LDA technique is developed from disk-dominated galaxies, its accuracy and precision apply best to galaxy samples that

match the properties of the simulated galaxies used to construct the technique.

4.4.6 Testing the Technique on SDSS Galaxies

To preliminarily test the performance of the LDA technique on real images of galaxies, we apply the major and minor merger classification techniques to a sample of SDSS galaxies that have been identified as mergers, spirals, and ellipticals in GalaxyZoo (Lintott et al. 2008, 2011). We randomly select 50 galaxies from each galaxy morphology classification (merger, spiral, and elliptical) using a ‘superclean’ cutoff value of $p_{\text{merg}}, p_{\text{el}}, p_{\text{CS}} > 0.95$, where p_{merg} is the probability that the galaxy is a merger, p_{el} is the probability that the galaxy is classified as elliptical, and p_{CS} is the probability that the galaxy is classified under the umbrella classification of ‘combined spirals’. The probabilities are the percentage of GalaxyZoo users that selected a given morphology type. We require that these galaxies exceed the $\langle S/N \rangle$ cutoff value of 2.5.

We apply the major and minor merger combined LDA techniques to each of the three subsamples of galaxy types and determine the fraction of galaxies that are classified by the LDA technique as merging and nonmerging. We show some example classifications for the major merger classification tool in Figure 4.13. For the major merger classification tool, we find that 86% of the GalaxyZoo mergers are identified as mergers, 73% of the GalaxyZoo elliptical galaxies are identified as mergers, and 14% of the Galaxy Zoo spirals are classified as mergers. We show images of these classification categories in Figure 4.13 for the major merger classifier. For the minor merger classification, 93% of GalaxyZoo mergers are classified as mergers, 61% of the GalaxyZoo ellipticals are classified as mergers, and 43% of the GalaxyZoo spirals are classified as mergers.

The difficulty in using the GalaxyZoo sample as a test sample is that we do not know a priori which galaxies are merging. We are able to use the GalaxyZoo merger sample as ‘true’ mergers since they are obvious visual mergers (classified as such by GalaxyZoo users), so the fraction of true positives and false negatives is reliable. The GalaxyZoo users were

conservative, only reluctantly classifying the most obvious mergers as such (Darg et al. 2010). However, we are unable to adequately establish the relative fractions of false positives and true negatives since the samples of GalaxyZoo ellipticals and spirals may be contaminated by merging galaxies that lack the obvious visual signs of clear major mergers such as tidal tails. Therefore, our discussion mainly relies upon the fraction of true positives and false negatives from the classification of the GalaxyZoo mergers and only briefly discusses true negatives and false positives from the GalaxyZoo ellipticals and spirals population. We plan to delve into this discussion in more depth in future work that presents the classification of real galaxies (Nevin et al. (2019, in prep)).

The major merger classifier recovers $\sim 86\%$ of the GalaxyZoo mergers. This fraction agrees with the fraction of true positives and false negatives from the simulation measured in Appendix B.7, where 82% of true mergers are identified as such. Figure 4.13 shows a failure mode of the major merger classifier. The classifier fails to identify the GalaxyZoo merger in the top right of the figure as a merger because while it appears to be two separate galaxies by eye, the two galaxies are symmetrically aligned in such a way that A and A_S are low. We plan to investigate the failure modes of the technique in more detail in Nevin et al. (2019, in prep).

The minor merger classification identifies 93% of the GalaxyZoo mergers as such which is more than predicted (62%) when testing on simulated galaxies. It is important to note that the GalaxyZoo mergers are more likely to be major mergers in their early phases with clear visual disturbances. Therefore, the minor merger tool performs better than expected since it is applied to galaxies that are more easily identified than most minor mergers in the simulated galaxy sample.

The fraction of nonmergers (according to GalaxyZoo) that are identified as mergers by the LDA technique is low for the spiral galaxies and high for the elliptical galaxies. For instance, the major merger classifier tool identifies 73% (14%) of the GalaxyZoo elliptical (spiral) galaxies as mergers. The spiral galaxy false positive rate is closer to the 3% false

positive rate from the major merger classifier when it is tested on simulated galaxies. However, there are an excess of galaxies identified as mergers in the GalaxyZoo elliptical galaxy population. It is not obvious that these galaxies have undergone mergers recently from visual inspection. While it is possible that some of these galaxies have recently merged, many of them may be false positives. It is important to note that the galaxies that are classified as mergers among the GalaxyZoo elliptical galaxies have p_{merg} values that are barely above the 0.5 threshold we define here for the LDA classification. In future work, we plan to set multiple probability thresholds to eliminate false positives amongst our merger samples. Finally, since the LDA technique was constructed from disk-dominated galaxies, it is most accurate and precise at classifying galaxies that most closely match the specifications of the simulated sample. Therefore, it may not be as accurate for elliptical galaxies. We plan to address this concern in future work (Nevin et al. (2019, in prep)) when we apply the classification to SDSS galaxies.

There is an interesting discrepancy between the false positive rate of the major and minor merger technique for the sample of GalaxyZoo spirals. The major merger technique identifies 14% of the sample as merging whereas the minor merger technique identifies 43% of the sample as merging. Of the GalaxyZoo spirals, there are 16 galaxies that are classified as merging by the minor merger technique that are classified as nonmerging by the major merger technique. We visually inspect these galaxies, and find that $\sim 50\%$ could be classified as spirals with disturbed structure while $\sim 40\%$ have a secondary point source component that could either be a star forming region or a stellar bulge. More followup work is required here, but preliminarily, it appears that the minor merger technique is identifying some possible minor mergers that have been missed by GalaxyZoo users. It is possible that it could also be identifying star forming regions because while we prescribe a 10% flux threshold for the fitting of n , it could be fitting bright star forming regions that exceed this threshold. More work is required to distinguish between these two possibilities. It is expected that the major merger technique also misses some of these minor mergers. We show an example of

a possible minor merger that was detected by the minor merger technique but not by the major merger technique in Figure 4.14. This galaxy has disturbed spiral structure and some possible secondary point sources that could be star forming regions.

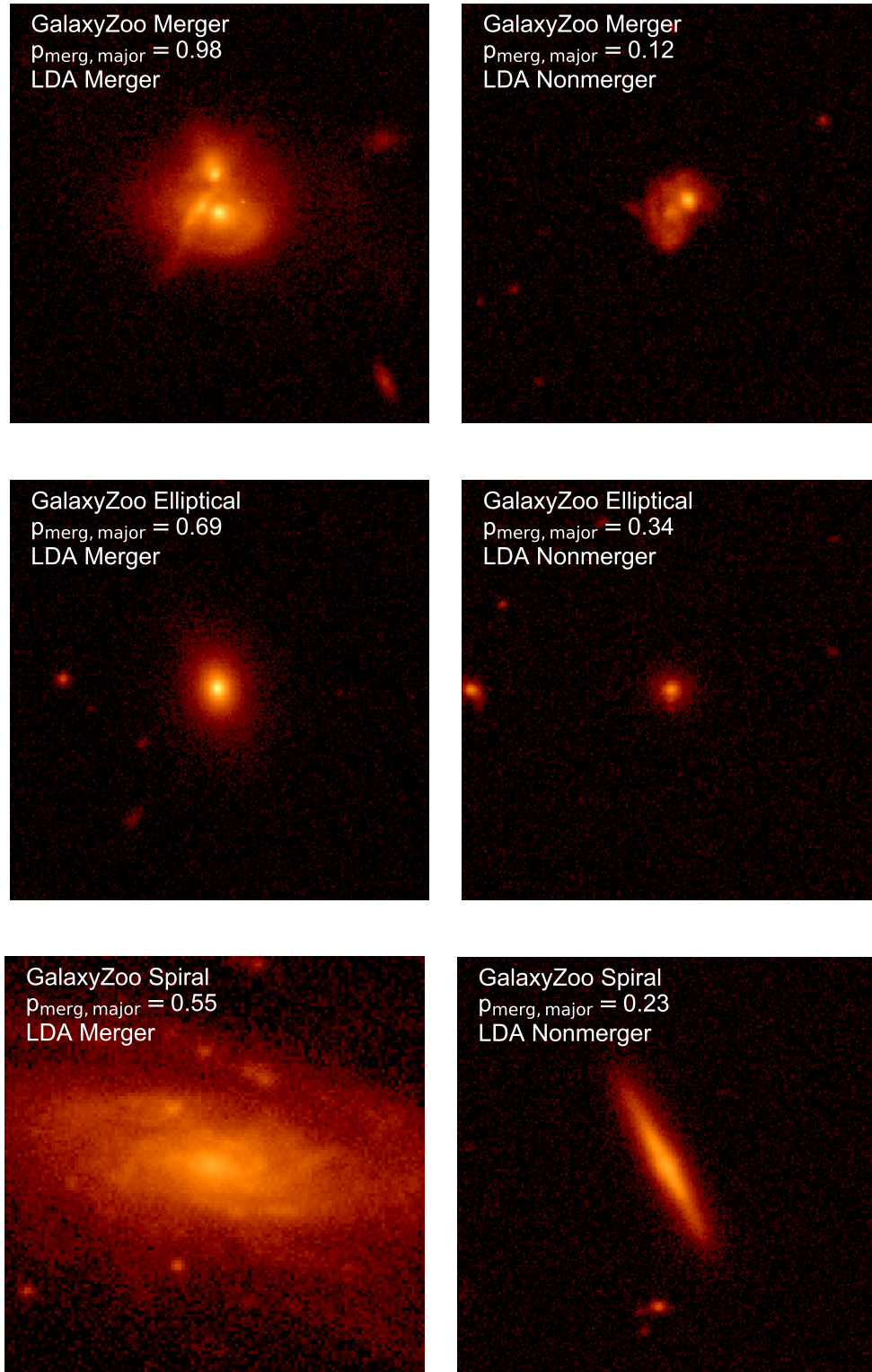


Figure 4.13: r -band images of GalaxyZoo mergers (top), elliptical galaxies (middle), and spiral galaxies (bottom) that are classified as mergers (left column) and nonmergers (right column) by the major merger classification technique. For each case, the probability that the galaxy is a merger as classified by the major merger technique ($p_{\text{merg, major}}$) is given.

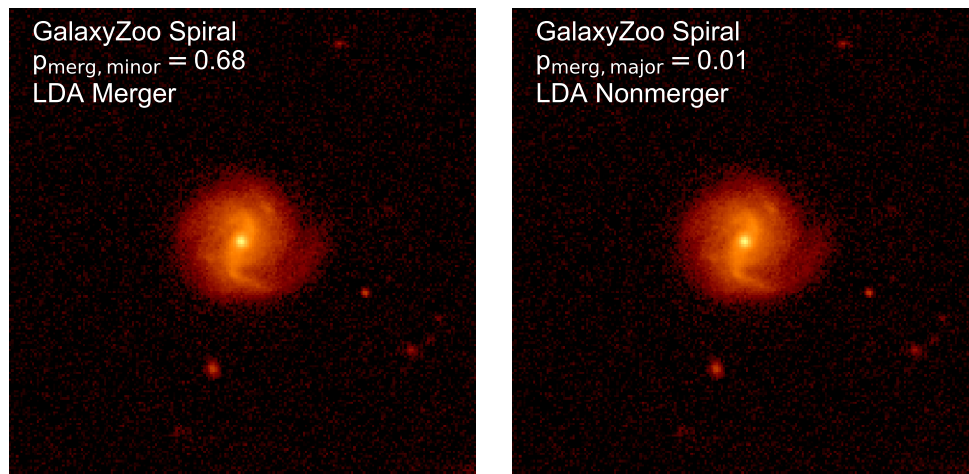


Figure 4.14: r -band images of a GalaxyZoo spiral galaxy that is identified as a merger by the minor merger technique (left) and a nonmerger by the major merger technique (right). The probabilities that the galaxy is a merger are listed.

4.5 Conclusion

We create a suite of merging and nonmerging disk-dominated galaxies with different gas fractions, mass ratios, and bulge-to-total mass ratios using **GADGET-3** hydrodynamics simulations. We use the dust radiative transfer code **SUNRISE** to produce resolved dust-attenuated optical spectra from the simulations, from which we extract SDSS r -band images at ~ 0.1 Gyr intervals. These snapshots cover the early, late, and post-coalescence stages of the simulated mergers. We then ‘SDSS-ize’ the simulated images of galaxies, introducing residual noise and convolving to the seeing limit of the SDSS survey. We use these ‘SDSS-ized’ images to measure seven different imaging predictors ($Gini$, M_{20} , concentration (C), asymmetry (A), clumpiness (S), Sérsic index (n), and shape asymmetry (A_S)), which we combine to create a Linear Discriminant Analysis (LDA) classification scheme. This classification technique is able to accurately identify merging galaxies over a range of mass ratios, gas fractions, viewing angles, and merger stages. We create two overall classifications, one for major mergers and one for minor mergers, that we will apply to classify SDSS galaxies, assigning each galaxy a posterior probability of being a merging galaxy. Based on these results we make the following conclusions:

- The LDA technique outperforms previous merger identification methods such as $Gini - M_{20}$, A , and A_S in terms of accuracy and precision. While the precisions of $Gini - M_{20}$, A , and A_S are high with few false positives, the accuracies vary between 40 – 90%, and change with merger mass ratio. The LDA technique improves upon this with accuracies of 85% (81%) and precisions of 97% (94%) for the combined major (minor) merger simulations. The LDA accuracy and precision varies little with merger initial conditions ($< 10\%$), indicating that the LDA technique is more stable and accurate than individual predictor merger identification techniques.
- The LDA technique lengthens the timescale of observability of merging galaxies (> 2 Gyr) and the galaxy mergers are identified at all stages (early, late, and post-

coalescence) of a merger. The observability timescales for $Gini - M_{20}$, A , and A_S are $0.2 - 0.8$, < 0.1 , and $2.2 - 7.8$ Gyr, respectively. The LDA technique incorporates many imaging predictors and is therefore able to combine the strengths of all these imaging predictors to be sensitive to all stages of the galaxy mergers.

- The predictor coefficients of LD1 change little with gas fraction and are most affected by the mass ratio of the merging galaxies. For instance, A and A_S are important for major mergers due to their visually disturbed morphology while C and $Gini$ are more important for minor mergers, since they show consistent enhancement in light concentration as the merger progresses. This supports the idea that even minor mergers can build stellar bulges. A is an important coefficient for a range of mass ratios, identifying major and minor mergers alike.

We plan to apply this imaging LDA technique to the SDSS galaxies (Nevin et al. (2019, in prep)). Additionally, since the MaNGA survey is an imaging and IFS survey, we will incorporate several kinematic predictors based on the stellar velocity and stellar velocity dispersion maps from the hydrodynamics simulations into this analysis to improve the classification.

Chapter 5

Accurate Identification of Galaxy Mergers with Kinematics

Merging galaxies are an important driver of galaxy evolution yet due to heterogeneous samples of merging galaxies, current work disagrees on the relative importance of mergers for evolutionary processes such as star formation and AGN activity in the universe. Previously, we used **GADGET-3/SUNRISE** simulations of merging galaxies and a linear discriminant analysis (LDA) to create a precise and accurate merging galaxy classifier from a number of different imaging predictors. Here, we build upon our previous work and develop a complementary tool that is based on kinematic predictors, which trace the disorder of the stellar kinematics in galaxies observed with integral field spectroscopy (IFS). This tool utilizes eight kinematic predictors (the difference between the kinematic and imaging PAs, the asymmetry in the velocity map, the asymmetry in the velocity dispersion map, the **kinemetry** residuals, the specific angular momentum, the ellipticity, the weighted asymmetry in the Radon profile, and the asymmetry in the Radon profile) to create a merging galaxy classifier. The classifier differs significantly with mass ratio but not with gas fraction, so we create a combined major and minor merger classification. We find the minor mergers to be more reliant on the difference between the kinematic and imaging PA, while the major mergers rely more on the asymmetry in the Radon profile, which is more sensitive to warps in the stellar kinematics. By combining all of the kinematic predictors into one classifier, we find that the observability timescale for the LDA classification is $\sim 60\%$ of the duration of the merger. The classification has an accuracy of $\sim 60\%$ and a precision of $\sim 90\%$, meaning that there are few false positives

in the technique while a significant number of mergers are missed. This kinematic technique is currently a stand-alone identification method but our goal is to combine and compare this tool with the imaging technique in future work.

5.1 Introduction

Observations of galaxies reveal that they evolve over cosmic time from smaller, bluer, more irregular star-forming galaxies at higher redshifts to larger, redder, more elliptical galaxies in the local universe (Glazebrook et al. 1995; Lilly et al. 1995; Giavalisco et al. 1996). Additionally, the bimodality of galaxy properties such as color, mass, or star formation rate at low redshift implies that galaxies are quenching, or shutting down their star formation, in the local universe as well (e.g., Schawinski et al. 2009; Masters et al. 2010; Weigel et al. 2017). Galaxy evolution, or changes in the size, structures, and star formation properties of galaxies, is largely driven by the accretion of gas and/or the prevention of this gas from forming stars. Many different processes can drive this evolution, ranging from those that operate over short timescales like feedback from active galactic nuclei (AGNs) and/or galaxy mergers (Silk & Rees 1998; Di Matteo et al. 2005; Kaviraj 2013) to longer-lived processes like ‘cold flow’ accretion from the cosmic web (Dekel et al. 2009), mass quenching (Peng et al. 2010, 2012), or morphological quenching (due to structures such as bars or stellar bulges; Sheth et al. 2005).

While the current Λ CDM framework for structural formation in the universe points to the import of mergers for assembling dark matter halos (White & Rees 1978; White & Frenk 1991; Cole et al. 2008), the relative contribution of mergers to galaxy evolution through processes such as star formation, AGN activity, and/or morphological transformation remains unclear. This disagreement stems from the difficulty of building large, unambiguous samples of merging galaxies. Galaxy mergers are inherently difficult to identify; they persist for \sim Gyr and they have a diversity of identifying characteristics based on the merger stage and the parameters of the merger. The difficulty of identifying merging galaxies is responsible for the

uncertainty in the observed merger fraction (f_{merg} , the fraction of mergers in a sample) at high and low redshifts (e.g., López-Sanjuan et al. 2008). It is known, however, that the fraction of merging galaxies evolves over time, peaking at redshifts $z \sim 2$ (e.g., Conselice et al. 2008); this has contributed to a relative wealth of studies of higher-redshift merging galaxies which are the target of the next generation of large telescopes (*JWST*, TMT). Currently, there is a paucity of understanding of local mergers, which are relatively less frequent. In order to build an understanding of mergers at all epochs, it is important to construct techniques that can aid in the understanding of local mergers and their contribution to evolution in the nearby universe. This is the main goal of this work.

A variety of imaging techniques exist to identify merging galaxies, all of which are susceptible to their own individual biases. These often rely upon individual imaging tools, or predictors, such as galaxy pair studies, the *Gini* – M_{20} methodology, or the asymmetry of the galaxy light in imaging. One approach to overcome these biases is to utilize simulations of merging galaxies to better understand the shortcomings of individual tools and to characterize the observability timescales of these methods. For example, the length of time that a major merger is observable by the *Gini* – M_{20} and asymmetry metric is 0.5 Gyr and 0.3 Gyr, respectively, meaning that merging galaxies are visible as mergers using these techniques for only a short time during the \sim Gyr duration of the merger (e.g., Lotz et al. 2008; Lotz et al. 2010b,a). Another strategy is to combine the predictors to create a single classification tool that dramatically lengthens the observability timescale by capitalizing on the strengths of the individual methods (e.g., Goulding et al. 2018; Snyder et al. 2019).

In Nevin et al. (2019) (henceforth N19), we pursue both of these approaches and utilize **GADGET-3/SUNRISE** simulated galaxies to build a merger identification technique that combines seven imaging predictors to create one more accurate and precise classifier that incorporates the strength of all of these predictors, lengthening the observability timescale to >2 Gyr. The simulated sample of galaxies that we use in this approach are vital for constructing a more complete picture of the different stages of a merger as well as providing

an a priori sample of which galaxies are merging or not to hone the identification technique before it is applied to actual galaxies.

Kinematic predictors provide a promising addition to imaging predictors since they are capable of probing stages of mergers that are ‘invisible’ in imaging. For instance, some morphological disturbances like tidal tails can fade on a ~ 500 Myr timescale following final coalescence and are faint compared to the light of the galaxy (e.g., Hung et al. 2014; Wen & Zheng 2016). This means that they fade at large distances due to surface brightness dimming. Kinematic disturbance in the stars of a galaxy can persist for longer (up to \sim Gyr after final coalescence; Hung et al. 2016). Additionally, they more directly track the dynamical history of the galaxies by probing baryonic matter and dark matter, which can trace the interaction and growth histories of galaxies (Glazebrook 2013). It is also possible that kinematic predictors may clear up ambiguities from imaging; for instance, some clumpy star forming galaxies appear to be mergers in imaging due to their disturbed morphologies (Miralles-Caballero et al. 2011; Petty et al. 2014), yet some appear to be nonmerging spiral galaxies that simply have clumps of star formation in their centers or in their spiral arms (Alonso-Herrero et al. 2006; Haan et al. 2011). This type of clumpy star-forming galaxy is even more abundant at intermediate and high redshifts, where a higher fraction of galaxies are expected to be actively merging, yet many isolated (non-merging) galaxies are also inherently clumpy (e.g., Guo et al. 2015). Since high-redshift galaxies present a host of additional complications, in this work we focus on local galaxies in order to develop the groundwork for a method that could eventually be extended to the more distant universe.

However, like every other merger identification tools, kinematic predictors also come with their own set of ambiguities and limitations. For instance, in gas-rich mergers, disks are able to survive the merger and these recently-merged galaxies can masquerade as isolated disk galaxies. Hung et al. (2015) find that relying upon kinematics alone to classify a sample of ULIRGs identifies many merging galaxies as isolated disks and would provide a false negative merger identification for up to 50% of ULIRGs. Additionally, the identification

technique depends strongly on the merger stage and the choice of kinematic predictor. Other work confirms that some mergers with highly disturbed visual morphology exhibit a distinct lack of disturbance in the stellar kinematics (Bellocchi et al. 2013; Hung et al. 2016). It is therefore important to probe the kinematics of merging galaxies using simulations in order to understand the biases and limitations of these tools before applying them to real galaxies.

There is currently a wealth of work dedicated to the imaging approach to identifying merging galaxies from large surveys. While there are many detailed case studies of the kinematics of individual local mergers (e.g., Dasyra et al. 2006; Piqueras López et al. 2012), there is a lack of detailed statistical-sized kinematic studies of local mergers. Recent years have brought a revolution in more and more capable integral field spectroscopy (IFS) surveys, creating opportunities to identify merging galaxies using kinematic signatures. Surveys such as CALIFA (Sánchez et al. 2012), SAMI (Bryant et al. 2015), MaNGA (Bundy et al. 2015), and HECTOR (Bryant et al. 2016) offer a promising avenue to study the spatially-resolved properties of an astounding number of galaxies. Here, we focus on the nearing-completion Mapping Nearby Galaxies at Apache Point Observatory (MaNGA) survey. MaNGA is an IFS survey of $>10,000$ local galaxies (with a median redshift $z \sim 0.03$) with a spectral resolution of $R \sim 2000$ and a spatial sampling of $1 - 2$ kpc (Bundy et al. 2015). One of MaNGA’s primary scientific goals is to help disentangle the evolutionary pathways of galaxies and to focus on incorporating simulations of merging galaxies with observations. It is thus uniquely well-suited for this project, where the goal is to create a merger classification technique from the kinematics of simulated galaxies, which we will then apply to the kinematics of the $>10,000$ galaxies in the MaNGA survey in order to identify mergers.

This paper is organized as follows: Section 5.2 reviews the **GADGET-3/SUNRISE** simulations from N19, describes the process of creating mock stellar kinematic maps from the SEDs of the galaxy merger simulations, introduces the kinematic predictors, and reviews the linear discriminant analysis (LDA) technique used in N19 and in this work. Section 5.3 describes the results of the LDA classification, including the coefficients of the LDA, the observability

timescales, and the accuracy and precision of the method. Section 5.4 describes the behavior of the LDA coefficients in the context of previous work on mergers, how the classification changes with mass ratio and gas fraction, and examines the accuracy and precision of the kinematic classification in the context of other tools and statistical methods. We present our conclusions in Section 5.5. A cosmology with $\Omega_m = 0.3$, $\Omega_\Lambda = 0.7$, and $h = 0.7$ is assumed throughout.

5.2 Methods

In order to construct a merger identification framework from the kinematics of simulated galaxies, we follow a detailed procedure to best mimic observations from the MaNGA survey. We first describe the relevant details of the galaxy merger simulations in Section 5.2.1. Then, we describe the process for preparing mock kinematic maps from the simulated galaxies in Section 5.2.2 and discuss how we address AGN contamination in the galaxies in Section 5.2.3. We make the deliberate choice to extract the stellar kinematics from the SEDs produced by **SUNRISE**, as opposed to relying directly on particle velocities. We discuss the implications of this choice and compare the extracted stellar velocity maps and stellar velocity dispersion maps to the inherent velocity of the simulation particles in Section 5.2.4. Finally, we introduce the kinematic predictors that we utilize in the kinematic classification in Section 5.2.5 and briefly introduce the relevant details of the Linear Discriminant Analysis (LDA) technique (from N19) in Section 5.2.6.

5.2.1 GADGET-3/SUNRISE Overview

As in N19, we utilize **GADGET-3/SUNRISE** simulations of merging galaxies. **GADGET-3** (Springel & Hernquist 2003; Springel 2005) is a smoothed particle hydrodynamical (SPH) and N-body code that models processes such as radiative heating, radiative cooling, star formation, supernova feedback, and the multi-phase interstellar medium (ISM) using sub-resolution models. **GADGET-3** also includes SMBH accretion as well as AGN feedback (this is

achieved by coupling 5% of the accreted luminosity to the gas as thermal energy). **GADGET** has been used for many different astrophysical applications, including wide use in studies of merging galaxies (e.g., Di Matteo et al. 2005; Blecha et al. 2011; Snyder et al. 2013; Blecha et al. 2013).

We present the five galaxy merger simulations and the matched isolated merger simulations in Table A.24. These simulations are identical to those used in N19. Three of the simulations are major mergers (where the mass ratio of the progenitors is less than 1:4) and two of the simulations are minor mergers. The major mergers have mass ratios of 1:2, 1:3, and 1:3. The gas fraction of these simulations is $f_{\text{gas}} = M_{\text{gas,disk}} / (M_{\text{gas,disk}} + M_{*,\text{disk}})$. The 1:2 and 1:3 mass ratio major mergers have a relatively high gas fraction of 0.3 and one of the 1:3 mass ratio major mergers has a relatively low gas fraction of 0.1.

We verify that the different gas fractions of the simulations (0.1 and 0.3) are representative of the sample of MaNGA galaxies. The mean gas fraction in MaNGA is defined as:

$$\mu_{\text{gas}} = \frac{\Sigma_{\text{gas}}}{\Sigma_{\text{gas}} + \Sigma_{*}}$$

where Σ_{*} is the stellar mass density and Σ_{gas} is the gas mass density.

Barrera-Ballesteros et al. (2018) find that the mean gas fraction for the MaNGA galaxies has a range of $-1.2 < \log(\mu_{\text{gas}}) < 0$ and a mean value ranging from $\log(\mu_{\text{gas}}) = -0.5$ to $\log(\mu_{\text{gas}}) = -0.8$, which corresponds to gas fractions of 0.16 to 0.32. This means that $f_{\text{gas}} = 0.1$ is below the mean for MaNGA galaxies and thus relatively gas poor, while $f_{\text{gas}} = 0.3$ is at the top of the range of mean values for the sample and relatively gas rich.

These simulations are named for their mass ratio and gas fraction; for instance, the gas rich 1:2 mass ratio major merger is q0.5_fg0.3, the gas rich 1:3 mass ratio major merger is q0.333_fg0.3, and the gas poor 1:3 mass ratio major merger is q0.333_fg0.1. All of the major mergers have a bulge-to-total mass (B/T) ratio of zero. The minor mergers have a

B/T ratio of 0.2, meaning that they are slightly less disk-like than the major mergers and both are gas rich. These simulations are named q0.2_fg0.3_BT0.2 (the 1:5 mass minor merger) and q0.1_fg0.3_BT0.2 (the 1:10 minor merger). The isolated galaxies are matched for mass and gas fraction to each of the simulations. Some simulations have more than one matched isolated galaxy, but for the case where there is only one isolated galaxy, it is matched to the mass of the larger merging galaxy from the corresponding merger simulation. We additionally define snapshots of each simulated merger that fall before first pericentric passage or > 0.5 Gyr after final coalescence as isolated galaxies.

We couple **GADGET-3** with **SUNRISE** in order to directly compare the simulated galaxies with observations. **SUNRISE** is a 3D polychromatic Monte-Carlo dust radiative transfer code (Jonsson 2006; Jonsson et al. 2010). We utilize the same **SUNRISE** snapshots from N19 along with the full SEDs from the seven isotropically positioned viewpoints from each merger snapshot to produce the mock datacubes. In N19, we refer to the images produced from the SEDs as ‘snapshots’; in this work, we use the term ‘snapshot’ to refer to the datacube belonging to a single epoch of a merger. These snapshots occur at 50-100 Myr intervals during each merger, and we divide them into early-stage, late-stage, and post-coalescence stage snapshots. We define these stages using the r -band images from N19 where the early-stage mergers have average stellar bulge separations $\Delta x \geq 10$ kpc, late-stage mergers have separations $1 \text{ kpc} < \Delta x < 10 \text{ kpc}$, and post-coalescence mergers are no longer resolvable with separations $\Delta x \leq 1 \text{ kpc}$. With a 50-100 Myr cadence for snapshots, we find that we have 5-10 snapshots for each of these stages.

We utilize the full SEDs from **SUNRISE** to construct the mock datacubes. However, we find that there is an error in the **SUNRISE** approach to computing the shapes of the emission and absorption lines (private communication, Chris Hayward and Raymond Simons). This error applies to the ‘SCATTER’ extensions of the SEDs, which are produced when the dust radiative transfer is turned on, but does not happen for the ‘NONSCATTER’ extensions. The result is artificially broadened emission and absorption lines in the SCATTER

SEDs. To avoid this problem, we utilize only the NONSCATTER extensions. However, the NONSCATTER snapshots do not incorporate the effects of dust on the radiative transfer calculation, and therefore may have a significant effect on our analysis of merging galaxies.

Previous work has investigated the effects of dust in SUNRISE SEDs in depth. For instance, Stickley & Canalizo (2016) compare measurements of the stellar velocity dispersion, specifically $m\sigma_*$ (from the GADGET-3 particle velocity dispersion) to $f\sigma_*$ (from the SUNRISE SEDs, which more closely mimic observations) and find that the offset between the two measurements can be as large as 20-30% for isolated galaxies and as large as 100% for extreme cases such as actively merging systems with disturbed morphologies. When comparing observations to simulations, it is important to incorporate dust, since dust tends to preferentially obscure younger stars, elevating measurements of $f\sigma_*$ relative to $m\sigma_*$. Stickley & Canalizo (2016) find that the distribution of the dust is more important than the total attenuation due to dust in this offset.

By incorporating radiative transfer calculations from everything except dust in our mock datacubes, we predict that we are underestimating the velocity dispersion relative to that of the SCATTER SEDs. We plan to investigate the difference between SCATTER and NONSCATTER in more detail in the future to determine the effects of excluding dust in the current analysis.

5.2.2 Preparing Mock MaNGA Kinematic Maps

To produce stellar kinematics for our sample of simulated galaxies, we mimic the procedure of MaNGA to create a datacube of spectra and then we mimic the MaNGA Data Analysis Pipeline (DAP) to extract stellar kinematics to use in our kinematic classification. Examples of finalized MaNGA-ized stellar velocity maps are presented in Figure 5.1 alongside the r -band flux maps. In this section, we describe how we mimic the observational techniques of MaNGA to degrade the spatial and spectral resolution of the simulations to create a MaNGA-ized datacube, place an appropriately sized fiber bundle over each galaxy,

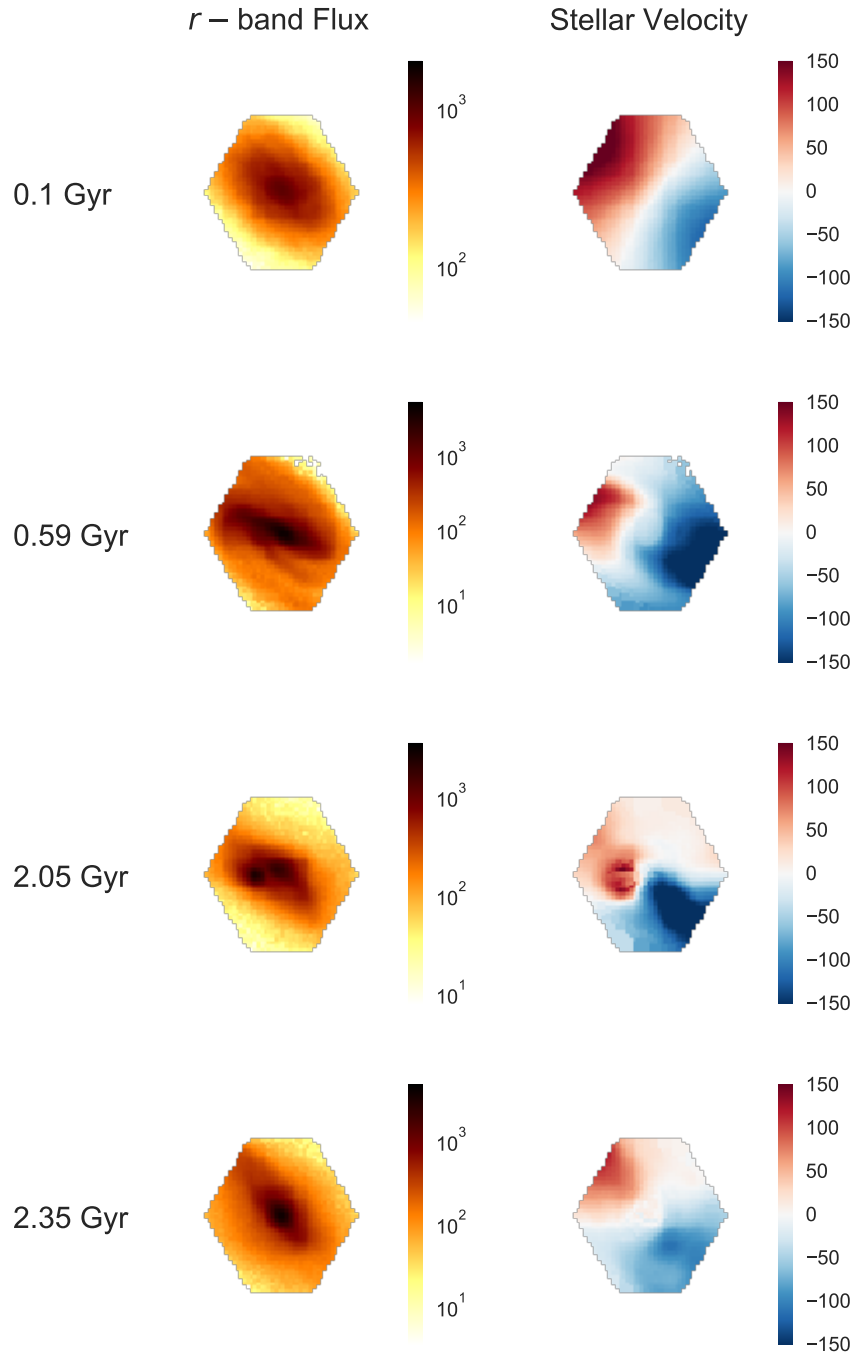


Figure 5.1: Snapshots of images and stellar velocity maps from the q0.5_fg0.3 simulation. We include snapshots that are used as isolated galaxies (before first pericentric passage; top row), early-stage mergers (second row), late-stage mergers (third row), and post-coalescence mergers (bottom row). The colorbar for the left column is in units of counts while the velocity bar for the right column is in km s^{-1} .

and fit each spaxel with **ppxf** (a penalized pixel-fitting method from Cappellari & Emsellem 2004; Cappellari 2017) to obtain the velocity and velocity dispersion of the stars at each spatial position.

We first describe the specifications of the MaNGA survey, which are key for producing mock kinematic maps. MaNGA is an imaging and IFS survey. It has a spectroscopic channel spatial resolution of 1-2 kpc; the primary sample of galaxies (which is 2/3 of the full sample) has coverage out to 1.5 times the effective radius of the galaxy (Bundy et al. 2015; Drory et al. 2015). The average redshift of the MaNGA survey is $z \sim 0.03$, and the full range is $0.01 \leq z \leq 0.15$.

To create the mock datacubes, we begin with the 3D SUNRISE SEDs, which we extract at the median redshift of the MaNGA survey ($z = 0.03$). To prepare the mock datacubes, we follow this procedure (which mirrors the MaNGA DAP):

- (1) Convolve the SEDs in the spatial and spectral dimensions.
- (2) Rebin in the spatial and spectral dimensions.
- (3) From the g -band imaging, find the average g -band S/N per spaxel and mask all spaxels that fall below a S/N cutoff value of 1.
- (4) Mask the datacube using the appropriate size of the MaNGA hexagonal fiber bundle based on the effective radius measured from the r -band imaging.
- (5) Introduce noise to each remaining spaxel that is characteristic of the typical inverse variance of the MaNGA data.
- (6) Rebin spatially using a Voronoi binning scheme with g -band S/N of 10.

In more detail, we first convolve the simulated galaxy SEDs to match the spatial and spectral resolution of MaNGA. The spatial resolution of MaNGA is $2''.5$, so we convolve the spectral cubes with a $2''.5$ FWHM PSF in the spatial direction. Then, we convolve

the extracted spectra to match the spectral resolution of the BOSS spectrographs used by MaNGA ($\lambda/\Delta\lambda \sim 2000$) using an adaptive rebinning procedure.

After convolving the spectra spatially and spectrally, we rebin to match the wavelength and spatial sampling of MaNGA, which involves creating $0''.5$ sized spatial pixels (known as spaxels). The next step is to utilize the **SUNRISE** g -band and r -band images to determine which spaxels to include in the subsequent steps. We follow the procedure in N19 to convolve, rebin, and introduce noise characteristic of SDSS g - and r -band images. The spatial convolution uses a $1''.61/1''.43$ FWHM PSF and the noise has a mean value of $0.77/0.33$ dn and a standard deviation of $3.73/5.23$ for the g -band/ r -band imaging. We rebin the images to match the spatial binning of the mock cubes ($0''.5$). Then, we mask all spaxels that have a g -band S/N less than one (Westfall et al. 2019).

From the r -band imaging, we use **statmorph** (Rodriguez-Gomez et al. 2019) to measure the imaging position angle (PA_{img}), which we will later use to compare to the kinematic position angle. We also measure the half light radius using **statmorph** and use this value to determine which sized hexagonal fiber bundle to use to mask the mock datacube. MaNGA has five different fiber bundles, equipped with 19, 37, 61, 91, and 127 fibers (the largest fiber bundle is known as the ‘frankenbundle’); each fiber has a $2''.0$ diameter with $2''.5$ spacing between fibers (Yan et al. 2016a; Wake et al. 2017). These fiber bundles range from $7''.5$ to $32''.5$ in diameter. The primary MaNGA sample is covered to 1.5 effective radii (R_e) and the secondary sample is covered to $2.5 R_e$. We cover our galaxies to $1.5 R_e$ since the majority of galaxies are included in the primary sample and select the appropriate fiber bundle to obtain this coverage. We select the smallest fiber bundle if the angular extent of the galaxy is smaller than $7''.5$ and the largest fiber bundle if the angular size exceeds $32''.5$. We mask each datacube using the appropriate hexagonal size and the following steps apply to the unmasked spaxels.

Next, we introduce noise to each spaxel using the typical inverse variance (ivar) of the MaNGA datacubes. We average the median inverse variance trend for the central spaxel of

20 MaNGA galaxies and convert to a median S/N value (Figure 5.2). These 20 galaxies are randomly selected from each fiber bundle (we choose four galaxies per fiber bundle). We test how this trend changes for the location of the spaxel with relation to the center of the galaxy and find that there is less variation with location in the galaxy than between different MaNGA galaxies. We utilize this median S/N trend with wavelength to introduce fake noise to each spaxel at each wavelength bin. We multiply the noise value by a random normal Gaussian with a mean of zero and a standard deviation of one. We find that the noise level is very low relative to the signal (Figure 5.3) and has a minimal effect on the `ppxf` fit and subsequent errors on the kinematic maps.

Our final step prior to fitting for the stellar velocity and velocity dispersion is to introduce a Voronoi binning scheme to the datacubes (Cappellari & Copin 2003). We create spatial bins that have a g -band S/N of 10, reproducing the procedure described in Westfall et al. (2019). When a Voronoi bin contains more than one spaxel, the new spectrum is the masked average of all constituent spectra while the error spectrum for that bin is determined by co-adding the percent error spectra in quadrature. We account for covariance between neighboring spaxels in our Voronoi bin calculation. In order to avoid the computational cost of incorporating the covariance matrix for all spaxels, we instead use the correction from Law et al. (2016) for the Voronoi bins that have more than one spaxel. The correction is a factor of the number of spaxels in a bin (N_{bins}):

$$n_{\text{measured}}/n_{\text{no covar}} = 1 + 1.62 \times \log(N_{\text{bins}})$$

where n_{measured} is the corrected noise level after the correction is applied to the co-added error where covariance is not considered ($n_{\text{no covar}}$).

We have now completed the steps that prepare the mock datacubes for fitting with `ppxf`. We summarize the steps of this procedure visually in Figure 5.3.

The final step of the creation of mock kinematic maps is to pass the Voronoi binned spectra through `ppxf` (Cappellari & Emsellem 2004; Cappellari 2017). `ppxf` is a penal-

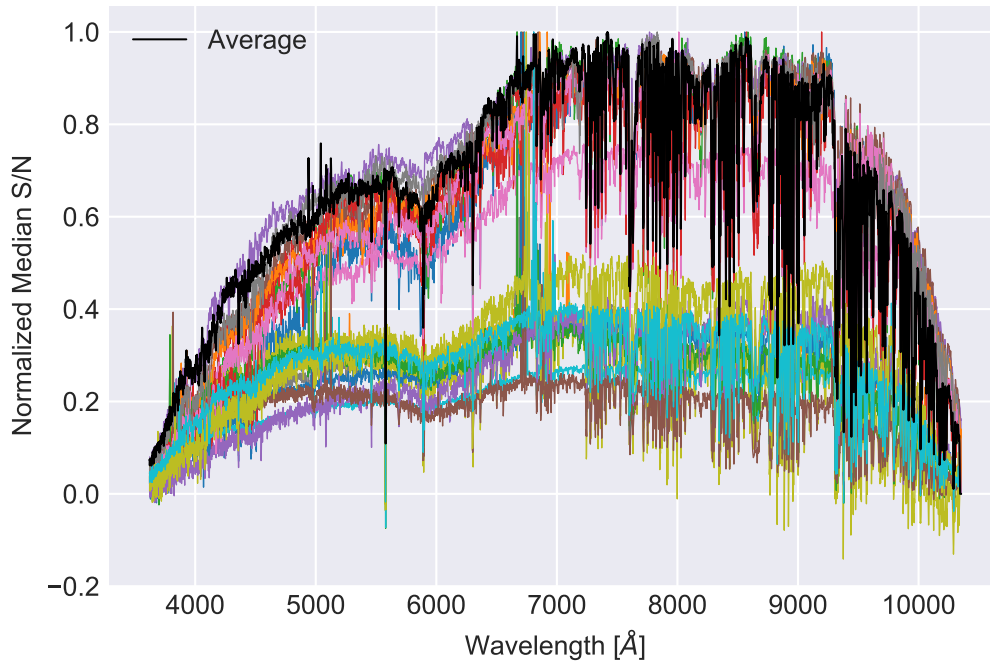


Figure 5.2: Normalized median trend of the S/N with wavelength for the central spaxel of 20 MaNGA galaxies. The largest variation happens galaxy to galaxy as opposed to spaxel to spaxel, so we take the average S/N spectrum (black) to use as our characteristic S/N, which we scale to the flux of each simulated spaxel to produce an error spectrum.

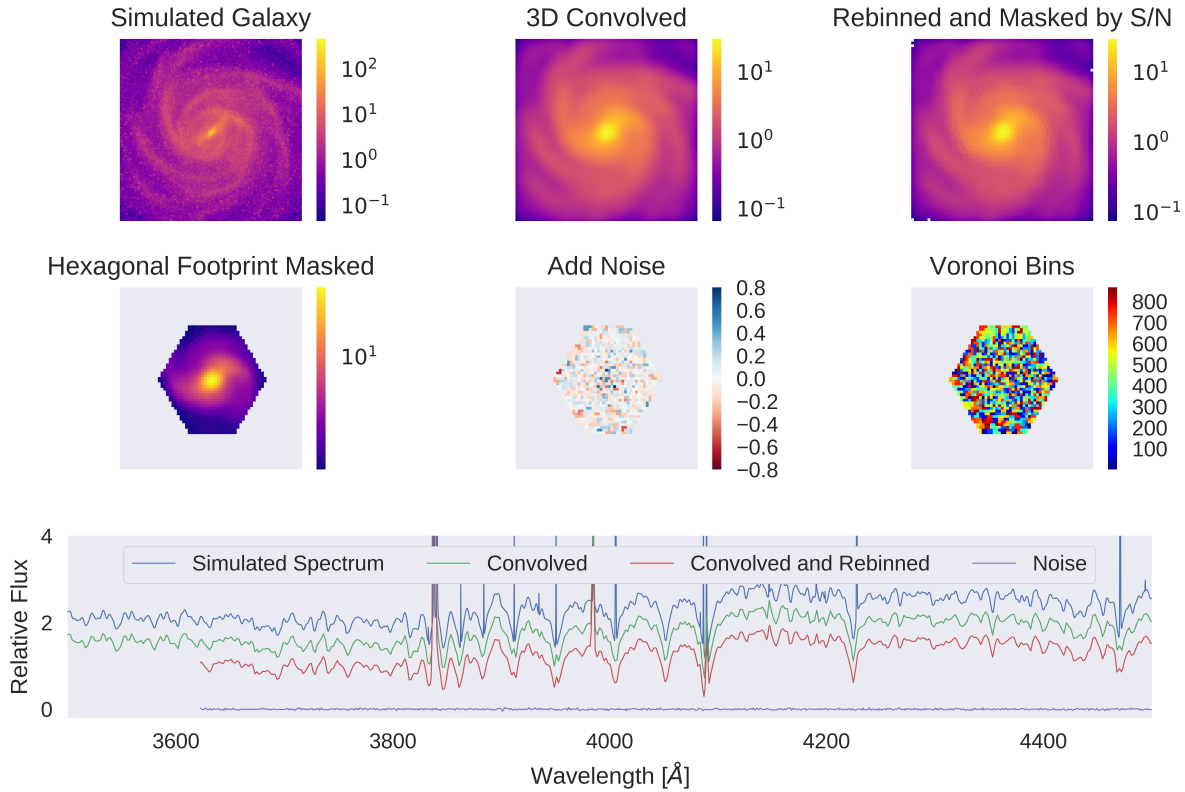


Figure 5.3: An illustration of the process of creating MaNGA-ized datacubes from the simulated datacubes. All images are $32''$ by $32''$. We first convolve the cubes spatially and spectrally using a spatial kernel with a FWHM of $2''.5$ and convolving to a spectral resolution of $R \sim 2000$ (top middle). We then rebin to $0''.5$ spaxels and the spectral sampling of MaNGA and mask using a g -band S/N value of one (top right). Next, we choose the appropriately sized hexagonal footprint based on the half light radius in the r -band imaging and use this to further mask the datacube (middle left). Then, we add noise that is characteristic of the typical inverse variance of MaNGA datacubes (middle middle). We introduce this noise using a Gaussian randomization for every wavelength unit. Finally, we rebin using a Voronoi binning scheme, with an assigned S/N per Voronoi bin of 10 (middle right). The average spectra for each step are shown in the bottom panel, where we scale the flux to be offset for each step for display purposes.

ized pixel-fitting method which assumes that a galaxy spectrum is a combination of stellar templates that are convolved with the line-of-sight velocity distribution (LOSVD) function.

In order to prepare the datacube for `ppxf`, we follow these steps from the DAP:

- Normalize the flux data so that the mean over all templates is unity.
- Mask the spectra to match the wavelength range of the `MILES-HC` library (3600-7400 Å).
- Mask the emission lines using the DAP module `StellarContinuumBitMask()`.

After the preparatory steps are completed, we run `ppxf` in two fit iterations, as in Westfall et al. (2019). Using the same techniques as the MaNGA DAP, we utilize the `MILES-HC` spectral library to globally fit each datacube and then individually fit each spatial bin using the templates that are selected by the global fit. The final product of our MaNGA-izing procedure is a stellar velocity map and a stellar dispersion map, both with associated error maps from the fit to the stellar continuum. We show the example maps in the right hand column of Figure 5.1.

5.2.3 AGN Contamination

We find that the AGNs that turn on during the gas rich major merger simulations are major contaminants to fitting the stellar kinematics. In other words, `ppxf` and the MaNGA DAP are not equipped to fit broad AGN emission lines and regions with elevated continuum from the AGNs. This AGN-dominated emission swamps out the stellar absorption lines; MaNGA active galaxies are plagued by this same problem, and the AGNs are often masked by the DAP fitting procedure. An example of this failure to fit the stellar kinematics is shown in Figure 5.4, in the stellar velocity and stellar velocity dispersion maps for a snapshot the q0.5_fg0.3 simulation with strong AGN emission.

The simulation suite was originally created in Blecha et al. (2013) to determine the timeline of the activation and fueling of AGNs during mergers. However, most MaNGA

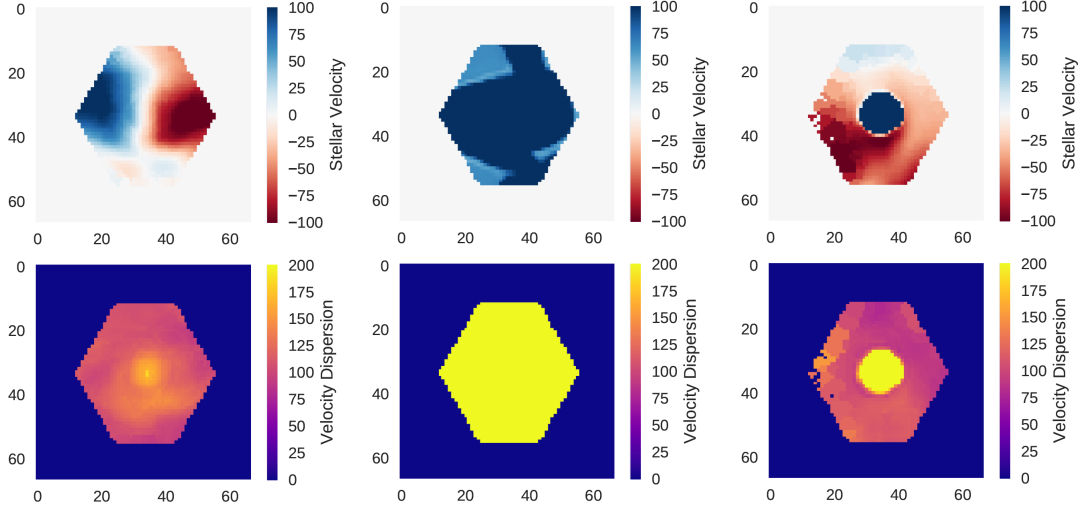


Figure 5.4: Stellar velocity (top) and stellar velocity dispersion (bottom) maps for a snapshot of the `q0.5_fg0.3` simulation without an AGN (left) and with the AGN (middle). We also show an additional viewpoint of the same snapshot with the AGN (right). When the AGN is not removed, `ppxf` is unable to fit the absorption lines and the values of stellar velocity and stellar velocity dispersion converge at the bounds of `ppxf`, which are 1000 km s^{-1} for both velocity and velocity dispersion. These snapshots are not reliable for the extraction of the kinematic predictors. In the middle case, the AGN is bright enough from this viewpoint to contaminate the entire datacube; at the right, the AGN simply leaves a ‘hole’ with a 1000 km s^{-1} velocity and velocity dispersion of size $2''.5$ in the center of the galaxy, which is the size of the spatial resolution of MaNGA.

galaxies do not host AGNs, and it is therefore unrealistic to use a simulation suite that is dominated by AGNs to classify MaNGA galaxies. The other side of this problem is that it is very difficult to measure the values of kinematic predictors when there is a hole in the datacube. We explore multiple different options for removing the AGN contamination. The simplest approach is to rerun the simulations without AGNs. Another approach is to determine the PSF of the AGN emission and subtract this from the datacube and then fit the stellar kinematics.

We take the first approach. We rerun the q0.5_fg0.3 and q0.333_fg0.3 snapshots that have AGN contamination (quantified as those where any spaxel converges to a value >1000 km s $^{-1}$, which indicates that `ppxf` failed to fit the spatial bin due to continuum contamination from an AGN). In Nevin et al. (2019, in prep) we plan to return to this issue and explore the option of fitting the wavelength-dependent AGN PSF to remove the contamination for future work. In this way, when we apply the imaging + kinematic identification to real MaNGA galaxies, we can also apply it to active galaxies.

In N19, we did not consider AGN contamination, meaning that the imaging side of the technique is developed with the AGNs present. Since we did not remove the AGNs from the N19 analysis, they could be enhancing the r -band concentration of the gas rich major mergers. However, we find that the AGNs are active during the majority of the mergers, and remain active for >0.5 Gyr following the final coalescence. This means that the concentration of the light in the postmerger isolated galaxies is also enhanced, so the AGNs are not only affecting the merger snapshots.

Additionally, the most important predictors for the gas rich major mergers are asymmetry-based, which indicates that the classification relies more on the lower surface brightness features of the major mergers and is not dominated by the central AGN light. We plan to readdress the AGN contamination concern in both kinematics and imaging in Nevin et al. (2019, in prep).

5.2.4 Comparing Velocity Maps

To verify our methodology of creating the kinematic maps, we compare the extracted stellar kinematics (from the MaNGA-ized NONSCATTER SUNRISE SEDs) to the particle velocity and velocity dispersion (directly from GADGET-3) in Figure 5.5.

We find that the velocity maps extracted from the SEDs match the particle velocities within 1σ errors (upper row). We also find that the stellar velocity error increases with decreased S/N as expected. We find a larger difference between the particle velocity dispersions (mass-weighted) and the stellar velocity dispersions from the MaNGA-ized NONSCATTER SEDs (flux-weighted). The stellar velocity dispersion from the NONSCATTER SEDs is slightly elevated relative to the particle velocities. Although we do not include the effects of dust since these are the NONSCATTER SEDs, the velocity dispersion could still be affected by the location of the stellar populations in the merger. This effect is another motivation for more directly investigating the difference between the inclusion and exclusion of dust on the SEDs.

5.2.5 Preparing Kinematic Predictors

Next, we describe the predictors extracted from the stellar kinematic maps. We specifically focus on the stellar kinematics, as opposed to the gas kinematics, since the stellar kinematics more directly trace the assembly histories of galaxies while the gas kinematics can also trace gas inflows and outflows.

The kinematic predictors are based on previous work to identify merging galaxies from the stellar kinematics of observed and simulated galaxies. All of these predictors are sensitive to different orientations, merger stages, and/or merger mass ratios and gas fractions of merging galaxies. Our goal is to combine them into one LDA classification to best identify a variety of different types and epochs of merging galaxies.

We use multiple kinematic predictors from galactic disk fitting codes as well as indepen-

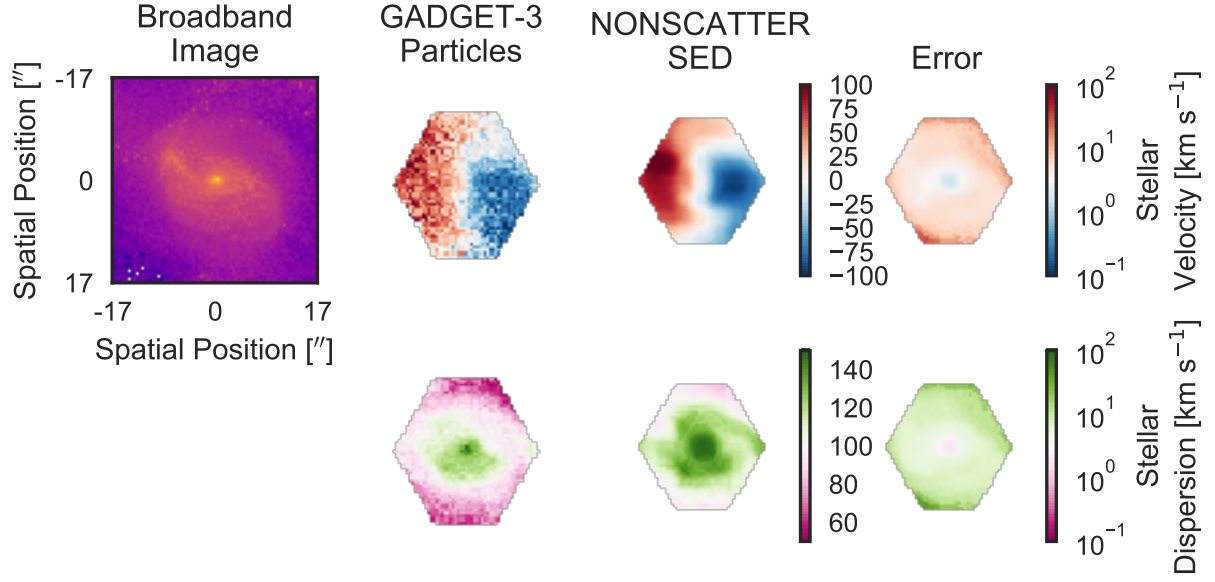


Figure 5.5: A comparison of the stellar velocity and velocity dispersion maps for a galaxy snapshot. We show the summed broadband flux over all wavelength channels (left top). We include a comparison between velocities in the top row and velocity dispersions in the bottom row, where the **GADGET-3** particle velocities and velocity dispersions are in the middle left column, the velocity and velocity dispersions measured from the MaNGA-ized **SUNRISE** SEDs are in the middle right column, and the error maps for the MaNGA-ized **SUNRISE** SEDs are in the rightmost column.

dent kinematic predictors such as λ_{R_e} , which is a measurement of the angular momentum. We first describe the kinematic predictors that we extract from the disk fitting codes.

We utilize the Radon Transform from Stark et al. (2018). It is a simple, non-parametric tool for characterizing velocity fields. To measure the Radon Transform, we first transform the velocity maps into circular coordinates. The velocity maps are parameterized using ρ and θ . Given some spaxel on the velocity map, ρ is the distance between the spaxel and the center of the velocity map, which is also known as the kinematic center of the galaxy (defined below), and θ is the angle between the positive x-axis and the line segment from the kinematic center to the spaxel. θ ranges from 0 to 180 in the CCW direction and ρ is from $-\infty$ to ∞ , where negative values of ρ describe the portion of the velocity map below the positive x-axis. The Radon Transform is defined as:

$$R(\rho, \theta) = \int_0^L v(x, y) dl$$

where the velocity is summed over a line integral, where the line is perpendicular to the kinematic center of the galaxy, and defined by the point (ρ, θ) . L is the length of a line segment that extends to the edge of the velocity map.

The Radon Transform is calculated at all values of ρ and θ . We additionally calculate the Absolute Radon Transform, R_A , and the bounded Absolute Radon Transform, R_{AB} . The Absolute Radon Transform is instead integrated over the absolute value of the difference between the velocity at each point and the mean value along the line segment, and the bounded Absolute Radon Transform is only integrated over a limited distance, which is often defined in terms of the effective radius of the galaxy. Both are described in more detail in Stark et al. (2018). As in Stark et al. (2018) we follow the procedure to integrate R_{AB} over an aperture distance of $r_{ap} = R_e$ where R_e is the effective radius in the r -band imaging.

We present the bounded Absolute Radon Transform in Figure 5.6, where we also compute the Radon profile. The Radon profile is the best fit value of θ ($\hat{\theta}$), or the estimated

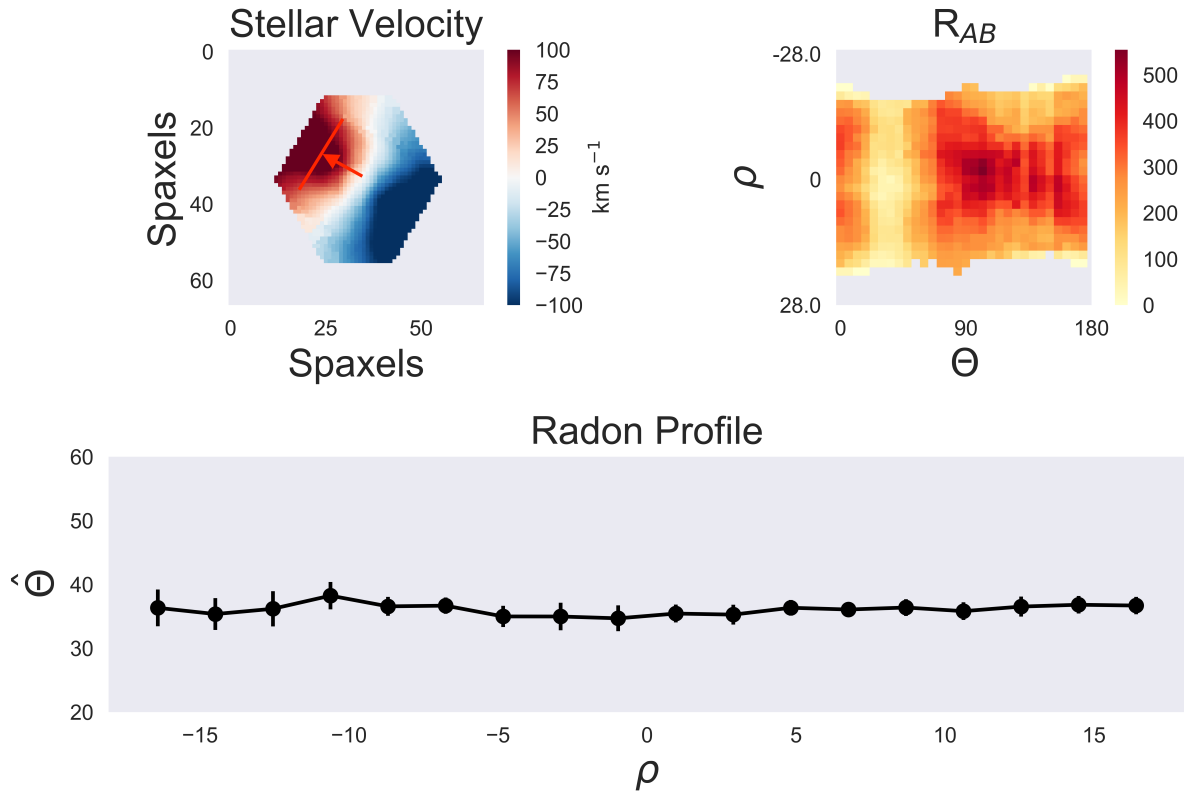


Figure 5.6: Stellar velocity map (left top), bounded Absolute Radon Transform (right top), and Radon Profile (bottom). The velocity field can be transformed into θ and ρ coordinates, where $\theta \subseteq [0, 180]$ and $\rho \subseteq [-\rho, +\rho]$, where the location ($\theta=35$, $\rho=10$) is indicated by the upward left pointing arrow. θ is measured CCW from the top of the map. The bounded Absolute Radon Transform is then calculated by creating line integrals over a grid of (ρ, θ) positions, where the line is perpendicular to the kinematic center of the map. It is bounded, since the line integral is limited to the length R_e . The units on the colorbar are km s^{-1} . We find the minima (shown in lighter yellow) of R_{AB} at each ρ , to measure the Radon Profile (bottom). In this case, $\hat{\theta}$ is ~ 35 , which is the axis of maximal rotation, or the kinematic PA.

kinematic position angle, for each value of ρ from the bounded Absolute Radon Transform. In other words, it is the minimum (in lighter yellow in Figure 5.6) at each value of ρ of the R_{AB} map. Since the kinematic position angle is determined at each value of ρ , it is not global. The estimated value $\hat{\Theta}$ follows the direction of maximal rotation in the stellar velocity maps and is therefore the kinematic PA. The deviation of $\hat{\theta}$ from a straight line can reveal how much the velocity map of a galaxy deviates from ordered rotation.

We also follow the procedure from Stark et al. (2018) to determine the galaxy’s kinematic center. We use the photometric center as the initial input, but find that the photometric center is not always the same as the kinematic center. Since an incorrect kinematic center can cause variations in the calculation of the Radon Transform, we directly determine the kinematic center using the Radon profile and then utilize the kinematic predictors extracted using this kinematic center. The kinematic center is the location where the weighted kinematic asymmetry (A) is minimized, which is the asymmetry in the Radon profile or $\hat{\theta}$ values, which are measured from the bounded Absolute Radon Transform. A is also a kinematic predictor that we utilize in our classification scheme, which is defined as:

$$A = \frac{\sum |\hat{\theta} - \hat{\theta}_{flip}|}{2N_{i,j}} w_{i,j}$$

where $\hat{\theta}$ is reversed to make $\hat{\theta}_{flip}$ and $N_{i,j}$ is the number of values in the $\hat{\theta}$ array at the current ‘center’, and $w_{i,j}$ is a weight factor:

$$w_{i,j} = \frac{N_{0,0}}{N_{i,j}}$$

where $N_{0,0}$ is the number of values at the photometric center.

We iteratively measure A in a 3×3 spaxel grid centered on the photometric center, and select the spaxel with the lowest value as the kinematic center, while taking the minimized A value as our A predictor for each snapshot. If the spaxel with the lowest value of A is consistent within errors with the photometric center, we select the photometric center as the kinematic center. If the spaxel with the lowest value is on the edge of the spaxel grid, we

expand the grid by a factor of two and rerun the determination of the kinematic center.

If the kinematic center is again at the edge of the grid, we do not expand the grid, but take the photometric center as the kinematic center. In this case, the kinematic center is not well-determined, often due to a disorganized velocity map, so the photometric center is a fair guess for the kinematic center. In Stark et al. (2018), the galaxies where the kinematic center is not well-determined are eliminated from the analysis, but in this case, there are a large fraction of galaxies that have disordered kinematics, so we include them in the analysis, using photometric center as the kinematic center.

We also quantify the asymmetry of the Radon profiles using the kinematic predictor A_2 , also from Stark et al. (2018):

$$A_2 = \sum_i \frac{\delta\hat{\theta}}{\sigma_{\delta\hat{\theta},i}}$$

where $\delta\hat{\theta}$ is the absolute magnitude of the difference between θ_i on one side of the Radon profile to the other (same ρ , different sign), $\sigma_{\delta\hat{\theta}}$ is the uncertainty on $\delta\hat{\theta}$, and the expression is summed over the i values of $\hat{\theta}$.

We use both A and A_2 as kinematic predictors in this analysis; both terms incorporate the absolute magnitude of the difference between the measured kinematic PA on one side of the galaxy to the other. We therefore expect that A and A_2 will be enhanced for merging galaxies, since mergers can introduce warps in the stars in a galaxy (e.g., Shapiro et al. 2008), which cause the kinematic position angle to change with radius.

When we extract the kinematic predictors from the Radon Transform, we do not properly treat the uncertainty; we ignore covariance in this calculation. We do so in the interest of computational time, since Stark et al. (2018) utilizes a Monte Carlo process to iteratively compute the Radon profile, or $\hat{\theta}$. This calculation incorporates the covariance between spaxels. By ignoring covariance, we estimate that we underestimate the error on $\hat{\theta}$ by a factor of ~ 5 . While this has an effect on the predictor A_2 , one of the strengths of an LDA analysis is

that it is a relative classification that does not rely upon absolute numbers. We use this to our advantage in this instance. However, this means that we cannot use the $A_2 > 3$ cutoff from Stark et al. (2018) as a direct indication of an asymmetric galaxy.

We next use the LOSVD (line of sight velocity distribution) fitting program **kinemetry** to extract the velocity and velocity dispersion moments from the stellar velocity maps. Our goal is to quantify the chaotic velocity patterns expected for interacting systems in the velocity and velocity dispersion maps using the degree of kinematic asymmetries from the **kinemetry** output. Specifically, we utilize the technique from Shapiro et al. (2008) and Hung et al. (2016), which uses the higher order terms of the LOSVD to define kinematic asymmetry. We also use **kinemetry** to measure the global kinematic position angle (PA_{kin}), which is the major axis of the best fit model of a rotating disk. We describe **kinemetry** in this section and how we apply it to the stellar kinematics.

Functionally, **kinemetry** fits the line of sight velocity and velocity dispersion maps by dividing them into a set of nested elliptical rings. The best fit model at each radius is fit using different values of PA and flattening factor $q = 1-e$, where e is the ellipticity of the ring in the plane of the galaxy. These models use a decomposition of the moment maps into harmonic Fourier coefficients in polar coordinates. For instance, the velocity or velocity dispersion map, $K(r, \psi)$ can be expanded into a finite number of harmonic frequencies:

$$K(r, \psi) = A_0(r) + \sum_{n=1}^N A_n(r) \sin n\psi + B_n(r) \cos n\psi$$

where r is the semimajor axis of the ellipse, ψ is the azimuthal angle, $A_0(r)$ is the systemic velocity, N is the number of ellipses fit, and A_n and B_n are the coefficients of the harmonic expansion. The best-fitting ellipses are obtained by minimizing χ^2 for the linear combination of the A_n and B_n coefficients. The amplitude and phase coefficients (k_n and ϕ_n) can be calculated from the A_n and B_n coefficients:

$$k_n = \sqrt{A_n^2 + B_n^2}$$

$$\phi_n = \arctan\left(\frac{A_n}{B_n}\right)$$

An ideal rotating disk can be described using only the B_1 term, which represents the cosine term for the circular velocity of a galaxy's rotating disk:

$$V(r, \psi) = V_c(r) \sin i \cos \psi$$

where r is the radius in the plane of the galaxy, ψ is the azimuthal angle, $V_c(r)$ is the circular velocity, and i is the inclination of the galaxy disk.

The higher order A_n and B_n terms represent deviations from an ideal rotating disk. We quantify these perturbations with v_{asym} and σ_{asym} , which are measured from the k_n amplitude coefficients of the model velocity and velocity dispersion maps, respectively (Krajnovic et al. 2006; Shapiro et al. 2008; Hung et al. 2016; Bellocchi et al. 2016):

$$v_{\text{asym}} = \left\langle \frac{\sum_{n=2}^5 k_{n,v}/4}{B_{1,v}} \right\rangle_r, \quad \sigma_{\text{asym}} = \left\langle \frac{\sum_{n=1}^5 k_{n,v}/5}{A_{0,v}} \right\rangle_r$$

where the expression is averaged over all radii, r . The amplitude coefficients, $k_{n,v}$, are summed and averaged for the n higher order moments. We exclude the $k_{1,v}$ term from the calculation of v_{asym} since it represents radial outflow, which is not associated with stars (Shapiro et al. 2008). We normalize v_{asym} by the circular velocity term and σ_{asym} by the A_0 term, which is the amplitude of the velocity dispersion maps, as in Krajnovic et al. (2006).

v_{asym} and σ_{asym} increase for disordered velocities and velocity dispersions. While this effect is more dramatic for ionized gas (Shapiro et al. 2008), we also expect that disordered stellar velocity and stellar velocity dispersion fields should also lead to enhanced v_{asym} and σ_{asym} values.

To determine the best fit Fourier coefficients to calculate v_{asym} and σ_{asym} , we run **kinemetry** multiple times. We center on the kinematic center, which is defined from the Radon Transform. We first allow the best fit PA to vary for each elliptical radius fit. After determining a median value of the PA, or the global PA (PA_{kin}), we then allow the value of q to vary, which is the ellipticity. After determining the global values for PA and q , we

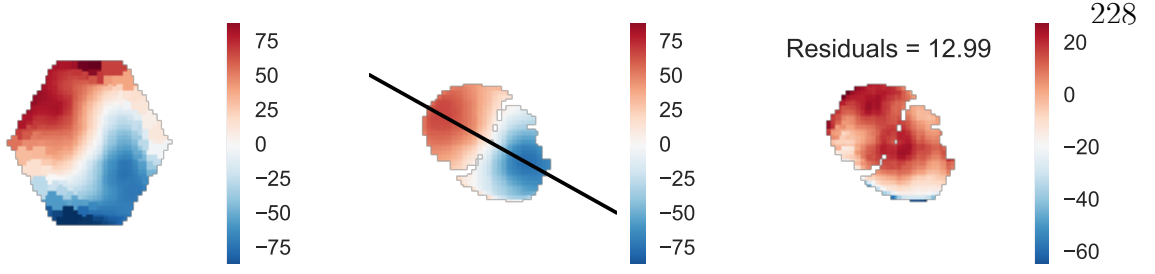


Figure 5.7: Example **kinemetry** fits to a galaxy with observed stellar velocity map (left), best fit **kinemetry** model (middle), and $v_{\text{obs}} - v_{\text{kinemetry}}$ residual map (right). The color bar shows the velocity in km s^{-1} . We utilize the residuals as a predictor, which we refer to as ‘resids’ or ‘**kinemetry** residuals.’

do a final run to determine the values of the higher order kinematic moments and therefore v_{asym} and σ_{asym} , which are the kinematic predictors we use in our LDA technique. We then compare the PA of the kinematic major axis (PA_{kin}) from **kinemetry** to the imaging major axis (PA_{img} , measured using **statmorph** from the r -band imaging) to create our predictor ΔPA (Barrera-Ballesteros et al. 2015). Since ΔPA traces the recent global misalignments of stars, it should be elevated for the merging galaxies.

The final predictor that we extract using the **kinemetry** fitting process is the velocity residuals or ‘resids’, as we refer to it. This predictor is quantified:

$$\text{resids} = \frac{\sum_{i,j}^N |v_{\text{obs}} - v_{\text{kinemetry}}|}{N}$$

where v_{obs} is the observed velocity map, $v_{\text{kinemetry}}$ is the best fit model from **kinemetry**, and N is the number of spaxels fit. We include this normalization factor in order to penalize the fits that converge to a very inclined galaxy in order to avoid fitting disordered kinematics in the exterior regions of the galaxy. We show an example of a simulated galaxy snapshot from the q0.5_fg0.3 simulation fit with **kinemetry** and its velocity residuals in Figure 5.7.

Finally, we extract λ_{R_e} , the specific angular momentum, which is defined by Emsellem et al. (2007):

$$\lambda_{R_e} = \frac{\langle R|V| \rangle}{\langle R\sqrt{V^2 + \sigma^2} \rangle} = \frac{\sum_{n=1}^N F_n R_n |V_n|}{\sum_{n=1}^N F_n R_n \sqrt{V_n^2 + \sigma_n^2}}$$

where F_n is the (r -band) flux, R_n is the distance from the kinematic center, V_n is the stellar velocity, and σ_n is the stellar velocity dispersion. λ_{R_e} is only measured to the r -band effective radius.

The ellipticity of a galaxy, ϵ , is measured from the r -band photometry. ϵ is specifically extracted using **statmorph**, and is distinct from the ellipticity parameter used by **kinemetry** to fit rotation curves.

Both λ_{R_e} and ϵ can be used in combination to define the fast/slow rotator division for elliptical galaxies from Emsellem et al. (2011):

$$\lambda_{R_e} < 0.08 + \epsilon/4$$

where slow rotators fall below this line.

This division is discussed in more detail as it applies to the simulated galaxies in this work in Section 5.3.3. In Emsellem et al. (2004) and Smethurst et al. (2018), it is applied to galaxies in the SAMI and MaNGA surveys, where it is used to divide the galaxies with disordered or slow rotation from the galaxies with fast or organized rotation.

The more predictive of the two axes of this classification is λ_{R_e} , which decreases more dramatically for galaxies with more disordered rotation, so we predict that it will decrease for merging galaxies. While ϵ is technically an imaging predictor, we include it in this work for direct comparison with previous papers that examine fast/slow rotators. Since $\epsilon = 0$ is a more spherical galaxy, we predict that ϵ will decrease slightly for the post-coalescence stages of the merger, where the extended tidal features have faded, and the light is more concentrated, as we found in N19.

To summarize, we extract the following kinematic predictors: ΔPA , v_{asym} , σ_{asym} , resids , λ_{R_e} , ϵ , A , and A_2 .

5.2.6 Linear Discriminant Analysis

The classification in this work relies upon a LDA technique that separates nonmerging galaxies from merging galaxies based upon a combination of the input kinematic predictors. This same technique was presented in N19, but for imaging predictors. Here, instead of including all of the kinematic predictors in the final classification, we first utilize the LDA technique as a selection technique to determine which predictors are most informative and then create the final classification based on these selected predictors. In order to directly compare the imaging classification to the kinematic classification, we utilize the same snapshots from all simulations.

Relevant details of the LDA technique from N19 include:

- All predictors are standardized prior to the LDA technique, meaning that predictors with higher values (such as A_2) do not have an outsized effect on the analysis.
- We utilize priors on the relative fraction of merging and nonmerging galaxies in nature vs in the simulations; this accounts for the fact that we have more merging galaxy snapshots (relative to nonmerging snapshots) for each simulation. We use the same priors from N19; $f_{\text{merg}} = 0.1$ for the major mergers and $f_{\text{merg}} = 0.3$ for the minor mergers.
- We include interaction terms to explore correlations between predictors.
- Machine learning techniques like LDA do not often come with statistical errors on the returned classification coefficients. Therefore, we use k -fold cross-validation in order to obtain 1σ errors on the predictor coefficients.
- In order to select which coefficients are necessary for the classification, we use a forward stepwise selection technique, which orders and includes only the relevant terms and interaction terms.

For complete details, including the full mathematical formulation for LDA, see N19.

5.3 Results

After creating mock MaNGA datacubes from the five simulations of merging galaxies (with matched isolated galaxies), we extract the eight kinematic predictors introduced in Section 5.2.5 (ΔPA , v_{asym} , σ_{asym} , resids , λ_{Re} , ϵ , A , and A_2). Our next step is to prepare the input data for the LDA, initialize the classification by running the LDA as first a predictor selector (to eliminate unnecessary predictors), and then rerun it as a classification. We describe our process for preparing the data and examining it in the context of assumptions of LDA in Section 5.3.1, the selection process in Section 5.3.2, and the final classification results in Section 5.3.3. In Section 5.3.3, we also combine the major and minor mergers into a combined ‘Major Merger’ and ‘Minor Merger’ classification, respectively, as in N19. We do this with our ultimate goal in mind, which is to create a combined imaging and kinematic classification in Nevin et al. (2019, in prep) that we will apply to the galaxies in MaNGA. Finally, we measure the observability timescales for the kinematic classifiers in Section 5.3.4 and the accuracy and precision of the LDA classification for each simulation in Section 5.3.5.

5.3.1 LDA Data Preparation

LDA assumes multivariate normality, homoscedasticity, and the absence of multicollinearity, meaning that all the predictors are normally distributed, the covariance among the merging and nonmerging classes is equal, the predictors are not strongly correlated with one another, and there are not significant outliers in the data¹. Here, we test these four assumptions by closely examining the data. We carry out the same statistical tests as in N19 to test for normality, homoscedasticity, multicollinearity, and outliers. In N19, for the imaging predictors, we found that the data violated multivariate normality and homoscedasticity while passing the test for multicollinearity and extreme outliers. The kinematic predictors

¹ When we refer to ‘data’ in this section, we mean the set of predictor values for each simulation. For instance, an outlier in the data is a galaxy snapshot for which one or multiple predictor values are outliers relative to the distribution of predictor values of the other galaxy snapshots.

also violate multivariate normality and homoscedasticity; in addition, some predictors are collinear, and there are outliers in the data. In this section, we briefly justify why the data are not normal or homoscedastic, we remove a predictor to eliminate multicollinearity, and we then describe our treatment of outliers.

We conduct a Shapiro-Wilke and Kolmogorov-Smirnov test for normality on the marginalized predictor distributions and are able to reject the null hypothesis that the data are drawn from a normal distribution for the majority of predictors. This means that the marginal distributions are not normal. It naturally extends that the data are not multivariate normal since each individual marginal distribution must be normal and so must their joint distributions. Using visual examination, we find that the predictors have skewed distributions as opposed to multi-modal distributions. Thus, the violation of non-normality is not extreme.

Given that the predictors are not normal, it is unsurprising that the data also violate the homoscedasticity assumption. The covariances for the nonmerging and merging classes are not equal; the Levene test allows us to confirm that the variances between groups are not equal for most predictors. However, as we discussed in N19, LDA is fairly robust to violations of normality and homoscedasticity, and our large sample sizes and standardization of the predictors prior to conducting the LDA make this analysis more robust to these violations (Duda et al. 2001; Li et al. 2006). Additionally, some work has found that if the LDA dataset violates homoscedasticity and has unbalanced priors, the classification will predict in favor of the largest group, which is the nonmergers (Fan & Wang 1999). In our case, this makes for a more conservative classifier that is not prone to misidentify nonmergers as mergers, which minimizes false positives.

We screen for multicollinearity and find that many predictors have positive correlations. All Pearson's r values fall below the value of 0.99, which is the official threshold for complete multicollinearity, so while some of the predictors have high Pearson's r values (A and A_2 have an r -value of 0.97), they do not exceed the limit for multicollinearity. However, we run

an ordinary least squares linear fit on the data and we find that the covariance matrix has a high condition number for many runs; this indicates that while the individual Pearson's r values between predictors do not exceed the 0.99 cutoff, there still may be collinearity within the data. In order to avoid this multicollinearity within the data, we remove the A predictor, which is very similar to the A_2 predictor (they have the same numerator). The A predictor also has less predictive power (than A_2) according to the ordinary least squares linear fit. We remove it and rerun the analysis, finding that our next largest Pearson's r value is ~ 0.6 - 0.7 for most runs.

Next, since LDA can be sensitive to outlier values, we clean the data. We carry out an outlier analysis for all of the input predictors for each simulation. To demonstrate this process visually, we include Figure 5.8, which is a box and whisker plot, used to identify outliers for the q0.2_fg0.3_BT0.2 simulation. A box and whisker plot splits the data into quartiles, where the center line of the box is the median of the distribution for the merger or nonmerger class, the edges of the box are the upper and lower quartiles of the data, and the whiskers span the remaining quartiles of the distribution of the predictor values. Points that fall outside the whiskers are outliers; outliers can either be influential points or significant errors in measurement.

We want to avoid overcleaning the data, or removing outliers that are not measurement errors, so we first examine the outliers point by point and remove the outliers that are related to measurement errors, which amount to ~ 1 - 2 galaxy snapshots for each simulation. Again, 'data points' refers to the predictor values from a galaxy snapshot. Measurement errors are points where the imaging or kinematic portion of the pipeline has failed, for instance, **statmorph** very rarely fits a negative ellipticity value.

The remaining outliers are influential points, which we also examine individually. We find that the majority of outliers have elevated values in ΔPA , v_{asym} , and A_2 and are associated with the nonmerger class. These points have a viewpoint that is 100% face-on. We demonstrate this problem for the v_{asym} predictor in Figure 5.9, where we show that v_{asym} is

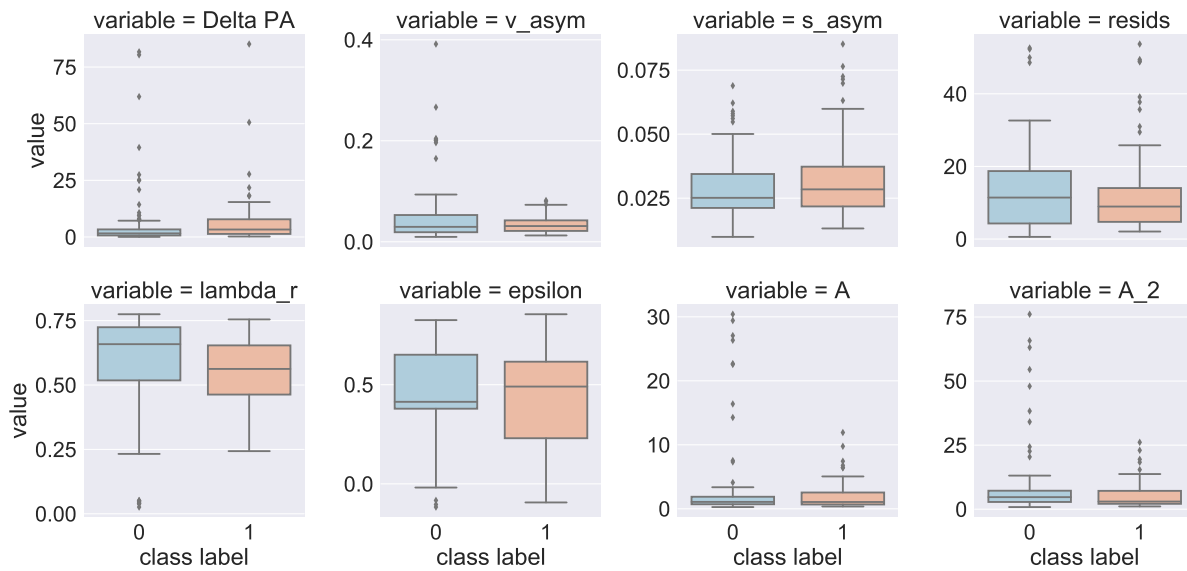


Figure 5.8: The initial (pre-cleaned) box and whisker plot distributions of the q0.2_fg0.3_BT0.2 simulation. Class 0 (blue) is the nonmergers and class 1 (salmon) is the mergers. We plot the distribution of the values for each input predictor. There are many outlier points; we eliminate points that are measurement errors and points that are associated with the 100% face-on isolated viewpoints. This plot also demonstrates that the distributions are skewed non-normal distributions.

elevated, particularly for nonmerger snapshots that have close to zero ellipticity, or face-on viewpoints. However, this is not a general trend with ϵ ; in other words, this effect cannot be accounted for with the $v_{\text{asym}} * \epsilon$ cross-term; instead this is a problem that must be addressed by cleaning the data. Additionally, for all of the simulations, the isolated simulations have slightly different viewing angles for the seven isotropic viewpoints relative to the merging simulations. For instance, the most face-on viewing angle is 100% face-on for the isolated galaxies while the most face-on viewing angle is not 100% face-on for the merging galaxies because they are slightly inclined. This difference is significant when examining the predictors that are sensitive to viewing angle; since these isolated samples are not matched (in exact viewing angle) with the merging galaxies and since it would be rare to identify a 100% face-on galaxy in MaNGA, we remove all of the face-on isolated galaxy viewpoints from the sample. This accounts for $\sim 10\%$ of the isolated data points, which is acceptable since there are of order 100 isolated snapshots for each simulation. After removing these outliers, we are prepared to run the LDA to select which of the remaining seven predictors to retain.

5.3.2 Predictor Selection

We first run all of the simulations through the LDA with all seven predictors, after eliminating A due to multicollinearity concerns. We present the results for these seven primary predictors in Table A.25. As in N19, the predictor selection process is a forward stepwise selection. This means that starting with zero terms, we add in the term that minimizes the number of misclassifications at each step. If this selected term is an interaction term, then we also include the relevant primary terms. For example, if the $\epsilon * A_2$ is selected, we also include the primary ϵ and A_2 terms. We terminate the forward stepwise selection when adding more terms does not significantly (to 1σ) decrease the number of misclassifications. We additionally use k -fold cross-validation to assign each predictor coefficient with a value and associated error. We bold terms in Table A.25 that are significant to 3σ given this error. We implement this process for each classification individually.

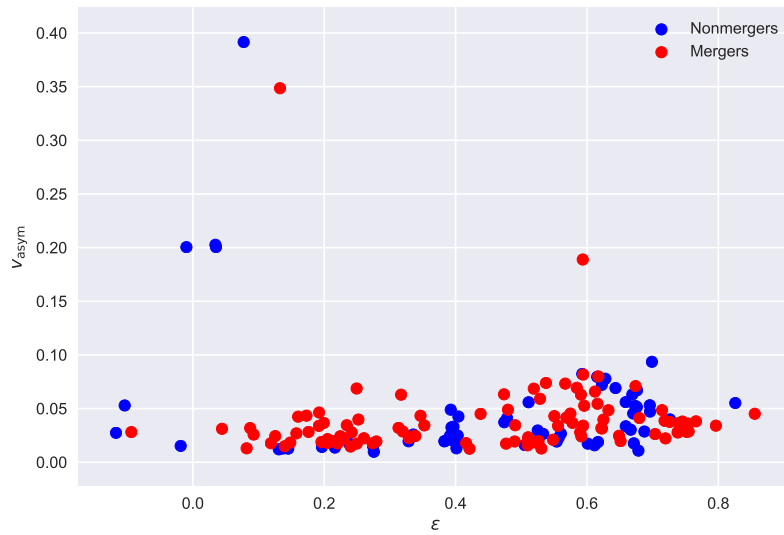


Figure 5.9: The distribution of ellipticity (ϵ) and v_{asym} values for the q0.2_fg0.3_BT0.2 simulation for the merging (red) and matched nonmerging (blue) sample of galaxies before we clean the data. We find that v_{asym} is elevated for the face-on galaxies; these same galaxies have ϵ values close to zero. Since there are no mergers that are 100% face-on, we eliminate the isolated galaxy snapshots that are 100% face-on from the analysis.

We then eliminate predictors that are not selected by the forward stepwise selection technique by any simulation. The v_{asym} predictor is unimportant for all simulations so it is the only term that we eliminate from the analysis. So although v_{asym} increases for many of the merging galaxies it is not selected as a useful predictor by the preliminary LDA run. Upon closer examination, we find that v_{asym} and σ_{asym} are correlated, and that σ_{asym} is less sensitive to viewing angle. Therefore, σ_{asym} captures the relevant information while v_{asym} is superfluous to the analysis.

5.3.3 Classification Results

We eliminate the v_{asym} predictor and rerun the LDA as a classifier. For this final iteration of the classification, we combine the three major mergers into a combined major merger classification and the two minor mergers into a combined minor merger classification. We present the new results for the primary predictor coefficients in Table A.26 and the interaction term coefficients in Table A.27. We also rerun the classification without interaction terms in Table A.26 and we discuss the motivation for this in this section. Finally, we also briefly discuss the main results of the LDA classification for each simulation, which we examine in more detail in Section 5.4.

We present the values of LD1 for the nonmerging and merging populations of each simulation in Figures 5.10 and 5.11 for the major mergers and minor mergers, respectively. LD1 is the first discriminant axis of the LDA classification: the higher the value, the more likely the galaxy is merging, so this axis best separates the two classes of merging and nonmerging galaxies. We find that the classification is better able to separate the merging and nonmerging classes for the major merger simulations.

Here we briefly discuss the relative importance of the primary predictor coefficients for each simulation since they represent the most easily interpretable outcome of the classification. However, these are the linear terms, and there are also important interaction terms that affect this analysis. In order to more directly assess the relative importance of the

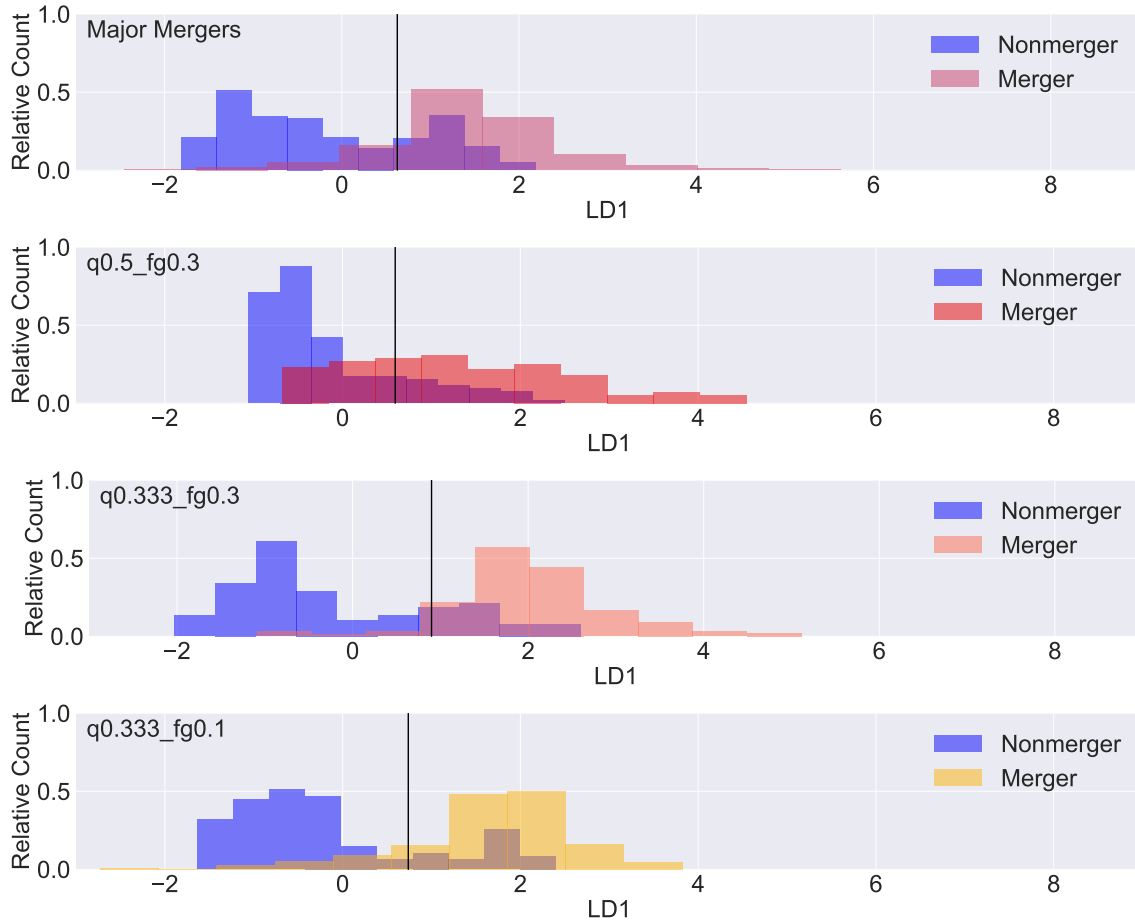


Figure 5.10: Histograms of LD1 for the populations of merging and nonmerging galaxies for the combined major merger (top) simulation and all of the individual major merger simulations. All of the matched nonmergers are blue. The vertical black line is the decision boundary; it is the midway point between the mean of the nonmerger and merger populations. If the LD1 value of a galaxy falls above this line, the galaxy is more likely to be classified as a merger.

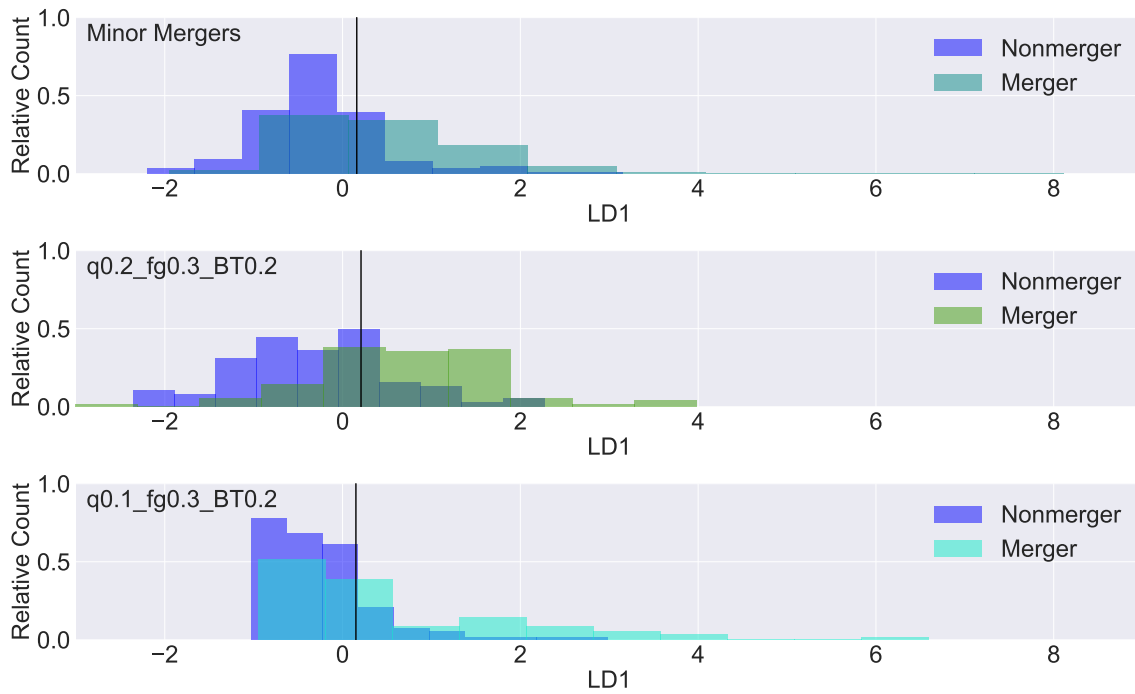


Figure 5.11: Histograms of LD1 for the populations of merging and nonmerging galaxies for the combined minor merger (top) simulation and all of the individual minor merger simulation. All of the matched nonmergers are blue. The vertical black line is the decision boundary; it is the midway point between the mean of the nonmerger and merger populations. If the LD1 value of a galaxy falls above this line, the galaxy is more likely to be classified as a merger.

primary predictors, we rerun the LDA without interaction terms and report the results in Table A.26. It is very important to note that the classification is different without interaction terms; the interaction terms are accounting for relationships between the predictors that we cannot perceive as easily by eye in the predictor space and therefore these terms increase the accuracy of the classification by a minimum of 10%. So although the interaction terms do not facilitate an easy analysis of how individual predictors affect the classification, they are important for the overall method. We describe here how to properly analyze the primary predictor coefficients with particular attention to these interaction terms.

We find that for the simulations where there are few and/or small interaction terms, the order of importance of the linear primary predictor coefficients more closely matches that of the primary coefficients for the LDA run without interaction terms. For instance, LD1 is fairly simple for q0.5_fg0.3 since it has only three important terms:

$$\text{LD1}_{\text{q0.5_fg0.3}} = 1.69\sigma_{\text{asym}} + 0.69A_2 - 0.19\sigma_{\text{asym}} * A_2$$

In this case, the primary predictors dominate since their coefficients are larger, and the interaction term is a combination of the two primary predictors. This interaction term describes the way that σ_{asym} changes relative to the A_2 predictor. For instance, if we want to know how LD1 changes relative to σ_{asym} when $A_2 = 0$, we can ignore the interaction term since it goes to zero, and we simply use the primary predictor for σ_{asym} . However, this is rarely the case. Instead, the interaction term changes sign if the value of A_2 or σ_{asym} drops below the mean of the distribution (recall, the predictors are standardized to a mean value of 0). For instance, if $A_2 = -1$, and σ_{asym} is also less than zero, then LD1 will decrease towards the nonmerger classification. In this case, since the interaction term coefficient value is much less than the primary coefficients, the primary coefficients still dominate the analysis, so we can safely claim that if the value of σ_{asym} increases, the galaxy is more likely to be merging and likewise for A_2 . In this case, it is also straightforward to claim that σ_{asym} is more important than A_2 . When we run just the primary predictor terms through the LDA

without any interaction terms, we find that the σ_{asym} and A_2 coefficients have this same order of importance.

The picture with interaction terms becomes more complicated for simulations such as the major merger combined simulation, where there are many more interaction terms that have large relative coefficients. In this case, LD1 is (in order of the absolute value of the term coefficients):

$$\begin{aligned} \text{LD1}_{\text{major, combined}} = & 3.09\sigma_{\text{asym}} * \lambda_{R_e} - 1.94\lambda_{R_e} + 1.74\text{resids} - 1.27\text{resids} * \lambda_{R_e} \\ & - 1.13\sigma_{\text{asym}} * \text{resids} - 0.82\sigma_{\text{asym}} * \epsilon - 0.7\sigma_{\text{asym}} \\ & + 0.55\epsilon + 0.53A_2 + 0.38\Delta\text{PA} - 0.14\Delta\text{PA} * A_2 \end{aligned} \quad (5.1)$$

The largest coefficient belongs to an interaction term. The largest primary predictor coefficient is λ_{R_e} , so if all other predictors are perfectly at zero, then if λ_{R_e} decreases, LD1 will move towards the merger classification. However, in the case where σ_{asym} is large, then increasing λ_{R_e} will actually move LD1 towards the merger classification. Therefore, it is extremely difficult to directly compare the primary predictor coefficients for this simulation. In this case, we rely upon the run without interaction terms to compare the primary predictor coefficients.

When we examine the LDA run without interaction terms for the major merger combined simulation, we find that σ_{asym} is the most important predictor coefficient, followed by ΔPA and A_2 . We find that all of the simulations have too many interaction terms for a straightforward interpretation of the interaction terms (except q0.5_fg0.3), so we use the LDA run without interaction terms for all others. We find that in the majority of cases, the primary coefficient terms selected by the LDA run without interaction terms agree with the terms selected by the full LDA run, although the predictor coefficients may not be in the same order. For the minor merger combined simulation, the most important primary term is σ_{asym} , followed by resids , and ΔPA . For q0.333_fg0.3, the important predictors are λ_{R_e} , then σ_{asym} , then ϵ and A_2 , which are tied for third. For q0.333_fg0.1, the most important

term is λ_{R_e} , followed by σ_{asym} , ϵ , and A_2 . For the q0.2_fg0.3_BT0.2 run, the most important predictors are σ_{asym} , resids , λ_{R_e} , ϵ , and ΔPA . For the q0.1_fg0.3_BT0.2 simulation run, the important selected terms are ΔPA , resids and σ_{asym} , and ϵ and A_2 . All of our discussion in Section 5.4.1 of the relative import of the primary predictor coefficients for different simulations as well as the sign of each coefficient (does it decrease or increase for the merging galaxy population) is based on the runs without interaction terms while the final classification is based on the full LDA run. This is justified as a first-order analysis of the behavior of the predictor coefficients due to the similar behavior of the predictor coefficients between the two models. We discuss the importance of the non-linear interaction terms in the context of the non-linear evolution of the kinematic predictors in Section 5.4.2.

We next briefly analyze which terms are included in the overall LDA run. We can also assess the relative complexity of each simulation using the number of total primary and interaction predictor terms that are necessary. For instance, the combined major merger simulation has 11 total terms, the combined minor merger simulation has five, the q0.5_fg0.3 simulation has two, the q0.333_fg0.3 simulation has seven, the q0.333_fg0.1 simulation has six, the q0.2_fg0.3_BT0.2 simulation has four, and the q0.1_fg0.3_BT0.2 simulation has two. The minor merger simulations require fewer overall terms. The majority of simulations tend to rely upon the σ_{asym} , resids , and λ_{R_e} predictors. The major mergers tend to rely upon A_2 , while this coefficient is unimportant for the individual minor merger simulations. ΔPA and ϵ are only important for a few simulations, where ΔPA is more important for the minor mergers. We discuss the importance of mass ratio to the classification in Section 5.4.3.

We can directly compare the q0.333_fg0.3 to the q0.333_fg0.1 simulation in order to differentiate between the effects of gas fraction. These two simulations are not significantly different and we discuss the lack of differences between the LDA classifications for gas fraction in Section 5.4.4.

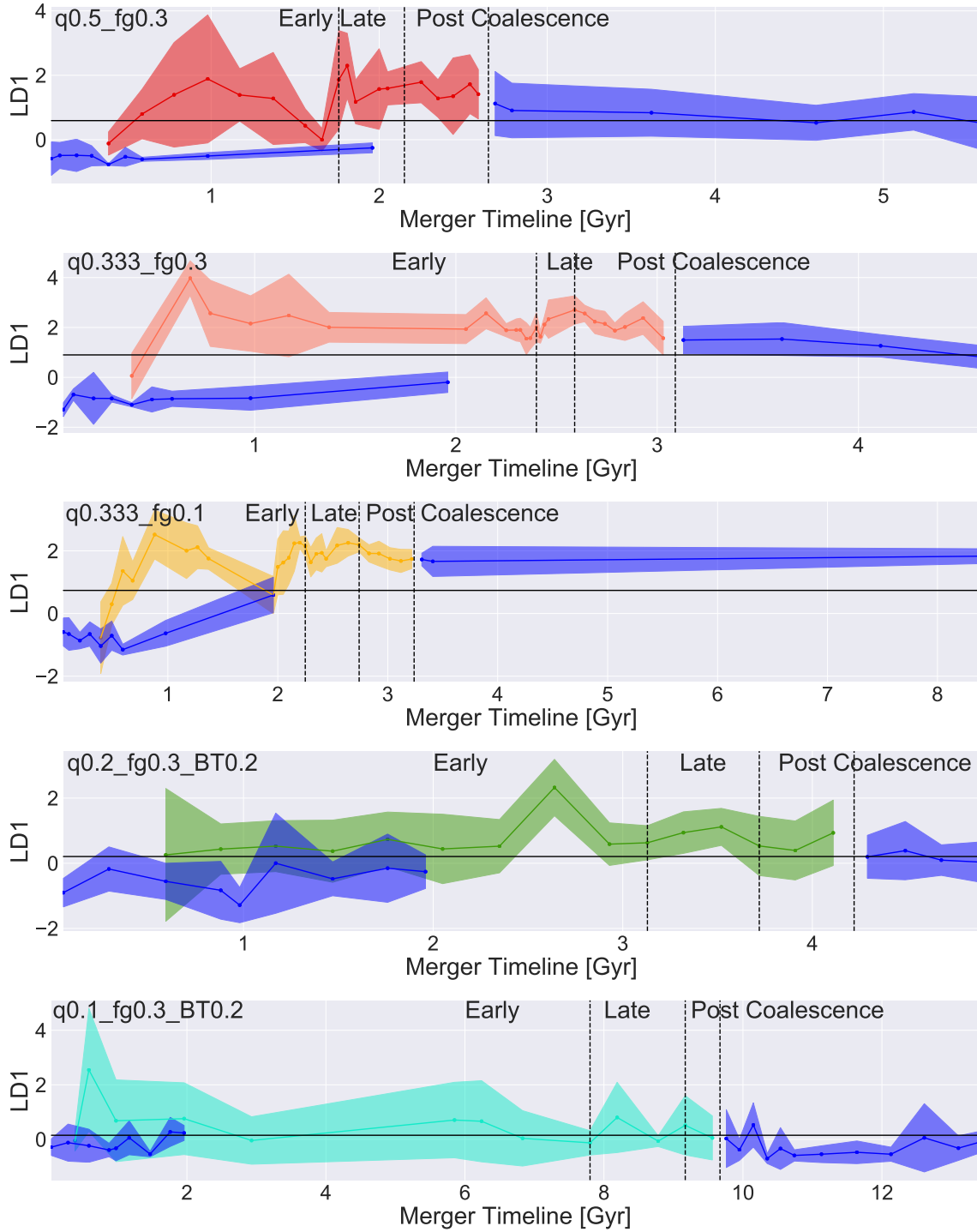


Figure 5.12: LD1 sensitivity with time. The points are the viewpoint-averaged value of LD1 for each snapshot in time along with the shaded 1σ confidence intervals of the LD1 values for each snapshot. We divide each plot into the early, late and post-coalescence stages of the merger. The blue lines and shaded 1σ confidence intervals are the isolated galaxies for each simulation, from the matched isolated galaxies that evolve for ~ 2 Gyr and the snapshots that are before first pericentric passage and > 0.5 Gyr after final coalescence. The horizontal black line is the decision boundary, which is the halfway point between the means of the merging and nonmerging population.

5.3.4 Observability Timescale

We define the LDA observability timescale in N19 to be the sum of all snapshots where the average LD1 value for a given snapshot (averaged over all the viewpoints for that snapshot) is greater than the decision boundary. The decision boundary is halfway between the means of the merging and nonmerging galaxy distributions. We present the observability timescales for all of the simulations in Table A.28 along with the total merger duration for each simulation and the fraction observability, or fraction of the duration of the merger that it is observable by the LDA technique. We exclude the combined major and minor mergers from this table since they are not one continuous merger and so it is impossible to calculate an observability timescale for them.

With the exception of the 1:5 minor merger (q0.2_fg0.3_BT0.2), which is observable for 100% of the duration of the merger, the major mergers have a larger fraction of observability. The major merger simulations are observable for $\sim 70\%$ of the duration of the merger, and the 1:10 minor merger (q0.1_fg0.3_BT0.2) is only observable for 36% of the duration of the merger. We present a visualization of how the mean values of LD1 change throughout the lifetime of each merger in Figure 5.12. This shows the viewpoint-averaged value of LD1 for each snapshot as well as the 1σ confidence interval on this value. We also plot the decision boundary for each simulation. The minor mergers do not fall significantly above this line; even though the viewpoint-averaged LD1 values for the q0.2_fg0.3_BT0.2 simulation fall above the decision boundary, they overlap the decision boundary to 1σ confidence. This means that not all viewpoints are significantly above this boundary. On the other hand, the major merger simulations are significantly above this boundary for the majority of their duration. We discuss the implications of the different observability timescales in more depth in Section 5.4.5.

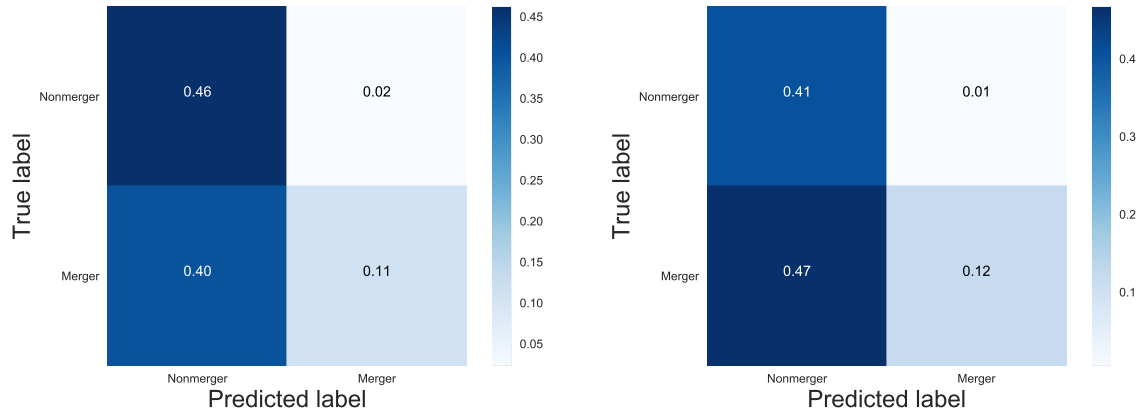


Figure 5.13: Confusion matrices to visualize the relative numbers of true negatives (upper left quadrant), false positives (upper right), false negatives (lower left), and true positives (lower right) for the minor merger (left) and major merger (right) combined simulations.

5.3.5 Accuracy and Precision

Here, we measure the relative accuracy and precision of the various simulations. We present these results using a confusion matrix for the major and minor combined simulations in Figure 5.13, which shows the relative fraction of known mergers and nonmergers that are classified by the LDA as merging and nonmerging. We quantify the accuracy and precision for all simulations in Table A.29.

The accuracy for a given simulation is defined as the number of correct classifications of nonmergers as nonmergers (true negatives) and the number of correct classifications of mergers as mergers (true positives) divided by the number of total classifications:

$$A = \frac{TP + TN}{TP + TN + FP + FN}$$

where FP is the number of false positives, or nonmerging galaxies that are classified as mergers, and FN is the number of false negatives, or mergers that are classified as nonmerging.

A more accurate classifier maximizes the number of true classifications.

Precision is defined as the number of true positive classifications over the total number

of positive classifications:

$$P = \frac{TP}{TP + FP}$$

A precise classifier maximizes the fraction of true positive classifications relative to false positives (nonmergers that are classified as mergers). In this work, we seek to eliminate false positives from the sample, or nonmerging galaxies that are incorrectly classified as mergers. Figure 5.13 demonstrates that the classifiers are precise and not as accurate. We do not optimize these classifications by either of these metrics here, although it is possible to do so by adjusting the decision boundaries. For example, if we wish to increase the accuracy of the methods by sacrificing a small degree of precision, we could move the decision boundaries to lower values of LD1 (to the left in Figures 5.10 and 5.11). We discuss the implications of the accuracy and precision of the classifications in more depth in Section 5.4.6.

5.4 Discussion

In this section, we discuss the kinematic LDA classifications and their implications for merging galaxies. We specifically discuss the individual LD1 coefficients in Section 5.4.1. We discuss how the values of the predictors change with time in Section 5.4.2. We mirror the discussion from N19 in Sections 5.4.3 and 5.4.4, where we explore the differences between simulations of different mass ratio and gas fraction, respectively. We consider the implications of the observability timescale of the kinematic LDA technique in Section 5.4.5 and the accuracy and precision of the technique in 5.4.6. Finally, we explore some alternative machine learning techniques in Section 5.4.7.

5.4.1 The behavior of the LD1 coefficients are consistent with previous work

Since the interaction terms affect how changing a given predictor will change the dependent variable (LD1), we use our analysis from the LDA run without interaction terms for

this discussion. The LDA run without interaction terms is a different classification from the original with the interaction terms; it decreases the accuracy and precision of the classifier and is not the final classifier we plan to apply to the MaNGA galaxies. We therefore restrict the discussion here to a first-order more general discussion of the selected coefficients for each run, whether they are positive or negative, and the significance of which classifications rely on each predictor. Here, when a predictor coefficient has a positive value, this means that a larger value of this predictor will lead to a larger value of LD1, increasing the likelihood that the galaxy is merging.

We also supplement this discussion with visuals of how the pre-standardized values of the predictors change during the merger simulations. In this discussion, we carefully distinguish between the behavior of the LD1 predictor coefficients and the pre-standardized predictor values. The LD1 coefficients are the values that correspond to each predictor in Table A.26; they accompany primary predictors or interaction terms. The pre-standardized predictors are the measured values of each predictor, prior to standardizing to a mean of zero and a standard deviation of one. When classifying a single galaxy, one multiplies each standardized predictor value by the corresponding coefficient and sums all of the relevant terms to calculate LD1. While the predictor coefficients are not the same as the values of the pre-standardized predictors, the behavior of the two are closely related since the classification is built from the standardized predictors. In this way, it is intuitive and informative to examine the behavior of these ‘raw’ pre-standardized predictor values to understand the behavior of the predictor coefficients.

5.4.1.1 The difference between the kinematic PA and the imaging PA (Δ PA)

The predictor coefficient that corresponds to the difference between the global photometric and kinematic position angles (Δ PA) is positive, meaning that merging galaxies are more likely to have a larger value of Δ PA. These position angles (kinematic and photometric) are both global measurements of the position angle, since they do not vary with radius.

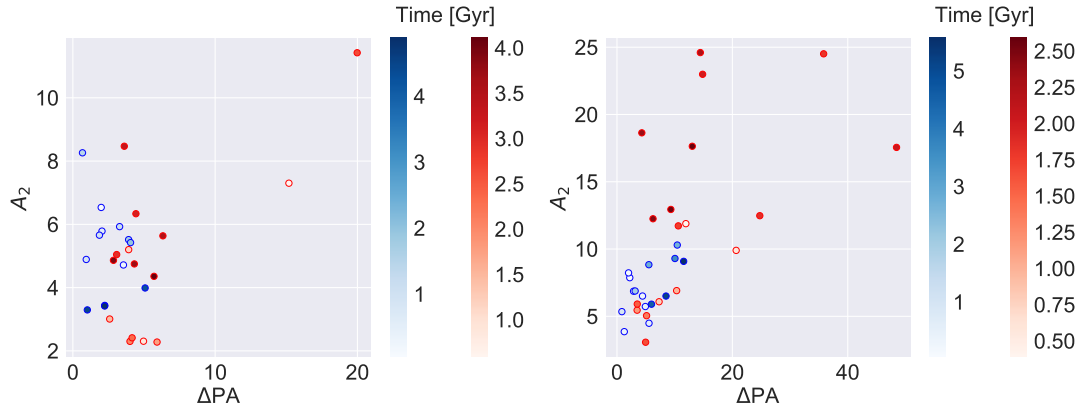


Figure 5.14: Time evolution of the merging (red) and matched nonmerging (blue) galaxies in ΔPA - A_2 predictor space for the q0.2_fg0.3_BT0.2 minor merger (left) and the q0.5_fg0.3 major merger (right). Here we show the pre-standardized predictor values. Note that the axes ranges change, such that the q0.5_fg0.3 simulation spans a larger range of ΔPA and A_2 .

Barrera-Ballesteros et al. (2015) investigate the kinematic misalignments of optically-identified merging CALIFA galaxies at different stages. They do this for the stellar and gas components of the system. We focus on the results that pertain to the stellar velocity field; the gas velocities are beyond the scope of this paper, but are an intriguing future direction. Barrera-Ballesteros et al. (2015) find that 43% of their sample of major mergers have stellar morpho-kinematic misalignments larger than the control sample of non-interacting galaxies. This verifies our result, that the ΔPA coefficient increases for merging galaxies.

The ΔPA predictor coefficient is important for both the major and minor merger simulations, and is relatively more important for the minor merger simulations. This result is also seen in the pre-standardized ΔPA values. When we examine this behavior in Figure 5.14, we find that for a few snapshots, the average value of ΔPA is elevated for the q0.2_fg0.3_BT0.2 simulation to values of $> 10^\circ$, which explains why it is still an important predictor for these simulations. For q0.5_fg0.3, ΔPA is markedly more elevated for the merging snapshots. So while ΔPA tends to be greater for the major mergers, it is still slightly elevated for the minor mergers relative to the isolated population of galaxies, which is why it is still a key predictor

for the minor mergers.

5.4.1.2 The asymmetry in the velocity dispersion map (σ_{asym})

The σ_{asym} coefficient is positive, meaning that a merging galaxy is more likely to have a greater value of σ_{asym} . σ_{asym} is also one of the more important predictor coefficients for merger identification. We present the $v_{\text{asym}}\text{-}\sigma_{\text{asym}}$ predictor space diagram in Figure 5.15 for the q0.2_fg0.3_BT0.2 and the q0.5_fg0.3 simulations, where the σ_{asym} pre-standardized predictor values also increase for the merger population.

The positive σ_{asym} predictor coefficient as well as the increased pre-standardized predictor values for the merging population is confirmed in previous work, which finds that merging galaxies have enhanced values of both v_{asym} and σ_{asym} in observed and simulated mergers (Shapiro et al. 2008; Bellocchi et al. 2012; Hung et al. 2016). We compare the degree of increase for the various simulations in this work to some of these studies. However, this is not a direct comparison since Shapiro et al. (2008), Bellocchi et al. (2012), and Hung et al. (2016) use the gas kinematics to calculate v_{asym} and σ_{asym} and a different method to calculate σ_{asym} . Since they rely upon the gas kinematics, they use the $B_{1,v}$ (rotation curve) coefficient as the normalization factor to calculate σ_{asym} as opposed to the $A_{0,v}$ term, which traces the mass of the system. The $B_{1,v}$ term is more appropriate for the gas component since the gas component does not always trace the mass of the system and the gas component can have decreased radial coverage that corresponds to a loss in the dynamic range of the asymmetries. Therefore, this section offers rough comparisons to the findings of previous work, but avoids directly comparing the values of v_{asym} , σ_{asym} , and the K_{asym} measurement, which is the total kinematic asymmetry ($K_{\text{asym}}^2 = \sigma_{\text{asym}}^2 + v_{\text{asym}}^2$).

Shapiro et al. (2008) study σ_{asym} of warm ionized gas for observed $z \sim 2$ galaxies. They find that 50% of their 11 systems have kinematics consistent with major mergers, which they classify as $K_{\text{asym}} > 0.5$. These are highly disordered higher redshift systems, and the study focuses on ionized gas, which is often more disturbed than the stellar component of the

velocity field. However, the same principle applies to the stellar velocity field of our lower-redshift galaxies; σ_{asym} , which traces the disorder in the higher order terms of the fit to the velocity dispersion field, should increase for major merging galaxies, which we confirm in this work. The relative increase of the galaxies in this work is less, but the overall trend is similar. We overplot the $K_{\text{asym}} > 0.5$ line from Shapiro et al. (2008) on Figure 5.15 for comparison. Again, it is important to note that not only is this divide determined for inherently more kinematically disturbed $z \sim 2$ galaxies, but it is calculated for the gas velocity as opposed to the stellar velocity (the gas tends to be more disturbed). Additionally, σ_{asym} is measured with a normalizing coefficient of $B_{1,v}$ as opposed to the $A_{0,\sigma}$ term used in this work.

Bellochi et al. (2012) study local luminous infrared galaxies (LIRGs), which are major mergers, with the VLT/VIMOS IFU and find that the threshold value of K_{asym} changes with spatial resolution. When they artificially move the sample of galaxies to higher redshift, the galaxies appear more symmetric in their kinematic maps, and the threshold value for major mergers decreases from $K_{\text{asym}} > 0.135$ for local galaxies to $K_{\text{asym}} > 0.096$ for $z \sim 3$ simulated galaxies.

Hung et al. (2016) define a K_{asym} threshold of 0.15 for the lower redshift simulated galaxies in their work, which is calculated from the gas velocity of particles from simulated SUNRISE mergers. We add this classification threshold to Figure 5.15. Hung et al. (2016) find that the mergers in their sample exceed this threshold for 0.2-0.36 Gyr and are most visible during the ‘strong interaction’ or late stage of merging, where the 1:4 mass ratio minor merger has an observability timescale on the lower end of that range, and the 1:1 major merger has an observability timescale on the upper end of that range. While we measure the stellar kinematics (as opposed to the gas kinematics), we also find similar results, that the major merger simulations show the most heightened values of σ_{asym} for the late stages of the merger, where they do exceed the threshold $K_{\text{asym}} > 0.15$ threshold from Hung et al. (2016) for a few snapshots. We expect the ‘observability time’ for σ_{asym} and v_{asym} to increase if they were measured from the gas velocities.

We find that all of our merging galaxies fall below the threshold value of 0.5 from Shapiro et al. (2008). Therefore, a better analog for the local disk-dominated galaxies in this work would be the LIRGs from Bellocchi et al. (2012) or the simulated local merging galaxies from Hung et al. (2016).

We find that σ_{asym} is not as sensitive to the minor mergers, which undergo a smaller disturbance in the stellar velocity maps of the primary. This is consistent with Hung et al. (2016), who find that the simulated minor mergers have a shorter observability timescale in this predictor. We examine Figure 5.15 to explore the difference between the minor and major merger simulations; the minor mergers show little offset between v_{asym} and σ_{asym} between the populations of isolated nonmerging and merging galaxies, whereas the merging galaxies show enhanced values of v_{asym} and σ_{asym} for the merging galaxies.

One advantage of the LDA technique (in addition to the utility of relying upon multiple different predictors) is that we can rely upon the trend of increasing σ_{asym} values as opposed to measuring a new classification line. This is an appropriate approach given that the galaxies in this work span a specific range of predictor space; they are disk-dominated local mergers. This also allows us to avoid the pitfalls of using a specific threshold value that was derived from galaxies with different resolutions, inherent properties, and/or measurement techniques for v_{asym} and σ_{asym} that would lead to systematic offsets in the values of v_{asym} and σ_{asym} .

5.4.1.3 The kinemetry residuals (resids)

For the LDA run without interaction terms, the **kinemetry** residuals (**resids**) coefficients are negative for the minor merger simulations, meaning that the residuals are lower for the mergers. This is surprising because it indicates that a larger disagreement between the best fit disk model and the observed data means that the galaxy is more likely to be nonmerging. We are still investigating if this is an effect of the technique utilized to measure this predictor, a concern with the **kinemetry** disk fit, or a physical reflection of the simulated galaxy merging and nonmerging galaxy populations. Here we briefly discuss how

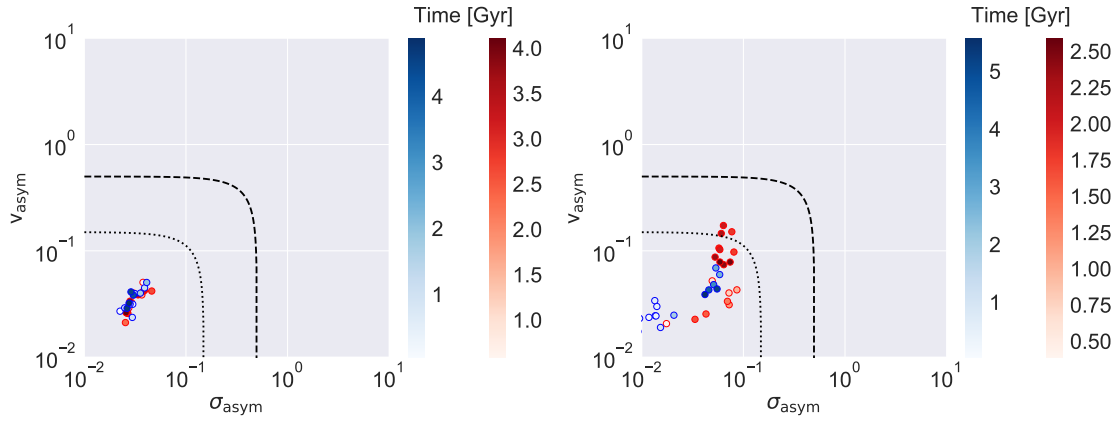


Figure 5.15: Time evolution of the merging (red) and matched non-merging (blue) galaxies for the `q0.2_fg0.3_BT0.2` simulation (left) and `q0.5_fg0.3_BT0.2` simulation (right) on the v_{asym} - σ_{asym} diagram. Here, we show the pre-standardized predictor values. The $K_{\text{asym}} = 0.5$ (dashed) and $K_{\text{asym}} = 0.15$ (dotted) diagnostic lines are included from Shapiro et al. (2008) and Hung et al. (2016).

this predictor relates to other predictors and why it is not important for the major merger classifications. We also discuss some potential concerns with the resids statistic, which is our leading theory as to why it is the only coefficient that behaves counter to our expectation.

The **kinemetry** model disk fit is only one aspect of this classification, we also directly rely upon σ_{asym} , which is a positive coefficient in the classification. The resids and σ_{asym} predictors are similar in that they are both constructed from the **kinemetry** disk model; the resids exclude the higher order harmonic terms in the model while σ_{asym} quantifies the disorder in these higher order terms. Epinat et al. (2012) study the ionized gas kinematics of galaxies in the MASSIV survey and find that the residuals of the modeled velocity field and the deviation of the morphological major axis with the ionized gas position angle are useful in separating ‘rotating’ from ‘non-rotating’ galaxies. Interestingly, Epinat et al. (2012) find that the velocity field residuals are well-correlated with σ_{asym} . So although σ_{asym} and resids are slightly different measurements, they are still fundamentally related (we also find that they are correlated), which is part of the reason why it is surprising that the resids coefficient is negative while the σ_{asym} coefficient is positive.

It is unsurprising that the resid coefficient is unimportant for the major merger classifications; all of the merging galaxies in this work are disk-dominated and appear disk-like at many epochs of the merger. Even during the most disturbed phases, it is still possible for **kinemetry** to converge on a disk model. This could be why kinematic predictors that are more sensitive to smaller deviations in a rotating disk such as A_2 are more important for the major merger classifications.

The measurement of the resids may be sensitive to systematics from **kinemetry** itself. For instance, the **kinemetry** models focus on the centers of the galaxies to determine a best fit disk, therefore, they are mostly ignoring the outskirts, which are often the most kinematically disturbed parts of a galaxy merger. Since we calculate the residuals only for the spaxels where the model has assigned a circular velocity value, these outer regions are not included in the measurement of resids. **kinemetry** is also more likely to terminate its fitting

at smaller radii when it encounters disorder at large radii; this leads to narrower disks fit to galaxies with highly disordered kinematics. We attempt to account for this by weighting the measurement of residuals with the number of spaxels that are measured. We plan to investigate this in more detail in the future.

5.4.1.4 The specific angular momentum (λ_{R_e})

The coefficient for λ_{R_e} is negative, indicating that the specific angular momentum of the merging galaxies is lower than the nonmerging galaxies. This is the case for both the minor mergers and the major mergers although it is more extreme for the major mergers. We present the λ_{R_e} - ϵ diagram for the combined major and minor merger simulations in Figure 5.16, where the pre-standardized λ_{R_e} values decrease as the merger progresses.

Naab et al. (2014) utilize cosmological merger tree simulations and find that major mergers can have a large effect on the angular momentum content of a galaxy; they can either spin up or spin down the remnant. We find that all of our galaxies begin with a λ_{R_e} value of ~ 0.7 and evolve towards lower values of λ_{R_e} . The major mergers evolve further in λ_{R_e} , down into the ‘slow rotator’ classification, which confirms that major mergers have a larger impact on λ_{R_e} .

Jesseit et al. (2007) use a sample of collisionless mergers and matched gas-rich mergers (where 10% of the disk mass is in gas) from Naab et al. (2006) to study the kinematic features of mergers. Some of the mergers in the study are major mergers with a 1:1 mass ratio and some have 1:3 mass ratio. The 2D kinematics are very different depending on mass ratio; the 1:1 major merger has very low rotation and can have kinematic misalignments and twists, which are enhanced with gas fraction. On the other hand, the 1:3 major mergers are faster rotating and have fewer twists. While the merger remnants in this work can have slight warps, they do not possess more exotic features like kinematically decoupled cores. However, our results are still consistent with the general picture from Jesseit et al. (2007) and Naab et al. (2014): the smaller the mass ratio of the merger, the greater the change in

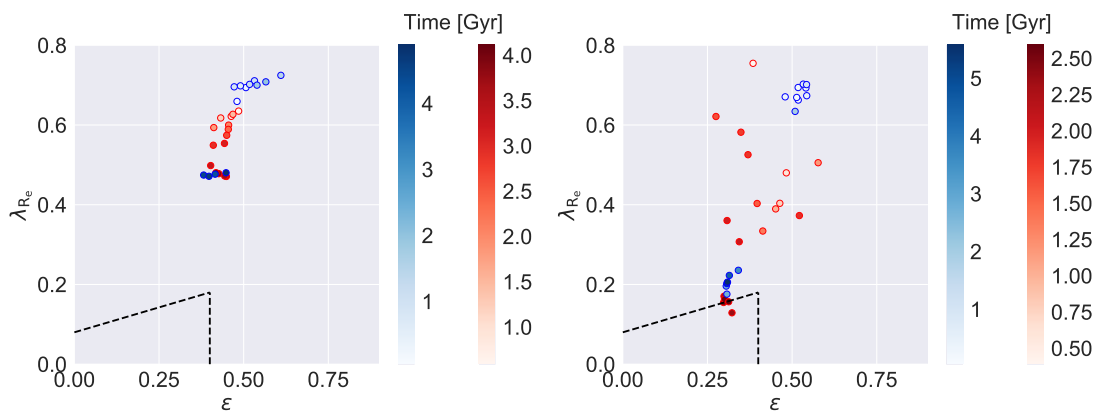


Figure 5.16: Time evolution of the merging (red) and matched non-merging (blue) galaxies for the q0.2_fg0.3_BT0.2 minor merger simulation (left) and the q0.5_fg0.3 major merger simulation (right) on the λ_{R_e} - ϵ diagram. Here, we show the pre-standardized predictor values. As the merger progresses (red points), the galaxies evolve towards decreased values of λ_{R_e} , which corresponds increasing levels of disorder in the kinematic maps.

kinematic properties like λ_{Re} .

Figure 5.16 demonstrates this for the comparison between the 1:2 major merger simulation q0.5_fg0.3 and the 1:5 minor merger simulation q0.2_fg0.3_BT0.2. We find that the λ_{Re} coefficient is important for most simulations, but that the pre-standardized values of λ_{Re} decrease more for the major mergers. In Figure 5.16, the q0.5_fg0.3 major merger moves into the slow rotator region at the end of the merger, showing that major mergers can dramatically affect the kinematic properties of the remnant.

5.4.1.5 The ellipticity (ϵ)

The ϵ predictor is technically an imaging predictor, but we include it here to pair with λ_{Re} . Its coefficient is positive in the classification, indicating that the ellipticity of the merging galaxies is greater than that of the nonmergers, which means that the mergers are slightly more disk-like. When we examine Figure 5.16, it becomes apparent that the merging galaxies have pre-standardized ellipticity values between that of the isolated galaxies and the isolated postmerger galaxies (the snapshots that fall > 0.5 Gyr after final coalescence). The mergers evolve towards lower ellipticity values with time, although there is significant scatter in this trend. The merging galaxies are becoming rounder with time, which is consistent with the expectation that mergers tend to build elliptical galaxies, which has been shown in detail for major mergers (Bendo & Barnes 2000; Bournaud et al. 2007) as well as minor mergers (Walker et al. 1996; Cox et al. 2008; Naab et al. 2014).

The scatter in the pre-standardized ellipticities may explain the positive ellipticity coefficient in LD1; since there is not much separation between the merging and nonmerging populations and some of the merging snapshots scatter towards higher ellipticity, the mergers tend to have higher ellipticities. However, this does not mean that they evolve towards higher ellipticity with time, in fact the opposite is true.

5.4.1.6 The asymmetry from the Radon profile (A_2)

The A_2 coefficient is an important term for the majority of the classifications, but is more important for the major mergers. The A_2 coefficient is positive in all cases, meaning that mergers have larger values of A_2 .

Figure 5.14 shows that the pre-standardized A_2 values are also greater for the merging galaxies. Stark et al. (2018) apply the Radon Transform to the stellar velocity maps of galaxies in the MaNGA survey and find that the majority of the galaxies have deviations from regular co-planar circular motion. Stark et al. (2018) classify a galaxy with $A_2 > 3$ as ‘asymmetric’. We avoid using a cutoff value for A_2 since we use a different approach to measure A_2 , but we do find that A_2 separates the merging and nonmerging snapshots for the q0.5_fg0.3 simulation in Figure 5.14. There are no isolated snapshots above a value of $A_2 \sim 10$. The separation is less clear for the minor mergers, where there is significant overlap between mergers and nonmergers and very few merger snapshots have an average value greater than 10.

A_2 measures how the kinematic PA changes with radius, which probes how much it deviates from a straight line. Epinat et al. (2012) also use this as a classification tool; galaxies with a larger deviation are classified as ‘non-rotating.’ These galaxies are different from the disk-dominated galaxies in this work, for which there is always a dominant rotational direction. The merging galaxies here are not totally kinematically disorganized; they still maintain a rotating axis. This is why A_2 is a powerful predictor: it can detect small kinematic warps in the rotation field.

5.4.2 The predictors evolve non-linearly with time; the LDA incorporates this behavior

As evident in Figures 5.14, 5.15, and 5.16, the predictor values evolve with time throughout the merger. In most cases, this evolution is non-linear. For instance, in Fig-

ure 5.16, the trend is towards decreased values of λ_{Re} , ending at the lowest values for the post-coalescence stages. However, then, there is a slight positive evolution for the snapshots that we classify as isolated because they take place > 0.5 Gyr after final coalescence. This is the case for all of the major merger simulations, which decrease in λ_{Re} until these isolated post-coalescence snapshots. For the minor mergers, the isolated post-coalescence snapshots are consistent with the lowest values of λ_{Re} from during the merger.

What does this mean for the LDA classifier? The interaction terms deal with this non-linear behavior of the predictor values with time. For instance, if we were to create a classifier with only the primary predictors, which we did to understand the first order evolution of these predictors, then the classifier would be inaccurate, classifying many of these isolated post-coalescence snapshots as mergers. However, the LDA includes interaction terms, which are sensitive to the values of the other predictors. In this way, the classifier can place less weight on certain areas of these predictor spaces, such as the lower values of λ_{Re} . By including interaction terms, we make the ‘linear’ discriminant analysis slightly less linear to account for some of these non-linear predictors.

It is also important to note that while many of the predictors have a non-linear evolution, some are more straightforward. For example, the LDA classifier for the q0.5_fg0.3 simulation relies on σ_{asym} and A_2 and has interaction term that is not significant to 1σ . Figure 5.14 displays this result for the q0.5_fg0.3 simulation, where A_2 is heightened for the mergers. Figure 5.15 shows this for the σ_{asym} predictor. These predictors are more cleanly able to separate the merger population than λ_{Re} , which is why λ_{Re} is not included in the classification for q0.5_fg0.3.

5.4.3 The classification changes with mass ratio

There have been a scarcity of studies of the properties of simulated mergers and how they affect kinematic predictors. Hung et al. (2016) have investigated this for a set of simulations of merging galaxies with mass ratios 1:1 and 1:4. They find that the mass ratio

is the most important input parameter and that the merger signatures in kinematics are most visible for the major mergers, where they can be visible for up to twice as long for the 1:4 major merger. While there are significant differences between the approach in Hung et al. (2016), which utilizes the **GADGET-3** particle velocities for the gas particles, and our mock datacubes, we still find that we produce markedly different classifications based on mass ratio.

The major and minor merger classifications are different in several ways. First of all, the minor merger classifications are less accurate and tend to have a shorter observability timescale. Second, they rely upon a different number of terms, where the minor merger classifications rely upon fewer terms. This could be a reflection of the decreased power of the kinematic predictors for these simulations. We have shown in Figures 5.14, 5.15, and 5.16 that the minor merger classification does not show a significant separation in predictor space between the merging and nonmerging galaxies. The major merger classifications have up to 11 significant terms for the major merger combined simulation, reflecting that the primary and interaction terms are all informative for the separation between groups.

Lastly, the significant terms differ between the major and minor classifications; resids and ΔPA are relatively more important for the minor merger classifications while A_2 is more important for the major mergers. Unpacking these results is an exercise in relativity. For instance, ΔPA is a relatively more important term for the minor mergers. This indicates that the global change of the position angle is relatively more important for the minor mergers, although it is key that the actual change in ΔPA is still greater for the major mergers. A_2 , on the other hand, is the asymmetry in the Radon profile. This means it measures the deviation of the kinematic position angle from a straight line, which identifies kinematically warped disks. We observe more visible warps in the major mergers.

5.4.4 The classification does not change with gas fraction

We find that the q0.333_fg0.3 simulation and the q0.333_fg0.1 simulation, which have the same mass ratio but different gas fractions, are very similar. Therefore, the gas fraction does not have a large effect on the kinematic predictors.

Observations and theory show that the gas fraction of merging galaxies can have a significant impact on their kinematics. For instance, the (stellar or gas) disks of gas-rich systems can survive mergers or reform to erase kinematic signatures of a merger (e.g., Springel & Hernquist 2005; Ueda et al. 2014). One specific prediction from Hopkins et al. (2009) is that a higher gas fraction will result in an increased chance of disk survival. While this work is for higher redshift, significantly gas-enhanced galaxies, the dependence of the fraction of surviving disks on gas fraction still applies here.

In the case of all the simulations in this work, the disk-like kinematics survive following the merger. This is consistent with N19, where although the morphology of the merger remnants is slightly enhanced in terms of concentration, the remnant is still disk-like. To summarize, the kinematics of the relatively gas-rich and gas-poor simulations in this work are not significantly different.

5.4.5 The observability timescale is long for most runs but shorter than for the imaging technique

Here we discuss the results of the observability timescale of the kinematic LDA classification for the different merger simulations. These results are presented in Section 5.3.4, where we show that the major mergers generally have a longer observability timescale that spans $\sim 60\%$ of the total merger time.

However, the q0.2_fg0.3_BT0.2 simulation is observable for 100% of the total merger. Figure 5.12 demonstrates that while the q0.2_fg0.3_BT0.2 simulation nominally has the longest fractional observability time, the standard deviation of each snapshot's mean value

of LD1 is large. If we were to instead incorporate the standard deviation into the calculation of observability time, requiring that the mean LD1 value minus one standard deviation fall above the decision boundary, the observability timescale of the q0.2_fg0.3_BT0.2 simulation would be much shorter relative to the other simulations. The same pattern holds for the q0.1_fg0.3_BT0.2 simulation; there is a large standard deviation on the LD1 value, indicating that some viewpoints are much more ‘observable’ than others. This is not a systematic that is associated with a specific viewpoint; the outlier viewpoints vary with each snapshot.

Another interesting observation to be made from Figure 5.12 is that the early stages of merging for all simulations show a larger standard deviation in the LD1 values. In other words, there is more variation among the kinematic predictors for the viewpoints of these earlier snapshots. As the merger progresses from the post-coalescence snapshots into the isolated snapshots that occur >0.5 Gyr after final coalescence, the value of LD1 does not decrease significantly. This is different than the trend in N19, where the value of LD1 decreases significantly with time for the isolated snapshots that fall >0.5 Gyr after final coalescence. Perhaps the kinematic signatures of a merger are longer lived, which is why we do not observe the drop-off in LD1 values for the set of isolated galaxies that are selected from the end of the merger simulations. We plan to discuss this in more detail when we combine the two techniques in Nevin et al. (2019, in prep).

This is consistent with Hung et al. (2015), who find that kinematic tracers of mergers tend to be most informative during the late stage of the merger, which is when the imaging predictors are also most useful. Additionally, they find that the kinematic classification results in a significant fraction of false negatives (mergers identified as nonmergers), meaning that various stages of the merger can be indistinguishable from disks. This stage of merging galaxy would also be a false negative in our technique, which leads us into the discussion of accuracy and precision of the classification in the next section.

5.4.6 The kinematic LDA is precise but not accurate at identifying merging galaxies

As we discuss in Section 5.3.5, the LDA technique has a significant number of false negatives and very few false positives. This means that the accuracy is relatively low while the precision high; In other words, there will be fewer total galaxies correctly classified but there are very few false positive classifications. This could be due to the skewness of some of the predictor populations. We discuss this in the context of the violation of multivariate normality in Section 5.3.1. To reiterate, Fan & Wang (1999) found that if multivariate normality and homoscedasticity are violated and there are unbalanced priors, the classification will favor the larger group, which is the nonmergers in our case (since the nonmerger prior is large). We find that there are more false negatives for the major merger classifications, where the prior is $f_{\text{nonmerg}} = 0.9$, as opposed to the minor merger simulations, where the prior is $f_{\text{nonmerg}} = 0.7$. Therefore, we suggest that the classification is more conservative in the sense of producing fewer false positives due to this skewness.

In this classification, accuracy and precision are a trade-off. We have the option to modify the decision boundary in favor of increasing the accuracy; in turn, the precision will decrease. This was not an issue with the imaging classifier since it was reasonably precise and accurate simultaneously. We save discussion of this modification for Nevin et al. (2019, in prep). Hung et al. 2016 recommend using kinematic predictors in combination with imaging predictors due to the frequency of false negatives in their investigation of kinematically-identified merging galaxies. In Nevin et al. (2019, in prep), we also plan to combine the imaging and kinematic classifications and balance the accuracy and precision of the kinematic classifier against that of the imaging classifier.

5.4.7 LDA is one of many statistical and machine learning classification techniques; it has limitations and advantages

Here we discuss the advantages and disadvantages of an LDA approach to the galaxy merger classification in the context of other available statistical and machine-learning methods.

Logistic regression is a binary classifier that is very similar to LDA. It is akin to a linear regression but with a binary dependent variable as opposed to a continuous dependent variable; in this way it is well suited for classification. We run logistic regression with the same primary coefficients as LDA and find similar results. However, there are a number of trade-offs between logistic regression and LDA, which is why we ultimately selected LDA as the statistical approach in N19. We also continue to utilize LDA here in order to directly compare the imaging and kinematic classifications in future work.

Here we briefly discuss the advantages and disadvantages of selecting the LDA technique over logistic regression. First, as was discussed in Section 5.3.1, LDA makes many assumptions about the distribution of the data. There has been a huge body of statistical studies about how robust LDA is under these violations. Some work suggests that LDA is very robust and can be used to obtain accurate classifications even under extreme violations of these assumptions (e.g., Duda et al. 2001; Li et al. 2006) whereas some work cautions that LDA is less accurate and precise than logistic regression when these violations are present (e.g., Fan & Wang 1999). In N19, the classification is very accurate and precise for all simulations. In contrast, in the kinematic analysis we find that the number of false negative classifications increases. It would be interesting to explore if these classifications would change if we used logistic regression with all the interaction terms. The disadvantages of logistic regression are that it is surprisingly unstable when the classes are well-separated and that it is more computationally expensive.

Another approach could be to use quadratic discriminant analysis (QDA), which we

pursue in N19 in order to compare the accuracy and precision. This method does not assume homoscedasticity; however the interpretation of the QDA coefficients are not as straightforward. We find that it does not significantly improve the classification in N19.

Along the same lines, there are other machine-learning techniques, such as support vector machines (SVM) or random forest classifiers, that could reduce the number of misclassifications. This class of technique tends to be more successful, yet the decisions that drive the classifications are more opaque. We ultimately chose to pursue a classifier that was based upon previous kinematic predictors so that we could directly compare the result to previous work. We wanted to create a classifier that could work for multiple stages of the merger. However, it would be interesting to investigate some of these other techniques with the goal of better separating different epochs of the merger. Since these more complicated machine learning techniques can create adaptive solutions (i.e., changing based on the merger stage), we could create a more complicated technique that classifies based on the epoch of the merger as well.

We chose to use LDA as our classification technique in N19 since it had a high accuracy and precision. It is also more explicit, meaning that the analysis of the classification decisions is more straightforward and applicable to the existing discussions in the literature. However, there may be some trade-offs with this decision; specifically, this technique may have a higher rate of misclassifications due to violations of the assumptions of LDA. To complete this paper, we plan to test the technique against logistic regression as well as some more opaque classifiers such as SVMs or random forest classifiers. This less explicit type of classifier could also be very informative in terms of discovering new kinematic predictors or features in kinematic maps that are useful as classifiers.

5.5 Preliminary Conclusions

In this work, we build upon the stand-alone imaging approach in N19 to create a parallel LDA classifier that utilizes kinematic predictors to identify merging galaxies. To

produce the classification we create mock MaNGA-ized datacubes from **SUNRISE** simulated galaxy SEDs, convolving to the spatial and spectral resolution of MaNGA, introducing noise, and binning following the Voronoi binning scheme used for the MaNGA datacubes. Using **ppxf**, we extract stellar velocity and stellar velocity dispersion maps from each datacube.

We then extract the following kinematic predictors from the 2D velocity and velocity dispersion maps: the difference between the kinematic PA and the imaging PA (ΔPA), the asymmetry of the velocity map (v_{asym}), the asymmetry of the velocity dispersion map (σ_{asym}), the **kinemetry** residuals (resids), the specific angular momentum (λ_{R_e}), the ellipticity (ϵ), the weighted asymmetry in the Radon profile (A), and the asymmetry in the Radon profile (A_2). We clean the input data and run the linear discriminant analysis (LDA) as a predictor selector first, and then as a classifier for all simulations individually as well as for the combined major merger simulation and the combined minor merger simulation. Our main conclusions are:

- The LDA classifications for mergers with different gas fractions are not significantly different.
- The major and minor merger combined LDA classifications are significantly different. The major mergers rely more on the A_2 coefficient, which encompasses the deviation of the kinematic PA from a straight line. The minor mergers rely more on ΔPA , which is the global offset of the kinematic PA from the imaging PA.
- The most important kinematic predictors (for all simulations) are the specific angular momentum (λ_{R_e}) and the asymmetry of the velocity dispersion map (σ_{asym}), both of which show significant evolution for the major merger simulations. This agrees with previous work that finds that major mergers have a larger effect on the 2D kinematics of galaxies.
- Many kinematic predictors evolve non-linearly with time throughout the merger; the interaction terms of the classification can account for this behavior. The interaction

terms are the multiplicative combinations of the input predictors, such as $\sigma_{\text{asym}}^* \epsilon$.

- Since we combine the sensitivities of many different kinematic predictors, we find that the observability timescale for the merger simulations is a significant fraction of the overall merger time ($\sim 60\%$).
- With the current LDA decision boundaries for separating mergers from nonmergers, the classifications are very precise ($\sim 90\%$) but less accurate ($\sim 60\%$), meaning that the classification leads to a significant number of false negatives, or missed mergers. The precision and accuracy could be adjusted by moving the decision boundary, but it should be noted that even with this adjustment, the kinematic technique will be less precise and accurate overall than the imaging technique.

In Nevin et al. (2019, in prep) we plan to combine the kinematic classification with the imaging classification presented in N19. In that paper we will describe the differences between the approaches and will further investigate whether various kinematic parameters enhance the existing imaging classifier. Also, we plan to apply the classifier to MaNGA galaxies, which will involve extensive work to determine the optimal amount to move the decision boundaries to create various levels of clean samples. For instance, as discussed in this work, we could move the decision boundaries to a lower value in order to identify more mergers, but this would have the effect of making the classification less precise with more false positives.

We will also investigate the possibility of splitting the classification into two different stages of the merger to identify early vs late-stage mergers. Our scientific goals include identifying how the star formation histories, metallicities, and AGN activity change for these different stages as well as for different mass ratios of merging galaxies.

Chapter 6

Conclusion

In this thesis, I have presented a novel technique to directly identify the kinematic origin of double-peaked narrow lines in integrated spectra (Chapter 2). The sample of double-peaked AGN (DPAGN) in this work are the 71 DPAGN at $z < 0.1$ identified in the Sloan Digital Sky Survey. The kinematic technique was critical for determining that the majority (86%) of the 71 Type-2 AGN with double-peaked emission lines are dominated by moderate-luminosity AGN outflows. I also examined the relationship between the size of the narrow-line region and the luminosity of the central AGN responsible for its photoionization. I found a relationship of $R_{\text{NLR}} \propto L_{[\text{OIII}]}$ ^{0.21±0.05}, which supports a clumpy two-zone ionization model for the photoionization of the NLR.

My work in Chapter 2 led directly into Chapter 3; I collected the 18 double-peaked AGN from Chapter 2 that were dominated by outflow signatures on all spatial scales. I applied an analytic Markov Chain Monte Carlo biconical outflow model (of my own development) to the spatially resolved kinematics of these DPAGN. I determined that multiple different bicone geometries best described the data, including asymmetric bicones, nested bicones, and symmetric bicones. For all 18 DPAGN, I was able to constrain mass outflow rates and energetics from the derived surface geometries and velocities of the best fit biconical models. This was critical for determining that 89% of the outflows were energetic enough ($L_{\text{KE}}/L_{\text{bol}} > 0.005$) to drive a two-staged feedback process in the disk of the host galaxies. I additionally utilized the model bicones to show that these moderate-luminosity AGN outflows

are very large for their luminosities with large opening angles that intersect the disk of the host galaxies, thus having the potential to couple their energy to the ISM. Finally, I investigated the properties of the host galaxies compared to a matched control sample and found that 23% were significantly redder and/or had a significantly lower specific star formation rate, which provided tentative evidence for negative feedback. Chapter 3 wrapped up the portion of this thesis that is dedicated to AGN feedback.

I then embarked on an investigation of how to improve the accuracy of galaxy merger identifications. In Chapter 4, I approached this using images from galaxy simulations (**GADGET-3** hydrodynamical simulations of merging galaxies with the dust radiative transfer code **SUNRISE**). I presented a suite of simulated merging galaxies with different merger parameters (gas rich/poor, major/minor) and matched isolated galaxies. The simulated snapshots have high temporal and spatial resolution and capture the different simulations from various viewpoints. I first built a pipeline to create mock SDSS images from the simulated galaxy images with the goal of identifying mergers directly from SDSS imaging. I then created tools to extract various different imaging predictors that have been utilized in the past to identify merging galaxies; I combined all of these predictors using a linear discriminant analysis (LDA) technique. I ran this classifier on all of the different simulated mergers and found that the mass ratio of the merger had the biggest effect on the classification while the gas fraction did not affect the LDA result. I then created a separate major and minor merger classification. By creating a classification that combined all of the individual techniques, I dramatically lengthened the observability timescale of the merger (>2 Gyr) and increased the accuracy and precision above that of the individual tools. I preliminarily applied the technique to GalaxyZoo galaxies and found good agreement with their merger classifications; I plan to apply it to a larger sample of SDSS images in the future.

Chapter 5 built off of Chapter 4 by extending the classification technique to kinematic predictors from the same set of simulated galaxies. This required creating mock datacubes to match the specifications of the MaNGA IFS survey of galaxies. The results were similar

in that the mass ratio of the mergers had the biggest effect of the classification, so I created a separate major and minor merger classification. I found that the kinematic side of the technique also increased the observability timescale of the merger beyond that of the individual kinematic predictors but that the accuracy was lower, with many false negatives, meaning that a significant fraction of merging galaxies were missed by the identification technique.

The results from Chapter 5 are very interesting in the context of Chapter 4. I plan to more directly compare the results of the two classifications in Nevin et al. (2019, in prep), when I apply both techniques individually and in combination to galaxies in MaNGA.

My immediate future plans also involve publishing the imaging and kinematic technique on Github. I have developed this technique to be adaptable to different imaging and IFS surveys; the suite of tools will be made available under the **MergerMonger** Github repository and can be adapted to telescopes such as *HST*, TMT, or *JWST*. My goal is to make this type of classification technique accessible to the astronomical community. I have embarked on a side projects to extend the merger identification technique to higher redshift *HST* imaging with Laura Blecha’s group at the University of Florida. I plan to continue working on this with her students in the future and to further extend this work to *JWST* imaging and IFS.

The more direct extension of Chapters 4 and 5 is to apply the imaging + kinematic merger classifications to the images and IFS of the MaNGA/SDSS surveys. Then, I plan to more directly address some of the questions posed about galaxy evolution using my samples of merging galaxies in MaNGA. I will first investigate the spatially resolved star formation in the MaNGA mergers since mergers are predicted to funnel gas to the center of a galaxy, fueling star formation. Recent work finds that there is a higher fraction of recent star formation for asymmetric galaxies, tentatively implying that galaxies that are undergoing mergers are actively forming stars (Rowlands et al. 2018). With spatially resolved metallicities from IFS, it is also possible to use the metallicity gradient (in this case, O/H) as a powerful complementary probe to star formation histories; the radial distribution of metals in a galaxy reveals the manner in which gas is accreted. For instance, major mergers have been observed

to have low central metallicities and flat metallicity gradients (e.g., Rupke et al. 2010), implying inflows of metal-poor gas as predicted by simulations (Mihos & Hernquist 1996).

I would investigate this in more detail with the spatially resolved stellar ages and metallicities of pre- and post-coalescence major and minor mergers. To do this, I first plan to modify the classification to identify pre- and post-coalescence mergers separately. I will then measure the star formation histories for each galaxy using the Pipe3D data product (Sánchez et al. 2016a,b) from the MaNGA survey. I plan to probe the star formation history as a function of the spatial position in the galaxy, so I will characterize the stellar age of spaxels at elliptical (deprojected) radial bins as a function of the Petrosian radius of the galaxy. I will then use the Bayesian inference code IZI (Blanc et al. 2015) to measure the metallicity at the same elliptical bins.

I also plan to further investigate the kinematic properties of galaxies in MaNGA. This project is highly exploratory and will probably occupy me for several years. For this project, I will use various machine learning techniques (supervised and unsupervised) to explore the kinematics of many different types of galaxies (not only mergers) in MaNGA. My goal is to use these machine learning tools to learn about the relationships between different kinematic classes of galaxies; in an era of an abundance of data from IFS, it is necessary to develop new tools to incorporate all of the information that is available. This project may expand to include non-kinematic information such as star formation histories. Since much of galaxy research is kinematic follow-up to morphological classifications, it could be highly informative to first classify galaxies by their kinematic properties.

Bibliography

- Abadi, M. G., Moore, B., & Bower, R. G. 1999, MNRAS, 308, 947
- Abazajian, K. N., Adelman-McCarthy, J. K., Agüeros, M. A., et al. 2009, ApJS, 182, 543
- Abolfathi, B., Aguado, D. S., Aguilar, G., et al. 2017, ArXiv e-prints, arXiv:1707.09322
- Abraham, R. G., van den Bergh, S., & Nair, P. 2003, ApJ, 588, 218
- Akaike, H. 1974, IEEE Transactions on Automatic Control, 19, 716
- Albareti, F. D., Allende Prieto, C., Almeida, A., et al. 2017, ApJS, 233, 25
- Allen, J. T., Schaefer, A. L., Scott, N., et al. 2015, MNRAS, 451, 3
- Alonso-Herrero, A., Rieke, G. H., Rieke, M. J., et al. 2006, ApJ, 650, 835
- Andrae, R., Jahnke, K., & Melchior, P. 2011, MNRAS, 411, 385
- Antonucci, R. R. J., & Miller, J. S. 1985, ApJ, 297, 621
- Arav, N., Borguet, B., Chamberlain, C., Edmonds, D., & Danforth, C. 2013, MNRAS, 436, 3286
- Baldwin, J. A., Phillips, M. M., & Terlevich, R. 1981, Publications of the ASP, 93, 5
- Barbosa, F. K. B., Storchi-Bergmann, T., McGregor, P., Vale, T. B., & Rogemar Riffel, A. 2014, MNRAS, 445, 2353
- Barrera-Ballesteros, J. K., García-Lorenzo, B., Falcón-Barroso, J., et al. 2015, A & A, 582, A21
- Barrera-Ballesteros, J. K., Heckman, T., Sánchez, S. F., et al. 2018, ApJ, 852, 74
- Barrows, R. S., Comerford, J. M., Greene, J. E., & Pooley, D. 2016, ApJ, 829, 37
- Barrows, R. S., Sandberg Lacy, C. H., Kennefick, J., et al. 2013, ApJ, 769, doi:10.1088/0004-637X/769/2/95
- Baskin, A., & Laor, A. 2005, MNRAS, 358, 1043

- Bell, E. F., McIntosh, D. H., Katz, N., & Weinberg, M. D. 2003, *ApJS*, 149, 289
- Bell, E. F., Wolf, C., Meisenheimer, K., et al. 2004, *ApJ*, 608, 752
- Bellocchi, E., Arribas, S., & Colina, L. 2012, *A & A*, 542, A54
- . 2016, *A & A*, 591, A85
- Bellocchi, E., Arribas, S., Colina, L., & Miralles-Caballero, D. 2013, *AAP*, 557, A59
- Bendo, G. J., & Barnes, J. E. 2000, *MNRAS*, 316, 315
- Bennert, N., Falcke, H., Schulz, H., Wilson, A. S., & Wills, B. J. 2002, *ApJ*, 574, 105
- Bershady, M. A., Verheijen, M. A. W., Swaters, R. A., et al. 2010, *ApJ*, 716, 198
- Bertin, E., & Arnouts, S. 1996, *A&AS*, 117, 393
- Bertone, S., & Conselice, C. J. 2009, *MNRAS*, 396, 2345
- Bianchi, S., Maiolino, R., & Risaliti, G. 2012, *Advances in Astronomy*, 2012, 782030
- Blanc, G. A., Kewley, L., Vogt, F. P. A., & Dopita, M. A. 2015, *ApJ*, 798, 99
- Blanton, M. R., Kazin, E., Muna, D., Weaver, B. A., & Price-Whelan, A. 2011, *AJ*, 142, 31
- Blanton, M. R., Bershady, M. A., Abolfathi, B., et al. 2017, *AJ*, 154, 28
- Blecha, L., Cox, T. J., Loeb, A., & Hernquist, L. 2011, *MNRAS*, 412, 2154
- Blecha, L., Loeb, A., & Narayan, R. 2013, *MNRAS*, arXiv:1201.1904
- Blecha, L., Snyder, G. F., Satyapal, S., & Ellison, S. L. 2018, *MNRAS*, 478, 3056
- Bluck, A. F. L., Mendel, J. T., Ellison, S. L., et al. 2014, *MNRAS*, 441, 599
- Bois, M., Emsellem, E., Bournaud, F., et al. 2011, *MNRAS*, 416, 1654
- Bondi, H., & Hoyle, F. 1944, *MNRAS*, 104, 273
- Boone, F., García-Burillo, S., Combes, F., et al. 2011, *A & A*, 525, A18
- Borguet, B. C. J., Arav, N., Edmonds, D., Chamberlain, C., & Benn, C. 2013, *ApJ*, 762, 49
- Bottorff, M. C., & Ferland, G. J. 2000, *MNRAS*, 316, 103
- Bournaud, F. 2016, in *Astrophysics and Space Science Library*, Vol. 418, Galactic Bulges, ed. E. Laurikainen, R. Peletier, & D. Gadotti, 355
- Bournaud, F., Combes, F., & Jog, C. J. 2004, *A & A*, 418, L27
- Bournaud, F., Jog, C. J., & Combes, F. 2005, *A & A*, 437, 69

- . 2007, *A & A*, 476, 1179
- Brown, M. J. I., Dey, A., Jannuzi, B. T., et al. 2007, *ApJ*, 654, 858
- Brusa, M., Bongiorno, A., Cresci, G., et al. 2015, *MNRAS*, 446, 2394
- Bryant, J. J., Owers, M. S., Robotham, A. S. G., et al. 2015, *MNRAS*, 447, 2857
- Bryant, J. J., Bland-Hawthorn, J., Lawrence, J., et al. 2016, in *Society of Photo-Optical Instrumentation Engineers (SPIE) Conference Series*, Vol. 9908, *Ground-based and Airborne Instrumentation for Astronomy VI*, 99081F
- Bundy, K., Bershadsky, M. A., Law, D. R., et al. 2015, *ApJ*, 798, 7
- Campbell, D., & Lele, S. 2013, *ArXiv e-prints*, arXiv:1305.3299
- Cappellari, M. 2017, *MNRAS*, 466, 798
- Cappellari, M., & Copin, Y. 2003, *MNRAS*, 342, 345
- Cappellari, M., & Emsellem, E. 2004, *Publications of the ASP*, 116, 138
- Cappellari, M., Emsellem, E., Krajnović, D., et al. 2011, *MNRAS*, 413, 813
- Carniani, S., Marconi, A., Maiolino, R., et al. 2016, *A & A*, 591, A28
- Catinella, B., Schiminovich, D., Kauffmann, G., et al. 2010, *MNRAS*, 403, 683
- Cicone, C., Maiolino, R., Sturm, E., et al. 2014, *A & A*, 562, A21
- Ciotti, L., Ostriker, J. P., & Proga, D. 2010, *ApJ*, 717, 708
- Cisternas, M., Jahnke, K., Inskip, K. J., et al. 2011, *ApJ*, 726, 57
- Coelho, P., & Gadotti, D. A. 2011, *ApJ*, 743, L13
- Cole, S., Helly, J., Frenk, C. S., & Parkinson, H. 2008, *MNRAS*, 383, 546
- Combes, F. 2014, *Proceedings of the International Astronomical Union*, 10, 182189
- Comerford, J. M., Gerke, B. F., Stern, D., et al. 2012, *ApJ*, 753, 42
- Comerford, J. M., Griffith, R. L., Gerke, B. F., et al. 2009a, *ApJ*, 702, L82
- Comerford, J. M., Schluns, K., Greene, J. E., & Cool, R. J. 2013, *ApJ*, 777, doi:10.1088/0004-637X/777/1/64
- Comerford, J. M., Gerke, B. F., Newman, J. A., et al. 2009b, *ApJ*, 698, 956
- Conselice, C. J. 2014, *ARA&A*, 52, 291
- Conselice, C. J., Bershadsky, M. A., Dickinson, M., & Papovich, C. 2003, *AJ*, 126, 1183

- Conselice, C. J., Bershad, M. A., & Jangren, A. 2000, *ApJ*, 529, 886
- Conselice, C. J., Rajgor, S., & Myers, R. 2008, 927, 909
- Conselice, C. J., Yang, C., & Bluck, A. F. L. 2009, *MNRAS*, 394, 1956
- Cooper, M. C., Newman, J. A., Davis, M., Finkbeiner, D. P., & Gerke, B. F. 2012, *spec2d: DEEP2 DEIMOS Spectral Pipeline*, Astrophysics Source Code Library, ascl:1203.003
- Cox, T. J., Younger, J., Hernquist, L., & Hopkins, P. F. 2008, in *IAU Symposium*, Vol. 245, *Formation and Evolution of Galaxy Bulges*, ed. M. Bureau, E. Athanassoula, & B. Barbuy, 63–66
- Crenshaw, D. M., Fischer, T. C., Kraemer, S. B., & Schmitt, H. R. 2015, *ApJ*, 799, 83
- Crenshaw, D. M., Fischer, T. C., Kraemer, S. B., & Schmitt, H. R. 2015, *ApJ*, 799, 83
- Crenshaw, D. M., & Kraemer, S. B. 2000, *ApJ*, 532, L101
- Crenshaw, D. M., & Kraemer, S. B. 2003, in *Astronomical Society of the Pacific Conference Series*, Vol. 290, *Active Galactic Nuclei: From Central Engine to Host Galaxy*, ed. S. Collin, F. Combes, & I. Shlosman, 195
- Crenshaw, D. M., & Kraemer, S. B. 2005, *ApJ*, 625, 680
- Crenshaw, D. M., & Kraemer, S. B. 2012, *ApJ*, 753, 75
- Crenshaw, D. M., Kraemer, S. B., & George, I. M. 2003, *Ann. Rev. Astron. & Astrophys.*, 41, 117
- Crenshaw, D. M., Schmitt, H. R., Kraemer, S. B., Mushotzky, R. F., & Dunn, J. P. 2010, *ApJ*, 708, 419
- Crenshaw, D. M., Kraemer, S. B., Hutchings, J. B., et al. 2000, *AJ*, 120, 1731
- Cresci, G., Mainieri, V., Brusa, M., et al. 2015, *ApJ*, 799, 82
- Croton, D. J., Springel, V., White, S. D. M., et al. 2006, *MNRAS*, 365, 11
- Daddi, E., Dickinson, M., Morrison, G., et al. 2007, *ApJ*, 670, 156
- Darg, D. W., Kaviraj, S., Lintott, C. J., et al. 2010, *MNRAS*, 401, 1043
- Das, V., Crenshaw, D. M., Deo, R. P., & Kraemer, S. B. 2006, *AJ*, 132, 42
- Das, V., Crenshaw, D. M., & Kraemer, S. B. 2007, *ApJ*, 656, 699
- Dasyra, K. M., Tacconi, L. J., Davies, R. I., et al. 2006, *ApJ*, 651, 835
- Davies, R. I., Hicks, E., Schartmann, M., et al. 2009, *International Astronomical Union*, doi:10.1017/S1743921310006496

- Davies, R. I., Burtscher, L., Rosario, D., et al. 2015, *ApJ*, 806, 127
- de Zeeuw, P. T., Bureau, M., Emsellem, E., et al. 2002, *MNRAS*, 329, 513
- de Zeeuw, T., & Franx, M. 1991, *ARA&A*, 29, 239
- Dekel, A., Birnboim, Y., Engel, G., et al. 2009, *Nature*, 457, 451
- D'Eugenio, F., Houghton, R. C. W., Davies, R. L., & Dalla Bontà, E. 2013, *MNRAS*, 429, 1258
- Di Matteo, T., Springel, V., & Hernquist, L. 2005, *Nature*, 433, 604
- Dopita, M. A., Groves, B. A., Sutherland, R. S., Binette, L., & Cecil, G. 2002, *ApJ*, 572, 753
- Draine, B. T., & Li, A. 2007, *ApJ*, 657, 810
- Draper, A. R., & Ballantyne, D. R. 2012, *ApJ*, 753, L37
- Drory, N., MacDonald, N., Bershadsky, M. A., et al. 2015, *AJ*, 149, 77
- Duda, R. O., Hart, P. E., & Stork, D. G. 2001, *Pattern Classification* (2nd Ed) (Wiley)
- Dwek, E. 1998, *ApJ*, 501, 643
- Efron, B. 1983, *Journal of the American Statistical Association*, 78, 316
- Elitzur, M. 2012, *ApJL*, 747, 33
- Elitzur, M., & Shlosman, I. 2006, *ApJ*, 648, L101
- Ellison, S. L., Mendel, J. T., Patton, D. R., & Scudder, J. M. 2013, *MNRAS*, 435, 3627
- Ellison, S. L., Patton, D. R., Mendel, J. T., & Scudder, J. M. 2011, *MNRAS*, 418, 2043
- Emsellem, E., Cappellari, M., Peletier, R. F., et al. 2004, *MNRAS*, 352, 721
- Emsellem, E., Cappellari, M., Krajnović, D., et al. 2007, *MNRAS*, 379, 401
- . 2011, *MNRAS*, 414, 888
- Engel, H., Davies, R. I., Genzel, R., et al. 2010, *A & A*, 524, A56
- Epinat, B., Tasca, L., Amram, P., et al. 2012, *A & A*, 539, A92
- Everett, J. E. 2005, *ApJ*, 631, 18
- Everett, J. E., & Murray, N. 2007, *ApJ*, 656, 93

- Faber, S. M., Phillips, A. C., Kibrick, R. I., et al. 2003, in , Vol. 4841, Instrument Design and Performance for Optical/Infrared Ground-based Telescopes, ed. M. Iye & A. F. M. Moorwood, 1657–1669
- Faber, S. M., Willmer, C. N. A., Wolf, C., et al. 2007, *ApJ*, 665, 265
- Fabian, A. C. 2012, *ARA&A*, 50, 455
- Fan, X., & Wang, L. 1999, *The Journal of Experimental Education*, 67, 265
- Faucher-Giguère, C.-A., & Quataert, E. 2012, *MNRAS*, 425, 605
- Ferrarese, L., & Merritt, D. 2000, *ApJ*, 539, L9
- Fischer, T. C., Crenshaw, D. M., Kraemer, S. B., & Schmitt, H. R. 2013, *ApJS*, 209, 32
- Fischer, T. C., Crenshaw, D. M., Kraemer, S. B., Schmitt, H. R., & Trippe, M. L. 2010, *AJ*, 140, 577
- Fischer, T. C., Crenshaw, D. M., Kraemer, S. B., Schmitt, H. R., & Turner, T. J. 2014, *ApJ*, 785, 25
- Fischer, T. C., Machuca, C., Diniz, M. R., et al. 2017, *ApJ*, 834, 30
- Fisher, D. B., & Drory, N. 2008, *AJ*, 136, 773
- Fogarty, L. M. R., Scott, N., Owers, M. S., et al. 2015, *MNRAS*, 454, 2050
- Foreman-Mackey, D., Hogg, D. W., Lang, D., & Goodman, J. 2013, *Publications of the ASP*, 125, 306
- Fraquelli, H. A., Storchi-Bergmann, T., & Binette, L. 2000, *ApJ*, 532, 867
- Fu, H., Myers, A. D., Djorgovski, S. G., & Yan, L. 2011, *ApJ*, 733, 103
- Gabor, J. M., & Bournaud, F. 2014, *MNRAS*, 441, 1615
- Gebhardt, K., Bender, R., Bower, G., et al. 2000, *ApJ*, 539, L13
- Gelbord, J. M., Weaver, K. A., & Yaqoob, T. 2004, in *Multiwavelength AGN Surveys*, ed. R. Mújica & R. Maiolino, 253–254
- Gialalisco, M., Steidel, C. C., & Macchetto, F. D. 1996, *ApJ*, 470, 189
- Glazebrook, K. 2013, *Publications of the Astron. Soc. of Australia*, 30, e056
- Glazebrook, K., Ellis, R., Santiago, B., & Griffiths, R. 1995, *MNRAS*, 275, L19
- Goodman, J., & Weare, J. 2010, *Communications in Applied Mathematics and Computational Science*, 5, 65

- Goulding, A. D., Greene, J. E., Bezanson, R., et al. 2018, PASJ, 70, S37
- Greene, J. E., Zakamska, N. L., & Smith, P. S. 2012, ApJ, 746, 86
- Groves, B., Dopita, M. A., Sutherland, R. S., et al. 2008, ApJS, 176, 438
- Gunn, J. E., & Gott, III, J. R. 1972, ApJ, 176, 1
- Gunn, J. E., Siegmund, W. A., Mannery, E. J., et al. 2006, AJ, 131, 2332
- Guo, Y., Ferguson, H. C., Bell, E. F., et al. 2015, ApJ, 800, 39
- Haan, S., Surace, J. A., Armus, L., et al. 2011, AJ, 141, 100
- Hainline, K. N., Hickox, R., Greene, J. E., Myers, A. D., & Zakamska, N. L. 2013, ApJ, 774, 145
- Hainline, K. N., Hickox, R. C., Greene, J. E., et al. 2014, ApJ, 787, 65
- Harrison, C. M., Alexander, D. M., Mullaney, J. R., & Swinbank, A. M. 2014, MNRAS, 441, 3306
- Hayward, C. C., Kereš, D., Jonsson, P., et al. 2011, ApJ, 743, 159
- Heckman, T. M., Kauffmann, G., Brinchmann, J., et al. 2004, ApJ, 613, 109
- Heckman, T. M., Miley, G. K., van Breugel, W. J. M., & Butcher, H. R. 1981, ApJ, 247, 403
- Hicks, E. K. S., Davies, R. I., Malkan, M. A., et al. 2009, ApJ, 696, 448
- Hopkins, P. F., Cox, T. J., Younger, J. D., & Hernquist, L. 2009, ApJ, 691, 1168
- Hopkins, P. F., & Elvis, M. 2010, MNRAS, 401, 7
- Hopkins, P. F., Hernquist, L., Cox, T. J., et al. 2005, ApJ, 630, 705
- Hopkins, P. F., Hernquist, L., Cox, T. J., & Kereš, D. 2008, ApJS, 175, 356
- Hopkins, P. F., Kereš, D., Oñorbe, J., et al. 2014, MNRAS, 445, 581
- Hopkins, P. F., Richards, G. T., & Hernquist, L. 2007, ApJ, 654, 731
- Hopkins, P. F., Somerville, R. S., Hernquist, L., et al. 2006, ApJ, 652, 864
- Hopkins, P. F., Wetzel, A., Kereš, D., et al. 2018, MNRAS, 480, 800
- Hubble, E. P. 1926, ApJ, 64, doi:10.1086/143018
- Hung, C.-L., Hayward, C. C., Smith, H. A., et al. 2016, ApJ, 816, 99
- Hung, C.-L., Sanders, D. B., Casey, C. M., et al. 2014, ApJ, 791, 63

- Hung, C.-L., Rich, J. A., Yuan, T., et al. 2015, *ApJ*, 803, 62
- Ishibashi, W., & Fabian, A. C. 2012, *MNRAS*, 427, 2998
- Ivezić, Ž., Lupton, R. H., Schlegel, D., et al. 2004, *Astronomische Nachrichten*, 325, 583
- Jahnke, K., & Macciò, A. V. 2011, *ApJ*, 734, 92
- James, G., Witten, D., Hastie, T., & Tibshirani, R. 2013, *An Introduction to Statistical Learning with Applications in R* (Springer)
- Jesseit, R., Cappellari, M., Naab, T., Emsellem, E., & Burkert, A. 2009, *MNRAS*, 397, 1202
- Jesseit, R., Naab, T., Peletier, R. F., & Burkert, A. 2007, *MNRAS*, 376, 997
- Jin, Y., Chen, Y., Shi, Y., et al. 2016, *MNRAS*, 463, 913
- Jog, C. J., & Chitre, A. 2002, *A & A*, 393, L89
- Jonsson, P. 2006, *MNRAS*, 372, 2
- Jonsson, P., Groves, B. A., & Cox, T. J. 2010, *MNRAS*, 403, 17
- Joseph, R. D., & Wright, G. S. 1985, *MNRAS*, 214, 87
- Karouzos, M., Woo, J.-H., & Bae, H.-J. 2016, *ApJ*, 833, 171
- Kauffmann, G., Heckman, T. M., White, S. D. M., et al. 2003, *MNRAS*, 341, 33
- Kaviraj, S. 2013, *MNRAS*, 437, 1
- Kereš, D., Katz, N., Fardal, M., Davé, R., & Weinberg, D. H. 2009, *MNRAS*, 395, 160
- Khalatyan, A., Cattaneo, A., Schramm, M., et al. 2008, *MNRAS*, 387, 13
- King, A. 2005, *ApJ*, 635, L121
- King, A., & Pounds, K. 2015, *ARA&A*, 53, 115
- King, A. R., Zubovas, K., & Power, C. 2011, *MNRAS*, 415, L6
- Kocevski, D. D., Faber, S. M., Mozena, M., et al. 2012, *ApJ*, 744, 148
- Kohavi, R. 1995, in *Proceedings of the 14th International Joint Conference on Artificial Intelligence - Volume 2, IJCAI'95* (San Francisco, CA, USA: Morgan Kaufmann Publishers Inc.), 1137–1143
- Komossa, S., Burwitz, V., Hasinger, G., et al. 2003, *ApJ*, 582, L15
- Kormendy, J., Fisher, D. B., Cornell, M. E., & Bender, R. 2009, *ApJS*, 182, 216
- Koss, M., Mushotzky, R., Treister, E., et al. 2012, *ApJ*, 746, L22

- Kraemer, S. B., Bottorff, M. C., & Crenshaw, D. M. 2007, *ApJ*, 668, 730
- Krajnović, D., Cappellari, M., de Zeeuw, P. T., & Copin, Y. 2006, *MNRAS*, 366, 787
- Krajnovic, D., Cappellari, M., Zeeuw, P. T. D., Copin, Y., & Lyon, D. 2006, *MNRAS*, 802, 787
- Krips, M., Martín, S., Eckart, A., et al. 2011, *ApJ*, 736, 37
- Krolik, J. H. 2007, *ApJ*, 661, 52
- Krolik, J. H., & Begelman, M. C. 1986, *ApJ*, 308, L55
- . 1988, *ApJ*, 329, 702
- Lada, C. J., & Fich, M. 1996, *ApJ*, 459, 638
- Lagos, C. D. P., Padilla, N. D., Strauss, M. A., Cora, S. A., & Hao, L. 2011, *MNRAS*, 414, 2148
- Lamastra, A., Bianchi, S., Matt, G., et al. 2009, *A&A*, 504, 73
- Law, D. R., Yan, R., Bershady, M. A., et al. 2015, *AJ*, 150, 19
- Law, D. R., Cherinka, B., Yan, R., et al. 2016, *AJ*, 152, 83
- Leitherer, C., Schaerer, D., Goldader, J. D., et al. 1999, *ApJS*, 123, 3
- Li, T., Zhu, S., & Ogihara, M. 2006, *Knowl. Inf. Syst.*, 10, 453
- Lilly, S. J., Tresse, L., Hammer, F., Crampton, D., & Le Fevre, O. 1995, *ApJ*, 455, 108
- Lintott, C., Schawinski, K., Bamford, S., et al. 2011, *MNRAS*, 410, 166
- Lintott, C. J., Schawinski, K., Slosar, A., et al. 2008, *MNRAS*, 389, 1179
- Liu, G., Zakamska, N. L., Greene, J. E., Nesvadba, N. P. H., & Liu, X. 2013a, *MNRAS*, 436, 2576
- . 2013b, 2345, 2327
- . 2013c, arXiv:1301.1677
- Liu, W.-J., Zhou, H.-Y., Jiang, N., et al. 2016, *ApJ*, 822, 64
- Liu, X., Shen, Y., Strauss, M. A., & Greene, J. E. 2010, *ApJ*, 708, 427
- López-Sanjuan, C., Balcells, M., Pérez-González, P. G., et al. 2009, *A & A*, 501, 505
- López-Sanjuan, C., García-Dabó, C. E., & Balcells, M. 2008, *Publications of the ASP*, 120, 571

- López-Sanjuan, C., Le Fèvre, O., Ilbert, O., et al. 2012, *A & A*, 548, A7
- Lotz, J. M., Jonsson, P., Cox, T. J., et al. 2011, *ApJ*, 742, 103
- Lotz, J. M., Jonsson, P., Cox, T. J., & Primack, J. R. 2010a, *MNRAS*, 404, 590
- . 2010b, *MNRAS*, 404, 575
- Lotz, J. M., Primack, J., & Madau, P. 2004, *AJ*, 128, 163
- Lotz, J. M., Patrik, J., Cox, T. J., et al. 2008, *MNRAS*, 391, 3
- Magorrian, J., Tremaine, S., Richstone, D., et al. 1998, *AJ*, 115, 2285
- Maiolino, R., & Rieke, G. H. 1995, *ApJ*, 454, 95
- Malarecki, J. M., Staveley-Smith, L., Saripalli, L., et al. 2013, *MNRAS*, 432, 200
- Masters, K. L., Mosleh, M., Romer, A. K., et al. 2010, *MNRAS*, 405, 783
- Masters, K. L., Nichol, R. C., Hoyle, B., et al. 2011, *MNRAS*, 411, 2026
- Matzner, C. D., & McKee, C. F. 1999, *ApJ*, 526, L109
- Mazzarella, J. M., Iwasawa, K., Vavilkin, T., et al. 2012, *AJ*, 144, doi:10.1088/0004-6256/144/5/125
- McConnell, N. J., & Ma, C.-P. 2013, *ApJ*, 764, 184
- Mcelroy, R., Croom, S. M., Pracy, M., et al. 2015, *MNRAS*, 446, 2186
- Merritt, D. 2000, in *Astronomical Society of the Pacific Conference Series*, Vol. 197, *Dynamics of Galaxies: from the Early Universe to the Present*, ed. F. Combes, G. A. Mamon, & V. Charmandaris, 221
- Mihos, J. C., & Hernquist, L. 1994, *ApJ*, 431, L9
- . 1996, *ApJ*, 464, 641
- Miralles-Caballero, D., Colina, L., Arribas, S., & Duc, P.-A. 2011, *AJ*, 142, 79
- Mor, R., Netzer, H., & Elitzur, M. 2009, *ApJ*, 705, 298
- Morganti, R. 2017, *Frontiers in Astronomy and Space Sciences*, 4, 42
- Mulchaey, J. S., Wilson, A. S., & Tsvetanov, Z. 1996, *ApJ*, 467, 197
- Müller-Sánchez, F., Comerford, J., Stern, D., & Harrison, F. A. 2016, *ApJ*, 830, 50
- Müller Sánchez, F., Davies, R. I., Genzel, R., et al. 2009, *ApJ*, 691, 749

- Müller-Sánchez, F., Malkan, M., Hicks, E. K. S., & Davies, R. I. 2013, in IAU Symposium, Vol. 292, Molecular Gas, Dust, and Star Formation in Galaxies, ed. T. Wong & J. Ott, 363–366
- Müller-Sánchez, F., Nevin, R., Comerford, J. M., et al. 2018, *Nature*, 556, 345
- Müller-Sánchez, F., Prieto, M. A., Hicks, E. K. S., et al. 2011, *ApJ*, 739, 69
- Müller-Sánchez, F., Comerford, J. M., Nevin, R., et al. 2015, *ApJ*, 813, 2
- Murray, N., & Chiang, J. 1995, *ApJ*, 454, L105
- Mutch, S. J., Croton, D. J., & Poole, G. B. 2013, *MNRAS*, 435, 2445
- Naab, T., Jesseit, R., & Burkert, A. 2006, *MNRAS*, 372, 839
- Naab, T., Oser, L., Emsellem, E., et al. 2014, *MNRAS*, 444, 3357
- Narayan, R., & McClintock, J. E. 2008, *New Astronomy Reviews*, 51, 733
- Narayanan, D., Dey, A., Hayward, C. C., et al. 2010, *MNRAS*, 407, 1701
- Nenkova, M., Sirocky, M. M., Ivezić, Ž., & Elitzur, M. 2008, *ApJ*, 685, 147
- Netzer, H. 2015, *ARA&A*, 53, 365
- Nevin, R., Blecha, L., Comerford, J., & Greene, J. 2019, *ApJ*, 872, 76
- Nevin, R., Comerford, J. M., Müller-Sánchez, F., Barrows, R., & Cooper, M. C. 2018, *MNRAS*, 473, 2160
- Nevin, R., Comerford, J. M., Müller-Sánchez, F., et al. 2016, *ApJ*, 832, 1
- . 2017, *ApJ*, in review
- Newman, J. A., Cooper, M. C., Davis, M., et al. 2013, *ApJS*, 208, 5
- Noeske, K. G., Weiner, B. J., Faber, S. M., et al. 2007, *ApJ*, 660, L43
- Oh, K., Sarzi, M., Schawinski, K., & Yi, S. K. 2011, *ApJS*, 195, 2
- Oke, J. B., & Gunn, J. E. 1982, *Publications of the ASP*, 94, 586
- Oliva, E. 1997, in *Astronomical Society of the Pacific Conference Series*, Vol. 113, IAU Colloq. 159: Emission Lines in Active Galaxies: New Methods and Techniques, ed. B. M. Peterson, F.-Z. Cheng, & A. S. Wilson, 288
- Osterbrock, D. E., & Ferland, G. J. 2006, *Astrophysics of gaseous nebulae and active galactic nuclei*
- Ownsworth, J. R., Conselice, C. J., Mortlock, A., et al. 2014, *MNRAS*, 445, 2198

- Pawlik, M. M., Wild, V., Walcher, C. J., et al. 2016, MNRAS, 456, 3032
- Peng, C. Y., Ho, L. C., Impey, C. D., & Rix, H.-W. 2002, AJ, 124, 266
- Peng, Y.-j., Lilly, S. J., Renzini, A., & Carollo, M. 2012, ApJ, 757, 4
- Peng, Y.-j., Lilly, S. J., Kovač, K., et al. 2010, ApJ, 721, 193
- Petty, S. M., Armus, L., Charmandaris, V., et al. 2014, AJ, 148, 111
- Piqueras López, J., Colina, L., Arribas, S., Alonso-Herrero, A., & Bedregal, A. G. 2012, A & A, 546, A64
- Rafter, S. E., Crenshaw, D. M., & Wiita, P. J. 2009, AJ, 137, 42
- Ramos Almeida, C., Levenson, N. A., Rodríguez Espinosa, J. M., et al. 2009, ApJ, 702, 1127
- Ramos Almeida, C., Levenson, N. A., Alonso-Herrero, A., et al. 2011, ApJ, 731, 92
- Reeves, J. N., O’Brien, P. T., Braito, V., et al. 2009, ApJ, 701, 493
- Revalski, M., Dashtamirova, D., Crenshaw, D. M., et al. 2018, ApJ, 867, 88
- Ricci, T. V., Steiner, J. E., & Menezes, R. B. 2015, MNRAS, 451, 3728
- Riffel, R. A., & Storch-Bergmann, T. 2011a, MNRAS, 411, 469
- . 2011b, MNRAS, 417, 2752
- Riffel, R. A., Storch-Bergmann, T., & Riffel, R. 2014, ApJ, 780, L24
- . 2015, MNRAS, 451, 3587
- Riffel, R. A., Storch-Bergmann, T., & Winge, C. 2013, MNRAS, 430, 2249
- Risaliti, G., Maiolino, R., & Salvati, M. 1999, ApJ, 522, 157
- Rodriguez-Gomez, V., Genel, S., Vogelsberger, M., et al. 2015, MNRAS, 449, 49
- Rodriguez-Gomez, V., Snyder, G. F., Lotz, J. M., et al. 2018, ArXiv e-prints, arXiv:1809.08239
- . 2019, MNRAS, 483, 4140
- Rothenberg, T. J. 1971, Econometrica, 39, 577
- Rowlands, K., Heckman, T., Wild, V., et al. 2018, MNRAS, 480, 2544
- Rubin, V. C., & Ford, Jr., W. K. 1970, ApJ, 159, 379
- Rubin, V. C., Ford, Jr., W. K., & Thonnard, N. 1978, ApJ, 225, L107

- Rupke, D. S. N., Kewley, L. J., & Chien, L.-H. 2010, *ApJ*, 723, 1255
- Sánchez, S. F., Kennicutt, R. C., Gil de Paz, A., et al. 2012, *A & A*, 538, A8
- Sánchez, S. F., Pérez, E., Sánchez-Blázquez, P., et al. 2016a, , 52, 21
- . 2016b, , 52, 171
- Sanders, D. B., & Mirabel, I. F. 1996, *ARA&A*, 34, 749
- Sarzi, M., Falcón-Barroso, J., Davies, R. L., et al. 2006, *MNRAS*, 366, 1151
- Satyapal, S., Ellison, S. L., McAlpine, W., et al. 2014, *MNRAS*, 441, 1297
- Schawinski, K., Lintott, C., Thomas, D., et al. 2009, *MNRAS*, 396, 818
- Schawinski, K., Urry, C. M., Simmons, B. D., et al. 2014, *MNRAS*, 440, 889
- Schinnerer, E., Eckart, A., Tacconi, L. J., Genzel, R., & Downes, D. 2000, *ApJ*, 533, 850
- Schmidt, G. D., Weymann, R. J., & Foltz, C. B. 1989, *Publications of the ASP*, 101, 713
- Schmitt, H. R., Donley, J. L., Antonucci, R. R. J., et al. 2003, *ApJ*, 597, 768
- Schmitt, H. R., & Kinney, A. L. 1996, *ApJ*, 463, 498
- Schnorr-Müller, A., Storch-Bergmann, T., Nagar, N. M., et al. 2014, *MNRAS*, 437, 1708
- Schnorr-Müller, A., Storch-Bergmann, T., Robinson, A., Lena, D., & Nagar, N. M. 2016, *MNRAS*, 457, 972
- Schoenmakers, R. H. M., Franx, M., & de Zeeuw, P. T. 1997, *MNRAS*, 292, 349
- Schönell, A. J., Riffel, R. A., Storch-Bergmann, T., & Winge, C. 2014, *MNRAS*, 445, 414
- Sérsic, J. L. 1963, *Boletín de la Asociación Argentina de Astronomía La Plata Argentina*, 6, 41
- Shapiro, K. L., Genzel, R., Förster Schreiber, N. M., et al. 2008, *ApJ*, 682, 231
- Sheldon, E. S., Cunha, C. E., Mandelbaum, R., Brinkmann, J., & Weaver, B. A. 2012, *ApJS*, 201, 32
- Shen, Y., Liu, X., Greene, J. E., & Strauss, M. A. 2011, *ApJ*, 735, doi:10.1088/0004-637X/735/1/48
- Sheth, K., Menendez-Delmestre, K., Scoville, N., et al. 2004, in *Astrophysics and Space Science Library*, Vol. 319, *Penetrating Bars Through Masks of Cosmic Dust*, ed. D. L. Block, I. Puerari, K. C. Freeman, R. Groess, & E. K. Block, 405
- Sheth, K., Vogel, S. N., Regan, M. W., Thornley, M. D., & Teuben, P. J. 2005, *ApJ*, 632, 217

- Shi, Y., Rieke, G., Lotz, J., & Perez-Gonzalez, P. G. 2009, *ApJ*, 697, 1764
- Silk, J. 2011, in *IAU Symposium*, Vol. 277, *Tracing the Ancestry of Galaxies*, ed. C. Carignan, F. Combes, & K. C. Freeman, 273–281
- Silk, J. 2013, *ApJ*, 772, 112
- Silk, J., & Rees, M. J. 1998, *A & A*, 331, L1
- Silverman, J., Green, P., Barkhouse, W., et al. 2006, European Space Agency, (Special Publication) ESA SP, 2, 795
- Simons, R. C., Kassin, S. A., Snyder, G. F., et al. 2019, arXiv e-prints, arXiv:1902.06762
- Smethurst, R. J., Masters, K. L., Lintott, C. J., et al. 2018, *MNRAS*, 473, 2679
- Smith, K. L., Shields, G. A., Bonning, E. W., et al. 2010, arXiv:arXiv:0908.1998v2
- Smith, K. L., Shields, G. A., Salviander, S., Stevens, A. C., & Rosario, D. J. 2012, arXiv:arXiv:1108.0383v2
- Snyder, G. F., Hayward, C. C., Sajina, A., et al. 2013, *ApJ*, 768, 168
- Snyder, G. F., Rodriguez-Gomez, V., Lotz, J. M., et al. 2018, ArXiv e-prints, arXiv:1809.02136
- . 2019, *MNRAS*, 486, 3702
- Sparke, L. S., & Gallagher, III, J. S. 2000, *Galaxies in the universe : an introduction*, 416
- Springel, V. 2005, *MNRAS*, 364, 1105
- Springel, V., & Hernquist, L. 2003, *MNRAS*, 339, 289
- . 2005, *ApJ*, 622, L9
- Stark, D. V., Bundy, K. A., Westfall, K., et al. 2018, *MNRAS*, 480, 2217
- Steinborn, L. K., Dolag, K., Comerford, J. M., et al. 2016, *MNRAS*, 458, 1013
- Stickley, N. R., & Canalizo, G. 2016, arXiv e-prints, arXiv:1610.02601
- Storchi-Bergmann, T., Simões Lopes, R. D., McGregor, P. J., et al. 2010, *MNRAS*, 402, 819
- Strauss, M. A., Weinberg, D. H., Lupton, R. H., et al. 2002, *AJ*, 124, 1810
- Tasca, L. A. M., Le Fèvre, O., López-Sanjuan, C., et al. 2014, *A & A*, 565, A10
- Taylor, E. N., Franx, M., Glazebrook, K., et al. 2010, *ApJ*, 720, 723
- Taylor, M. D., Tadhunter, C. N., & Robinson, T. G. 2003, *MNRAS*, 1008, 995

- Thompson, R., Davé, R., Huang, S., & Katz, N. 2015, ArXiv e-prints, arXiv:1508.01851
- Tombesi, F., Cappi, M., Reeves, J. N., & Braito, V. 2012, MNRAS, 422, L1
- Tombesi, F., Cappi, M., Reeves, J. N., et al. 2013, MNRAS, 430, 1102
- Tombesi, F., Cappi, M., Reeves, J. N., et al. 2011, ApJ, 742, 44
- Toomre, A. 1977, in *Evolution of Galaxies and Stellar Populations*, ed. B. M. Tinsley & R. B. G. Larson, D. Campbell, 401
- Treister, E., Schawinski, K., Urry, C. M., et al. 2012, ApJL, 758, 2
- Trujillo, I., Cenarro, A. J., de Lorenzo-Cáceres, A., et al. 2009, ApJ, 692, L118
- Tsatsi, A., Macciò, A. V., van de Ven, G., & Moster, B. P. 2015, ApJ, 802, L3
- Ueda, J., Iono, D., Yun, M. S., et al. 2014, ApJS, 214, 1
- Ueda, Y., Akiyama, M., Hasinger, G., Miyaji, T., & Watson, M. G. 2014, ApJ, 786, 104
- van der Wel, A., Holden, B. P., Zirm, A. W., et al. 2008, ApJ, 688, 48
- Van Wassenhove, S., Volonteri, M., Mayer, L., et al. 2012, ApJ, 748, L7
- Veilleux, S., Cecil, G., & Bland-Hawthorn, J. 2005, Ann. Rev. Astron. & Astrophys, 43, 769
- Veilleux, S., Kim, D.-C., & Sanders, D. B. 2002, ApJS, 143, 315
- Villforth, C., Hamann, F., Rosario, D. J., et al. 2014, MNRAS, 3356, 3342
- Vogelsberger, M., Genel, S., Springel, V., et al. 2014, MNRAS, 444, 1518
- Wake, D. A., Bundy, K., Diamond-Stanic, A. M., et al. 2017, AJ, 154, 86
- Walker, I. R., Mihos, J. C., & Hernquist, L. 1996, ApJ, 460, 121
- Wang, J.-m., Chen, Y.-m., Hu, C., et al. 2009, doi:10.1088/0004-637X/705/1/L76
- Weigel, A. K., Schawinski, K., Caplar, N., et al. 2017, ApJ, 845, 134
- Wen, Z. Z., & Zheng, X. Z. 2016, ApJ, 832, 90
- Westfall, K. B., Cappellari, M., Bershadsky, M. A., et al. 2019, arXiv e-prints, arXiv:1901.00856
- Westmoquette, M. S., Smith, L. J., & Gallagher, I. S. 2011, MNRAS, 414, 3719
- White, S. D. M., & Frenk, C. S. 1991, ApJ, 379, 52
- White, S. D. M., & Rees, M. J. 1978, MNRAS, 183, 341
- Whittle, M. 1985, MNRAS, 213, 1

- Woo, J. H., Bae, H. J., Son, D., & Karouzos, M. 2016, ApJ, 817, 108
- Woo, J.-H., Son, D., & Bae, H.-J. 2017, ApJ, 839, 120
- Wuyts, S., Cox, T. J., Hayward, C. C., et al. 2010, ApJ, 722, 1666
- Wylezalek, D., M, A. S., Zakamska, N. L., et al. 2016, 12, 1
- Yan, R., Bundy, K., Law, D. R., et al. 2016a, AJ, 152, 197
- Yan, R., Tremonti, C., Bershady, M. A., et al. 2016b, AJ, 151, 8
- York, D. G., Adelman, J., Anderson, Jr., J. E., et al. 2000, AJ, 120, 1579

Appendix A

Appendix of Tables

Here I include all of the tables from all four chapters and from Appendix B.

SDSS ID	Galaxy Name	z	Telescope/Instrument
J000249.07+004504.8	J0002+0045	$0.086735 \pm 3.9\text{E} - 5$	Lick/Kast
J000911.58-003654.7	J0009-0036	$0.073135 \pm 3.4\text{E} - 5$	MMT/Blue Channel
J013555.82+143529.7	J0135+1435	$0.072157 \pm 1.9\text{E} - 5$	Lick/Kast
J015605.14-000721.7	J0156-0007	$0.080964 \pm 1.8\text{E} - 5$	Lick/Kast

Table A.1: Optical longslit observations of double-peaked AGNs. Column 1: SDSS ID, also RA and Dec. Column 2: Redshifts and errors, determined from the velocity of the stellar absorption lines. Column 3: Observatory and spectrograph (This table is available in its entirety in the online journal.)

Galaxy	$L_{[\text{OIII}]} [\text{erg s}^{-1}]$	$L_{[\text{OIII}]}^c [\text{erg s}^{-1}]$	$L_{\text{bol}} [\text{erg s}^{-1}]$	kpc/''	Width	R [pc]
J0002+0045	$(2.252 \pm 0.397) \times 10^{41}$	$(1.516 \pm 0.267) \times 10^{42}$	$(6.886 \pm 1.216) \times 10^{44}$	1.62	11 ± 2	6330 ± 980
J0009-0036	$(4.813 \pm 0.420) \times 10^{41}$	$(4.444 \pm 0.388) \times 10^{42}$	$(2.0178 \pm 0.1764) \times 10^{45}$	1.39	19 ± 2	3610 ± 410
J0135+1435	$(1.104 \pm 0.142) \times 10^{41}$	$(4.52 \pm 0.58) \times 10^{41}$	$(6.42 \pm 0.82) \times 10^{43}$	1.37	12 ± 1	6430 ± 800
J0156-0007	$(1.420 \pm 0.221) \times 10^{41}$	$(5.69 \pm 0.88) \times 10^{41}$	$(8.08 \pm 1.26) \times 10^{43}$	1.53	14 ± 1	8330 ± 810

Table A.2: Measured properties for all galaxies. Column 1: Galaxy name. Column 2: Observed [OIII] luminosity before it is dereddened. Column 3: Dereddened [OIII] luminosity. Column 4: Bolometric luminosity. Column 5: Kpc per arcsecond conversion. Column 6: Akaike width of the NLR in pixels. Column 7: The corresponding radius of the NLR in parsecs. This is R_{NLR} in the size-luminosity relationship. (This table is available in its entirety in the online journal.)

SDSS ID	PA _{obs}	# of Rows with > 2 Components	Single Gauss V_r [km s ⁻¹]	Single Gauss σ [km s ⁻¹]	Double Gauss σ_1 [km s ⁻¹]	Double Gauss σ_2 [km s ⁻¹]	PA _{gal}	PA _[OIII]
J0002+0045	68	5/9	173.8 ± 3.3	1005.0 ± 8.7	655.8 ± 198.0	920.2 ± 59.8	65	64
	158	4/7	84.9 ± 0.8	1018.5 ± 9.6	408.5 ± 3.3	371.7 ± 1.2		
J0009−0036	23	5/11	144.4 ± 5.1	650.0 ± 4.3	736.2 ± 6.8	624.1 ± 206.7	135	51
	67	0/11	235.6 ± 1.9	619.4 ± 3.0	705.7 ± 8.7	610.7 ± 191.3		
J0135+1435	20	2/7	218.0 ± 0.9	536.5 ± 173.4	469.0 ± 169.7	298.9 ± 123.8	20	46
	81	3/5	78.2 ± 0.5	500.5 ± 3.7	515.1 ± 4.6	285.9 ± 174.7		
J0156−0007	29	1/5	140.0 ± 1.0	672.5 ± 282.6	698.3 ± 358.9	527.3 ± 227.0	119	113
	119	3/3	241.5 ± 3.0	618.4 ± 6.2	419.7 ± 20.5	616.4 ± 217.3		

Table A.3: The values for the parameters for quantitative classification for both observed PAs. Column 1: Galaxy name. Column 2: Observed position angle. Column 3: The number of rows that are best fit by > 2 Gaussians within the resolved center of emission (FWHM_{cont} ± 1 row). For instance, in row one, 5/9 indicates that out of the nine rows of the resolved center of emission, 5 rows are better fit by 3 Gaussians. Column 4: V_r refers to the line of sight velocity from the single Gaussian centroid. Column 5, 6, and 7: The values for the dispersion and error of one component, and each individual component for the two Gaussian fit. Column 8 and 9: We create a diagnostic for alignment by listing the position angles of the photometric major axis and the [OIII] emission. PA_{gal} is from SDSS r -band photometry. (This table is available in its entirety in the online journal.)

SDSS ID	> 2 Components Components?	V_r [km s ⁻¹]	σ [km s ⁻¹]	σ_1 and σ_2 [km s ⁻¹]	Aligned? $PA_{[\text{OIII}]} = PA_{\text{gal}}$	Classification
J0002+0045	> 2	< 400	> 500	> 500	yes	Outflow Composite
J0009-0036	2	< 400	> 500	> 500	no	Outflow
J0135+1435	> 2	< 400	\geq 500	> 500	no	Outflow Composite
J0156-0007	> 2	< 400	> 500	\geq 500 ^a	yes	Outflow Composite

Table A.4: Table of the official kinematic classification for each galaxy based upon the measurements in Table A.3. Column 1: Galaxy name. Column 2: The number of components is > 2 if at either position angle, more than half the rows within the spatial center of the galaxy have > 2 components as the best fit. Column 3: V_r is maximum line of sight radial velocity, measured from the single Gaussian fit for both position angles. Column 4: σ is given by the largest dispersion of the single Gaussian fit from both observed position angles. We include this measurement in the table because although it is not used in the classification scheme, it is discussed in Section 2.4.1. Column 5: Likewise, σ_1 or σ_2 is the largest dispersion of either of the two Gaussian fit fits from both position angles. Column 6: Alignment is determined from $PA_{[\text{OIII}]}$ and PA_{gal} . If these two measurements are within 20° of one another, the galaxy is aligned. Column 7: We provide a classification based upon these five columns and four properties. (This table is available in its entirety in the online journal.)

^aThe 1σ error on the measured value straddles the classification cutoff. However, the measured value greater than 500 km s^{-1} so we classify this galaxy as Outflow Composite. For all other galaxies in our sample in which the measured value straddles a given classification cutoff within error are classified according to the measured value.

Properties	Rotation Dominated	Ambiguous	Outflow	Outflow Composite
> 2 Gaussian	0/4 (0%)	2/6 (33.3%)	0/35 (0%)	26/26 (100%)
$V_r > 400 \text{ km s}^{-1}$	0/4 (0%)	0/6 (0%)	9/35 (25.7%)	2/26 (7.7%)
$\sigma > 500 \text{ km s}^{-1}$	3/4 (75%)	6/6 (100%)	28/35 (80.0%)	19/26 (73.1%)
$\sigma_1 \text{ or } \sigma_2 > 500 \text{ km s}^{-1}$	0/4 (0%)	0/6 (0%)	35/35 (100%)	26/26 (100%)
Aligned?	4/4 (100%)	0/6 (0%)	17/35 (48.6%)	10/26 (38.5%)

Table A.5: The statistics of the properties for each kinematic classification. Row 1: The fraction of galaxies in each classification that are best fit by more than 2 Gaussian components. Row 2: The fraction of galaxies with a radial velocity of the single Gaussian component fit in excess of 400 km s^{-1} . Row 3: The fraction of galaxies in each classification that have a single Gaussian component velocity dispersion greater than 500 km s^{-1} . Although this property is not used in the classification process, we discuss its value for the different classification categories below. Row 4: Velocity dispersion, but for the individual components of the two Gaussian fits. Row 5: The fraction of galaxies where the position angle of the [OIII] $\lambda 5007$ emission is aligned (within 20°) with the photometric major axis of the galaxy.

SDSS ID	[OIII] $\lambda 5007$ $\Delta V \text{ [km s}^{-1}]$ PA 1	[OIII] $\lambda 5007$ $\Delta V \text{ [km s}^{-1}]$ PA 2	H α $\Delta V \text{ [km s}^{-1}]$ PA 1	H α $\Delta V \text{ [km s}^{-1}]$ PA 2
J0736+4759 ^a	274 ± 6	283 ± 6	289 ± 118	273 ± 190
J1018+5127	298 ± 4	285 ± 4	312 ± 79	312 ± 79
J1250+0746	211 ± 8	218 ± 4	184 ± 2	158 ± 58
J1516+0517	292 ± 30	285 ± 50	320 ± 81	309 ± 61

Table A.6: Table of the separation in velocity space (ΔV) between the blue and red Gaussian component fits for the four rotation-dominated galaxies. Column 1: Galaxy name. Column 2 and 3: The velocity separation in [OIII] $\lambda 5007$ in km s^{-1} for PA 1 and PA 2 for each galaxy. Column 4 and 5: The velocity separation in H α in km s^{-1} for PA 1 and PA 2.

^aDue to a restricted wavelength coverage from the observations of J0736+4759, we lack a H α profile and instead compare to the H β profile.

SDSS ID	PA 1	PA 2	Instrument	Slitwidth (")	Seeing (") ^a	Dispersion (Å pix ⁻¹)
J0009−0036	23	67	MMT/ Blue Channel	1.0	0.8	0.50
J0803+3926	50	140	Palomar/DBSP	1.5	2.5	0.55
J0821+5021	43	133	Palomar/DBSP	1.5	2.5	0.55
J0854+5026	16	106	Palomar/DBSP	1.5	2.5	0.55
J0930+3430	21	111	Palomar/DBSP	1.5	2.5	0.55
J0959+2619	28	118	MMT/ Blue Channel	1.0	1.0	0.50
J1027+1049	75	165	APO/DIS	1.5	1.8	0.62
J1109+0201	31	121	APO/DIS	1.5	1.2	0.62
J1152+1903	17	107	Palomar/DBSP	1.5	1.9	0.55
J1315+2134	74	164	APO/DIS	1.5	1.5	0.62
J1328+2752	39	129	APO/DIS	1.5	1.7	0.62
J1352+0525	162	252	Keck/DEIMOS	0.75	0.9	0.33
J1420+4959	79	169	APO/DIS	1.5	1.5	0.62
J1524+2743	12	102	APO/DIS	1.5	1.5	0.62
J1526+4140	38	128	APO/DIS	1.5	2.0	0.62
J1606+3427	17	107	Keck/DEIMOS	0.75	0.9	0.33
J1630+1649	30	120	Keck/DEIMOS	0.75	1.0	0.33
J1720+3106	152	242	Keck/DEIMOS	0.75	0.6	0.33

Table A.7: The observed PAs and associated instrument used for the observations for each galaxy. Column 1: galaxy name, also SDSS ID. Column 2: the first observed PA, also often the PA of the photometric major axis of the galaxy in SDSS. Column 3: the second observed PA. Column 4: observatory and instrument. Column 5: the slitwidth of the longslit used. Column 6: the approximate seeing of each observation derived from the FWHM of the stellar PSF. Column 7: the dispersion of the instrument.

^aSeeing for Keck/DEIMOS is derived from the FWHM of the PSF of acquisition stars.

SDSS ID	Symmetric χ^2_ν	Asymmetric χ^2_ν	Nested χ^2_ν	Best Fit
J0009−0036	9146.3	243.0	>10000	Asymmetric
J0803+3926	5.1	18.1	100.3	Symmetric
J0821+5021	169.1	68.2	>10000	Asymmetric
J0854+5026	>10000	183.3	226.1	Asymmetric
J0930+3430	2874.3	4.6	50.0	Asymmetric
J0959+2619	73.2	>10000	5.0	Nested
J1027+1049	73.4	27.6	4.7	Nested
J1109+0201	150.5	65.8	63.8	Nested
J1152+1903	122.8	139.7	728.9	Symmetric
J1315+2134	559.5	14.7	16.0	Asymmetric
J1328+2752	10.8	2.3	>10000	Asymmetric
J1352+0525	131.7	87.1	176.3	Asymmetric
J1420+4959	32.12	11.87	1.03	Nested
J1524+2743	390.3	168.8	4.1	Nested
J1526+4140	1.8	0.5	0.3	Nested
J1606+3427	386.2	21.1	17.0	Nested
J1630+1649	2383.9	1086.1	1591.4	Asymmetric
J1720+3106	1240.8	547.4	235.8	Nested

Table A.8: We select the best fit biconical outflow model for each galaxy by selecting the model with the lowest χ^2_ν value.

SDSS ID	i [°]	PA _{bicone} [°E of N]	r_t [kpc]	$\theta_{1,\text{half}}$ [°]	V_{max} [km s ^{−1}]	$< V_{\text{obs}} - V_{\text{mod}} >$ [km s ^{−1}]
J0803+3926	40 ⁺¹⁸ _{−29}	20 ⁺²⁰ _{−10}	9 ⁺⁵ _{−3}	53 ⁺⁹ _{−9}	430 ⁺¹¹⁰ _{−70}	73
J1152+1903	42 ⁺⁶ _{−44}	40 ⁺²⁰ _{−40}	6 ⁺³ _{−2}	60 ⁺² _{−7}	370 ⁺⁹⁰ _{−50}	44

Table A.9: Column 1: galaxy name. Column 2: outflow inclination. Column 3: position angle of the bicone axis on the sky. Column 4: turnover radius in kpc. Column 5: half opening angle. Column 6: maximum velocity. Column 7: the mean modulus of the velocity residuals.

SDSS ID	i [°]	PA _{bicone} [° E of N]	r_t [kpc]	$\theta_{1,\text{half}}$ [°]	$\theta_{2,\text{half}}$ [°]	V_{max} [km s ⁻¹]	$< V_{\text{obs}} - V_{\text{mod}} >$ [km s ⁻¹]
J0009-0036	56 ⁺⁸ ₋₆	79 ⁺¹⁶ ₋₁₇	5 ⁺³ ₋₁	60 ⁺³ ₋₄	77 ⁺³ ₋₂	320 ⁺⁶⁰ ₋₈₀	139
J0821+5021	51 ⁺³⁴ ₋₈	6 ⁺¹⁹ ₋₇	9 ⁺⁵ ₋₃	50 ⁺⁷ ₋₁₁	72 ⁺⁴ ₋₆	360 ⁺⁶⁰ ₋₁₀₀	175
J0854+5026	60 ⁺¹⁶ ₋₈	205 ⁺¹⁴ ₋₁₆₉	7 ⁺² ₋₂	42 ⁺⁴ ₋₇	75 ⁺⁶ ₋₃	290 ⁺⁴⁰ ₋₅₀	46
J0930+3430	80 ⁺⁶ ₋₉	75 ⁺⁵⁵ ₋₄₉	10 ⁺⁴ ₋₆	37 ⁺¹² ₋₁₀	67 ⁺³ ₋₂	290 ⁺¹³⁰ ₋₃₀	27
J1315+2134	58 ⁺⁷ ₋₁₂	39 ⁺¹⁴ ₋₁₂	6 ⁺² ₋₂	48 ⁺⁴ ₋₄	78 ⁺³ ₋₂	600 ⁺¹³⁰ ₋₅₀	68
J1328+2752	78 ⁺⁹ ₋₁₃	52 ⁺⁸¹ ₋₃₉	6 ⁺⁴ ₋₃	48 ⁺¹⁵ ₋₁₉	81 ⁺³ ₋₅	230 ⁺²⁶⁰ ₋₈₀	106
J1352+0525	43 ⁺¹⁴ ₋₇	43 ⁺⁴² ₋₉	6 ⁺² ₋₁	61 ⁺³ ₋₆	78 ⁺² ₋₃	440 ⁺⁶⁰ ₋₈₀	78
J1630+1649	83 ⁺⁵ ₋₂₅	38 ⁺²⁹ ₋₃₄	6 ⁺³ ₋₁	40 ⁺¹⁶ ₋₇	82 ⁺² ₋₁	290 ⁺⁹⁰ ₋₃₀	92

Table A.10: Column 1: galaxy name. Column 2: outflow inclination. Column 3: position angle of the bicone axis on the sky. Column 4: turnover radius in kpc. Column 5: inner half opening angle. Column 6: outer half opening angle. Column 7: maximum velocity. Column 8: the mean modulus of the velocity residuals.

SDSS ID	i [°]	PA _{bicone} [° E of N]	r_t [kpc]	$\theta_{1,\text{half}}$ [°]	$\theta_{2,\text{half}}$ [°]	V_{max} [km s ⁻¹]	$< V_{\text{obs}} - V_{\text{mod}} >$ [km s ⁻¹]
J0959+2619	78 ⁺⁹ ₋₂₀	13 ⁺³¹ ₋₉	7 ⁺⁴ ₋₃	49 ⁺¹⁰ ₋₁₄	71 ⁺⁵ ₋₄	280 ⁺¹⁸⁰ ₋₁₀₀	46
J1027+1049	77 ⁺⁹ ₋₁₄	32 ⁺⁸¹ ₋₂₅	12 ⁺⁶ ₋₆	33 ⁺⁹ ₋₉	61 ⁺⁵ ₋₄	540 ⁺¹⁰⁰ ₋₈₀	43
J1109+0201	48 ⁺⁵ ₋₅	59 ⁺¹⁶ ₋₁₆	10 ⁺⁴ ₋₂	55 ⁺⁵ ₋₄	73 ⁺³ ₋₃	390 ⁺⁵⁰ ₋₄₀	86
J1420+4959	79 ⁺⁷ ₋₁₉	174 ⁺⁹⁸ ₋₁₂₆	5 ⁺⁴ ₋₃	41 ⁺¹⁰ ₋₁₆	70 ⁺⁶ ₋₅	390 ⁺¹⁷⁰ ₋₁₁₀	153
J1524+2743	83 ⁺⁵ ₋₁₀	100 ⁺²⁹ ₋₅₇	5 ⁺⁵ ₋₂	35 ⁺⁷ ₋₁₀	62 ⁺² ₋₂	720 ⁺¹⁰⁰ ₋₉₀	127
J1526+4140	74 ⁺¹² ₋₁₅	59 ⁺⁶⁶ ₋₄₅	10 ⁺⁷ ₋₅	44 ⁺¹⁵ ₋₁₄	62 ⁺¹¹ ₋₁₆	410 ⁺²⁷⁰ ₋₁₂₀	88
J1606+3427	81 ⁺⁵ ₋₉	114 ⁺⁴⁸ ₋₇₆	9 ⁺³ ₋₃	37 ⁺⁸ ₋₆	74 ⁺³ ₋₃	370 ⁺⁷⁰ ₋₄₀	71
J1720+3106	84 ⁺⁶ ₋₈	34 ⁺²⁸ ₋₂₄	14 ⁺⁴ ₋₃	18 ⁺¹¹ ₋₅	30 ⁺⁹ ₋₅	300 ⁺²⁰ ₋₁₀	152

Table A.11: Column 1: galaxy name. Column 2: outflow inclination. Column 3: position angle of the bicone axis on the sky. Column 4: turnover radius in kpc. Column 5: inner half opening angle. Column 6: outer half opening angle. Column 7: maximum velocity. Column 8: the mean modulus of the velocity residuals.

Modeled PAs	i [$^{\circ}$]	PA _{bicone} [$^{\circ}$ E of N]	r_t [kpc]	$\theta_{1,\text{half}}$ [$^{\circ}$]	$\theta_{2,\text{half}}$ [$^{\circ}$]	V _{max} [km s $^{-1}$]
Pseudo-IFS	62^{+16}_{-22}	75^{+121}_{-53}	11^{+5}_{-6}	38^{+23}_{-27}	81^{+5}_{-23}	320^{+290}_{-170}
21, 66	68^{+15}_{-29}	92^{+105}_{-45}	10^{+6}_{-6}	34^{+28}_{-27}	75^{+10}_{-14}	330^{+240}_{-170}
21, 111	80^{+6}_{-9}	75^{+55}_{-49}	10^{+4}_{-6}	37^{+12}_{-10}	67^{+3}_{-2}	290^{+130}_{-30}
21, 156	72^{+12}_{-25}	85^{+100}_{-63}	10^{+6}_{-7}	30^{+23}_{-23}	79^{+5}_{-14}	350^{+270}_{-170}
66, 156	55^{+26}_{-35}	128^{+119}_{-91}	11^{+8}_{-8}	23^{+24}_{-17}	63^{+18}_{-28}	360^{+300}_{-190}
66, 111	69^{+15}_{-20}	90^{+98}_{-56}	10^{+7}_{-7}	37^{+23}_{-19}	70^{+13}_{-14}	330^{+300}_{-180}
111, 156	69^{+14}_{-33}	105^{+105}_{-70}	11^{+5}_{-9}	29^{+25}_{-19}	76^{+6}_{-20}	390^{+330}_{-210}

Table A.12: Best-fit parameters for all observed PAs of J0930+3430 with 1σ errors. Column 1: PAs used in model. ‘Pseudo-IFS’ indicates that all four PAs were used. Column 2: outflow inclination. Column 3: position angle of the bicone axis on the sky. Column 4: turnover radius in kpc. Column 5: inner half opening angle. Column 6: outer half opening angle. Column 7: maximum velocity.

SDSS ID	Slit PA 1 [°E of N]	Slit PA 2 [°E of N]	PA _{gal} ^a [°E of N]	PA _{bicone} [°E of N]	$\theta_{2,\text{half}}^b$ [°]	Intersect? ^c	Aligned with PA _{gal} ? ^d	Perpendicular to PA _{gal} ? ^e
J0009-0036	23	67	65	79 ⁺¹⁶ ₋₁₇	77 ⁺³ ₋₂	yes	yes	no
J0803+3926	50	140	140	22 ⁺²² ₋₁₃	53 ⁺⁹ ₋₉	yes	no	yes
J0821+5021	43	133	133	6 ⁺¹⁹ ₋₇	72 ⁺⁴ ₋₆	yes	no	no
J0854+5026	16	106	16	25 ⁺¹⁴ ₋₁₆₉	75 ⁺⁶ ₋₃	yes	yes	yes
J0930+3430	21	111	110	75 ⁺⁵⁵ ₋₄₉	67 ⁺³ ₋₂	yes	yes	yes
J0959+2619	28	118	152	13 ⁺³¹ ₋₉	71 ⁺⁵ ₋₄	yes	no	no
J1027+1049	75	165	75	32 ⁺⁸¹ ₋₂₅	61 ⁺⁵ ₋₄	yes	yes	no
J1109+0201	31	121	31	59 ⁺¹⁶ ₋₁₆	73 ⁺³ ₋₃	yes	no	no
J1152+1903	17	107	37	40 ⁺²⁵ ₋₃₆	60 ⁺² ₋₇	yes	yes	no
J1315+2134	74	164	164	39 ⁺¹⁴ ₋₁₂	78 ⁺³ ₋₂	yes	no	no
J1328+2752	39	129	39	52 ⁺⁸¹ ₋₃₉	81 ⁺³ ₋₄	yes	yes	yes
J1352+0525	162	252	162	43 ⁺⁴² ₋₉	78 ⁺² ₋₃	yes	no	yes
J1420+4959	79	169	169	174 ⁺⁹⁸ ₋₁₂₆	70 ⁺⁶ ₋₅	yes	yes	yes
J1524+2743	12	102	102	101 ⁺¹⁰² ₋₆₃	62 ⁺² ₋₂	yes	yes	yes
J1526+4140	38	128	38	59 ⁺⁶⁶ ₋₄₅	62 ⁺¹¹ ₋₁₆	yes	yes	yes
J1606+3427	17	107	17	114 ⁺⁴⁸ ₋₇₆	74 ⁺³ ₋₃	yes	no	yes
J1630+1649	30	120	30	38 ⁺²⁹ ₋₃₄	82 ⁺² ₋₁	yes	yes	no
J1720+3106	152	242	153	34 ⁺²⁸ ₋₂₄	30 ⁺⁹ ₋₅	yes	no	yes

Table A.13: Column 1: galaxy name. Column 2 and 3: the observed position angles. Column 4: the position angle of the photometric major axis from the r -band from the SDSS. Column 5: the position angle of the bicone from the best fit model for each galaxy. Column 6: the larger half opening angle from the best fit model for each galaxy. Column 7: we determine if the bicone intersects the photometric major axis using the requirement $\text{PA}_{\text{gal}} = \text{PA}_{\text{bicone}} \pm \theta_{2,\text{half}}$ within the 1σ error margin for all parameters. Column 8: we determine if the bicone axis is aligned with the photometric major axis using the requirement $\text{PA}_{\text{gal}} = \text{PA}_{\text{bicone}}$ within the 1σ error margin. Column 9: we determine if the bicone axis is perpendicular to the photometric major axis using $\text{PA}_{\text{gal}} + 90^\circ = \text{PA}_{\text{bicone}}$, again with a 1σ error margin.

^aAssociated 1σ errors are $\sim 7^\circ$, ^bWe use $\theta_{1,\text{half}}$ for the galaxies that are best modeled as a symmetric bicone, J0803+3926 and J1152+1903, ^c $\text{PA}_{\text{gal}} = \text{PA}_{\text{bicone}} \pm \theta_{2,\text{half}}$, ^d $\text{PA}_{\text{gal}} = \text{PA}_{\text{bicone}}$, ^e $\text{PA}_{\text{gal}} + 90^\circ = \text{PA}_{\text{bicone}}$

SDSS ID	r_t [kpc]	$\theta_{1,\text{half}}$ [deg]	$\theta_{2,\text{half}}$ [deg]	V_{max} [km s ⁻¹]	$A_1 + A_2$ [kpc ²]	\dot{M} [M _⊙ yr ⁻¹]	L_{KE} [erg s ⁻¹]	L_{bol} [erg s ⁻¹]	$L_{\text{KE}}/L_{\text{bol}}$
J0009	$2.0^{+1.1}_{-0.3}$	60^{+3}_{-4}	77^{+3}_{-2}	320^{+60}_{-80}	$30.1^{+46.4}_{-9.1}$	250^{+260}_{-84}	$(7.9^{+8.7}_{-3.4}) \times 10^{42}$	$(2.0178 \pm 0.1764) \times 10^{45}$	0.002
J0803	$4.2^{+2.4}_{-1.6}$	53^{+9}_{-9}	77^{+0}_{-0}	430^{+110}_{-70}	$102.1^{+163.4}_{-53.5}$	1098^{+1537}_{-536}	$(6.7^{+9.1}_{-3.0}) \times 10^{43}$	$(3.1736 \pm 0.2616) \times 10^{45}$	0.011
J0821	$6.4^{+3.3}_{-1.8}$	50^{+7}_{-11}	72^{+4}_{-6}	360^{+60}_{-100}	$286.6^{+313.1}_{-130.1}$	2504^{+2912}_{-1246}	$(9.9^{+13.0}_{-5.8}) \times 10^{43}$	$(1.181 \pm 0.188) \times 10^{44}$	0.320
J0854	$4.5^{+1.1}_{-1.2}$	42^{+7}_{-7}	75^{+6}_{-3}	290^{+40}_{-50}	$133.4^{+63.4}_{-60.6}$	1019^{+385}_{-506}	$(2.6^{+1.2}_{-1.6}) \times 10^{43}$	$(6.44 \pm 0.99) \times 10^{43}$	0.168
J0930	$4.6^{+2.0}_{-2.6}$	37^{+12}_{-10}	67^{+3}_{-2}	290^{+130}_{-30}	$129.3^{+127.9}_{-105.3}$	1019^{+1205}_{-821}	$(2.8^{+4.3}_{-2.2}) \times 10^{43}$	$(1.175 \pm 0.37) \times 10^{44}$	0.054
J0959	$3.3^{+1.8}_{-1.3}$	49^{+10}_{-14}	71^{+5}_{-4}	280^{+180}_{-100}	$75.6^{+100.9}_{-46.0}$	468^{+765}_{-237}	$(1.1^{+5.0}_{-0.84}) \times 10^{43}$	$(8.14 \pm 0.88) \times 10^{43}$	0.038
J1027	$6.2^{+3.0}_{-3.1}$	33^{+9}_{-9}	61^{+5}_{-4}	540^{+100}_{-80}	$215.0^{+244.7}_{-162.9}$	3059^{+3181}_{-2191}	$(2.4^{+4.5}_{-1.7}) \times 10^{44}$	$(9.09 \pm 1.54) \times 10^{43}$	0.943
J1109	$4.9^{+1.9}_{-0.8}$	55^{+5}_{-4}	73^{+3}_{-3}	390^{+50}_{-40}	$181.8^{+139.0}_{-56.9}$	1918^{+940}_{-651}	$(8.9^{+4.7}_{-3.1}) \times 10^{43}$	$(1.023 \pm 0.142) \times 10^{44}$	0.562
J1152	$4.5^{+2.1}_{-1.7}$	60^{+7}_{-7}	73^{+0}_{-0}	370^{+90}_{-50}	$148.4^{+165.0}_{-101.0}$	1567^{+1053}_{-1053}	$(6.4^{+4.1}_{-4.0}) \times 10^{43}$	$(6.66e \pm 1.21) \times 10^{44}$	0.039
J1315	$3.2^{+1.3}_{-0.9}$	48^{+4}_{-4}	78^{+3}_{-2}	600^{+130}_{-50}	$70.8^{+70.9}_{-31.0}$	1131^{+988}_{-494}	$(1.3^{+1.2}_{-0.61}) \times 10^{44}$	$(8.835 \pm 0.914) \times 10^{44}$	0.089
J1328	$4.0^{+2.7}_{-1.9}$	48^{+15}_{-19}	81^{+3}_{-5}	230^{+260}_{-80}	$116.4^{+170.3}_{-80.5}$	746^{+890}_{-474}	$(1.1^{+4.4}_{-0.83}) \times 10^{43}$	$(7.47 \pm 1.21) \times 10^{43}$	0.047
J1352	$1.1^{+0.3}_{-0.2}$	61^{+3}_{-6}	78^{+2}_{-3}	440^{+80}_{-60}	$10.2^{+5.8}_{-2.9}$	111^{+52}_{-28}	$(7.0^{+3.4}_{-3.5}) \times 10^{42}$	$(9.92 \pm 1.93) \times 10^{43}$	0.034
J1420	$2.7^{+2.0}_{-1.5}$	41^{+10}_{-16}	70^{+6}_{-5}	390^{+170}_{-110}	$47.0^{+92.7}_{-37.7}$	451^{+642}_{-333}	$(2.0^{+3.5}_{-1.5}) \times 10^{43}$	$(4.576 \pm 1.445) \times 10^{44}$	0.011
J1524	$2.8^{+1.0}_{-1.0}$	35^{+7}_{-10}	62^{+2}_{-2}	720^{+100}_{-90}	$44.7^{+151.0}_{-24.3}$	788^{+2154}_{-403}	$(1.2^{+2.2}_{-0.55}) \times 10^{44}$	$(1.262 \pm 0.122) \times 10^{44}$	0.505
J1526	$0.8^{+0.5}_{-0.4}$	44^{+15}_{-14}	62^{+11}_{-16}	410^{+270}_{-120}	$3.2^{+4.6}_{-2.3}$	33^{+40}_{-24}	$(1.7^{+4.7}_{-1.2}) \times 10^{42}$	$(8.2 \pm 0.3) \times 10^{42}$	0.051
J1606	$1.1^{+0.3}_{-0.3}$	37^{+8}_{-6}	74^{+3}_{-3}	370^{+70}_{-40}	$7.7^{+6.1}_{-3.7}$	79^{+40}_{-37}	$(3.3^{+2.2}_{-1.3}) \times 10^{42}$	$(1.83 \pm 0.45) \times 10^{43}$	0.111
J1630	$0.5^{+0.3}_{-0.1}$	40^{+16}_{-7}	82^{+2}_{-1}	290^{+90}_{-30}	$1.5^{+2.9}_{-0.5}$	11^{+25}_{-4}	$(2.7^{+16.0}_{-0.89}) \times 10^{41}$	$(4.77 \pm 0.25) \times 10^{43}$	0.004
J1720	$2.9^{+0.8}_{-0.7}$	18^{+11}_{-5}	30^{+9}_{-5}	300^{+20}_{-10}	$21.9^{+18.3}_{-5.3}$	167^{+151}_{-39}	$(4.7^{+4.8}_{-1.0}) \times 10^{42}$	$(1.347 \pm 0.228) \times 10^{44}$	0.026

Table A.14: Column 1: galaxy name. Column 2: turnover radius in kpc. Column 3: inner half opening angle or half opening angle for the symmetric bicone galaxies. Column 4: outer half opening angle for the nested and asymmetric bicone galaxies. Column 5: maximum intrinsic velocity. Column 6: lateral surface area of the bicones. Column 7: mass outflow rate. Column 8: kinetic luminosity. Column 9: AGN bolometric luminosity from Nevin et al. (2016). Column 10: lower limit calculated from the asymmetric energy ratio distribution. We take the median value from the distribution and subtract the 1σ , or 34th percentile of the distribution ($L_{\text{KE}}/L_{\text{bol}} - \sigma_{\text{lower}}$). We use this ratio to assess if the energy ratio is above the 0.5% threshold value.

Group	\dot{M} Range [$M_{\odot} \text{ yr}^{-1}$]	Average \dot{M} [$M_{\odot} \text{ yr}^{-1}$]	Technique Used	n_e Assumed [cm^{-3}]
This work	$10^{0.5} - 10^{3.5}$	$10^{2.7}$	[OIII] kinematic modeling of a bicone	100
AGNIFS Group	$10^{-1} - 10^1$	$10^{0.5}$	HII luminosity of a bicone	500
Liu et al. (2013a)	$10^{2.5} - 10^{3.5}$	$10^{3.2}$	H α and H β luminosity of a sphere	100
Brusa et al. (2015)	$10^{1.5} - 10^3$	$10^{1.1}$	[OIII] luminosity of a sphere	100
Karouzos et al. (2016)	$10^{-2} - 10^{-1}$	$10^{-1.4}$	[OIII] luminosity of a sphere	200-800
Harrison et al. (2014)	$10^0 - 10^2$	$10^{1.4}$	H β luminosity of a sphere	100
Mcelroy et al. (2015)	$10^{1.5} - 10^3$	$10^{2.5}$	H α and H β luminosity of a sphere	100
(Schnorr-Müller et al., 2016)	$10^{-2.5} - 10^0$	$10^{-0.3}$	H α luminosity of a bicone	1350
Müller-Sánchez et al. (2011)	$10^0 - 10^2$	$10^{1.4}$	CLR kinematic modeling of a bicone	5000
Müller-Sánchez et al. (2016)	$10^{1.5} - 10^3$	$10^{2.4}$	P α kinematic modeling of a bicone	100

Table A.15: Mass outflow rates from the literature and methods used to determine outflow energetics.

Table A.16: Column 1: galaxy name. Column 2: number of galaxies in the matched sample. Column 3: redshift of the galaxy, and mean redshift and standard deviation of the matched sample of galaxies. Column 4: stellar mass of the galaxy, and mean stellar mass and standard deviation of the matched sample of galaxies. Column 5: AGN bolometric luminosity and error, and mean AGN bolometric luminosity and standard deviation of the matched sample of AGNs. Column 6: color index, and mean color index and standard deviation for the matched sample. If the galaxy's $g - r$ color is $> 1\sigma$ larger than the mean color of the matched sample, we label the galaxy 'Redder', if it is consistent, the galaxy is 'Consistent', and if it $> 1\sigma$ smaller than the mean color of the matched sample, the galaxy is 'Bluer'. Column 7: specific star formation rate, and mean specific star formation rate and standard deviation for the matched sample. If galaxy's sSFR is $> 1\sigma$ smaller than the mean sSFR of the matched sample, we label the galaxy 'Quenched', if it is consistent, the galaxy is 'Consistent', and if it is $> 1\sigma$ larger than the mean sSFR of the matched sample, the galaxy is 'Enhanced'.

SDSS ID	Num. in control sample	z	$\log M_*$ [M_\odot]	L_{bol} [$10^{42} \text{erg s}^{-1}$]	$g-r$ color [Magnitude]	$\log \text{sSFR}$ [yr^{-1}]
J0821+5021		0.095	10.96	130 ± 21	0.95 Consistent	-10.6 Consistent
	131	0.096 ± 0.011	10.94 ± 0.05	98 ± 18	$0.88^{+0.09}_{-0.10}$	$-10.5^{+10.2}_{-10.7}$
J0854+5026		0.096	10.91	69 ± 11	0.86 Consistent	-10.4 Consistent
	254	0.096 ± 0.011	10.89 ± 0.05	63 ± 15	$0.85^{+0.10}_{-0.09}$	$-10.5^{+10.4}_{-10.6}$
J0930+3430		0.061	10.74	110 ± 32	0.92 Redder	-11.0 Consistent
	54	0.064 ± 0.006	10.73 ± 0.05	93 ± 22	$0.78^{+0.12}_{-0.09}$	$-10.5^{+10.3}_{-10.7}$
J0959+2619		0.051	10.58	89 ± 10	0.74 Consistent	-10.6 Consistent
	29	0.049 ± 0.005	10.56 ± 0.06	73 ± 18	$0.71^{+0.12}_{-0.10}$	$-10.2^{+10.1}_{-10.5}$
J1027+1049		0.065	10.29	88 ± 14	0.74 Consistent	-10.1 Consistent
	39	0.067 ± 0.007	10.32 ± 0.05	70 ± 17	$0.75^{+0.08}_{-0.13}$	$-10.2^{+10.1}_{-10.4}$
J1109+0201		0.063	11.00	106 ± 8	0.86 Consistent	-11.6 Quenched
	59	0.066 ± 0.007	10.98 ± 0.04	97 ± 22	$0.83^{+0.09}_{-0.08}$	$-10.8^{+10.4}_{-10.9}$
J1152+1903		0.097	11.08	728 ± 170	0.98 Consistent	-11.1 Consistent
	44	0.101 ± 0.011	11.04 ± 0.04	589 ± 145	$0.88^{+0.12}_{-0.08}$	$-10.5^{+10.0}_{-10.6}$
J1315+2134		0.07	10.95	892 ± 75	0.81 Consistent	-10.1 Consistent
	21	0.071 ± 0.008	10.95 ± 0.05	749 ± 196	$0.8^{+0.08}_{-0.12}$	$-10.4^{+10.0}_{-10.6}$
J1328+2752		0.091	10.76	84 ± 14	0.83 Consistent	-10.7 Consistent
	228	0.092 ± 0.011	10.75 ± 0.05	72 ± 18	$0.83^{+0.10}_{-0.10}$	$-10.3^{+10.3}_{-10.5}$

Continued on next page

Table A.16 – continued from previous page

SDSS ID	Num. in control sample	z	$\log M_*$ [M_\odot]	L_{bol} [$10^{42} \text{ erg s}^{-1}$]	$g-r$ color [Magnitude]	$\log \text{sSFR}$ [yr^{-1}]
J1420+4959		0.063	10.62	125 ± 39	0.81 Consistent	-10.6 Consistent
	41	0.065 ± 0.007	10.61 ± 0.05	93 ± 18	$0.74^{+0.10}_{-0.08}$	$-10.4^{+10.4}_{-10.6}$
J1524+2743		0.068	10.99	128 ± 11	0.83 Consistent	-10.5 Consistent
	62	0.071 ± 0.007	10.97 ± 0.04	99 ± 18	$0.82^{+0.09}_{-0.06}$	$-10.8^{+10.3}_{-10.9}$
J1606+3427		0.055	10.51	22 ± 6	0.90 Redder	-11.8 Quenched
	95	0.057 ± 0.006	10.50 ± 0.05	20 ± 5	$0.78^{+0.08}_{-0.09}$	$-10.6^{+10.4}_{-10.8}$
J1630+1649		0.034	10.40	47 ± 3	0.71 Consistent	-10.7 Consistent
	13	0.034 ± 0.003	10.39 ± 0.06	36 ± 11	$0.75^{+0.08}_{-0.08}$	$-10.5^{+10.5}_{-10.7}$

Model	i [$^\circ$]	PA _{bicone} [$^\circ$ E of N]	r_t [kpc]	$\theta_{1,\text{half}}$ [$^\circ$]	$\theta_{2,\text{half}}$ [$^\circ$]	V_{max} [km s $^{-1}$]
IFS	11 ± 4	-2 ± 3	3.2 ± 0.2	39 ± 6	66 ± 4	188 ± 14
Longslit	11^{+26}_{-7}	60^{+110}_{-50}	1^{+4}_{-1}	44^{+39}_{-33}	—	300^{+630}_{-180}

Table A.17: Best-fit parameters for the IFS and longslit model of the outflow in J0749+4514 with 1σ error bars. Column 1: data used in model. Column 2: outflow inclination. Column 3: position angle of the bicone axis on the sky. Column 4: turnover radius in kpc. Column 5: inner half opening angle. Column 6: outer half opening angle if applicable. Column 7: maximum velocity. The best-fit longslit model is the symmetric bicone, so it has no outer opening angle. The IFS model for the outflow has a wall of finite thickness that can be described with both an inner and an outer opening angle.

Model	M_{tot} [$10^{11} M_\odot$]	Stellar Mass [$10^{10} M_\odot$]	Gas Fraction	Mass Ratio
q0.5_fg0.3	20.8	5.9	0.3	1:2
q0.333_fg0.3	18.7	5.2	0.3	1:3
q0.333_fg0.1	18.7	6.3	0.1	1:3
q0.2_fg0.3_BT0.2	16.8	5.0	0.3	1:5
q0.1_fg0.3_BT0.2	15.1	4.6	0.3	1:10

Table A.18: Key parameters of our suite of high-resolution **GADGET-3** galaxy merger simulations.

Model	M_{tot} [$10^{11} M_\odot$]	Stellar Mass [$10^{10} M_\odot$]	f_{gas}	Matched Model(s)
m1_fg0.3	13.9	3.9	0.3	q0.5_fg0.3, q0.333_fg0.3
m0.5_fg0.3	6.9	2.0	0.3	q0.5_fg0.3
m1_fg0.1	14.0	4.7	0.1	q0.333_fg0.1
m0.333_fg0.1	4.7	1.6	0.1	q0.333_fg0.1
m1_fg0.3_BT0.2	13.7	4.2	0.3	q0.2_fg0.3_BT0.2, q0.1_fg0.3_BT0.2

Table A.19: Key parameters of the matched sample of isolated galaxies. These are matched to the mass of the primary or secondary galaxy in the merger for each simulation and the gas fraction. The gas fraction is the same for each merger progenitor in a given simulation.

Simulation	\hat{w}						\hat{w}_0
	<i>Gini</i>	M_{20}	<i>C</i>	<i>A</i>	<i>S</i>	<i>n</i>	A_S
All Major	0.69 \pm 0.21	–	3.84 \pm 0.23	5.78 \pm 0.21	–	–	13.14 \pm 0.61
All Minor	8.64 \pm 1.14	–	14.22 \pm 1.66	5.21 \pm 0.26	–	–	2.53 \pm 0.2
q0.5_fg0.3	–	0.75 \pm 0.29	-0.82 \pm 0.16	9.93 \pm 0.39	–	–	5.89 \pm 0.19
q0.333_fg0.3	4.18 \pm 0.22	–	–	6.15 \pm 0.68	–	–	22.17 \pm 1.2
q0.333_fg0.1	–	–	5.38 \pm 0.19	5.66 \pm 0.28	–	–	11.41 \pm 0.39
q0.2_fg0.3_BT0.2	19.34 \pm 2.89	-4.08 \pm 3.29	24.69 \pm 1.87	5.88 \pm 0.43	–	–	3.97 \pm 0.31
q0.1_fg0.3_BT0.2	11.39 \pm 1.17	–	33.27 \pm 2.0	29.74 \pm 2.33	–	–	-5.05 \pm 1.95
							-0.81 \pm 0.05
							-0.87 \pm 0.04
							-2.76 \pm 0.05
							-0.44 \pm 0.14
							-0.56 \pm 0.1
							-0.87 \pm 0.07
							-1.75 \pm 0.11

Table A.20: LD1 predictor coefficients with 1σ confidence intervals. Bolded values are significantly greater than zero (to 3σ). We include only the predictors that are selected by the forward stepwise selection; for example, in q0.5_fg0.3, M_{20} , C , A , and A_S are excluded by this selection. \hat{w} and \hat{w}_0 are the weight vector (composed of the predictor coefficients) and the intercept, respectively. Together, they describe the LD1 hyperplane that best separates the populations of merging and nonmerging galaxies for each simulation. The coefficients have positive or negative values; a positive coefficient indicates that increasing the corresponding predictor increases the likelihood that the galaxy is a merger.

	\hat{w}									
Simulation	$G * M_{20}$	$G * C$	$G * A$	$G * S$	$G * n$	$G * A_S$	$M_{20} * C$	$M_{20} * A$	$M_{20} * S$	
All Major	-	-	-	-	-	-3.68 ± 0.93	-	-	-	
All Minor	-	-20.33 ± 2.53	-	-	-	-	-	-	-	
q0.5_fg0.3	-	-	-	-	-	-	-2.01 ± 0.43	-	-	
q0.333_fg0.3	-	-	-	-	-	-19.09 ± 1.14	-	-	-	
q0.333_fg0.1	-	-	-	-	-	-	-	-	-	
q0.2_fg0.3_BT0.2	2.98 ± 3.57	-38.04 ± 2.88	-	-	-	-	-	-	-	
q0.1_fg0.3_BT0.2	-	-39.29 ± 2.88	-27.95 ± 2.48	-	-	28.81 ± 2.04	-	-	-	
	$M_{20} * n$	$M_{20} * A_S$	$C * A$	$C * S$	$C * n$	$C * A_S$	$A * S$	$A * n$	$A * A_S$	
All Major	-	-	-	-	-	-6.5 ± 0.5	-	-	-6.12 ± 0.27	
All Minor	-	-	-	-	-	-	-	-	-4.32 ± 0.39	
q0.5_fg0.3	-	-	-	-	-	-	-	-	-9.52 ± 0.44	
q0.333_fg0.3	-	-	-	-	-	-	-	-	-6.03 ± 0.91	
q0.333_fg0.1	-	-	-	-	-	-8.57 ± 0.34	-	-	-5.92 ± 0.3	
q0.2_fg0.3_BT0.2	-	-	-	-	-	-	-	-	-5.21 ± 0.47	
q0.1_fg0.3_BT0.2	-	-	7.16 ± 0.73	-	-	-20.28 ± 0.86	-	-	-6.88 ± 0.34	
	$S * n$	$S * A_S$	$n * A_S$							
All Major	-	-	-							
All Minor	-	-	-							
q0.5_fg0.3	-	-	-							
q0.333_fg0.3	-	-	-							
q0.333_fg0.1	-	-	-							
q0.2_fg0.3_BT0.2	-	-	-							
q0.1_fg0.3_BT0.2	-	-	-							

Table A.21: Same as Table A.20 but for the interaction terms of all runs.

Simulation	Total Merger Time	LDA	$Gini - M_{20}$	A	A_S
q0.5_fg0.3	2.20	1.96	0.59	< 0.1	2.20
q0.333_fg0.3	2.64	2.45	0.34	< 0.1	2.64
q0.333_fg0.1	2.83	2.05	0.78	< 0.1	2.34
q0.2_fg0.3_BT0.2	3.52	3.52	0.19	< 0.1	3.52
q0.1_fg0.3_BT0.2	9.17	8.78	0.73	< 0.1	7.79

Table A.22: Observability timescales in Gyr for the four different merger identification techniques compared in Section 4.3.2 as well as the total time of the merger.

Simulation	Accuracy	Precision	Recall	F_1 Score
All Major	0.85	0.97	0.80	0.88
All Minor	0.81	0.94	0.66	0.78
q0.5_fg0.3	0.91	0.98	0.82	0.90
q0.333_fg0.3	0.90	0.97	0.87	0.92
q0.333_fg0.1	0.86	0.96	0.83	0.89
q0.2_fg0.3_BT0.2	0.88	0.96	0.78	0.86
q0.1_fg0.3_BT0.2	0.89	0.89	0.79	0.84

Table A.23: LDA performance. We list the accuracy, precision, recall, and F_1 score as defined in Appendix B.7 for all runs of the LDA classification.

Simulation	Mass Ratio	Gas Fraction	Matched Isolated Galaxies
q0.5_fg0.3	1:2	0.3	m0.5_fg0.3, m1_fg0.3
q0.333_fg0.3	1:3	0.3	m1_fg0.3
q0.333_fg0.1	1:3	0.1	m0.333_fg0.1, m1_fg0.1
q0.2_fg0.3_BT0.2	1:5	0.3	m1_fg0.3_BT0.2
q0.1_fg0.3_BT0.2	1:10	0.3	m1_fg0.3_BT0.2

Table A.24: Key simulation parameters and matched isolated galaxies.

Table A.25: LD1 predictor coefficients with 1σ confidence intervals prior to the predictor selection. Bolded values are significantly greater than zero (to 3σ). We include only the predictors that are selected by the forward stepwise selection; for example, in q0.5_fg0.3, v_{asym} , resids, λ_{R_e} , and ϵ are excluded by this selection. \hat{w} and \hat{w}_0 are the weight vector (composed of the predictor coefficients) and the intercept, respectively. Together, they describe the LD1 hyperplane that best separates the populations of merging and nonmerging galaxies for each simulation.

Simulation	\hat{w}					
	ΔPA	v_{asym}	σ_{asym}	resids	λ_{R_e}	ϵ
q0.5_fg0.3	2.16 ± 0.23	–	2.19 ± 0.07	–	–	0.49 ± 0.11
q0.333_fg0.3	–	–	3.11 ± 0.4	0.94 ± 0.11	-3.33 ± 0.27	1.42 ± 0.25
q0.333_fg0.1	–	–	0.75 ± 0.2	–	-2.42 ± 0.15	0.78 ± 0.12
q0.2_fg0.3_BT0.2	-0.9 ± 0.3	–	1.79 ± 0.21	-1.28 ± 0.35	-0.95 ± 0.08	–
q0.1_fg0.3_BT0.2	1.25 ± 0.14	–	–	0.22 ± 0.08	–	–

Table A.26: The final LD1 predictor coefficients with 1σ confidence intervals after term selection. Bolded values are significantly greater than zero (to 3σ). We include the term coefficients for the full LDA runs (with interaction terms, top half) as well as the primary coefficients for the LDA run without interaction terms (bottom half).

Simulation	$\hat{\vec{w}}$						\hat{w}_0
	ΔPA	σ_{asym}	resids	λ_{R_e}	ϵ	A_2	
All Major	0.38 \pm 0.07	-0.7 \pm 0.06	1.74 \pm 0.09	-1.94 \pm 0.09	0.55 \pm 0.07	0.53 \pm 0.05	-1.98 \pm 0.01
All Minor	1.01 \pm 0.14	1.08 \pm 0.07	-0.43 \pm 0.14	—	—	0.28 \pm 0.06	-0.83 \pm 0.02
q0.5_fg0.3	—	1.69 \pm 0.07	—	—	—	0.69 \pm 0.12	-2.37 \pm 0.03
q0.333_fg0.3	—	3.02 \pm 0.34	1.01 \pm 0.09	-2.22 \pm 0.18	—	1.48 \pm 0.19	-1.4 \pm 0.13
q0.333_fg0.1	—	0.86 \pm 0.22	0.53 \pm 0.08	-2.55 \pm 0.16	0.71 \pm 0.12	0.35 \pm 0.15	-1.88 \pm 0.04
q0.2_fg0.3	-0.9 \pm 0.3	1.79 \pm 0.21	-1.28 \pm 0.35	-0.95 \pm 0.08	—	—	-0.79 \pm 0.03
q0.1_fg0.3	1.25 \pm 0.14	—	0.22 \pm 0.08	—	—	—	-0.93 \pm 0.02
No Interaction Terms							
All Major	0.41 \pm 0.04	0.99 \pm 0.02	—	—	—	0.36 \pm 0.04	-2.09 \pm 0.01
All Minor	0.55 \pm 0.14	0.89 \pm 0.08	-0.73 \pm 0.07	—	-0.05 \pm 0.09	—	-0.84 \pm 0.01
q0.5_fg0.3	—	1.59 \pm 0.06	—	—	—	0.57 \pm 0.06	-2.37 \pm 0.03
q0.333_fg0.3	—	1.33 \pm 0.11	—	-1.82 \pm 0.17	0.59 \pm 0.11	0.58 \pm 0.09	-1.68 \pm 0.07
q0.333_fg0.1	—	1.11 \pm 0.05	—	-2.21 \pm 0.1	0.86 \pm 0.05	0.48 \pm 0.04	-1.89 \pm 0.04
q0.2_fg0.3	0.4 \pm 0.1	1.39 \pm 0.13	-1.33 \pm 0.15	-1.18 \pm 0.16	0.76 \pm 0.17	—	-0.79 \pm 0.03
q0.1_fg0.3	0.77 \pm 0.07	0.64 \pm 0.09	-0.69 \pm 0.08	0.22 \pm 0.06	—	0.18 \pm 0.04	-0.94 \pm 0.02

Table A.27: Same as Table A.26 but for the interaction terms of all runs.

Simulation	\hat{w}						
	$\Delta PA * \sigma_{\text{asym}}$	$\Delta PA * \text{resids}$	$\Delta PA * \lambda_{R_e}$	$\Delta PA * \epsilon$	$\Delta PA * A_2$		
All Major	—	—	—	—	-0.14 \pm 0.04		
All Minor	—	—	—	—	-0.53 \pm 0.26		
q0.5_fg0.3	—	—	—	—	—		
q0.333_fg0.3	—	—	—	—	—		
q0.333_fg0.1	—	—	—	—	—		
q0.2_fg0.3_BT0.2	-0.77 \pm 0.3	—	1.89 \pm 0.35	—	—		
q0.1_fg0.3_BT0.2	—	-0.76 \pm 0.15	—	—	—		
Simulation	\hat{w}						
	$\sigma_{\text{asym}} * \text{resids}$	$\sigma_{\text{asym}} * \lambda_{R_e}$	$\sigma_{\text{asym}} * \epsilon$	$\sigma_{\text{asym}} * A_2$	$\text{resids} * \lambda_{R_e}$	$\text{resids} * \epsilon$	$\text{resids} * A_2$
All Major	-1.13 \pm 0.05	3.09 \pm 0.11	-0.82 \pm 0.09	—	-1.27 \pm 0.12	—	—
All Minor	-0.47 \pm 0.14	—	—	—	—	—	—
q0.5_fg0.3	—	—	—	-0.19 \pm 0.13	—	—	—
q0.333_fg0.3	-3.18 \pm 0.21	1.94 \pm 0.2	—	-1.35 \pm 0.22	—	—	—
q0.333_fg0.1	-0.52 \pm 0.11	0.51 \pm 0.21	—	—	—	—	—
q0.2_fg0.3_BT0.2	-0.17 \pm 0.42	—	—	—	—	—	—
q0.1_fg0.3_BT0.2	—	—	—	—	—	—	—
Simulation	$\lambda_{R_e} * \epsilon$			$\epsilon * A_2$			
	$\lambda_{R_e} * \epsilon$	$\lambda_{R_e} * A_2$	$\epsilon * A_2$	$\lambda_{R_e} * \epsilon$	$\lambda_{R_e} * A_2$	$\epsilon * A_2$	
All Major	—	—	—	—	—	—	
All Minor	—	—	—	—	—	—	
q0.5_fg0.3	—	—	—	—	—	—	
q0.333_fg0.3	—	—	—	—	—	—	
q0.333_fg0.1	—	—	—	—	—	—	
q0.2_fg0.3_BT0.2	—	—	—	0.14 \pm 0.17	—	—	
q0.1_fg0.3_BT0.2	—	—	—	—	—	—	

Simulation	Merger Duration	LDA Observability Time	Fraction Observability
q0.5_fg0.3	2.20	1.61	0.73
q0.333_fg0.3	2.64	2.16	0.82
q0.333_fg0.1	2.83	1.71	0.60
q0.2_fg0.3_BT0.2	3.52	3.52	1.00
q0.1_fg0.3_BT0.2	9.17	3.31	0.36

Table A.28: The duration of the merger, LDA observability time, and fraction observability (LDA observability time/merger duration) for each simulation.

Simulation	Accuracy	Precision
All Major	0.53	0.96
All Minor	0.57	0.83
q0.5_fg0.3	0.69	0.94
q0.333_fg0.3	0.69	0.94
q0.333_fg0.1	0.63	0.91
q0.2_fg0.3_BT0.2	0.63	0.83
q0.1_fg0.3_BT0.2	0.69	0.77

Table A.29: Accuracy and precision for all LDA runs.

Appendix B

Appendices of Chapters 3 and 4

Here I include the appendices for Chapters 3 and 4. At the beginning of each section, I state which chapter the appendix accompanies.

B.1 Investigating Outflow vs Rotational Kinematics

This section accompanies Chapter 3.

In this Appendix we discuss the outflow-dominated kinematics of this sample. We compare these AGN outflows to other galaxies that demonstrate rotation-dominated kinematics on large scales (e.g., Fischer et al. 2017) to explain why we are motivated to model only outflowing components for our sample. Additionally, we present a case study of a galaxy from Nevin et al. (2016) that was not included in this work. This galaxy offers insight into rotational and outflow kinematics and sheds light on the nature of the sample of 18 galaxies in this work.

We first discuss the previous work on the full sample of 71 AGNs in Nevin et al. (2016) as well as other general properties of this sample of AGNs that lead to our conclusion that the 18 galaxies in this work are dominated by outflow kinematics, not large-scale rotation. In Nevin et al. (2016), we kinematically classify the full sample of 71 double-peaked AGNs as either outflow-dominated or rotation-dominated. The outflow-dominated AGNs are further classified as outflow or outflow composite. Outflow composite AGNs are best fit with > 2 kinematic components and outflow AGNs are best fit with 2 kinematic components. The

outflow-dominated classification requires that one of the kinematic components have a velocity dispersion $\sigma > 500 \text{ km s}^{-1}$ or a velocity offset $v > 400 \text{ km s}^{-1}$ for at least one spatial position. While outflows can also have lower velocity dispersions or velocity offsets, these cutoffs are meant to conservatively eliminate rotation-dominated kinematics as the origin of the kinematic components.

For this work, we carefully select 18 of the outflow-dominated galaxies from Nevin et al. (2016) with the best quality data to model as biconical outflows. We describe this selection in Section 3.2.1. The classification in Nevin et al. (2016) previously identified these 18 AGNs as those with outflow-dominated kinematics apparent at one or more spatial positions in the galaxy. The selection in this work further required that these AGNs have double-peaked profiles consistent with a bicone at all of the modeled spatial positions. Therefore, we are selecting for AGN outflows to model that have outflow-dominated kinematics and that are double-peaked on large spatial scales.

Additionally, the double-peaked nature of the [OIII] λ 5007 profiles at all spatial positions indicates that the 18 galaxies in this work are indeed dominated by outflow kinematics because rotation cannot explain double-peaked profiles at all spatial scales. This was one of the main outcomes of Nevin et al. (2016). Unlike in some modeled Seyfert galaxies, where the profiles are double peaked towards the center, but single-peaked and rotation-dominated at spatial extremes (e.g., Fischer et al. 2017), we found profiles for the 18 galaxies that were double-peaked at all spatial positions.

The 18 galaxies are outflow-dominated and not rotation-dominated, but as another test we examine how well a rotating structure can fit the gas velocity in each galaxy. We create spatially-resolved velocity maps for each galaxy by superimposing each of the two observed longslit PAs and fitting a single Gaussian peak to the [OIII] λ 5007 profile at each position along each slit. We determine whether the spatially-resolved velocity map for each galaxy is rotation-dominated using two criteria: The velocity map must be centered on zero velocity (systemic velocity for the galaxy) and it must demonstrate symmetric rotation, where if one

extreme of an observed PA is redshifted, the other must be blueshifted by the same amount. We find that while three AGNs potentially demonstrate disk-like rotation on large spatial scales (J0009–0036, J0803+3926, and J1152+1903), the other 15 do not have large-scale rotation.

These results are unsurprising given Figure 3.1, which plots the double-peaked [OIII] λ 5007 profile of each galaxy from the SDSS spectra. If these galaxies were entirely dominated by a disk on a large scale and if this disk has a bright integrated flux, we would expect the integrated profiles to be centered on zero velocity. However, that is not the case for most galaxies in our sample and only two galaxies (J0803+3926 and J1152+1903) are classified and modeled as a ‘Symmetric Bicone’ because their double-peaked velocity profiles are centered at zero velocity. These two galaxies are also two of the galaxies that show potential disk-like rotation in the spatially-resolved velocity maps. The third galaxy with disk-like rotation is J0009–0036, which is best described as an ‘Asymmetric Bicone’, but it does have velocities that are centered around zero velocity.

However, what may appear to be disk rotation in these figure*s could also mimic a symmetric slower velocity bicone in these spatially-resolved velocity maps. We further investigate the three galaxies that demonstrate disk-like rotation and find that individual component fits of J0009–0036 and J0803+3926 have large velocity dispersions ($\sigma > 500$ km s^{−1}). These large dispersions occur at large spatial scales. This indicates that they are outflow-dominated at these spatial positions. J1152+1903 has a few spatial positions with large velocity dispersions of its individual components, however they are overall better characterized as narrower ($\sigma < 500$ km s^{−1}). All three galaxies are double-peaked at all spatial positions. This is distinct from spatially compact outflows, where the outflow is confined to small spatial positions, and the double-peaked profile only appears at the center of the galaxy. We conclude that these three galaxies, while their spatially-resolved velocity maps mimic disk rotation, are dominated by outflows on all spatial scales due to the large velocity dispersions of their individual components (J0009–0036 and J0803+3926) and

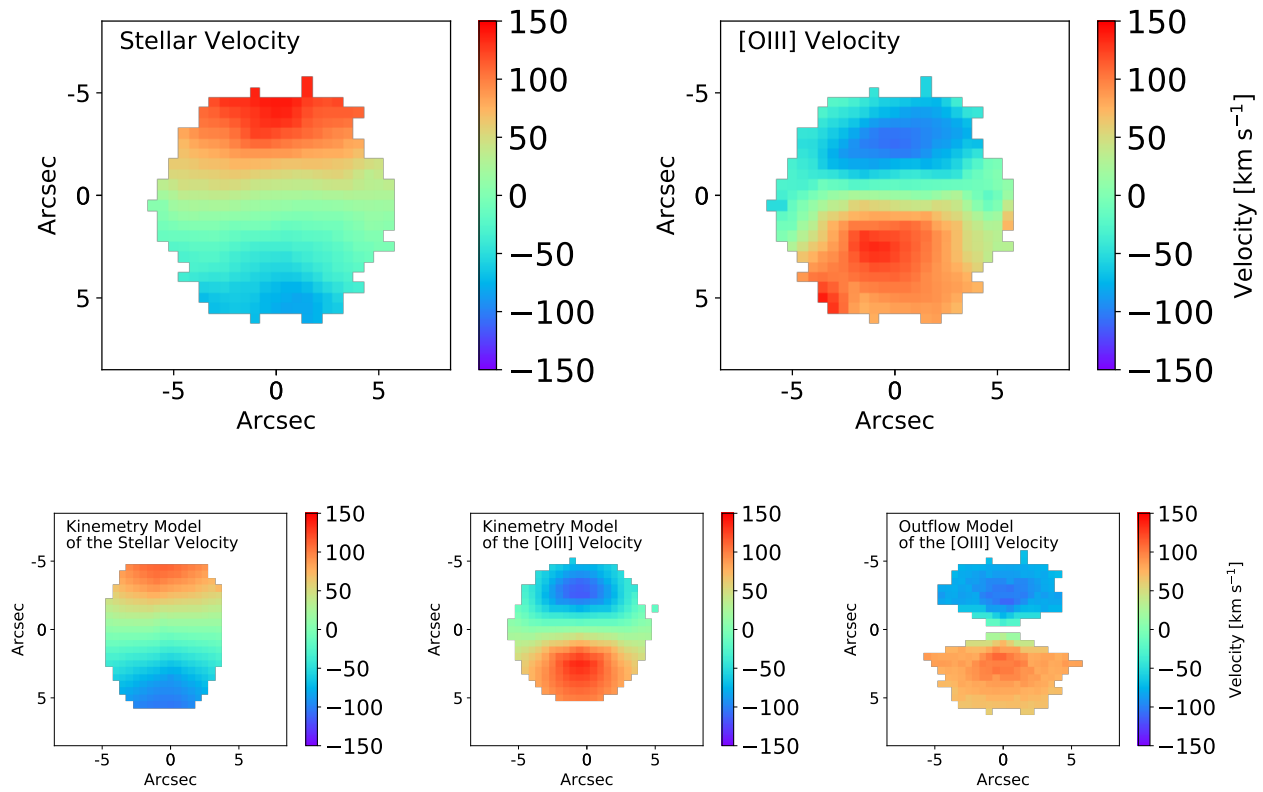


Figure B.1: IFS maps from MaNGA and models for J0749+4514. We plot the stellar velocity (top left) and the [OIII] gas velocity (top right). We show the kinemetry models (Krajnović et al. 2006) for the stellar velocity (bottom left). The [OIII] velocity map is anti-aligned to the stellar velocity and can be described as a counter-rotating disk (bottom middle). We also model a biconical outflow (Müller-Sánchez et al. 2016) along the plane of the galaxy (bottom right).

double-peaked profiles at all spatial positions (J0009–0036, J0803+3926, and J1152+1903).

Although the galaxies are dominated by outflows on all spatial scales, we now examine whether there could be smaller contributions from disk rotation. If this is the case, then the analytic models should take this into account by including the parameters for a rotating disk structure in the model in addition to those for a biconical outflow.

To investigate this situation, we make a spatially-resolved velocity map of the narrower component of the double-peaked profile for all 18 galaxies. We choose to track the narrower component because broader components are most often associated with outflow-dominated kinematics. We use the same criteria as above, where we identify a galaxy as rotation-dominated if its spatially-resolved velocity map is symmetric about zero velocity. We find that the velocity offset of the narrow component is not consistent with disk rotation for any of the 18 galaxies.

After our analysis of the kinematics of the 18 galaxies in this sample, we find that they are well described by outflow kinematics on all spatial scales with minimal small contributions from disk rotation. This is consistent with our findings of the biases of the selection of this double-peaked sample. We have selected a sample of energetic and large AGN outflows. They are distinct from the population of outflows in local Seyfert galaxies, for example the galaxy in Fischer et al. (2017) was selected for the biconical morphology of the $[\text{OIII}]\lambda 5007$ emission in imaging (not for double-peaked narrow lines). These types of outflows occur on smaller scales and the gas kinematics can be described by illuminated disk rotation on larger scales. This is consistent with the biases discussed in Section 3.4.2. The outflows in this work are larger and more energetic than samples of lower-luminosity AGNs, which often only have small-scale outflows (e.g., Fischer et al. 2017).

While we have determined that the large-scale kinematics of the 18 galaxies in this sample are best described as outflow-dominated, we investigate a single galaxy in more depth to determine the role of rotating structure in the kinematics of the galaxy. We examine the galaxy J0749+4514 more closely in a case study of an ‘Outflow Composite’ galaxy from

Nevin et al. (2016) that is most likely dominated by outflow components on large scales with some rotation on small scales. This galaxy is the only galaxy from our original sample of 71 galaxies that has been observed by the SDSS-IV Mapping Nearby Galaxies at Apache Point (MaNGA) IFS survey (Gunn et al. 2006; Bundy et al. 2015; Drory et al. 2015; Law et al. 2015; Yan et al. 2016b,a; Law et al. 2016; Abolfathi et al. 2017; Blanton et al. 2017). So while this is not one of the 18 galaxies selected for the biconical modeling in this work, it offers a unique opportunity to determine how disk rotation shapes the kinematics, and directly investigate how outflow modeling with longslit data compares to outflow modeling with IFS data.

In IFS, this galaxy has misaligned ionized gas with respect to the stellar disk (Figure B.1). This is a kinematic signature of either a counter-rotating disk produced by a merger or an outflow (Allen et al. 2015, Müller-Sánchez et al. 2011). To fully determine the kinematic origin of the [OIII] λ 5007 emission, we model it as a rotating disk, a counter-rotating disk, and an outflow using the IFS data. First, we use the modeling code `kinemetry` to model the higher-order moments of the LOS velocity distribution of the stellar velocity map as a rotating disk (Krajnović et al. 2006). At each radius, a small number of harmonic terms in a Fourier expansion are used to determine the best fitting ellipse for the stellar velocity map. While `kinemetry` finds a good fit to the stellar velocity map, this same model is a bad fit for the [OIII] velocity as indicated by a high velocity residual and a high χ^2_ν value (listed below). Second, we model the [OIII] velocity map as a counter-rotating disk. A counter-rotating disk can be produced by a merger, where gas is funneled to the center of the galaxy, but is misaligned with the stellar velocity (e.g., Allen et al. 2015). Third, we model the [OIII] λ 5007 emission using a biconical outflow model and give the parameters for the best-fit model in Table A.17. This analytic model from Müller-Sánchez et al. (2016) is a six parameter model that uses an inner and outer half opening angle, a position angle, a turnover radius, a maximum velocity, and an inclination to produce a biconical outflow model.

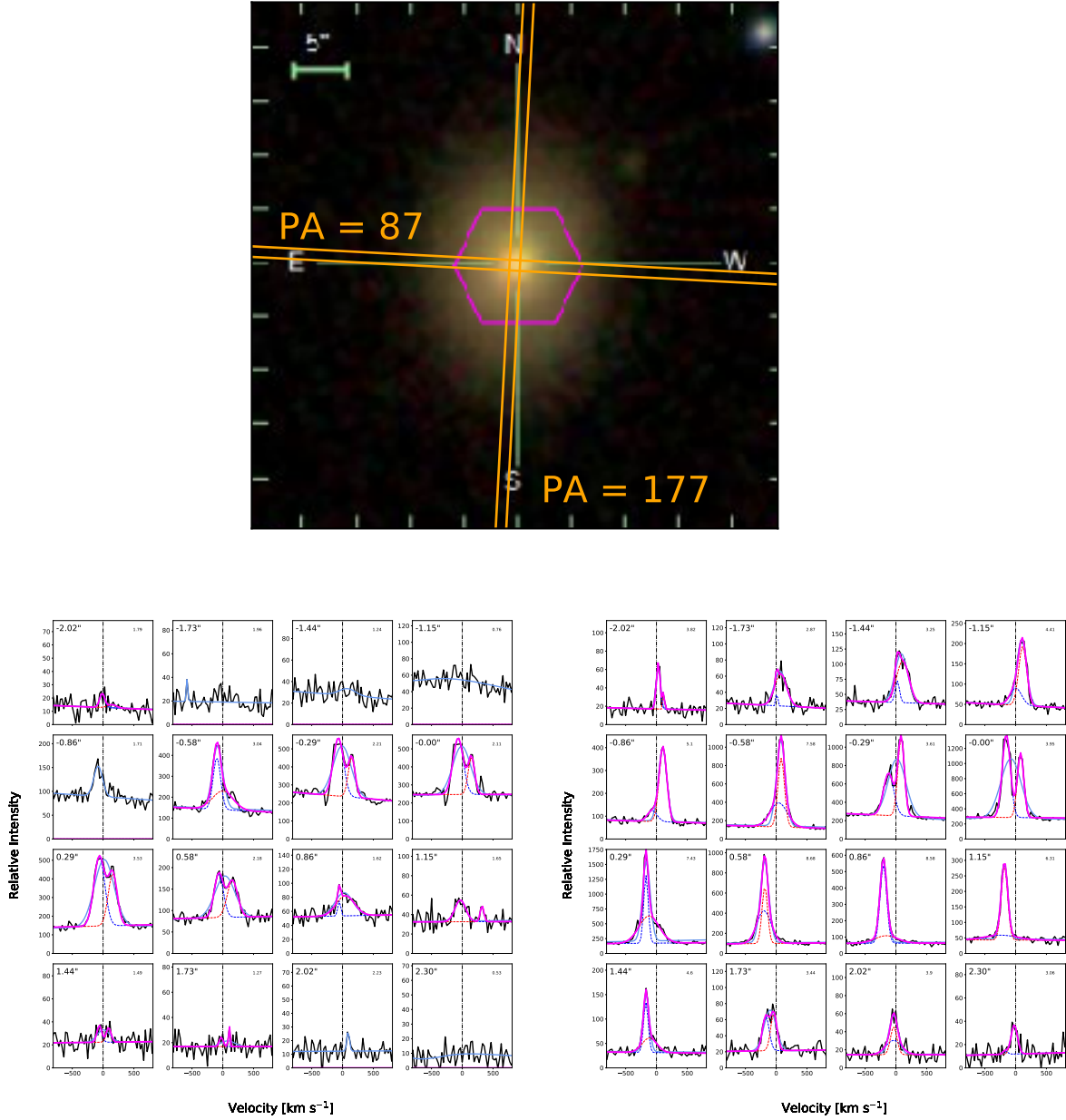


Figure B.2: The longslit PAs for J0749+4514 overlaid on the SDSS *gri* galaxy image and the MaNGA field of view (top). Longslit PA 87 (left bottom) and PA 177 (right bottom) observations. We label the spatial position in the upper left corner of each spatial panel, where positive directions are to the east (PA 87) and north (PA 177). The spatial positions of the longslit positions shown here are confined to the inner $2''.3$ radius of the galaxy, inside the magenta MaNGA fiber. We fit two Gaussians, blue and red corresponding to the blueshifted and redshifted profile respectively, and light blue corresponding to the one Gaussian fit. A vertical dashed line denotes systemic velocity.

We compare the χ^2_ν values from the rotating disk, counter-rotating disk, and outflow model and find values of 1691, 7, and 32, respectively. We find that the velocity residuals ($< |V_{\text{obs}} - V_{\text{mod}}| >$) are 126, 10, and 18 km s⁻¹, respectively. The numerical best fit is the counter-rotating disk, but both the counter-rotating disk and the outflow are good fits to the data and also have low velocity residuals.

While the χ^2_ν values indicate that both a counter-rotating disk and an outflow describe the data well, an outflow origin for the kinematics in J0749+4514 is a more likely explanation. First, J0749+4514 has BPT ratios from MaNGA consistent with an AGN origin for the ionized gas on all spatial scales. Second, this AGN is classified as an ‘Outflow Composite’ in Nevin et al. (2016) and as discussed below, has double or triple peaked lines at many spatial positions, especially near the center, where one of these components is broader. As discussed for the full sample, double-peaked profiles at nearly all spatial positions indicates an outflow origin for the gas kinematics. Third, J0749+4514 is an isolated galaxy in SDSS imaging so it is unlikely that a merger is producing a counter-rotating disk. Fourth, outflows are more ubiquitous than counter-rotating disks (e.g., Allen et al. 2015). An outflow origin is a better explanation but does not fully explain all of the kinematics in the IFS data.

While the IFS data offers insight into the kinematics of this galaxy, we can also use the longslit data to investigate the kinematics and verify that any conclusions from the longslit observations are consistent with those from the IFS data. We present the MMT longslit data for this galaxy in Figure B.2. PA 87 is the kinematic minor axis of the galaxy (as seen in stellar kinematics); it has double peaks at many spatial positions but is also spatially compact. PA 177 is aligned with the photometric major axis of the galaxy, which is also the kinematic major axis. PA 177 has double or triple peaks at all spatial positions as well, but one component dominates. The dominating component at the spatial extremes of PA 177 is anti-aligned with the stellar velocity maps from MaNGA and cannot be described as stellar rotation. It is redshifted to the south and blueshifted to the north, which is consistent with the [OIII] λ 5007 maps from MaNGA. This dominating component is narrower ($\sigma < 500$ km

s^{-1}) at the spatial extremes of PA 177 and could be either a counter-rotating disk or an outflow, which is consistent with the interpretation from the IFS data for the $[\text{OIII}]\lambda 5007$ maps.

This galaxy was classified as Outflow Composite due to the presence of three kinematic components in the longslit maps. For instance, at row $0''.288$ in PA 177 (Figure B.2), there are three kinematic components. First, there is a dominating narrower component that is anti-aligned with respect to the stellar rotation as seen in the IFS maps. This component is the same component that dominates at large spatial positions. Second, a compact lower flux narrow component tracks the stellar rotation. Third, a broader lower flux component is centered around zero velocity.

There could be multiple kinematic explanations for these three components. First, outflows can have many kinematic components so all three could be attributed to an AGN outflow. Second, the low flux narrow compact component that is aligned with the stellar velocity map could be tracking the rotating disk while the other two components correspond to the walls of an outflow. Third, the dominating high flux narrow component could track a counter-rotating disk, while the low flux narrow compact component is the stellar disk and the broader component is a very small scale outflow. The presence of multiple interacting kinematic components in the longslit and IFS data may cause the observed ambiguity in the modeling using both the IFS and longslit data. This also underscores why we did not include this galaxy in the 18 outflows modeled in this work due to the presence of multiple kinematic processes.

We are conservative in selecting which galaxies we model as outflows, which is why we excluded this galaxy and others like it from the final sample for this work. This galaxy was excluded due to the spatially compact nature of PA 87 and the difficulty of tracking individual components for PA 177. But while we did not include J0749+4514 in the 18 galaxies selected for this work, we model it here as a biconical outflow to compare our longslit model to the IFS model for the outflow. As discussed above, due to the isolation of

the galaxy, the ubiquity of AGN outflows, and the BPT ionization origin for the emission lines, the large-scale dominating component is most likely an outflow. We find consistent results from each model (within 2σ) and an outflow with parameters given in Table A.17.

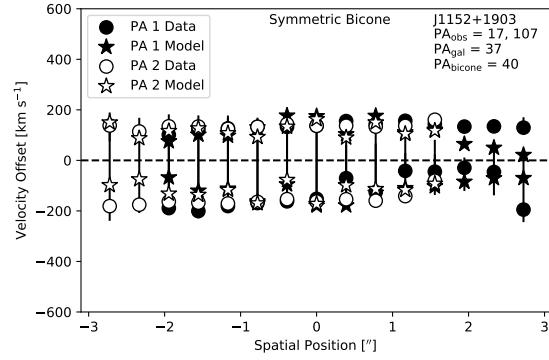
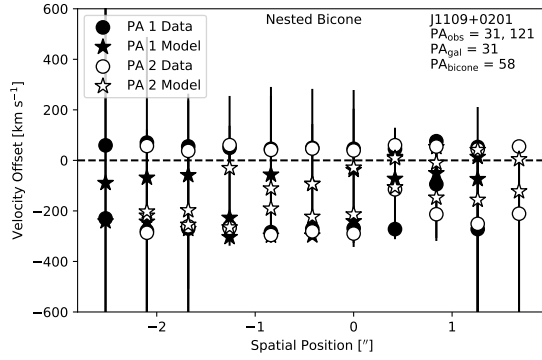
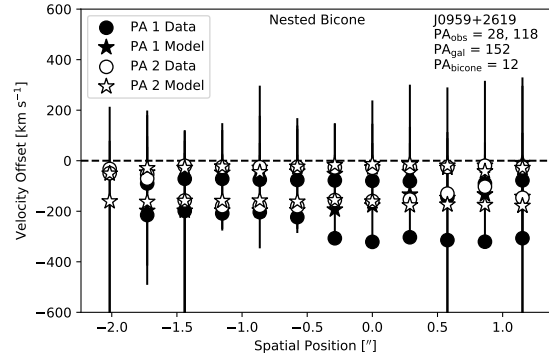
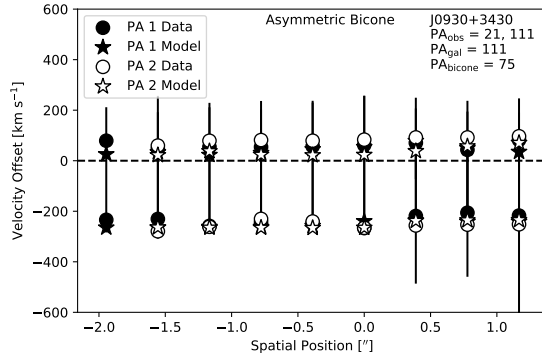
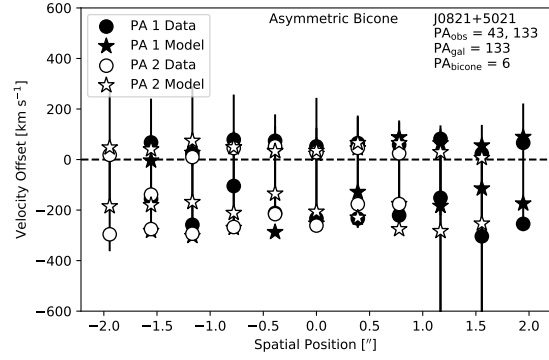
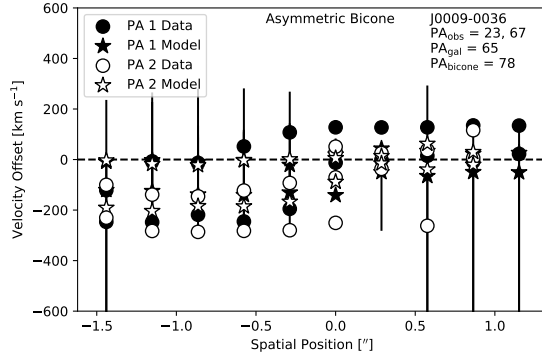
The longslit outflow model has large uncertainties associated with the best-fit parameters. This is an indication of the success of our selection criteria in this paper to select the 18 galaxies to further model and correctly exclude those galaxies that will produce larger uncertainties on the best-fit parameters. Instead of just modeling the two walls of a biconical outflow, it is possible that we are incorrectly attributing small-scale rotational components to the walls of an outflow as discussed above. However, it is impractical to include a rotating component in our model in addition to the biconical outflow model because we do not have enough data points to satisfy the $n > 2k$ selection criterion for a bicone and a rotating disk. If we attempted to introduce more parameters, the model would be under constrained.

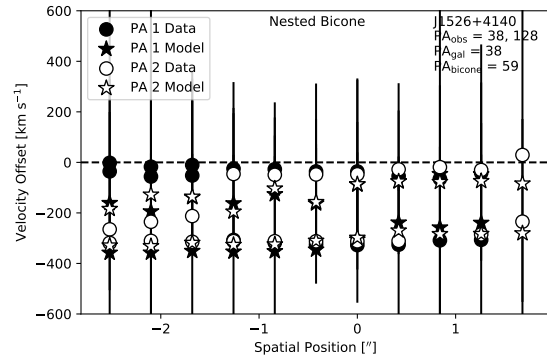
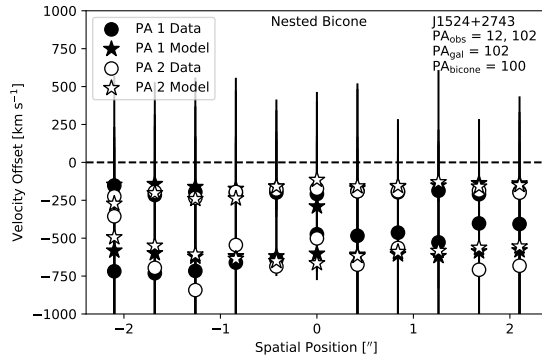
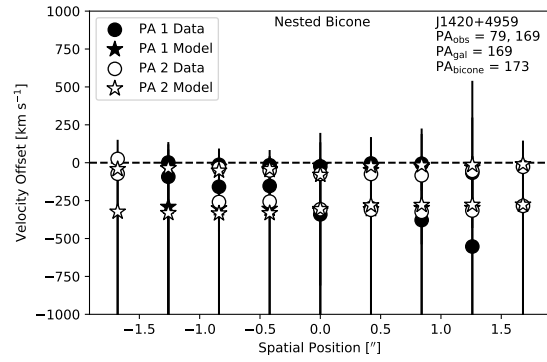
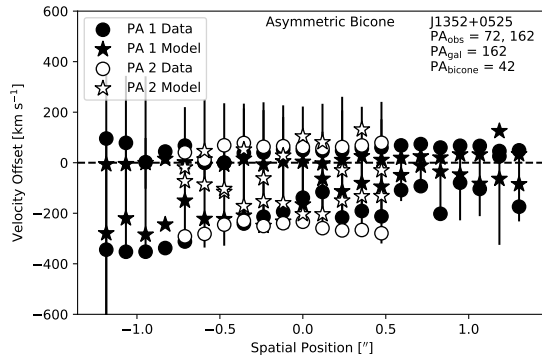
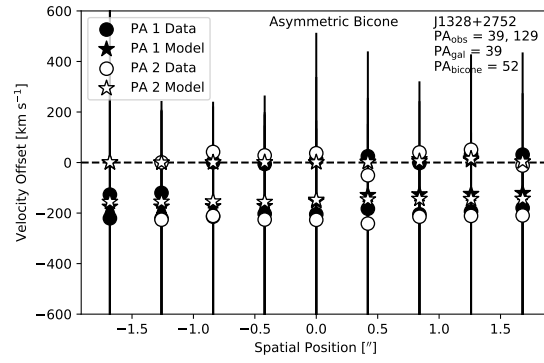
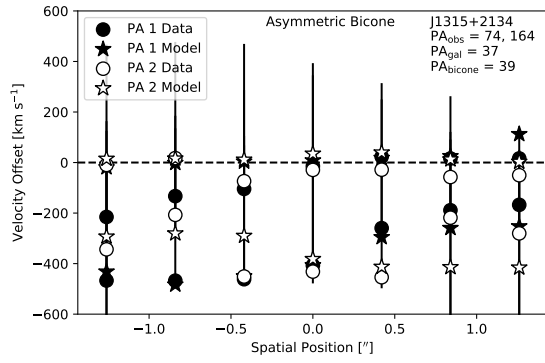
The outflow models done with longslit and IFS data agree within 1σ errors for all but one parameter ($\text{PA}_{\text{bicone}}$). We have shown in our sensitivity analysis in Section 3.2.3 that $\text{PA}_{\text{bicone}}$ is not well determined. In this case, one of our observed PAs is aligned with the axis of the bicone from the IFS model, but the other does little to constrain the motion of the outflow. Therefore, we are unable to constrain this parameter in the longslit model. This is reflected in the large uncertainty associated with it. The values for $\text{PA}_{\text{bicone}}$ from each model do agree to 2σ uncertainty. Overall, the models agree but the longslit model has larger uncertainties associated with it, justifying our conservative selection criteria which allows us to use longslit data for modeling purposes only when it can better constrain the bicone geometry.

B.2 18 Biconical Models

This section accompanies Chapter 3.

Here we show the best fit bicone models for all 18 galaxies.





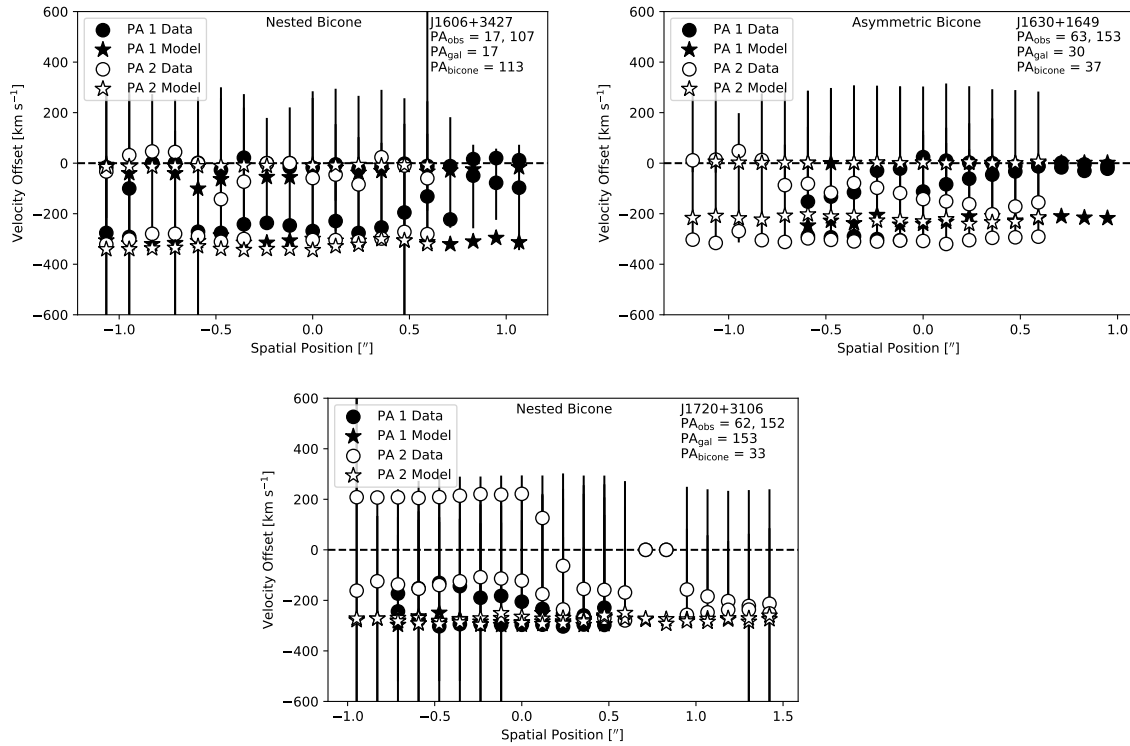


Figure B.3: As Figure 3.3, but for the remaining 15 galaxies not shown there.

B.3 Initial Conditions

This section accompanies Chapter 4.

We vary the initial masses, mass ratios, gas fractions, and B/T (bulge-to-total mass) ratios of the merging galaxy models based upon previous work with similar merger simulations (e.g., Cox et al. 2008; Lotz et al. 2008; Blecha et al. 2011, 2018). Additionally, we select the values for these initial conditions based upon the range of observed values for present day galaxies in SDSS as in Cox et al. (2008). Our goal is to produce simulated mergers that are typical of merging galaxies in SDSS and also comparable to previous work with the imaging predictors of simulated galaxies (e.g., Cox et al. 2008; Lotz et al. 2008).

Our simulations span a range in total stellar mass $10.6 < \log M_{\star}(M_{\odot}) < 10.8$, which agrees well with the fiducial models used in Cox et al. (2008) that have a range in total mass $9.0 < \log M_{\star}(M_{\odot}) < 10.7$. SDSS galaxies span a range in stellar mass (for individual galaxies) of $9 < \log M_{\star}(M_{\odot}) < 11$. When we compare this to the total mass of the merger simulations (which combine two galaxies), we find that the simulated galaxies are in the middle of the expected mass range for SDSS galaxies.

We vary the total mass ratio between 1:2 and 1:10 to capture three major merger simulations and two minor merger simulations. We are able to compare to Lotz et al. (2010a) and Cox et al. (2008), who choose mass ratio ranges of 1:1-1:20 and 1:1-1:22.7, respectively.

We select gas fractions between 0.1 – 0.3. This range is typical of the SDSS galaxies, which have gas fractions between 0 and 0.5 (Catinella et al. 2010). The mean gas fraction of the SDSS population is $\sim 0.2 - 0.3$, which is in good agreement with our choice to run most galaxy simulations with a gas fraction of 0.3. Additionally, Cox et al. (2008) and Lotz et al. (2010b) vary the gas fraction between 0.2 – 0.4 and 0.2 – 0.5, respectively, providing a good amount of overlap for comparison of results.

Most of our simulations do not have stellar bulges, but we do include bulges in the minor merger simulations. Cox et al. (2008) demonstrate that bulges act to stabilize the disk

of the galaxy for large mass ratio mergers (they see this effect primarily for 1:5 to 1:20 mass ratio mergers), leading to less disturbed morphology than bulgeless mergers. Since this effect is most prominent for minor mergers, we include stellar bulges in the progenitor galaxies for these simulations. We lack the computation resources to additionally investigate this effect for major mergers.

The B/T ratio depends on the total stellar mass of a galaxy and SDSS galaxies range between $9 < \log M_*(M_\odot) < 11$. Measured B/T ratios for this stellar mass range for galaxies in SDSS span $0 - 0.6$ (Bluck et al. 2014). Therefore, our choice of a B/T ratio of 0.2 for the minor merger simulations is typical of SDSS galaxies. We use a matched sample of isolated galaxies so that the slightly enhanced C and n values for the minor mergers (relative to the major mergers) are accounted for in the LDA technique.

B.4 Merging Galaxy Priors

This section accompanies Chapter 4.

LDA requires a prior to characterize the dataset if the relative numbers of objects in each class are not representative of the overall population. If the frequency of merging and nonmerging galaxies in our simulated dataset exactly matched the frequency of merging and nonmerging galaxies in nature, our priors would be $[0.5, 0.5]$ and would not need to be specified. However, since we have a lower frequency of nonmerging galaxies in our inputs to LDA relative to the frequency of nonmerging galaxies in reality, we use the fraction of merging galaxies in the universe (f_{merg}) as our prior.

We use a different fraction for major and minor mergers. For major mergers, we use the fraction of merging galaxies, $f_{\text{merg}} = 0.1$ from Lotz et al. (2011). This is an average, calculated from different f_{merg} measurements that rely upon *Gini*- M_{20} and A to determine merger fractions for galaxies in the local universe (Lotz et al. 2008; Conselice et al. 2009; López-Sanjuan et al. 2009; Shi et al. 2009). We choose not to use pair fractions to determine f_{merg} as they tend to underestimate the fraction of merging galaxies since pair studies are

only sensitive to the early stages of a merger.

It is important to note that Lotz et al. (2011) use individual predictors (such as $Gini - M_{20}$ or A alone) to identify mergers, and find short timescales of observability ($\sim 0.2 - 0.6$ Gyr). As discussed in Section 4.3.2, we find timescales of observability > 2 Gyr from the LDA technique and therefore $f_{\text{merg}} = 0.1$ is a conservative estimate. In reality, observed merger fractions may be underestimated in the local universe (particularly for minor mergers) since the observability timescales of past imaging methods are short. Using merging galaxies in the Millennium simulation, Bertone & Conselice (2009) find that the estimate of f_{merg} for minor and major mergers increases by a factor of $2 - 10$ if the observability timescale is increased from 0.4 Gyr to 1 Gyr.

While the fraction of minor mergers is less certain, studies have indicated that it is $3 - 5$ times greater than the major merger rate, so we use $f_{\text{merg}} = 0.3$ for the minor merger simulations (e.g., Bertone & Conselice 2009; Lotz et al. 2011).

For comparison purposes, we also estimate f_{merg} from the Illustris simulation. Using estimations of the timescale of the merger, we convert from merger rate (measured directly from Illustris to be $\sim 0.1 \text{ Gyr}^{-1}$ (Rodriguez-Gomez et al. 2015)) to the merger fraction of galaxies in the local universe. If we multiply this rate by the ~ 2 Gyr timescale estimate from our work, we find $f_{\text{merg}} = 0.2$, which is in good agreement with the 0.1 value for f_{merg} from observations of merging galaxies in the literature. If we use the $0.2 - 0.6$ Gyr timescale from Lotz et al. (2008), we find a much lower merger fraction of $f_{\text{merg}} = 0.02 - 0.06$.

Since the estimates of f_{merg} are so uncertain, we compare the results of using different values for f_{nonmerg} on the outcome of the LDA in Figure B.4. For each simulation, we have more snapshots of merging galaxies than nonmerging, which is not reflective of reality. We use the LDA accuracy to measure the sensitivity of the technique to the input priors. We find that the LDA is relatively insensitive to prior selection within a range of priors on the fraction of merging and nonmerging galaxies. This range exists from $0.1 < f_{\text{nonmerg}} < 0.9$. As we increase f_{nonmerg} above 0.9, we start to see the accuracy decline from $\sim 80 - 90\%$

correct identifications to 60–70%. While this is a significant decline, the decline is somewhat asymptotic. Therefore, at our chosen prior for major mergers (0.9), the accuracy has declined to around 90% for the three major merger simulations pictured, which is still very high. Additionally, while the minor merger simulations are less accurate as f_{nonmerg} increases, the prior for minor mergers is 0.7, so they do not fall off as fast in accuracy at this point.

B.5 Testing the Assumptions of LDA with Multivariate Analysis

This section accompanies Chapter 4.

We carry out a simple multiple linear regression analysis to test the assumptions of LDA and examine the input predictors. Many of these techniques as well as an introduction to LDA are covered in James et al. (2013). The key assumptions of LDA include multivariate normality, homoscedasticity (that the covariance among groups is equal), and an absence of multicollinearity. However, it should also be noted that LDA is relatively robust to slight violations of these assumptions and can still be reliable even when certain assumptions are violated (Duda et al. 2001; Li et al. 2006). We conduct a preliminary multivariate analysis of the input predictors to screen for multicollinearity and violations of normality and homoscedasticity. We present our results for the major merger and minor merger combined simulations and show plots just for the major merger combined simulation.

We first address the multivariate normality assumption by examining the individual histograms of the input predictors for both of the combined simulations (the major merger combined simulation is Figure B.5). Visually, the predictors do not seem to be drawn from a normal distribution. We conduct Shapiro-Wilke and Kolmogorov Smirnov tests for normality and in both cases we are able to reject the null hypothesis that the data are drawn from a Gaussian multivariate normal distribution for the majority of predictors.

We also address the homoscedasticity assumption in Figure B.5. By examining the distributions of the values for each class for a cross-section of input predictors, we are able to determine that the covariances for each class are not equal. We conduct a Levene test

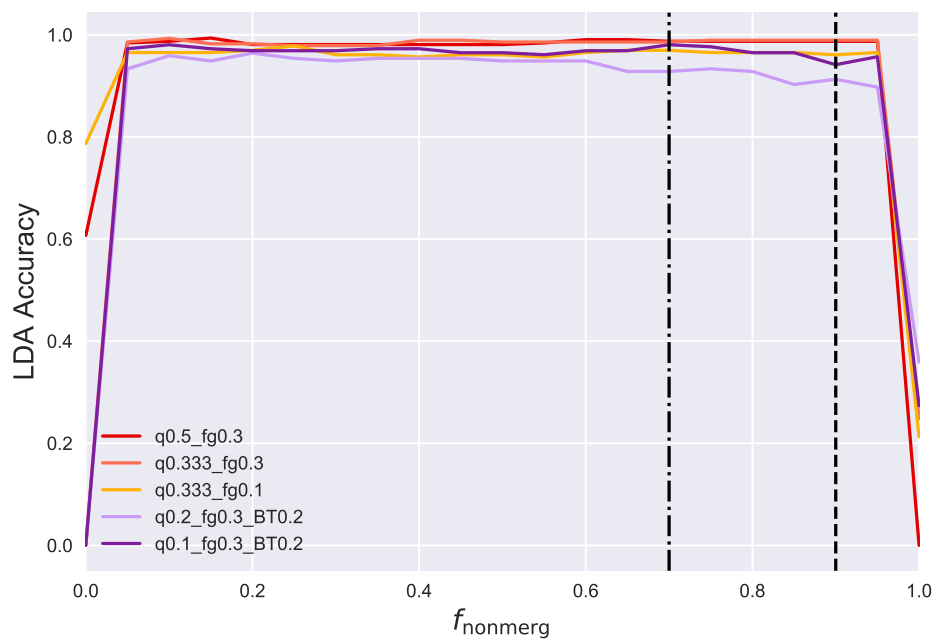


Figure B.4: Accuracy of the LDA with varying choices for the priors, or the fraction of galaxies that are merging and nonmerging. The vertical dashed lines represent our choice of priors for minor ($f_{\text{nonmerg}} = 0.7$) and major mergers ($f_{\text{nonmerg}} = 0.9$).

and confirm that we can reject the null hypothesis and that the covariance matrices are not equal. This is unsurprising given that multivariate normality is also violated.

We next examine the relationships between predictors to determine if the predictors demonstrate multicollinearity. A violation of multicollinearity could lead to a decrease in the predictive ability of LDA. We screen for multicollinearity visually in Figure B.6 using a Hinton visual diagram where the size and color of the boxes indicate the strength and sign (positive is red and negative is blue) of the correlation. We find that many predictors have a large positive correlation. We further examine the strength of the correlation and find that n and C have the most significant correlation for the major mergers with a Pearson's r value of 0.72. For the minor mergers, M_{20} and A have the largest correlation with an r value of 0.66. All Pearson's r values are below 0.99, the threshold value for multicollinearity, so we can rule out multicollinearity in this dataset. However, we must still deal with these correlations using interaction terms, which remove cross-correlation effects from the coefficients of LD1 so that we can individually assess trends with the seven main coefficients (James et al. 2013).

To screen for outliers we use box and whisker plots. Outliers can affect the LDA classification, dominating the analysis. We find that a few inputs are greater than 1.5 times the interquartile range (as indicated by the extent of the whiskers). However, overall, there are very few outliers. We also calculate the z scores for each predictor and find that none are outside 3σ from the sample mean.

To verify that each predictor is necessary in the LDA, we conduct Ordinary Least Squares (OLS) fitting. We first linearly regress each predictor against the class label (a binary variable for merger/nonmerger classification). While a logit regression would be a better tool with more than two classes, a linear regression is appropriate here since the response is binary (James et al. 2013). Additionally, for a binary response variable, LDA is quite similar to multiple linear regression. We find that almost all predictors have a p -value for the t -test below 0.05, indicating that there is a significant relationship between the predictor and the class, or in other words, that the predictor is required for classification. The

only predictors that fail this test are the *Gini*, M_{20} , and S predictor, which fail for the minor merger simulations, and the n predictor, which fails for the major merger simulation. We also find in our LDA modeling that the *Gini*, M_{20} , and S predictors are fairly unimportant for the minor merger simulation and that n is unimportant for the major merger simulation. We also run the OLS fitting for all simulations and find that there are no predictors that are unimportant across the board. Therefore, we include all of the predictors in the LDA classification. We ultimately discover that all predictors are important according to the forward stepwise selection for certain simulations, so we cannot eliminate them prior to the LDA.

Overall, the data violate multivariate normality and homoscedasticity while passing the tests for multicollinearity and extreme outliers. For classification purposes, LDA is very robust to varying distributions of the data and can still achieve good performance even when the covariance matrices are not equal and normality assumptions are violated (Duda et al. 2001; Li et al. 2006).

One alternative approach to LDA is to utilize Quadratic Discriminant Analysis, which does not rely on the equality of covariance matrices. We test the accuracy, precision, recall, and F_1 score of both an LDA and a QDA method (see Appendix B.7 for the accuracy of LDA). We find that the LDA classifier performs very well and while the QDA classifier increases accuracy, recall, and F_1 score by $\sim 5\%$, the LDA classifier is still above $\sim 85\%$ for accuracy on all simulations. A downside to using QDA is that it is inherently nonlinear and does not allow us to directly interpret each predictor individually. We choose to use LDA since it allows for a more practical interpretation of the imaging predictors and since it does an adequate job of separating the merging and nonmerging classes across all simulations.

Additional ways to prepare the input data for better classification include increasing the number of observations (number of galaxy snapshots) and standardizing the data. We already have at least 20-30 snapshots per class and are therefore more robust to violations of normality and homogeneity of covariance. Also, when we combine all the individual runs

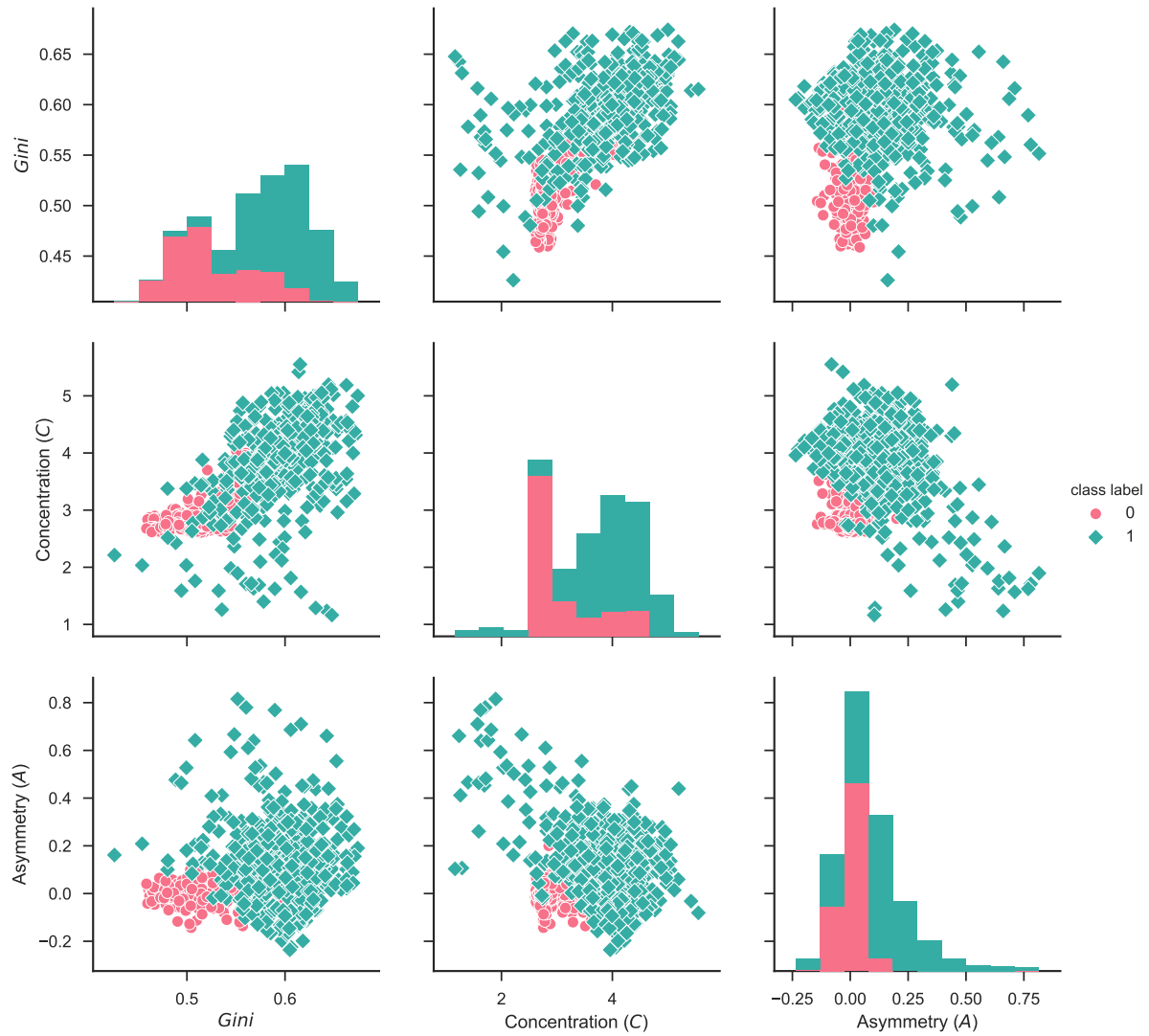


Figure B.5: Scatter plots and marginalized histograms of the distribution for three input predictors ($Gini$, C , and A) for the major merger combined simulation. The nonmerging class is pink (0) and the merging class is green (1). The predictors violate normality and homoscedasticity assumptions.

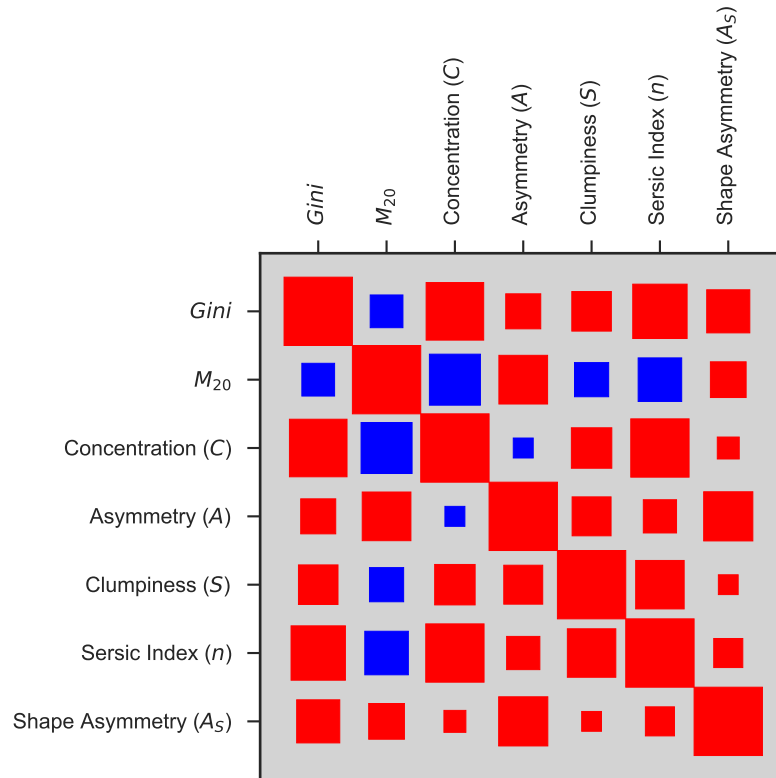


Figure B.6: Hinton visual correlation matrix for the major merger combined simulation. A red box represents a positive correlation and a blue box is a negative correlation. The size of the box is the strength of Pearson's r correlation coefficient. For scale, the diagonal boxes have a Pearson's r values of one.

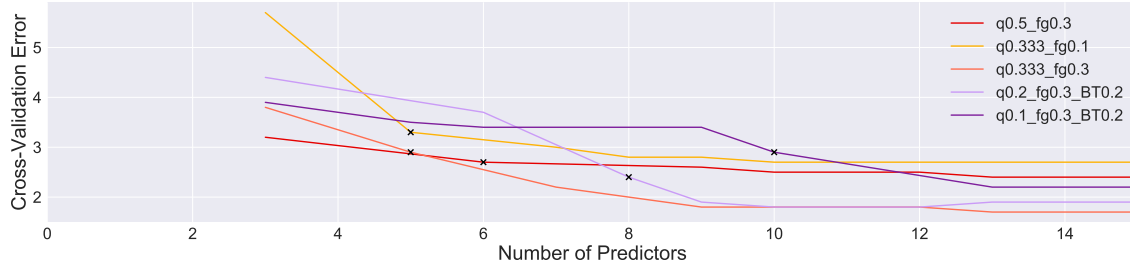


Figure B.7: Forward stepwise selection of the number of predictors for each run of LDA. We mark the minimum number of ‘required’ predictors for each run with black xs. This point is within one standard error of the minima of the cross-validation error curve for each run. We run LDA for each simulation using the predictors selected from this method.

of LDA for the final combined major and minor merger runs, we increase the sample size to at least 100 observations per class. This final analysis is robust to violations of normality and homoscedasticity.

We also find that the predictors require standardization prior to the input to LDA; they have very different means and standard deviations, which could affect the output of LDA. For instance, if one variable has a large mean, it could dominate the first discriminant axis (LD1). We standardize the input predictors to all have a mean of zero and a standard deviation of one prior to our LDA classification.

B.6 Forward Stepwise Variable Selection and k-fold Cross-Validation

This section accompanies Chapter 4.

A limitation of LDA is that there are no standard errors on the LDA predictor coefficients. We use the stratified k -fold cross-validation method with ten folds to return an estimate of the underlying distribution of possible values for the LDA coefficients given the data. k -fold cross-validation functions by dividing the sample into k equal sized samples, where the first $k-1$ samples will be used as the training set and the k th sample will be used as the test set. We repeat the LDA k times and estimate the mean and standard deviation

of the LDA coefficients from the data. Stratified cross-validation specifically requires that the test sample includes a number of snapshots from each class that are representative of the overall sample.

This method is effective for minimizing bias and variance given the correct choice of k (James et al. 2013). For instance, Efron (1983) prove that k -fold cross-validation is ‘almost unbiased’ if k is large and the sampling is random (this approaches leave one out cross-validation (LOOCV), when $k = n$ where n is the sample size). However, LOOCV has a high variance since it involves finding the variance of n fitted models which are trained on nearly identical data. The mean of highly correlated quantities has a higher variance, so we choose an intermediate value of k so that we avoid high bias and high variance. Kohavi (1995) find that stratified k -fold cross-validation with ten folds is the most effective at model selection even if computation power allows for more folds. We also find that $k=10$ is a good choice to ensure that the number of misclassifications (cross-validation error) is minimized and that the mean and standard error of the LD1 coefficients is stable.

We use forward stepwise selection with k -fold cross-validation to determine which predictors are necessary to build LD1 for each simulation. The purpose of this process is to avoid introducing excess predictors that are unnecessary to the separation of the merging and nonmerging galaxies along LD1. We choose forward stepwise selection since it is less computationally expensive than best subset selection (James et al. 2013).

Forward stepwise selection begins with a model without predictors. It then determines which predictor to add by comparing the cross-validation error for each predictor. The cross-validation error is also the number of misclassifications corresponding to each model. For instance, the first step of forward stepwise selection is comparing the cross-validation error from a model with only one predictor (i.e., *Gini*) to all other possible models with only one term (i.e., a model with M_{20} , a model with $M_{20} * Gini$, etc.). The one-term model with the lowest number of misclassifications is selected. Next, the forward stepwise election iteratively attempts to add all remaining predictors to the model. It chooses to add a term only if

the cross-validation error of the overall model is less than that of the previous step. Again, it adds the term that minimizes the cross-validation error as compared to all other possible terms.

The forward stepwise selection proceeds until no more terms are required to decrease the cross-validation error. We refer to the predictors in the final model as the ‘required’ predictors. We show the process in Figure B.7, where we determine the number of predictors necessary for the LD1 for each simulation by minimizing the cross-validation error with forward stepwise selection. We additionally use the one-standard-error rule from James et al. (2013) to select the best overall model. This allows us to select the simplest model for which the estimated cross-validation error is within one standard error of the lowest point on the curve in Figure B.7. The standard error of the cross-validation error is the standard deviation of the number of misclassifications for all ten k -folds.

B.7 LDA Performance: Accuracy and Precision of the Classifier

This section accompanies Chapter 4.

We investigate the performance of the classifier using the confusion matrix (Figure B.8). The confusion matrix is constructed using the ten randomized test and training sets of galaxies, which were created in the k -fold method described in Appendix B.6. It is the mean confusion matrix from the ten k -fold runs.

The confusion matrix shows the number of nonmerging galaxies from the test set that were correctly classified as nonmerging (upper left) and the number of merging galaxies that were correctly identified as merging (lower right), which are referred to as ‘True Negatives’ (TN) and ‘True Positives’ (TP), respectively. The top right corner of the confusion matrix is the galaxies that were classified as merging although they are in fact nonmerging. These are the ‘False Positives’ or FP. The bottom left square is the galaxies that are merging but were not correctly identified as merging, or the ‘False Negatives’ or FN. In Figure B.8 we show the normalized percentage of galaxies that fall into each category for the final combined major

and minor merger runs of LDA.

From the confusion matrix, we quantify accuracy, precision, recall, and F_1 score of the LDA classification in order to assess the overall performance of the LDA method for each simulation.

The accuracy is the number of correct classifications divided by the total number of classifications:

$$A = \frac{TN + TP}{TN + TP + FN + FP}$$

We assess the precision of the LDA, or the fraction of correct positive predictions:

$$P = \frac{TP}{TP + FP}$$

Recall is the fraction of true positives that are classified as such:

$$R = \frac{TP}{TP + FN}$$

The F_1 score is the harmonic mean of recall and precision:

$$F_1 = \frac{2TP}{2TP + FN + FP}$$

We collect the accuracy, precision, recall, and F_1 score values for all simulations in Table A.23. We find that the LDA classification performs well, with all performance metrics around or above $\sim 0.7 - 0.9$. Accuracy ranges from $0.85 - 0.91$ while precision is between $0.89 - 0.98$ for all runs. This confirms our discussion from Section B.5; the LDA method is accurate, and therefore we are not concerned that our violations of normality and homoscedasticity are detrimental to the classification.

The LDA has a very high precision value. This indicates that it does an excellent job of identifying all merging galaxies as merging. This is critical to the next phase of analysis, which will include classifying SDSS galaxies; we do not wish to misidentify mergers and are

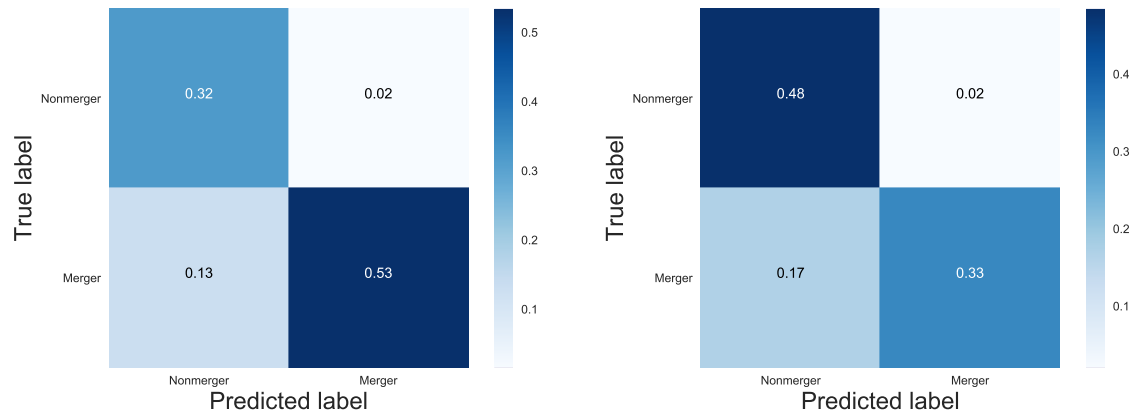


Figure B.8: Confusion matrices for the major (left) and minor (right) combined simulations. The y axis represents the true categories of the test set of galaxies from the simulation. The x axis is the predicted category from the LD1 classifier for the test set of galaxies.

more tolerant with false positives than false negatives, given that this initial classification is created from simulated galaxies.